523

SQUEEZE FILM AIR BEARINGS WITH FLEXIBLE SUPPORTS

By

Fernando Pina da Silva, Mech. Eng. (Dipl. I.S.T.)

A thesis submitted for the degree
of Doctor of Philosophy of
the University of London and for
the Diploma of Imperial College

March 1980

Mechanical Engineering Dept.,
Imperial College,
London SW7

I dedicate this work to

my wife, Sara, for sharing the moments of defeat, and those of success, that will not be written on the following pages.

My Parents, Fernando and Salette, but I couldn't find the proper words.

ABSTRACT

Squeeze film bearings operate on high frequency vibration of one of the bearing surfaces. The time-averaged pressurisation effect is mainly due to the compressibility of the gas film and this degree of pressurisation depends on the amplitude and frequency of oscillation of the moving surface. If this supporting surface is sufficiently flexible, the amplitude of vibration is not uniform. An investigation on the effect of this non-uniformity on the performance of the squeeze film is presented. The characteristics of the supporting member are demonstrated to be critical as they dictate the frequency of operation at low input power. Cases considered respect discs and conical shapes. For discs a particular parameter, the ratio between the inner and the outer edges, is analysed. The amplitudes of vibration are experimentally measured using an optical technique. The resonant frequencies and the frequencies where the lift occurred are compared. It is shown that a close relationship exists between both frequencies. Theoretical procedures to obtain the value of the resonant frequency for the case of discs and cone bearing surfaces are considered. The results obtained are compared with those obtained experimentally. The methods used for the solution of the Reynolds equation for the case of non-uniform vibrations are also discussed.

ACKNOWLEDGEMENTS

The author gratefully acknowledges the following personalities for their contribution to this work:-

- Dr Ramsey Gohar for his guidance and supervision,

- Professor Luciano Faria who suggested and encouraged this work,

- The Calouste Gulbenkian Foundation for the student-ship awarded and the very good service provided by its Scholarship Department,

- The Instituto de Alta Cultura for permitting the leave from the Instituto Superior Tecnico (Libson University) during this research,

- The Admiralty Compass Observatory, and especially Mr. Huxley, for the interest, support and facilities dedicated to this project,

- The Science Research Council for the equipment grant,

- Mr. Mike Sainsbury for his invaluable advice and suggestions on vibrations,

- My colleague Julio Montalvao for his assistance on some experiments of Chapter Five and Mr. Ray Gunn for his ever friendly help on many technical matters,

- Mrs. Archer of the Mechanical Engineering Library,

for only her patience made possible the use of some references quoted,

- Mrs. Shelagh Murdock and Mrs. Izabel d'Oliveira Neves for the excellent typing,
- all my friends for their cheerful encouragement.

CONTENTS

CONTENTS (Contd)

CONTENTS (Contd)

CONTENTS

TABLES

NOMENCLATURE

A - amplitude of vibration for rigid body, constant

A_c - ceramic base area

A_r - bearing area (for Boyle's law)

B - constant (in disc motion expression)

C - constant (in disc motion expression)

D - constant (in disc motion expression)

$\bar{D}$ - flexural rigidity

E - Young Modulus

e_o - voltage applied to piezoelectric ceramic

F - bearing force

F^* - dimensionless force = $\dfrac{F}{\pi p_a r_b^2}$

F_b - force applied to the bearing base

F_c - force applied to the piezoelectric ceramic

F_d - force applied to the bearing disc

H - dimensionless film thickness = $\dfrac{h}{h_o}$

h - film thickness, local

h_d - plate thickness

h_n - "neck" height

h_o - minimum film thickness

h_s - cone thickness

h^* - quadrature stiffness

k - frequency parameter $\left(\frac{\rho\, h_d\, \omega^2}{\bar{D}}\right)^{1/4}$

K_c - stiffness of piezoelectric ceramic

L - squeeze film prototype bar length

M_θ - bending moment component on θ coordinate

M_r - bending moment component on r coordinate

M_z - bending moment component on z coordinate

$M_{r\theta}$ - twisting moment

P_a - atmospheric pressure

P_b - correted boundary pressure (Boyle's law)

P_{max} - maximum value of pressure in one cycle of squeeze motion

P_{min} - minimum value of pressure in one cycle of squeeze motion

P_{v_1} - pressure correspondent to volume v_1

$P_{v_1\ sat}$ - pressure of saturation for volume v_1

P - dimensionless pressure $\left(\frac{P}{P_a}\right)$

$\bar{P}$ - pressure mean value

Q_{mech} - mechanical Q factor

Q,q - transverse force, transverse force per unit of perimeter

r - radial coordinate

R - typical bearing dimension

R^* - dimensionless radius $\left(= \frac{r}{R_o} \right)$

Q_{mech} - mechanical Q factor (defined in 7.3.3)

R_o - disc bearing radius

$\bar{r}=\frac{\omega}{\rho_o}$ - dimensionless frequency variable

t - time coordinate

t_c - ceramic thickness

T - dimensionless time coordinate ($=\omega t$)

u - tangential displacement component (cone s)

u_n^j - step value for point n at j iteration

v - displacement component along the generator (cone analysis)

$\vec{V}$ - vector sum of the absolut sliding velocities of the bearing surfaces.

z - coordinate normal to the shell mean plane

w - displacement component normal to the middle plane of the shell

W^*, W

$W_{resonance}$ - amplitude vibration at frequency of resonance of system

w_1 - amplitude of vibration ($=\frac{w_{resonance}}{\sqrt{2}}$)

w_b - displacement at point r_b

w_{exp} - amplitude of vibrational motion, experimental

w_{the} - amplitude of vibrational motion, theoretical

w^* - velocity associated with displacement w

$\Delta_A, \Delta_B, \Delta_C, \Delta_D$ - determinants used for the disc receptance expressions in Appendix 5

J_o, Y_o, I_o, K_o - Bessel functions of zero order

J_i, Y_i, I_i, K_i - Bessel functions of first order

GREEK SYMBOLS

α - cone half apex angle

α_b - receptance for base unit at point P

α_{bb} - receptance expression for point at radius r_b and excitation force at the same point

α_c - receptance for piezoelectric ceramic

α_d - receptance for disc at a point of the inner boundary

α_{rb} - receptance expression, general

ε_o - excursion ratio $(= \frac{A}{h_o})$

γ - fluid density

μ - fluid viscosity

σ - squeeze number $(= \frac{12 \mu \omega}{P_a R_o^2})$

η - loss factor (defined in 7.3.3)

Λ - compressibility number $(= \frac{6 \mu \omega L}{P_a h_o})$

ν - position's ratio

$\vec{\chi}$ - vector of coordinate components $\begin{Bmatrix} x \\ y \end{Bmatrix}$

$\vec{\chi}$ - vector of coordinate components $\begin{Bmatrix} x_b \\ y_b \end{Bmatrix}$

ψ - dimensionless variable (=PH)

Γ - compression ratio

ω - circular frequency

θ - angular coordinate

ϕ - density

ΔE - energy dissipated in a system in one cycle

ΔE_{ω_1} - energy dissipated at amplitude of vibration ω_1

Abbreviations

ACO - Admiralty Compass Observatory

ASME - American Society of Mechanical Engineery

CLA - Center line average

S.F - Squeeze film

MTI - Mechanical Technology Incorporate

E.P. - Externally pressurised (bearing)

CHAPTER 1

SQUEEZE FILM EFFECT

1.1 INTRODUCTION

Conventional gas lubricated bearings fall into two main classes:

- Aerostatic bearings, which require a feed of pressurised gas for their operation, and
- Aerodynamic bearings, self acting, which originate their own internal pressure build up by means of the fluid motion.

Recently, a third class was introduced, the squeeze film bearings, which are the subject of this thesis.

The working principle of the three types of bearings mentioned are represented in Fig. 1.1 and Fig. 1.2.

Fig. 1.1 shows the case of two flat plates with a lubricating film between the two, and the velocity gradients across the fluid flowing between the two plates. The case c) represents the self-induced pressure generation due to the converging surfaces as in self acting bearings. The externally pressurised bearings and the squeeze film bearings have a greater similarity, which is emphasised in Fig. 1.2.

In an externally pressurised bearing the air is supplied to the bearing surfaces through either a single control jet or a ring of jets between the bearing surfaces.

The application of the external load perpendicular to the surface reduces the clearance, increasing the aerodynamic resistance of the gap relative to that of the jet. When equilibrium is established the clearance adjusts itself and the total pressure force is equal to the applied load.

Externally pressurised bearings offer the possibility of starting under load and work at lower or zero speed. Self acting bearings do not require any pressure source, exhaust sink or filtering system, but they are only able to support a small load per unit of area as a function of the speed and are very prone to instability. Need for close tolerances is the other major disadvantage of this type of gas bearing.

These two types of gas bearing and the squeeze film bearing differ fundamentally on the origin of the fluid flow. In all cases the pressurisation effect is obtained by viscous retardation of flow. In a self acting bearing, adherence to the sliding surface and a varying gap geometry cause the pressure variation. In the externally pressurised bearing it is the highly pressurised air

supply that produces a gas pumping action. In the case of the squeeze film bearing it is the periodical variation of the gap volume containing the fluid that forces a successive sucking in and out of the gas.

1.2 REVIEW OF PREVIOUS WORK AND APPLICATIONS

Squeeze film bearings cannot be considered as well established, even though some work on the subject dates from the last fifteen years. It is the aim of this section to provide a resume of the work of previous researchers. This survey will be as complete as possible for the author. It was thought, however, to cut out some details and refer to them, where relevant, in the subsequent chapters, as variables and parameters are defined.

The first reference to gas squeeze films is due to Tipei in 1954 (1)*. Later, Professor Reiner in 1956 made a non-intentional contribution on the subject through an experiment presented at an Applied Mechanics Conference in Brussels in 1956 (2). His aim was to show the non-Newtonian properties of air, using two discs, one static and the other spinning at high speed. The supposed non-Newtonian effect was later demonstrated by Taylor and Saffman (3) to be due

* References are given on page 282

to the existing misalignment and the relative normal motion between the discs. They also concluded that this could lead to a time-averaged pressure higher than the ambient.

The paper that first specifically dealt with the squeeze film effect was published by Langlois (4). He derived the equation governing the pressure distribution in a parallel flat squeeze film thrust bearing under isothermal conditions using a first order perturbation technique. A finite difference method was developed by Michael (5) for application to the time-dependant Reynolds equation. This important procedure will be reviewed in detail in Chapter 3. Theoretical results obtained with this method were compared with experimental values by Salbu (6). This work is extremely important as it seems to be the first relating the conduction of a series of conclusive experiments with thrust and journal squeeze film bearings. The thrust bearings were essentially composed of two parallel coaxial, flat discs, one of which was held stationary while the other moved sinusoidally in a direction normal to the surfaces. For journal bearings, combined with thrust bearings, no conclusions were reported. These experiments were conducted using voice coils as motion generators. Simultaneously, a team conducted by Pan and including Chang,

Malanoski and Orcutt (7, 8, 9, 10) was working for Mechanical Technology Incorporated in a project on squeeze film bearings for gyroscopes. The three first papers referred to a very particular model of squeeze film bearings and were quite significant for the analysis of the characteristics of different supporting member-driving unit arrangements. In the other reference, an asymptotic approach was proposed for the calculation of pressure distribution and load capacity for flat disc bearings. This procedure was fully developed by Pan (11, 12). This theory was then applied in (13) by Pan, Broussard and others, for a cylindrical (journal) squeeze-film bearing.

This application was restricted to small eccentricity and uniform or parabolic variation of excursion ratio. Excursion being defined as the ratio between the vibration amplitude of motion and the mean gap between bearing surfaces.

Most of the work published since then made use of the asymptotic theory, which is valid for large squeeze numbers, usually found in practice. This is the case of (14) by Pan and others for a rotating spherical squeeze film bearing. It was shown that squeeze film and self-acting effects are superimposable. Beck and Strodman (15), also used the asymptotic theory for the study of the stability

of infinite length squeeze film journal bearings. An extension of the asymptotic theory to the dynamic performance of these bearings when the external disturbance can be considered small compared with the squeeze motion was proposed by Elrod (16). Using theory from Diprima (17) for the establishment of the boundary conditions, Pan and Chiang (18) applied this dynamic study to the spherical squeeze film hybrid bearing. More work on spherical shapes is due to Beck and Strodtman (19), who considered a radial excursion operation instead of an axial excursion. They reported an increase in load capacity of about 50%.

In the squeeze film analysis, it is generally accepted that the film behaves isothermally and Pan (20) provided a confirmation for its validity, at least for high squeeze frequencies. Furthermore, Pan and Chiang (21) analysed the origination of bearing torques, and their influence on gyroscope gimbal bearings, where error torque is critical. This is also discussed by Strodtman (22). The effect of the ratio of the length to diameter of journal bearings was studied by Beck and Strodman (23). Another analysis of Pan (24) using the same perturbation analysis extended the asymptotic theory to include edge effects. The influence of the supported mass motion was considered

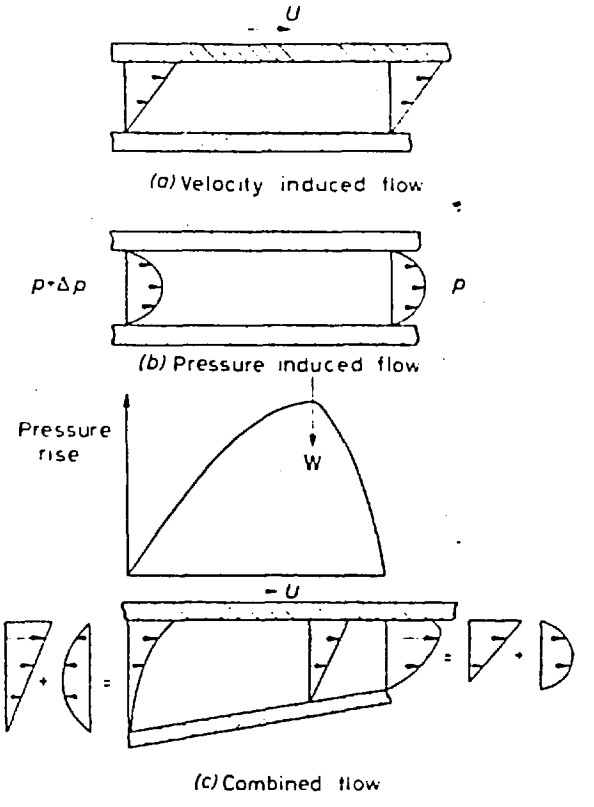

FIG.1.1 - Pressure building mechanism in self acting bearing (Ref. 32)

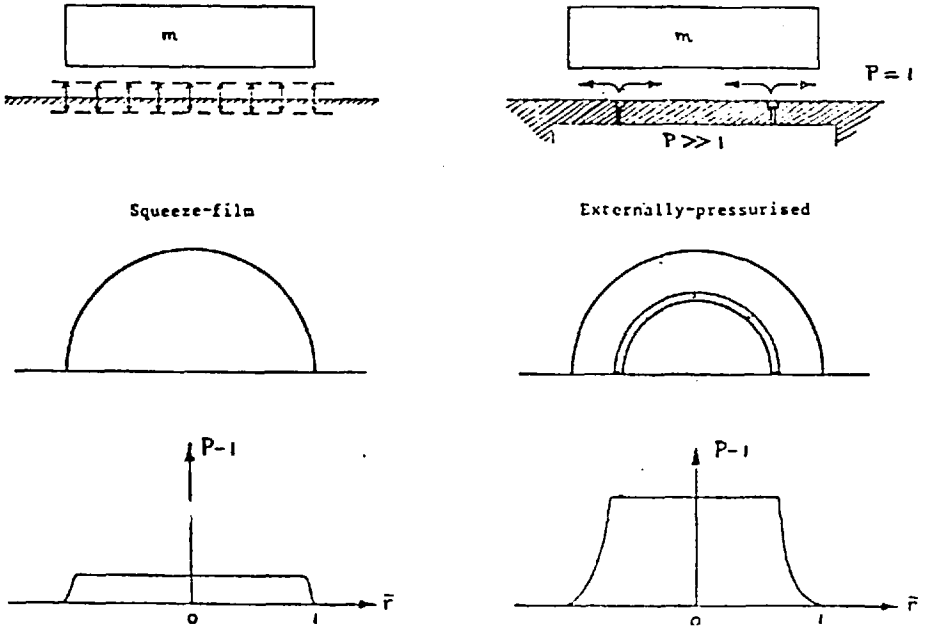

FIG. 1.2 - Comparison between pressure distributions for squeeze-film bearing and externally pressurised bearing (Ref. 29).

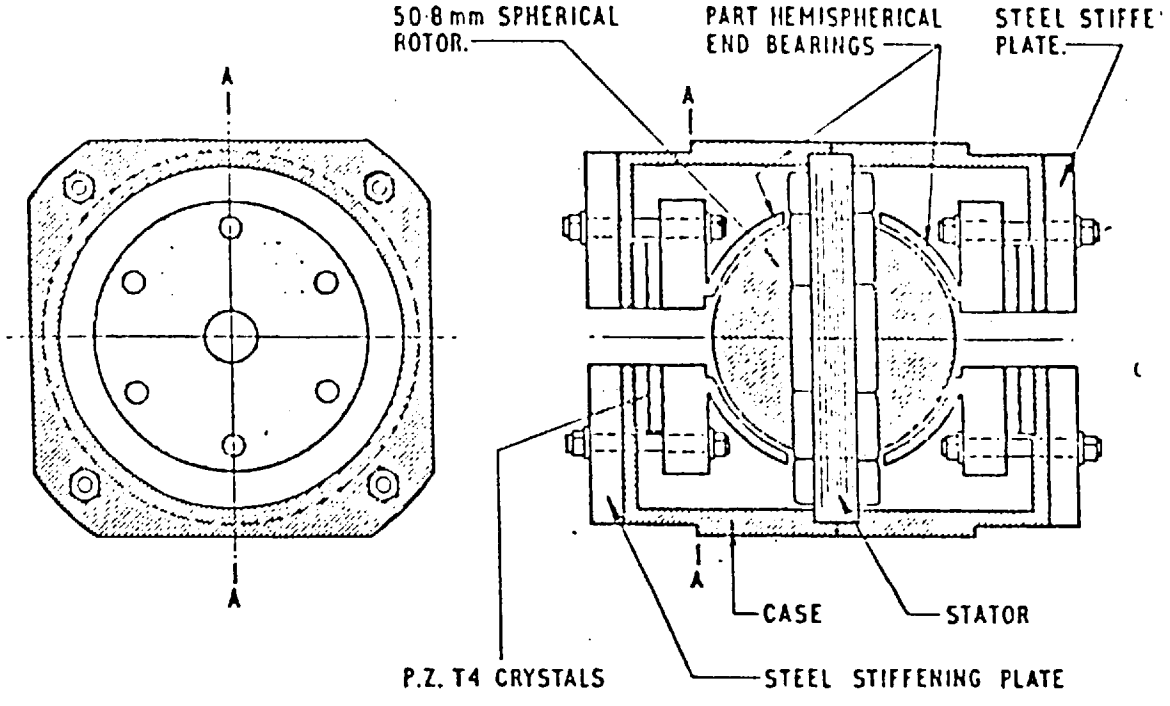

FIG. 1.3 Application of spherical squeeze film bearing to a gyroscope (Ref. 30).

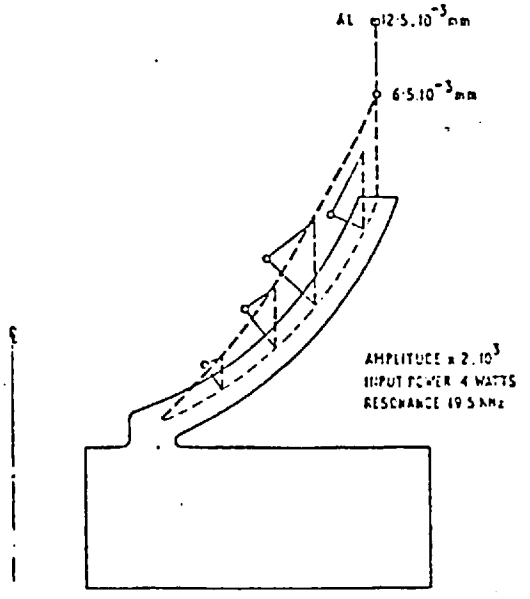

FIG. 1.4 Vibrational-mode shape for the spherical bearing of Fig. 1.3 (Ref. 30).

by Pan and Chiang (25) and again in another paper by Chiang and others (26). Earlier, Beck et al tackled this problem but without much success (27). Another important contribution was that of Constantinescu (28), about the influence of inertia forces on squeeze films. In another paper Strodtman (29) proposed an analytical solution for large values of eccentricity using a small parameter procedure. More recently, the tendency of research on squeeze film bearings has been conducted for the study of the influence of the incorporation of grooves. A very complete theoretical analysis has been provided by Cooke (30). This is an interesting work because, apart from a good physical interpretation of the fluid behaviour, there is a complete dynamical analysis. Huxley (31), working on the application of squeeze film bearings to navigational aids, suggested that the supporting member vibration modes could be a significant parameter on the performance of these bearings, Figs. 3 and 4. These are, to our knowledge, the latest research stages on this subject.

1.3 CONCLUSIONS

The two major applications of squeeze film bearings until now have been the support of gyroscope gimbals and slider bearings for the computer industry.

Thus, most of the work on this subject is due mainly to two teams of researchers, each one with an interest in either thrust or journal bearings. It is possible to see from the work mentioned in the previous section that the general approach to the problem is established, and the latest papers now detail the influence of the various parameters involved. Though most of this work is theoretical, there is no general consistent experimental verification of the results provided.

At this point it seems that the two main fields of improvement are the study of effective grooving and the use of the flexibility of the moving surface. This last aspect is the object of the subsequent chapters.

CHAPTER 2

RESEARCH APPROACH AND FUNDAMENTAL ASSUMPTIONS

2.1 INTRODUCTION

In the previous chapter the contribution of the various authors was reviewed in historical order. We will now consider the principle of the squeeze film bearing. This approach would simplify the definition of the parameters.

2.2 PRINCIPLE OF THE SQUEEZE FILM BEARING

The model we consider as representative of a squeeze film bearing is shown in Fig. 2.1 and Fig. 2.2. The dotted lines mean an ideal boundary. The supported member and the electric power supply are both excluded. Nevertheless they are still important. The supported member imposes the load on the bearing and its geometric shape and position dictate the type of bearing shape that must be used: thrust or journal, conical or spherical shape, eccentricity, etc. The electrical supply restricts the power available and the working frequency range. The two are related through the bearing performance. This is the main objective of the present study and thus we will only consider the elements within the referred boundary.

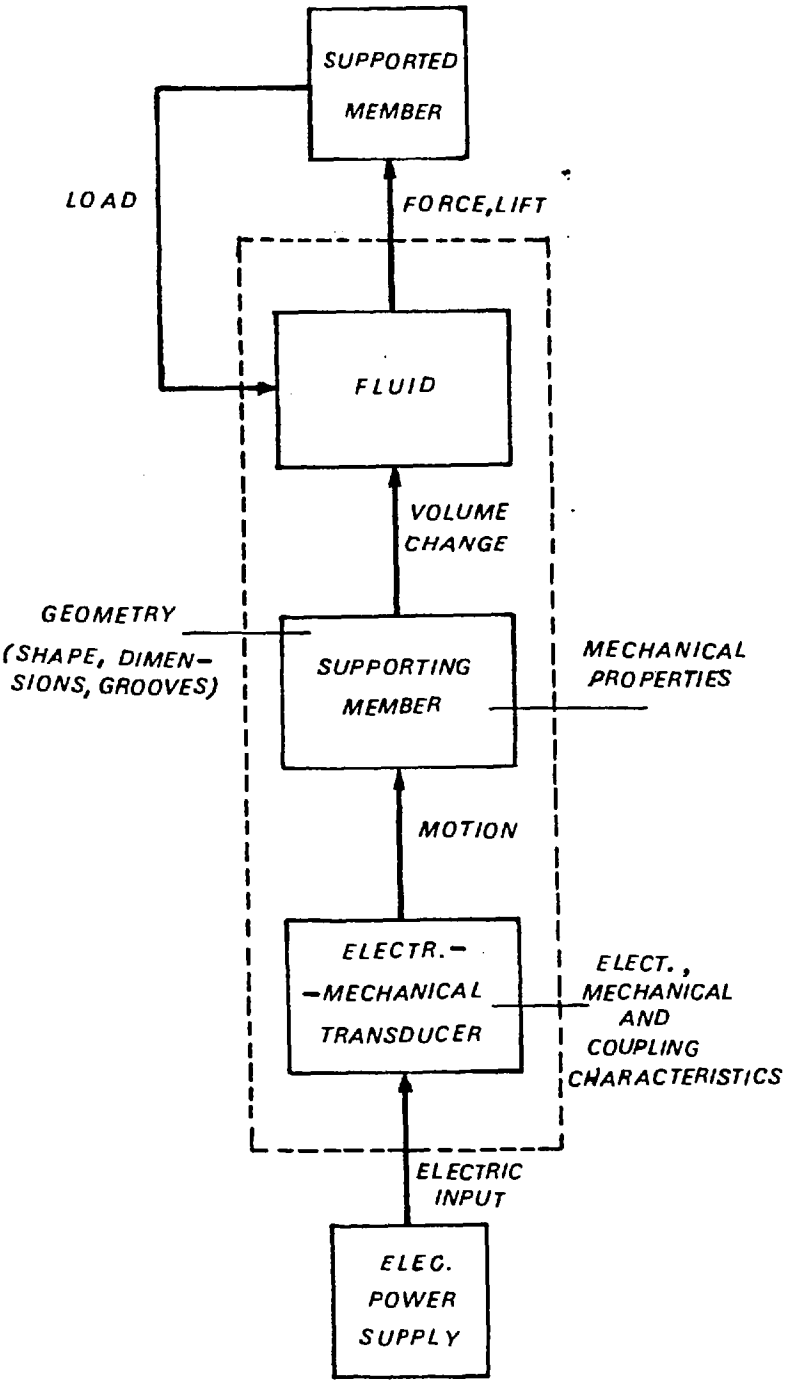

FIG. 2.1 Diagram for analysis main parameters.

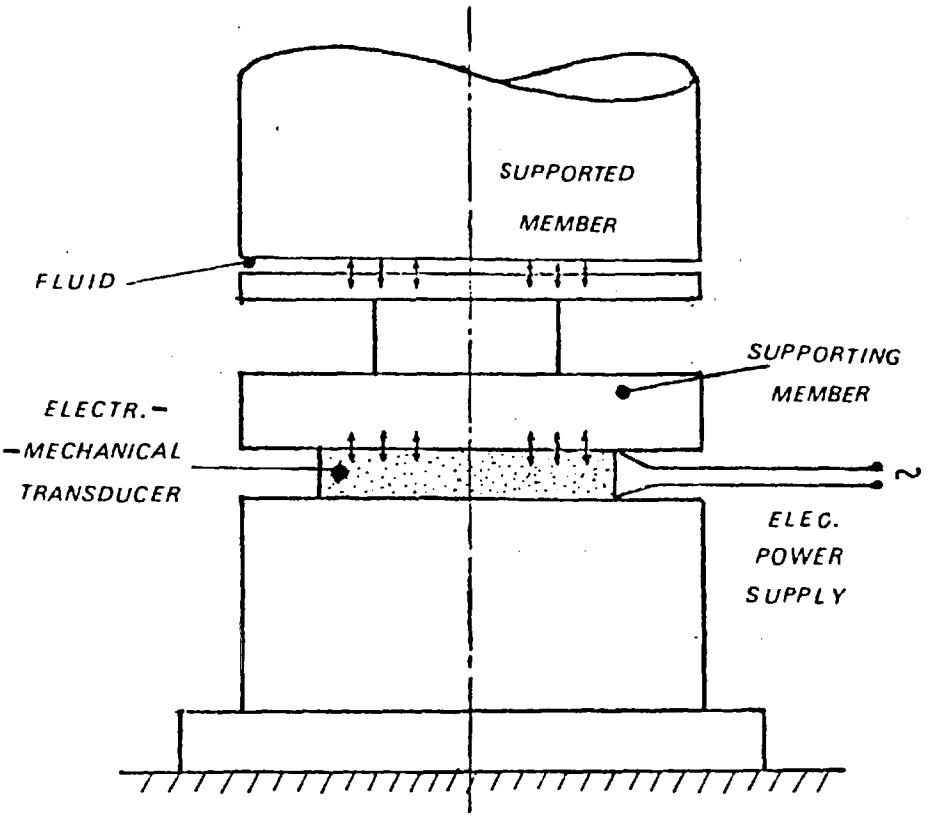

FIG. 2.2 Squeeze film bearing components.

The basic elements are three:-

1. The electromechanical transducer,

2. The supporting member that includes the bearing shape and any existing attachments to the electromechanical transducer,

3. The fluid.

The following sections will detail the parameters derived from these elements.

2.2.1 The Electromechanical Transducer

The squeeze film bearing pressure effect relies on the high frequency oscillation of the supporting member. In order to obtain this motion some kind of electromechanical device is necessary. A magnetic device was used in early experiments by Salbu[6] for electromechanical comparison. Magnetostatic materials have also been suggested, but it was soon realised that piezoelectric materials were most suitable for this purpose. Their main advantages are:

- small weight and size
- small power consumption
- good temperature stability
- availability in several sizes and shapes
- low internal power losses

Another extremely important advantage of these materials is their ability to be oscillated at high frequencies. The only major inconvenience of piezoelectric ceramics is their mechanical instability. During the operation of inducing the piezoelectric properties on the material, called 'poling', internal stresses are set up. During the life time of the piezoelectric ceramic there is a gradual relief of these internal stresses. This causes small changes of the ceramic shape and partial loss of some of the properties.

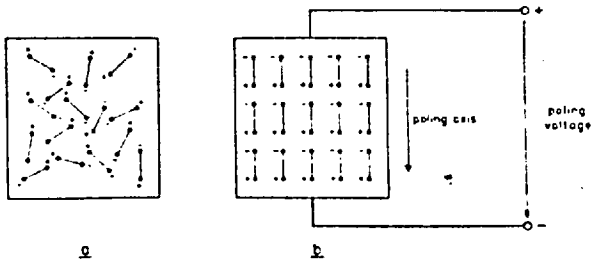

FIG. 2.3 Schematic representation of the poling phenomenon showing: a) random dipole orientation, and b) preferential orientation due to poling voltage.

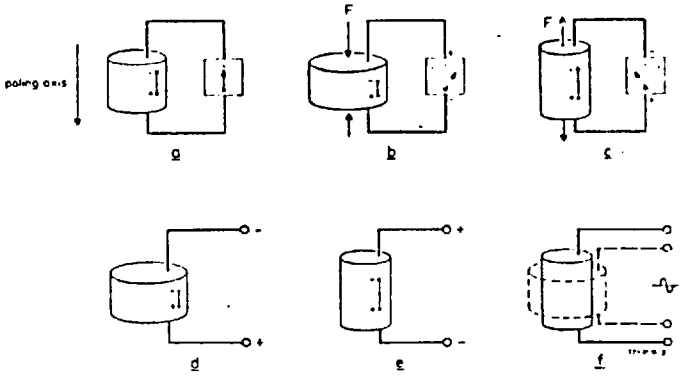

FIG. 2.4 Cylinder of piezoelectric material at rest in a), subjected to an external force in b) and c), and to voltage in d), e) and f).

However, ceramic materials are now well established as electromechanical transducers in squeeze film bearings. The operation of poling consists of the application of a voltage to the ceramic. This causes the mass of crystallites (electric dipoles) that constitute the piezoelectric material to become orientated in the direction of the applied voltage, Fig. 2.3(a) and (b). This electric field is applied at a temperature just below the Curie point*. After cooling the

---

* Curie point is the temperature at which ferromagnetic materials change to paramagnetic.

ceramic the dipoles cannot return to their original positions, the material is permanently piezoelectric and can convert mechanical energy into electric energy, and inversely. Fig. 2.4 illustrates the effect of the application of an external force to a cylinder of piezoelectric material. In a rest condition: (a) there is no voltage between the electrodes; if the applied force is compressive, (b) the generated voltage is of the same polarity as the poling one; when the force is tensile, (c) the polarity is reversed too. Shortening and lengthening of the crystal will occur if a voltage is applied between the electrodes (d), (e) and (f).

The two major parameters associated with the ceramics are the type of ceramic (composition) and its shape. There are natural piezoelectric materials like quartz, Rochelle salt and tourmaline. However, they have not been used in squeeze film applications as they are more expensive and difficult to cut to the appropriate shape. Materials that are currently in use are compositions of lead zirconite-barium titanate, commercially produced by the Clevite Company, under the series PZT. More recently, other varieties were made available from Mullard in their brand PXE, and also from Philips. Although the properties vary noticeably with the type of the material, there is no

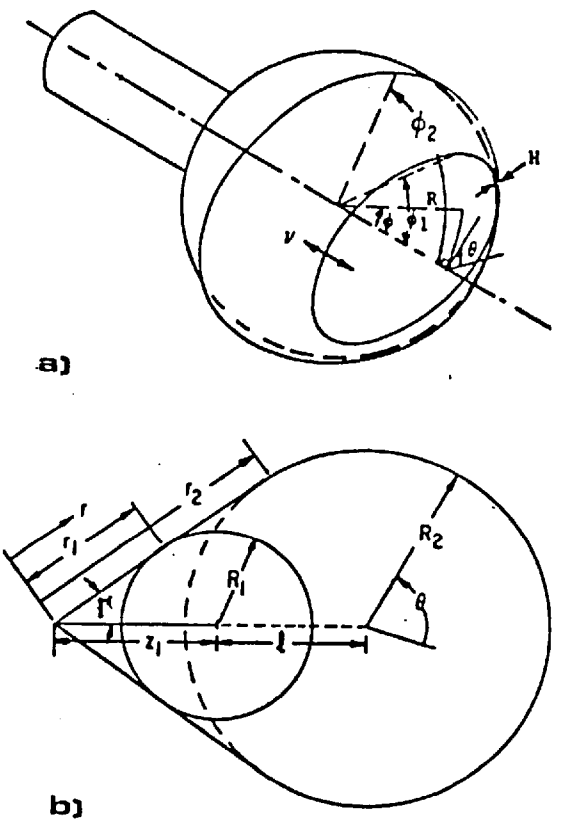

FIG. 2.5 Spherical a) and conical b) squeeze film geometries.

reference to any comparisons of the performance of these different materials.

The usual shapes for the piezoelectric ceramics are the simple disc for thrust bearings and the cylinder for the journal bearings, Fig. 2.6. Cylindrical shapes as used in journal bearings require very accurate tolerances and surface finish, and are therefore sensitive. In these examples the ceramics act directly as the supporting member. This means that the film thickness is directly dictated by

the vibrational modes of the ceramic. Reference to piezo-electric material characteristics will be included in Chapter 5.

2.2.2 The Supporting Member

2.2.1 Disc Bearings:

The mechanical expansion produced by the ceramic must usually be applied to a metallic shell acting as a moving member, Fig. 2.2. An exception already referred to is that of the journal bearings because of the difficulty of matching the dynamic behaviour of the ceramic and the metallic shell.

Discs have been initially used as supporting members by Salbu[6] with two different sizes, 1 in. and 1.75 in. diameters. Apart from reference of a higher load capacity for the larger diameter (7.5 and 15 lb. respectively), no other investigation was made on shape or dimension effects.

2.2.2.2 Spherical Bearings:

Discs are the simplest shape but can only carry axial load. For a combined axial and radial load carrying capacity, conical or spherical shapes are required. Spherical

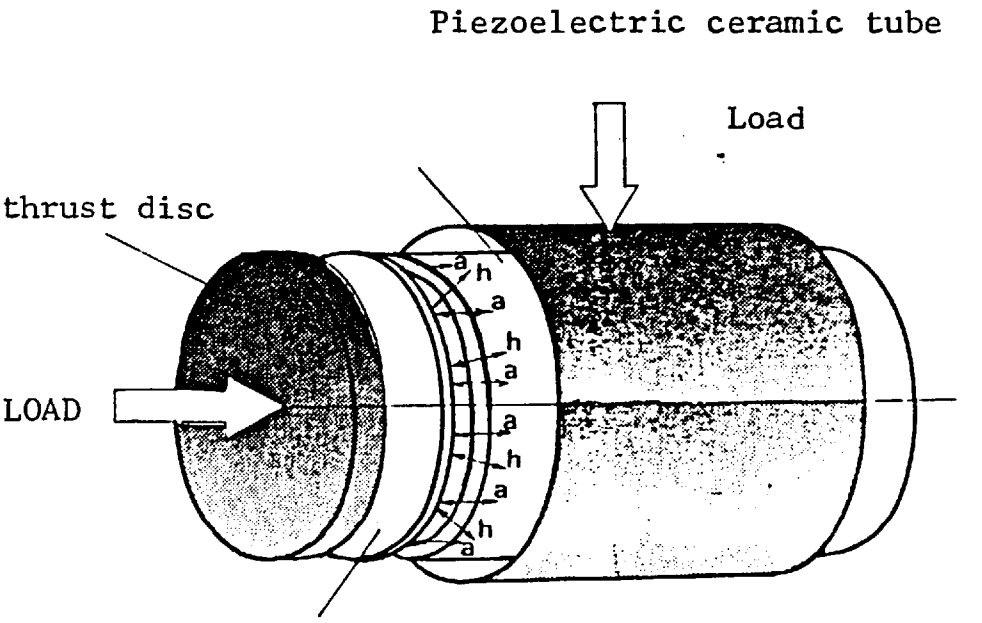

FIG. 2.6 Combined journal and thrust squeeze film bearing with axial (a) and radial, 'hoop', (h), motion.

bearings have the possibility of providing support in any direction but are the most expensive to make. Pan[14] investigated theoretically the performance of squeeze film bearings assuming an arbitrary mode of oscillation entirely in the axial direction and harmonic in time. The bearing geometry is represented in Fig. 2.6. The normalised film gap in these circumstances is:

$$H(\phi,\theta,\tau) = 1 + (\varepsilon\cos\tau + \eta_z)\cos\phi + \eta_r \sin\phi\cos\delta \qquad (2.1)$$

with ϕ - azimuthal angle,

θ - median angle,

η_r - dimensionless radial displacement ratio,

η_z - dimensionless axial displacement ratio,

$\tau = \Omega t$ - dimensionless time.

The asymptotic solution is used together with the perturbation method, and expressions for the pressure distribution are obtained. In his conclusions, Pan says that load capacity and axial stiffness are independent of radial displacement. However, no experimental confirmation was provided. Huxley[31] performed some work on spherical bearings for gyro support (see Fig. 1.1). In this case the amplitudes of vibration were determined experimentally using an optical device. He found that for the particular spherical shell used, driven by a piezoelectric ceramic, there was a first resonance at 16.5 KHz, with the modal shape as represented in Fig. 1.2. It seemed that radial and tangential motion added up to mainly an axial displacement, but the amplitude of vibration was not uniform and greatly increased at the boundary. The load capacity at 4 Watts input power was 1.25 lb. for a hemispherical bearing of 2 inches diameter. Other theoretical works, Refs. (18) and (19), further extended the use of the asymptotic theory on spherical squeeze film bearings, but no attempt was made to relate an actual mode with the theories established.

2.2.2.3 Conical Bearings:

Conical shapes, Fig. 2.5, have also been studied. They provide axial and radial capacity and are easier to produce than the spherical ones.

Pan[7] and Chiang[8] did some experiments on amplitudes of vibration. They also tried to establish some simple analysis to predict the amplitude of motion. Unfortunately difficulty was encountered on matching these calculations with the previous experiments. More detailed analysis of these results will be considered in Chapter 6, dealing with conical squeeze film bearings. Huxley[31] also performed measurement of amplitudes of vibration of this type of geometry. From his results he concluded that the effect of the flexibility of the shell could not be ignored and that non-uniform excursion was likely to occur in most practical cases.

2.2.2.4 Journal Bearings:

The journal bearings have been more extensively analysed. Its geometry, assuming uniform amplitudes of vibration, is represented in Fig. 2.7. The first experiments were performed by Salbu[6]. He considered also a simple approach, using Boyle's Law, to obtain the mean positive

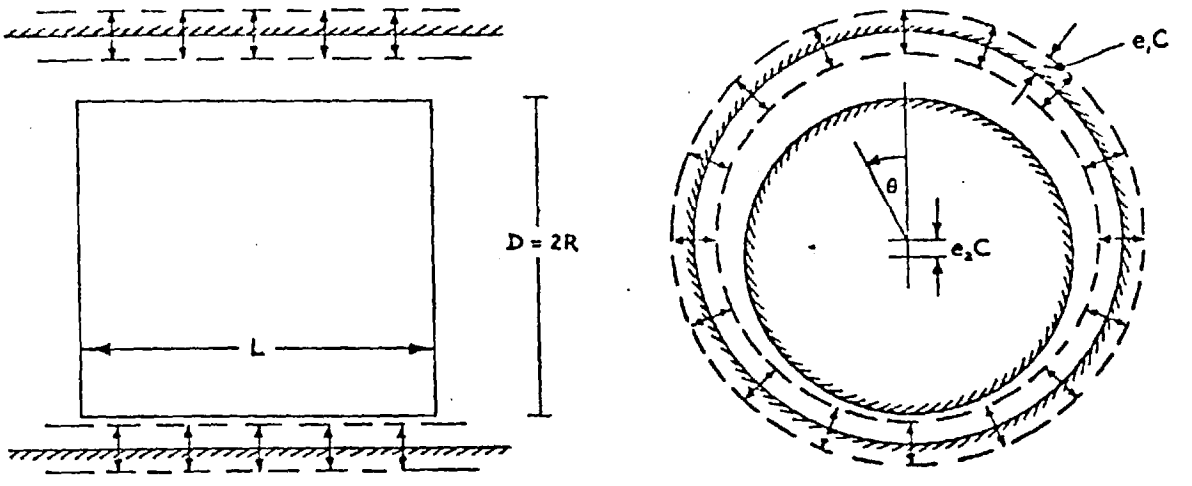

FIG. 2.7 Squeeze film journal bearing geometry with assumed uniform vibrational amplitude (Ref. 30).

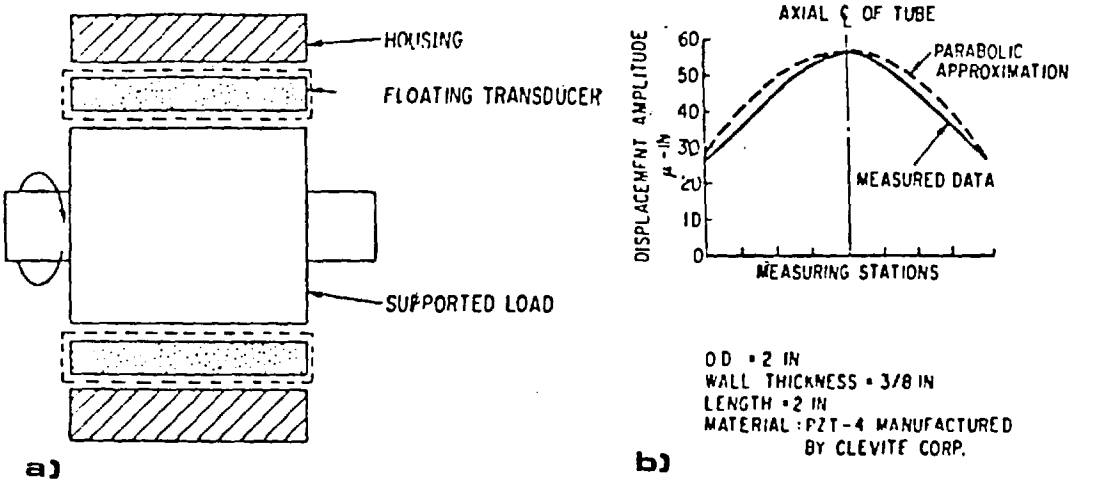

FIG. 2.8 Schematic representation of squeeze film journal bearing and actual modal shape showing non-uniform amplitude (Ref. 13).

film force. No details were obtainable on the materials or dimensions of the test specimen. More specific details were provided by Pan and others[13]. They analysed the journal bearing schematically represented in Fig. 2.8(a) using a 'floating transducer', providing two squeeze films. The clearance between the outer surface of the hollow shaft and the inner diameter of the transducer was 275 in. The radial clearance between the outer steel tube and the piezoelectric ceramic was 300 in. Other significant dimensions are given in Fig. 2.8(b). This figure also shows the experimentally obtained mode shape for the transducer. Apart from a hoop mode resonance it was noticed that due to the Poisson effect, there was also induced longitudinal motion. As the longitudinal stresses at the free ends of the transducer, Fig. 2.9, must be zero, this was the reason given for the non-uniform radial motion of the ceramic. This shape was theoretically approximated by a parabolic curve (Fig. 2.8(b)) and the load capacity predicted by the asymptotic theory compared with experimental results. The discrepancies between the values obtained in the two cases were of the order of 20%. The explanation for this discrepancy was based on unfavourable tolerances and the difference between the experimental and assumed squeeze motion. One of the relevant facts shown by

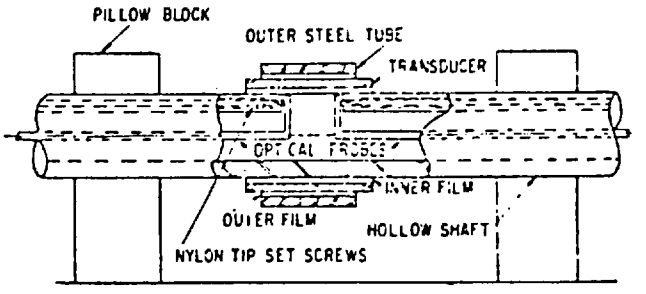

FIG. 2.9 Journal bearing as used for tests performed by Pan showing the positioning of the optical probes (Ref. 13).

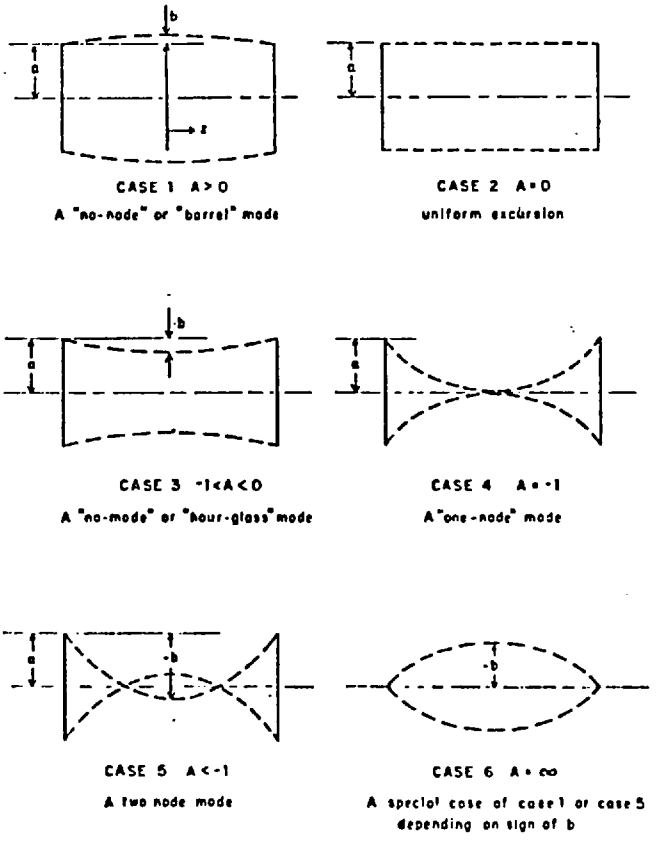

FIG. 2.10 Non-uniform transducer amplitudes as considered by Strodtman (Ref. 39).

these experiments is that, as opposed to the other cases, the journal bearing arrangement produces much smaller amplitudes at the boundaries than at the centre section of the bearing. Another analysis of journal squeeze film bearings is reported by Strodman[29], who has taken into account the non-uniform excursions. This is a pure theoretical work and the non-uniform excursions were considered in terms of a shape factor $A_s = a/b$. The six arbitrary shapes studied are represented in Fig. 2.10. a and b are geometric parameters, z is the longitudinal coordinate and z_{LC} the half length of the piezoelectric driver. He assumed that the radial motions of the piezoelectric cylinder can be expressed by the following cosine function:

$$h_1 = a + b \cos \frac{\pi}{2} \frac{z}{z_{LC}} \tag{2.2a}$$

or, introducing the shape factor,

$$h_1 = a(1 + A \cos \frac{\pi}{2} \frac{z}{z_{LC}}) = a\ S(z, z_{LC}) \tag{2.2b}$$

The amplitude of motion is then separated into a reference amplitude, a, and a shape function, S. The load capacity is obtained through the use of a small parameter approximation. Unfortunately the results obtained were not compared with experimental ones, but only with others obtained numerically. The major criticism of that analysis is that it requires practical confirmation and that mode

shapes are not properly related to actual ceramic behaviour.

Up to this stage no other shapes have been investigated. No particular research has been conducted on bearing materials either.

2.2.3 The Fluid

The lubricant fluid exists between the two bearing surfaces. It is influenced by the clearance and load of the supported member, and the motion of the supportine member that undergoes the vibrational motion.

We shall assume now that the usual conditions encountered in lubrication theory are satisfied, i.e.

- the flow is laminar,
- the inertia effects are negligible,
- the fluid has Newtonian behaviour,
- the fluid can be considered as a perfect gas,
- no pressure change across the film.

With these assumptions we can use the Reynolds equation to characterise the fluid behaviour. For a compressible fluid this equation is:

$$\frac{\partial}{\partial x_i}\left(h^3 p \frac{\partial p}{\partial x_i}\right) = 6\mu\left\{2\frac{\partial}{\partial t}ph + U\frac{\partial}{\partial x_i}(ph)\right\} \qquad (2.3)$$

The first r.h.s. term is known as the squeeze term. In most operational cases this term is small and its effect can be neglected. However, for high speed or high eccentricities the pressure variation caused by this term is significant. Using polar coordinates this equation can be rewritten as follows:

$$\frac{1}{R}\frac{\partial}{\partial R}\left(H^3 RP\frac{\partial P}{\partial R}\right)+\frac{1}{R^2}\frac{\partial}{\partial\theta}\left(H^3 P\frac{\partial P}{\partial\theta}\right)=$$

$$=\frac{12\mu\omega R_o^2}{pa\ h_o^2}\frac{\partial(PH)}{\partial T}+\frac{6\mu U R_o}{pa\ h_o^2}\left(\frac{\partial(PH)}{\partial\theta}\right)= \qquad (2.4a)$$

$$=\sigma\frac{\partial(PH)}{\partial T}+\Lambda\frac{\partial(PH)}{\partial\theta} \qquad (2.4b)$$

where R_o is a characteristic bearing dimension and h_o is the bearing clearance.

The first dimensionless parameter is the squeeze number, σ, and the second the bearing number, Λ. In the general case both of the bearing surfaces in two directions, normal to the surface and parallel to it, contribute to the film characteristics, and $P = f(R, \theta, T, \sigma, \Lambda, H)$.

For parallel surfaces, $P = f(R, T, \sigma, H)$ (2.5)

and the equation assumes a simpler form:

$$\frac{H^3}{R}\frac{\partial}{\partial R}\left(PR\frac{\partial P}{\partial R}\right)=\sigma\frac{\partial(PH)}{\partial T} \qquad (2.6)$$

We have now two independent variables only: P and H. Assuming that one of the surfaces is held stationary

while the other is oscillated sinusoidally about a mean clearance, the film thickness is:

$$h = h_o - A\cos\omega t \qquad (2.7)$$

Normalising with respect to h_o, the film thickness is now:

$$H = 1 - \varepsilon\cos\omega t = 1 - \varepsilon\cos T \qquad (2.8)$$

The variable ε, the excursion ratio, is a measure of the maximum relative volume change. The squeeze film characteristics depend uniquely upon the operating conditions, defined by the dimensionless parameters σ and ε.

At low squeeze numbers, when the frequency is low or there is a large mean clearance, the air is forced out when the clearance decreases and sucked in when it increases. As the forces due to viscosity are small and since those are the forces opposing the flow, there will be a corresponding radial flow,

$$\tau = \mu\frac{du}{dz} \sim \mu\frac{d}{dt}(1 - \varepsilon\cos\omega T) =$$
$$= \mu\omega\varepsilon\cos(\omega T - \pi/2) \qquad (2.9)$$

Under these conditions the pressure and the force generated are proportional to the squeeze velocity rather than the displacement. The phase angle between the minimum gap value, H(T), and the maximum instantaneous force, W(T),

$\gamma \longrightarrow \pi/2$ as $\sigma \longrightarrow 0$. This means that at small squeeze numbers the film behaves in a damping mode. If the excursion is increased, or the frequency is high, the viscous forces will increase and compressibility will occur, particularly when the clearance is minimum. The flow resistance will be so high as to introduce compressibility effects. The gas will be alternately compressed and expanded. The radial flow is restricted, and as the squeeze number increases, the flow will only occur at the narrow edge region near the boundaries.

The air now acts as a non-linear spring and the phase angle tends to zero.

In the next subsection the influence of the two main parameters, σ and ε, will be analysed.

2.2.3.1 Excursion Ratio:

The excursion ratio, $\varepsilon = \frac{h}{h_o}$, is partially imposed by the initial clearance between the two bearing surfaces. The only way it can be varied is through the amplitude of the squeeze motion.

The large excursions are also limited by the condensation effect. For an isothermal compression the

condensation is ruled by the Gibbs-Dalton's law[32].

Defining the compression ratio, Γ:

$$\Gamma = \frac{p_{max}}{p_{min}} \tag{2.10}$$

and $$\Phi = \frac{p_{v_1}}{p_{v_1}(sat)} = \text{relative humidity} \tag{2.11}$$

where: p_{max} and p_{min} are respectively the maximum and minimum values of the pressure curve in a cycle,

p_{v_1} is the pressure corresponding to volume v_1,

$p_{v_1}(sat)$ is the pressure at conditions of saturation for volume v_1.

Condensation will occur if:

$$\Phi \Gamma \geq 1 \tag{2.12}$$

When this happens there is a reduction of the effective mean clearance. This causes difficulty in restarting the bearing, as was experienced by Salbu[6].

The excursion ratio has a definite influence on the predicted mean squeeze film force (W_n). This is shown in Fig. 2.11. There is an increase of the force with the increase in ε (the curves were obtained through a numerical procedure). This justifies the search for large vibration amplitudes. Because these large amplitudes require large power inputs, it seems logical to try to obtain large values of excursion using the bearing material flexibility.

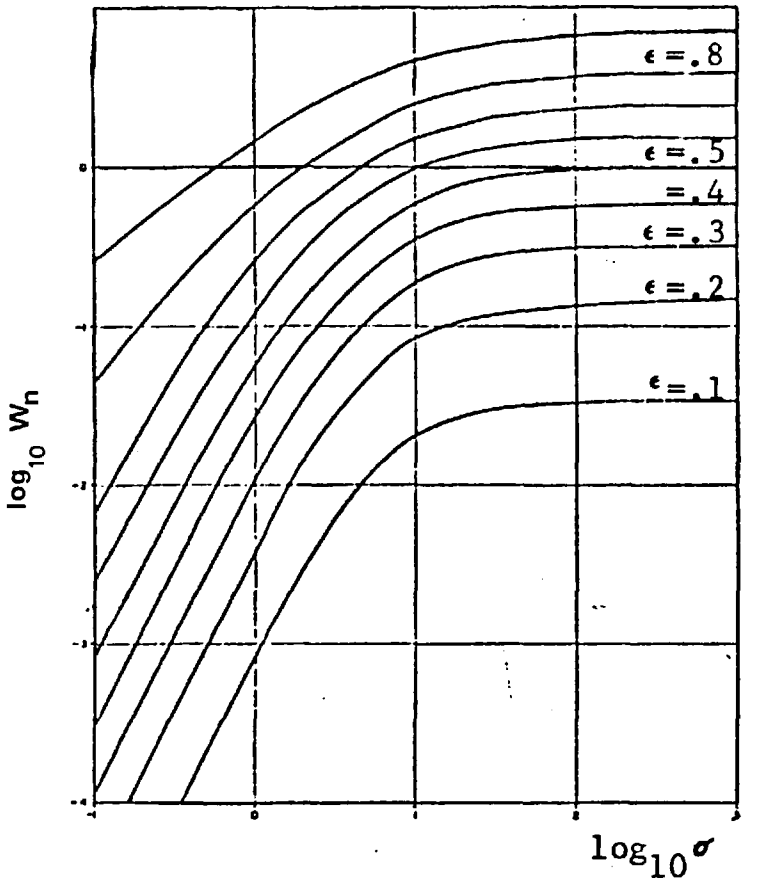

FIG. 2.11 Mean squeeze film force variation with the squeeze number, σ , and the excursion ratio, ϵ , (Ref. 6).

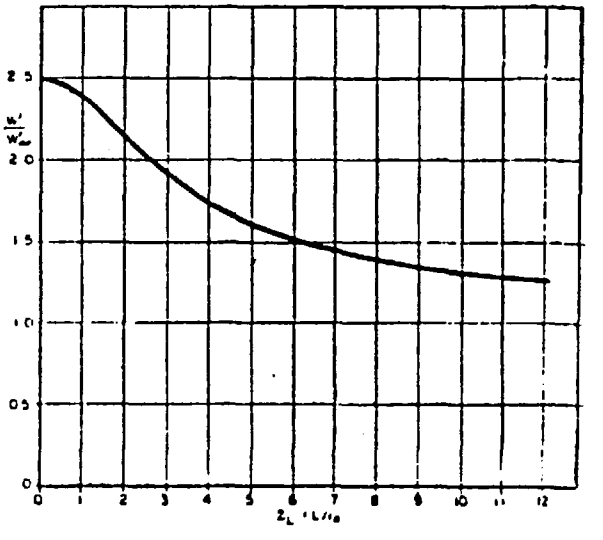

FIG. 2.12 Effect of length on lift-journal bearing- (Ref. 23).

Beck[23], analysing the effect of the bearing length on the load supported by a journal squeeze film, Fig. 2.12, considered the effect of the boundary excursion. He used a small parameter analysis to calculate the load support of infinitely long and infinitely short journal bearings, Fig. 2.12. The expressions of the dimensionless lift per unit length, W', obtained, are:

i) Infinitely long bearing:

$$W'_{\infty} \simeq -\frac{\pi}{2} \varepsilon_1^2 \varepsilon_2 \qquad (2.13)$$

ii) Infinitely short bearing:

$$W' \simeq -\frac{5}{4}\pi \varepsilon_1^2 \varepsilon_2 \qquad (2.14)$$

The variable ε_1 is the uniform excursion and ε_2 the dimensionless eccentricity. From expressions (2.13) and (2.14) one can see that the load supporting capacity of the infinitely short bearing is 2.5 times that of an infinitely long bearing.

To explain this fact Beck imagined a hypothetical bearing with the following characteristics: at the boundary and for an infinitesimal area, δ. into the interior of the bearing the excursion is ε_1; in the interior itself the excursion is constant, ε_c. For large squeeze numbers he calculated the following expression

for the load capacity:

$$W' = -\frac{\pi}{2}\varepsilon_2\left(\varepsilon_c + \frac{3}{2}\varepsilon_1^2 D_j\right) \qquad (2.15)$$

where D_j is a variable assuming the value zero when the bearing length $\longrightarrow \infty$. Comparing expressions (2.13) and (2.15), Beck concluded that the boundary excursion had an increasing effect on the lift. He also suggested that an improvement on load capacity could be achieved by generation of maximum excursion at the boundaries of the bearing.

2.2.3.2 Squeeze Number:

The other main parameter governing the fluid behaviour is the squeeze number, σ. This dimensionless parameter represents the influence of the fluid viscosity, squeeze motion frequency, ambient pressure and a geometric factor. This geometric factor is the ratio between a typical dimension of the bearing, R_o, and the mean gap between bearing surfaces, h_o. The squeeze number can be interpreted as the ratio between the pressure drop required to cause the gas to flow out against the viscous forces and the pressure rise due to compression. The influence of σ on the generated force is shown in Fig. 2.11, already referred to. There is an exponential increase of the force with σ up to $\sigma = 10^3$. At this value the force is independent of σ.

This relationship is generally accepted by all the authors. The fact that for large values of σ the force is constant stands as the basis of one of the theories interpreting the squeeze film effect, the 'asymptotic theory'.

2.2.3.3 The Effect of the Boundaries (Grooving):

The incorporation in the bearing surface of grooves (narrow and deep channels), where the fluid is at the ambient pressure, is one of the latest developments in squeeze film research. These grooves are commonly used in other types of bearings, namely self-acting gas bearings employed for gyroscopes. This subject was theoretically considered by Cooke[30]. He based his work on the fact, already discussed, than an improvement in the load capacity is obtainable by the edge effect. The analysis, for grooved and ungrooved journal bearings, of the variation of load capacity with the ratio length/diameter is shown in Fig. 2.13. The axial flow in the case of journal bearings is closely related to this variation of load capacity. The conclusions of Cooke on this subject can be stated thus:

- The axial flow is small and proportional to L/D for short bearings and in this case has a linear distribution.

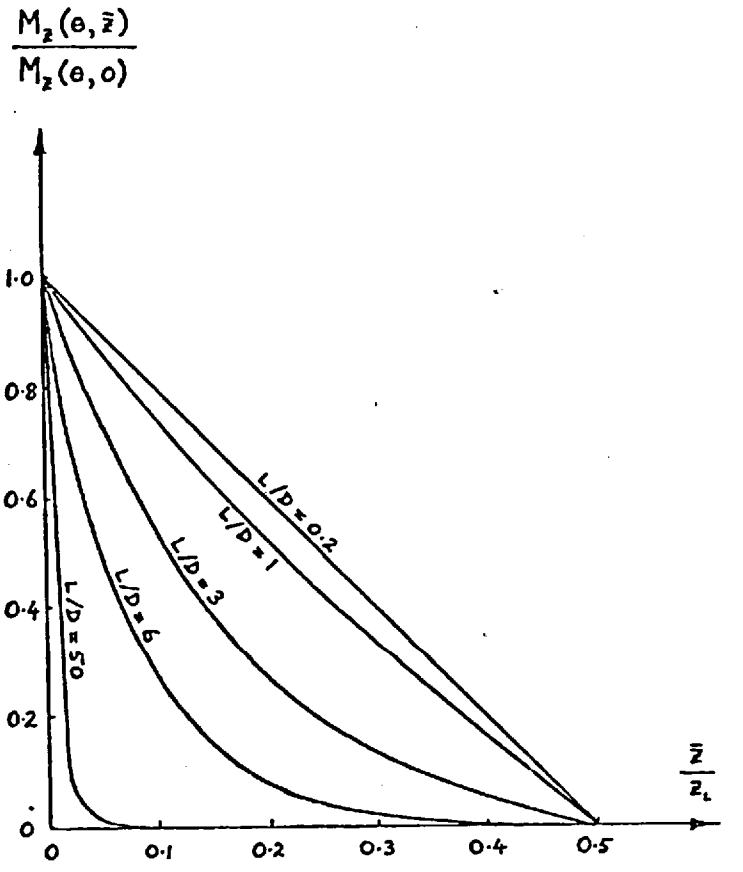

FIG. 2.14 Axial penetration of the mass flow rate for various values of L/D (Ref. 30).

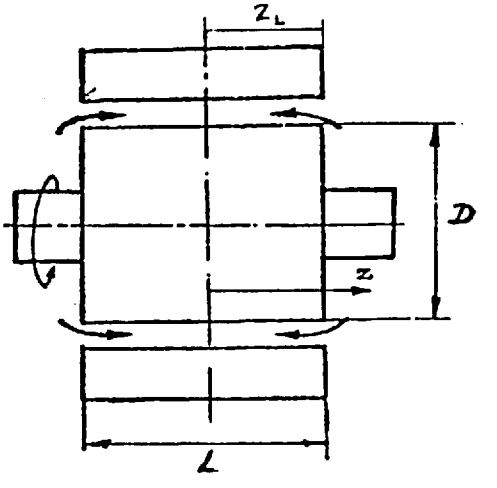

FIG. 2.15 Axial flow and geometry variables used in Fig. 2.14.

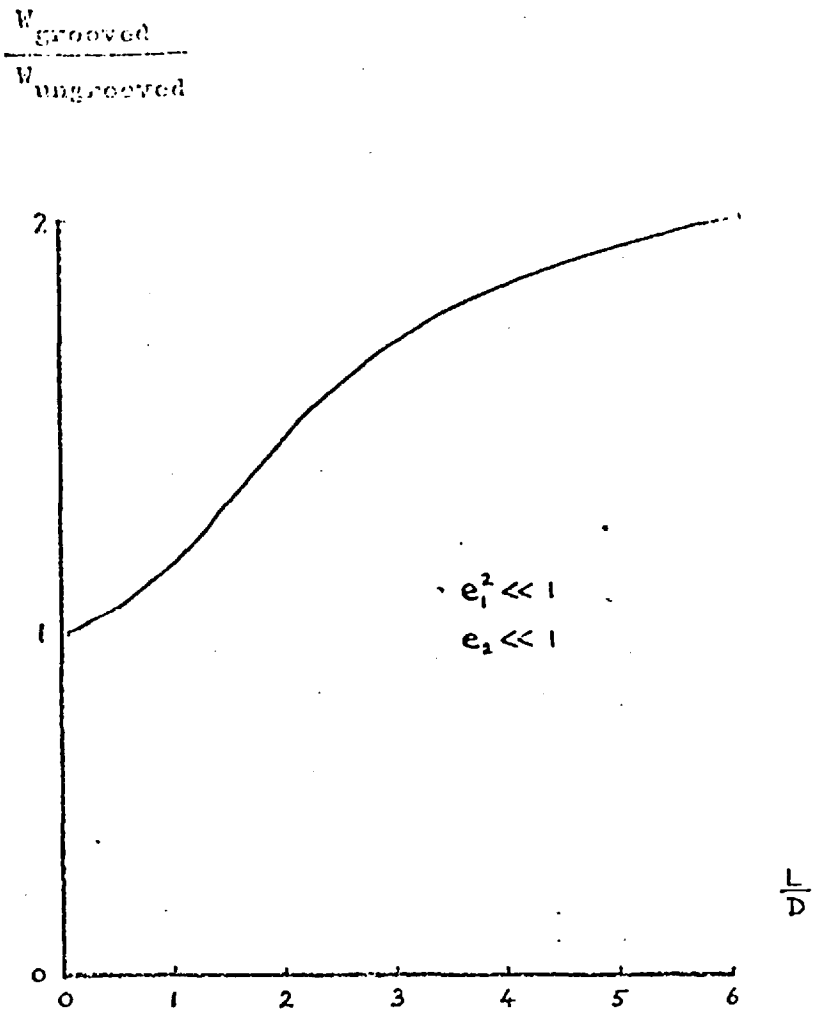

FIG. 2.13 Influence of ratio length/diameter on bearing force for grooved and ungrooved journal bearing, case of small excursion and eccentricity ratios (Ref. 30).

When the value of L/D increases there is no longer linearity between the flow rate per unit of width and the axial coordinate as in Fig. 2.14. This means that the pressure gradient is greatest near the ambient boundary and decreases with the axial coordinate, Fig. 2.15.

It is a phenomenon similar to that of a thrust plate, where most of the radial flow occurs near the boundary. The circumferential flow is also affected (in journal bearings). For small ratios of L/D the circumferential flow is small and has the same value throughout the bearing at any radial position. When the ratio L/D increases (L/D >1) there is greater circumferential flow near the boundaries. For very short journal bearings the pressure is constant and can be expressed in a dimensionless form as a function of the excursion ratio ε_1 and the eccentricity, ε_2:

$$\bar{P} = 1 + \frac{5}{4}\varepsilon_1^2 + \frac{5}{2}\varepsilon_1^2\varepsilon_2 \cos\theta \qquad (2.16)$$

For a very long bearing:

$$\bar{P} = 1 + \frac{5}{4}\varepsilon_1^2 + \varepsilon_1^2\varepsilon_2 \cos\theta \qquad (2.17)$$

where θ is the circumferential bearing coordinate as represented in Fig. 2.7.

The axial pressure gradient at the ambient boundary is:

$$\left(\frac{\partial \bar{P}}{\partial z}\right)_{z=0} = -\frac{3}{2}\varepsilon_1^2\varepsilon_2 \cos\theta \tanh\frac{L}{D} \qquad (2.18)$$

and as the mass flow rate is proportional to the pressure gradient it is also proportional to $\tanh\frac{L}{D}$ for any radial position. This suggested to Cooke that axial or

circumferential grooves should be placed where the excursion ratio is high. Therefore he proposed in (30) the use of grooves in the middle plane of journal bearings, where maximum excursion occurs. He also refers to the application of a vent hole to an hemispherical bearing. In his opinion the larger excursion would exist at the polar region and so a polar vent should be located there. Experimentally it was found, as shown in Fig. 1.2, that this does not occur, and the largest excursions are at the edge. So grooving should be considered near this edge instead.

2.3 CONCLUSIONS

The squeeze film bearing is basically a very simple system. This is one of its main advantages.

We referred briefly to the major parameters governing its performance. The fluid behaviour can be interpreted in terms of well known lubrication theory. However, the driving element and the bearing surface characteristics have not been extensively studied

Piezoelectric ceramics can provide only small amplitudes of vibration. In journal bearings they have

been used as the bearing surface, because it is difficult to achieve a good contact between the ceramic cylinder and the cylindrical metallic surface. In this case, besides the small vibration amplitudes, we have the disadvantages already referred to in Section 2.2.1. Thrust bearings (discs, cones or spheres) give more possibilities of improvement because it is possible to have the ceramic driving the metallic bearing surface, as in Fig. 2.2. Therefore one can choose the bearing surface material and its arrangement with the piezoelectric ceramic. This makes it possible to obtain greater amplitudes than those provided by the ceramic itself. The more important contribution for load capacity seems to be due to the "pumping" action at the boundaries. This leads to two ways of possible performance improvement:

1) The generation of extra boundaries, using grooves in the bearing surface.

2) An increase of amplitude of vibration at these boundaries.

Most previous studies assumed the excursion to be uniform over all the bearing surfaces. Other authors[13,29] assumed an arbitrary variation for it. Actually, these arbitrary variations do not agree with the experimental evidence. So, the theoretical treatment of the lubricant

film based on this premise will not agree with experiment. The investigation of the flexibility of the bearing surface is very important in predicting the true film thickness. At the same time it introduces a new way of improving bearing performance.

CHAPTER 3

THE SOLUTION OF FLUID GOVERNING EQUATIONS FOR SQUEEZE-FILM BEARINGS

3.1 BOYLE'S LAW

We have earlier referred to some results obtained numerically, or using the asymptotic theory.

In a simple analysis, Boyle's Law is a reasonable approach. Before considering a more complete analysis provided by the Reynolds equation, we will use this theory.

Let us assume two surfaces, one of which vibrates sinusoidally with an amplitude A about a mean clearance h_o and a frequency ω.

The instant film thickness, h, is:

$$h = h_o + A\cos\omega t \tag{3.1}$$

or,

$$\frac{h}{h_o} = 1 + \frac{A}{h_o}\cos\omega t \tag{3.2}$$

the dimensionless film thickness $H = \frac{h}{h_o}$,

$$H = 1 + \varepsilon_o \cos\omega t \tag{3.3}$$

where ε_o is the excursion ratio.

If the frequency is high or there are very small

clearances, the viscous shearing is considerable. As we saw before, they are proportional to ω and inversely proportional to the clearance. The radial flow is retarded and this originates successive compression and expansion of the gas film. The operating conditions are closer to those of a piston inside a closed cylinder. Assuming that the temperature is constant, it is permissible to use the Boyle's Law

$$p\,h\,A_b = p_a\,h_o\,A_b = \text{cte} \tag{3.4}$$

where p_a is atmospheric pressure and A_b the bearing area.

Using the following dimensionless variables,

$$\bar{P} = \frac{p}{p_a} = \text{dimensionless pressure,}$$

$$T = \omega t = \text{dimensionless time, and} \tag{3.5}$$

$$R^* = \frac{r}{R_o}, \quad \text{where } R_o \text{ is the bearing dimension,}$$

we obtain $$\bar{P} = \frac{1}{1 + \varepsilon_o \cos T} \tag{3.6}$$

This function is represented in Fig. 3.1.

The dimensionless bearing force <u>for the case of a disc</u> (this is the simpler geometry) is:

$$F^* = \frac{F}{p_a A_b} = \frac{F}{p_a \pi R_o^2}$$

$$= \int_0^1 2R^*(\bar{P}-1)dR^* = \frac{1}{\sqrt{1-\varepsilon_o^2}} - 1 \tag{3.7}$$

where: F = total force generated by film, and

$$P^* = \frac{1}{2\pi}\int_0^{2\pi} \bar{P}\,d\tau = \frac{1}{\sqrt{1-\varepsilon_o^2}} \tag{3.8}$$

For small values of the excursion ε_o,

$$P^* = 1 + \tfrac{1}{2}\varepsilon_o^2 + 0\left\{\varepsilon_o^4\right\} \tag{3.9}$$

and thus, the bearing force can be approximated by the expression

$$F^* \simeq \tfrac{1}{2}\varepsilon_o^2 \tag{3.10}$$

At the outer edge, the pressure is obviously the atmospheric, but the pressure obtained through Boyle's Law is $p_B > p_a$ with the condition

$$p\,h\,A_b = p_B\,h_o\,A_b \tag{3.11}$$

and

$$P = \frac{P_B}{(1 + \varepsilon_o \cos T)} \tag{3.12}$$

where

$$P_B = \frac{p_B}{p_a}$$

The averaged pressure distribution is

$$\bar{P} = \frac{p_B}{\sqrt{1-\varepsilon_o^2}} \tag{3.13}$$

Using this expression, and according to Salbu (6), the pressure value obtained for $\varepsilon_o = .5$ is 1.15 greater than the value calculated using, for initial condition, the true ambient pressure, as shown in Fig. 3.2.

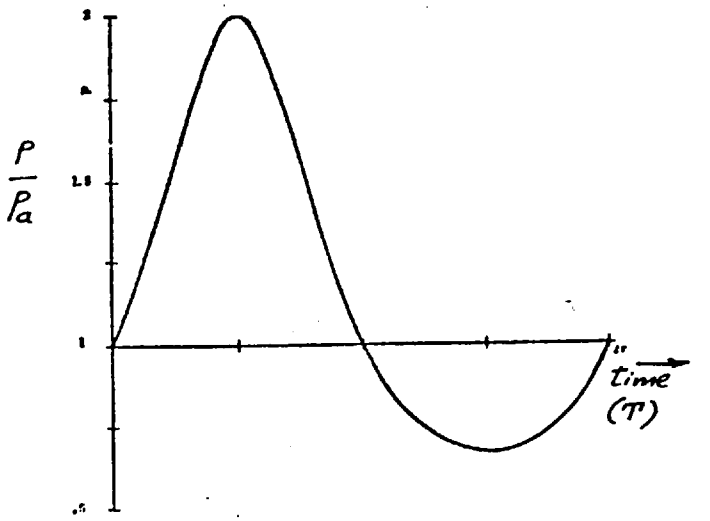

FIG. 3.1 Squeeze film pressure calculated from Boyle's law with ϵ = .5 (Ref. 6).

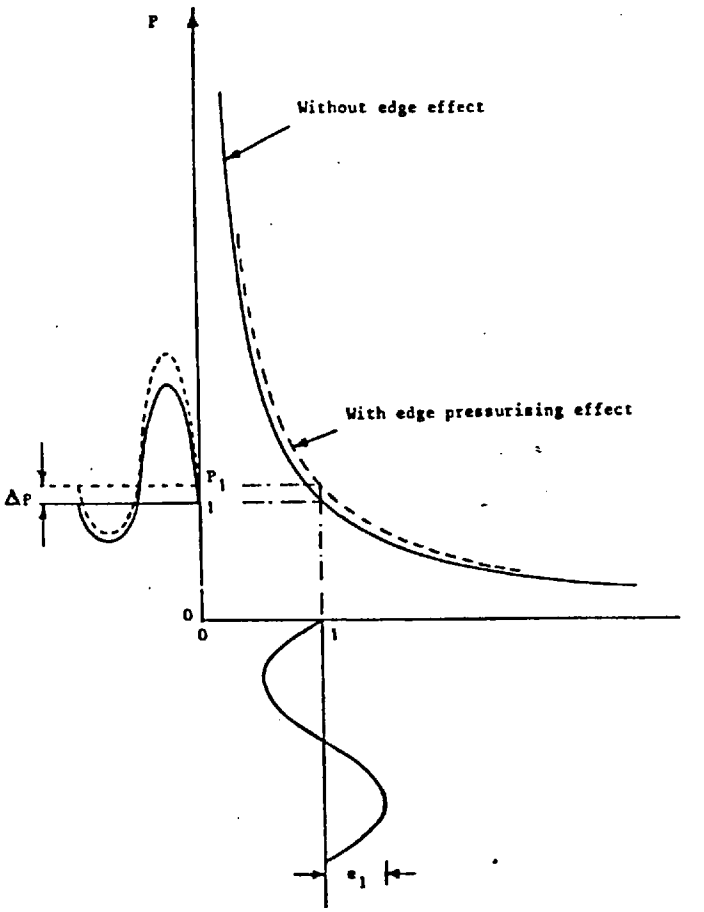

FIG. 3.2 The effect of the pressurisation at the edge, using Boyle's law (Ref. 30).

3.2 ASYMPTOTIC SOLUTION

3.2.1 Basic Assumptions

A more powerful analysis of the film behaviour is provided by the Reynolds equation. This is a non-linear (at least for compressible fluids), second order, partial differential equation of parabolic type. The derivation of this equation is based on the Navier-Stokes equations, the continuity equation, the energy equation and the equation of state.

It was demonstrated in (20) that as the film thickness in this type of bearings is very small compared with the other dimensions, the heat transfer between the gas and the surfaces maintains the film in an isothermal state.

Inertia terms can be ignored compared with the viscous shear forces (24,39). The criterion is that the transient Reynolds number of the squeeze motion must be

$$\frac{\rho \omega h_o^2}{\mu} \ll 1 \qquad (3.14)$$

μ being the fluid viscosity and ρ_f the density, and ω and h_o having the meaning already given.

The velocities in the direction normal to the surface are assumed to be large compared with those in the bearing surface plane. This is true, according to Cooke (30) if:

$$\sqrt{\sigma}\,\frac{h_o}{R_o} \ll 1 \qquad (3.15)$$

where σ is a parameter defined in 3.17a. For isothermal conditions the viscosity can be assumed to be constant as the pressure in these bearings is small. Therefore the density can be replaced by pressure in Reynolds equation. Full derivation of the Reynolds equation can be seen in Refs. (4) and (84).

3.2.2 Solution of Reynolds equation

A closed form solution, called the "asymptotic solution" for the Reynolds equation will be considered now.

The Reynolds equation in a vector form is:

$$\operatorname{div}\left\{-\frac{\rho h^3}{12}\operatorname{grad} p + \frac{\rho h \vec{v}}{2}\right\} + \frac{\partial}{\partial t}(\rho h) = 0 \qquad (3.16)$$

The vector $\vec{v}$ * is the sum of the absolute sliding velocities of the bearing surfaces.

We will make use of transformations (3.5) to obtain a dimensionless form for (3.16). Considering the surface differential operators, grad and div, in dimensionless form, we have:

$$\nabla_{\cdot}\left\{-PH^3\nabla P + \Lambda\vec{U}\,PH\right\} + \sigma\frac{\partial}{\partial T}(PH) = 0 \qquad (3.17)$$

where: $\nabla_{\cdot} = R^{*}\operatorname{div}$, $\nabla = R^{*}\operatorname{grad}$,

$$\vec{U} = \frac{\bar{V}}{\omega R^{*}}, \quad T = \omega t,$$

---

* In the case of squeeze film bearings, this velocity is very small and in most applications is negligible.

and
$$\begin{cases} \Lambda = \text{compressibility number} = \dfrac{6\mu\omega}{p_a}\left(\dfrac{R_o}{h_o}\right), \\ \sigma = \text{squeeze number} = \dfrac{12\mu\omega}{p_a}\left(\dfrac{R_o}{C}\right)^2. \end{cases} \tag{3.17a}$$

Assuming, as before, the fluid film thickness to be periodic in time and a defined function of $\vec{X}(x,y)$, vector of the coordinate components,

$$H(x,\ T+2\pi) = H(x,T) \tag{3.18}$$

with the boundary condition,

$$P(x_B,\ T) = 1 \tag{3.19}$$

When the steady state is established, then

$$P(x,\ T+2\pi) = P(x,T) \tag{3.19a}$$

For $\sigma \longrightarrow \infty$ (asymptotic theory),

$$\frac{\partial}{\partial T}(PH) = 0\left\{\frac{1}{\sigma}\right\} \tag{3.20}$$

If we call the product $PH = \psi$

$$\lim_{\sigma \longrightarrow \infty} \psi = \psi_\infty(x) + 0\left\{\frac{1}{\sigma}\right\} \tag{3.21}$$

At the boundaries:

$$\psi_B = H(x_B,T) \tag{3.22}$$

because

$$P(x_B,T) = 1 \tag{3.23}$$

With this notation we can write equation (3.17) with the form:

$$\operatorname{div}\left\{\frac{H}{2}\operatorname{grad}(\psi^2) - \psi^2 \operatorname{grad}H - \Lambda\vec{U}\psi\right\} = \sigma\frac{\partial\psi}{\partial T} \qquad (3.24)$$

Integration of this equation over one period gives:

$$\int_T^{T+2\pi} \operatorname{div}\left\{\frac{H}{2}\operatorname{grad}(\psi^2) - \psi^2\operatorname{grad}H - \Lambda\vec{U}\psi\right\} = \sigma\left\{\psi(T+2\pi) - \psi(T)\right\} \qquad (3.25)$$

or,

$$\int_T^{T+2\pi} \operatorname{div}\left\{\frac{H}{2}\operatorname{grad}(\psi^2) - \psi^2\operatorname{grad}H - \Lambda\vec{U}\psi\right\} dT = 0 \qquad (3.26)$$

Defining,

$$\bar{H} = \frac{1}{2\pi}\int_T^{T+2\pi} H\, dT \qquad (3.27)$$

and replacing ψ by its asymptotic value:

$$\operatorname{div}\left\{\frac{\bar{H}}{2}\operatorname{grad}(\psi_\infty)^2 - \psi_\infty^2 \operatorname{grad}\bar{H} - \Lambda\vec{U}\psi\right\} dT = 0 \qquad (3.28)$$

There are two regions in the film that must be considered separately, the inner layer and the boundary layer. Let us call

$$\psi_b = \psi\,(x \approx x_b) \qquad (3.29)$$

and η the coordinate normal to and measured from the boundary, then,

$$\frac{\partial\psi_b}{\partial\eta} = 0\left\{\sqrt{\sigma}\right\} \quad \text{at } x \approx x_b \qquad (3.30)$$

This was mathematically justified by Pan[11].

Equation (3.25) can now be rewritten:

$$\frac{\partial^2}{\partial\eta^{*2}}\int_T^{T+2\pi} \frac{H_b\psi_b^2}{2}\, dT = 0\left\{\frac{1}{\sqrt{\sigma}}\right\} \qquad (3.31)$$

where: $\eta^* = \sqrt{\sigma}\,\eta$ (3.32)

Neglecting terms of $0\left\{\frac{1}{\sigma}\right\}$, the "boundary layer" approximation near the edge is obtained:

$$\int_T^{T+2\pi} H_b \, dT = C_1 + C_2 \tag{3.33}$$

As $(\psi_b)_{\eta^*=0} = H_b$

$$C_1 = \tfrac{1}{2} \int_T^{T+2\pi} H_b^3 \, dT \tag{3.34}$$

To guarantee convergence as $\eta^* \longrightarrow \infty$, C_2 must be set to zero.

The matching of the interior and the boundary solutions then give:

$$\lim_{x \longrightarrow x_b} \psi_b = \lim_{\eta^* \longrightarrow \infty} \psi_b \tag{3.35}$$

or,

$$\psi^2(x_b) \int_T^{T+2\pi} \frac{H_b}{2} dT = \tfrac{1}{2} \int_T^{T+2\pi} H_b^3 \, dT \tag{3.36}$$

$$\psi_\infty^2(x_b) = \frac{\int_\tau^{\tau+2\pi} H_b^3 \, d\tau}{\int_\tau^{\tau+2\pi} H_b \, d\tau} \tag{3.37}$$

This equation represents the required boundary condition for equation (3.26). A general derivation of this solution is given in (11). We will now consider two applications of this theory.

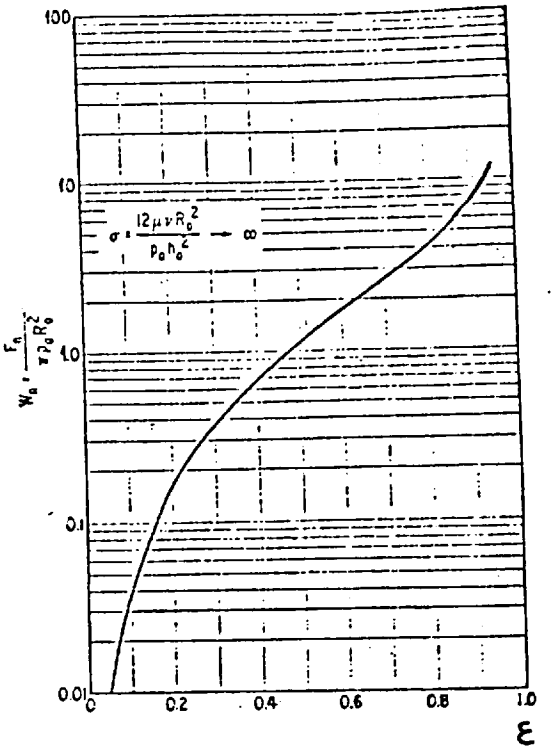

FIG. 3.3

Mean squeeze force, using asymptotic theory, flat discs, (Ref. 10).

3.2.3 Case of circular thrust disc with uniform excursions

If the film thickness can be expressed in the dimensionless form

$$H = 1 + \varepsilon \cos T \tag{3.38}$$

the corresponding asymptotic solution is

$$\lim_{\sigma \longrightarrow \infty} PH = \psi_{\infty} = \sqrt{1 + 3/2\,\varepsilon^2} \tag{3.39}$$

In this case the unit axial force is (11)

$$W_n = \frac{F}{p_a A_b} = \frac{1}{2\pi} \int_0^{2\pi} (P-1)dt = \sqrt{\frac{1 + \frac{3}{2}\varepsilon^2}{1 - \varepsilon^2}} - 1 \tag{3.40}$$

and it is represented in Fig. 3.3 for several excursion values.

The unit axial stiffness is

$$\frac{K_z h_o}{p_a A_z} = -\frac{h_o}{p_a A_b}\frac{\partial F}{\partial h} = \frac{5}{2}\frac{\varepsilon^2}{\sqrt{(1-\varepsilon^2)^3(1+\frac{3}{2}\varepsilon^2)}} \quad (3.41)$$

where $K_z = \dfrac{\partial F}{\partial h}$.

3.2.4 Conical bearing with uniform excursion

Assuming the conical geometry of Fig. 2.5b, Pan also developed expressions for the axial pressure and associated bearing force. The film thickness in dimensionless form is:

$$H = 1 + \eta_r \cos\Gamma \cos(\theta - \theta_r) + \eta_\Gamma \frac{r}{r_2}\cos(\theta - \theta_\Gamma) + \varepsilon_z \sin\Gamma \cos T \quad (3.42)$$

This expression includes the influence of the radial and rotational eccentricity through the respective eccentricity ratios η_r and η_Γ. The angles θ_r and θ_Γ are reference angles for the radial and rotational displacements, see Fig. 2.5b. The value of the unit axial force is now given by:

$$\frac{F}{p_a A_b} = \sqrt{\frac{1 + \frac{3}{2}\varepsilon_z \sin^2\Gamma}{1 - \varepsilon_z^2 \sin^2\Gamma}} - 1 \quad (3.43)$$

A_b being now the projected bearing area.

This result is identical to that of the squeeze film plate replacing the excursion amplitude for $\epsilon_z h \sin\Gamma$.

3.3 NUMERICAL SOLUTIONS

The previous section dealt with two methods of analysis of the squeeze film effect where closed expressions for the pressure distribution were obtained. Numerical solutions based on finite differences were studied by Michael (5). We will refer now to them because one of the methods, Crank-Nicholson, will be used later to calculate the pressure distribution for non-uniform excursions.

All the previous assumptions about the fluid properties will be maintained in this analysis.

Using the usual transformations $\psi = PH$ and (3.5), the dimensionless form for the Reynolds equation is:

$$\frac{\partial}{\partial X}\left[\psi\left(H\frac{\partial\psi}{\partial H} - \psi\frac{\partial H}{\partial X}\right)\right] + \frac{\partial}{\partial Y}\left[\psi\left(H\frac{\partial\psi}{\partial Y} - \frac{\partial H}{\partial Y}\right)\right] = \Lambda\frac{\partial\psi}{\partial X} + \sigma\frac{\partial\psi}{\partial T} \qquad (3.44)$$

Or in another form:

$$L(\psi) = \frac{\partial\psi}{\partial T} - F\left(X,Y,T,\psi,\frac{\partial\psi}{\partial X},\frac{\partial\psi}{\partial Y},\nabla^2\psi\right) = 0 \qquad (3.45)$$

where X and Y are dimensionless coordinates in the x and y axis and ∇^2 is the Laplacian operator.

In cases of axisymmetry, like disc and conical bearings, or for the infinitely long bearing, there is need for only one variable. For uniform notation we will replace the variable ψ by u in the following expressions. The equation can now be rewritten:

$$L(u) \equiv \frac{\partial u}{\partial T} - F(X,T,u,\frac{\partial u}{\partial X},\frac{\partial^2 u}{\partial X^2}) = 0 \qquad (3.46)$$

where $$F(X,T,w,\xi,\gamma) = \frac{1}{\sigma}\left[H\omega\gamma - \omega^2 \frac{\partial^2 H}{\partial X^2} + H\xi^2 - \omega\xi\frac{\partial H}{\partial X} - \Lambda\xi\right] \qquad (3.47)$$

3.3.1 The family of difference approximations

Let us assume the space interval $[0,1]$ divided into N+1 subintervals and the time axis is in intervals ΔT. The proposed approximation to the equation (3.44) consists of the following family of difference equations:

$$\mathcal{L}_j^n(u) \equiv (u_j^{n+1}-u_j^n)/\Delta T - F\{j\Delta X,\ (n+\theta)\Delta T,$$

$$\theta u_j^{n+1} + (1-\theta)u_j^{n+1} + (1-\theta)u_j^n,$$

$$[\theta(u_{j+1}^{n+1} - u_{j-1}^{n+1}) + (1-\theta)(u_{j+1}^n - u_{j-1}^n)]/(2\Delta X),$$

$$[\theta'(u_{j+1}^{n+1} - 2u_j^{n+1} + u_{j-1}^{n+1}) + (1-\theta')$$

$$(u_{j+1}^n - 2u_j^n + u_{j-1}^n)]/(\Delta X)^2\} = 0 \qquad (3.48)$$

where $j = 1, 2, \ldots, N$ and $n = 0, 1, 2, \ldots$

In this expression θ and θ' are parameters for the family of difference approximations.

Regarding these parameters, we shall consider four cases:

a) $\theta = 0$ and $\theta' = 0$

In this case the u_j^{n+1} values are obtained explicitly from the u_j^n values. We start with the initial value u_j^0 and the next u_j^1 are calculated from these, and so on.

b) $\theta = 1$ and $\theta' = 1$

This is an implicit formula with u_j^{n+1} determined from the u_j^n through a system of non-linear algebraic equations.

c) $\theta = 0$ and $\theta' = 1$

This is a difference approximation that was initially devised by Lees and is detailed in Ref. 35.

d) $\theta = \frac{1}{2}$ and $\theta' = \frac{1}{2}$

For this case the equation (3.48) assumes a symmetric form. The algebraic equations are now non-linear and must be solved by iteration.

This formulation is a serious contender against the asymptotic solution, although the last method has been considerably used.

Respecting these numerical procedures we only consider the one-dimensional bearing problem. For two space variables some more complexity is involved (5).

The main factors that govern the choice of any of these numerical methods are:

i) stability,

ii) truncation error,

iii) programming requirements.

i) The stability is a function of ΔX, ΔT, and the parameters θ and θ'. Stability conditions have been discussed by Michael [5]. The procedure is that of Von Neumann and Richtmeyer [36]. The stability is shown to be unaffected by θ. This means that the stability is not influenced by the lower order space derivatives. It is also demonstrated that the implicit formula ($\theta = \theta' = 1$) is unconditionally stable. The Lees modified implicit formula ($\theta=0$, $\theta'=1$), and the Crank-Nicholson formula ($\theta = \theta' = \frac{1}{2}$) are also unconditionally stable. The explicit formula ($\theta = \theta' = 0$) requires for stability

$$\frac{H^2 P \Delta T}{\sigma(\Delta X)^2} \leqslant \tfrac{1}{2} \qquad (3.49)$$

This inequality must hold at every node of the grid, which requires ΔT to be properly adjusted.

ii) The local truncation error for case (a) is $O((\Delta X)^2 + \Delta T)$ and the same applies to (b) and (c). For case (d), the truncation error was demonstrated by Crank and Nicholson [37] to be reduced to $O((\Delta X)^2+(\Delta T)^2)$.

iii) The programming requirements will be considered in the following sections about the algorithms for the explicit formula and for the Crank Nicholson procedure.

The Lee's implicit formula was discarded because for an increased programming complexity it requires very small time steps ΔT, with the same order of magnitude of the stability condition of the explicit method.

3.3.2 Explicit method

In the explicit method one assumes the conditions existing at the start as the initial values u_j^0, where $j = 1,\ldots, N$.

The successive values of u_j are

$$u_j^{n+1} = u_j^n + \Delta T\ F(j\Delta X, n\Delta T, \bar{\omega}, \xi, \gamma) \qquad (3.50)$$

with $$\xi = (u^n_{j+1} - u^n_{j-1})/(2\Delta X) \qquad (3.51)$$

$$\gamma = (u^n_{j+1} - 2u^n_j + u^n_{j-1})/(\Delta X)^2 \qquad (3.52)$$

and $F(j\Delta X, n\Delta T, \bar{\omega}, \xi, \gamma)$ is given by equation (3.47).

The value of ΔT must be adjusted from the stability condition (3.49).

3.3.3 Crank-Nicholson formulation

As in the previous case the initial values u^0_j must be set as the pressure distribution dictates at $T = 0$.

For the several values of $n = 0, 1, 2, \ldots$ the variables H, $\frac{\partial H}{\partial X}$ and $\frac{\partial^2 H}{\partial X^2}$ are calculated at the time points $T = (n + \frac{1}{2})\Delta T$.

These calculations must be done at all coordinates $X = j\Delta X$, for $j = 1, 2, \ldots, N$. To solve the difference equations we can use the Newton-Raphson procedure, described here.

Let us assume that the values u^{n+1}_j can beapproximated by U^0_j $(j = 1, 2, \ldots, N)$ with U_o and U_{N+1} denoting the boundary values u^{n+1}_0 and u^{n+1}_{N+1}. Setting the variables

$$\bar{\omega} = (U^{(m-1)}_j + u^n_j)/2 \qquad (3.53)$$

and $$\xi = (U^{(m-1)}_j - U^{(m-1)}_{j-1} + u^n_{j+1} - u^n_{j-1})/(4\Delta X) \qquad (3.54)$$

and defining,

$$F_1 = \frac{1}{\sigma}\left(-\bar{\omega}^2 \frac{\partial^2 H}{\partial X^2} + H\xi^2 - \bar{\omega}\xi \frac{\partial H}{\partial X} - \Lambda\xi\right) \tag{3.55}$$

and $$F_2 = \frac{H\bar{\omega}}{\sigma} \tag{3.56}$$

and differentiating:

$$\frac{\partial F_1}{\partial \bar{\omega}} = -\frac{1}{\sigma}\left(2\bar{\omega}\frac{\partial^2 H}{\partial X^2} + \xi \frac{\partial H}{\partial X}\right) \tag{3.57}$$

$$\frac{\partial F_1}{\partial \xi} = \frac{1}{\sigma}\left(2H\xi - \frac{\partial H}{\partial X} - \Lambda\right) \tag{3.58}$$

$$\frac{\partial F_2}{\partial \bar{\omega}} = \frac{H}{\sigma} \tag{3.59}$$

with, obviously, $\frac{\partial F_2}{\partial \xi} = 0.$ (3.60)

The arguments X and T being defined as before:

$$X = j\Delta X, \quad T = (n + \tfrac{1}{2})\Delta T.$$

These expressions enable us to give a new form to the approximated family of difference equations (3.48):

$$U_j - u_j^n - \Delta T F_1\left[j\Delta X, (n+\tfrac{1}{2})\Delta T, (U_j + u^n)/2, (U_{j+1} - U_{j-1} + u^n_{j+1} - u^n_{j-1})/4\Delta X\right] -$$

$$\frac{\Delta T}{2(\Delta X^2)} F_2\left[j\Delta X, (n+\tfrac{1}{2})\Delta T, (U_j + u^n_j)/2, (U_{j+1} - U_{j-1} + u^n_{j+1} - u^n_{j-1})/(4\Delta X)\right].$$

$$(U_{j+1} - 2U_j + U_{j-1} + u^n_{j+1} - 2u^n_j + u^n_{j-1}) = 0 \tag{3.61}$$

for $j = 1, 2, \ldots, N$. Or, in a short form:

$$G_j(U_1, U_2, \ldots, U_n) = 0 \quad (j = 1, 2, \ldots, N) \tag{3.62}$$

Considering $u_1^{(0)}$, $u_2^{(0)}$, ..., $u_N^{(0)}$ as an approximation to the exact solution, U_1, U_2, ..., U_N, the following expansion will apply:

$$G_j(U_1,U_2,\ldots,U_n) = G_j(U_1^0,U_2^0,\ldots,U_n^0) + \sum_{K=1}^{N} \frac{\partial G_j}{\partial U_k}(U_1^0,U_2^0,\ldots,U_n^0)(U_K-U_K^{(0)}) + \ldots = 0 \qquad (3.63)$$

with j = 1, 2, ..., N.

Truncating the series to these terms and equating them to zero we define an approximate solution:

$$U_1^{(1)},\ U_2^{(1)},\ \ldots,\ U_n^{(1)}$$

Repeating this process, a sequence $\left\{U_j^{(m)}\right\}$ is generated, which, according to Kantorovich [38] converges to the exact solution.

For each iteration of this process, and in order to obtain the referred approximate solution, we have to compute the values of $\frac{\partial G_j}{\partial U_j}$, $\frac{\partial G_j}{\partial U_{j+1}}$ and $\frac{\partial G_j}{\partial U_{j-1}}$.

From (3.59):

$$\frac{\partial G_j}{\partial U_j} = 1 - \frac{\Delta T}{2}\frac{\partial F_1}{\partial \omega} - \frac{\Delta T}{4(\Delta X)^2}(U_{j+1} - 2U_j + U_{j-1} + u_{j+1}^n - 2u_j + u_{j-1}^n)\frac{\partial F_2}{\partial w} + \frac{\Delta T}{(\Delta X)^2}F_2 \quad (j = 1, 2, \ldots, N)$$

$$\frac{\partial G_j}{\partial U_{j+1}} = -\frac{\Delta T}{4\Delta X}\frac{\partial F_1}{\partial \xi} - \frac{\Delta T}{2(\Delta X)^2}F_2 \quad (j = 1, 2, ,,,, N-1)$$

$$\frac{\partial G_j}{\partial U_{j-1}} = \frac{\Delta T}{4\Delta X}\frac{\partial F_1}{\partial \xi} - \frac{\Delta T}{2(\Delta X)^2} F_2 \qquad (j = 2, 3, \ldots, N)$$

$$\frac{\partial G_j}{\partial U_K} = 0 \qquad (|j-K| \geq 2) \tag{3.64}$$

If $U_j^{(m-1)}$ is an approximate solution the next approximate solution can be obtained through the correction factor $\lambda^{(m)}$:

$$U_j^{(m)} = U_j^{(m-1)} + \lambda_j^{(m)} \tag{3.65}$$

The correction factors $\lambda_j^{(m)}$ are calculated from

$$\lambda_j^{(m)} = A_{j+1}\lambda_{j+1}^{(m)} + B_{j+1} \tag{3.66}$$

with $\lambda_{N=1}^{(m)} = 0$, and A_j and B_j satisfying:

$$A_{j+1} = \frac{a_j}{b_j - c_j A_j}$$

$$B_{j+1} = \frac{c_j B_j - d_j}{b_j - c_j A_j} \qquad (j = 1, \ldots N) \tag{3.67}$$

with $A_1 = 0$ and $B_1 = 0$.

The variables a_j, b_j and c_j and d_j include the derivatives (3.64):

$$a_j = \frac{\partial G_j}{\partial U_{j+1}}, \quad b_j = -\frac{\partial G_j}{\partial U_j}, \quad c_j = \frac{\partial G_j}{\partial U_{j-1}},$$

$$d_j = -U_j^{(m-1)} + u_j^n + \Delta T F_1 + \left[U_{j+1}^{(m-1)} - 2U_j^{(m-1)} + U_{j-1}^{(m-1)} + u_{j+1}^n - 2u_j^n + u_{j-1}^n\right]\Delta T \frac{F_2}{2(\Delta X)^2} \tag{3.68}$$

These variables are actually the coefficients of the tridiagonal system of the iteration corrections:

$$a_j \lambda_{j+1}^{(m)} - b_j \lambda_j^{(m)} + c_j \lambda_{j-1}^{(m)} = d_j \qquad (3.69)$$

For each iteration the relative error

$$\max_j \left| \lambda_j^{(m)} / U_j^{(m)} \right| \qquad (3.70)$$

can be checked against a predetermined tolerance, so establishing the requirement for another iteration.

When the desired accuracy is achieved the value $U_j^{(m)}$ obtained in (3.65) can be considered as the solution u_j^{n+1}. These values are then used to obtain the solution for the next time step. For the first iteration obviously $U_j \equiv u_j^n$ in expressions (3.53) and (3.54).

3.3.4 Practical application

In order to have a first idea of the results obtained for a non-uniform amplitude of motion a programme using the Crank-Nicholson procedure was prepared. It is presented in Appendix 2. For the sake of simplicity a simple thrust disc bearing was chosen as vibrating surface. The input date used was:

R_o - disc external radius = 42.5 mm.

th - thickness of the disc = 8.5 mm.

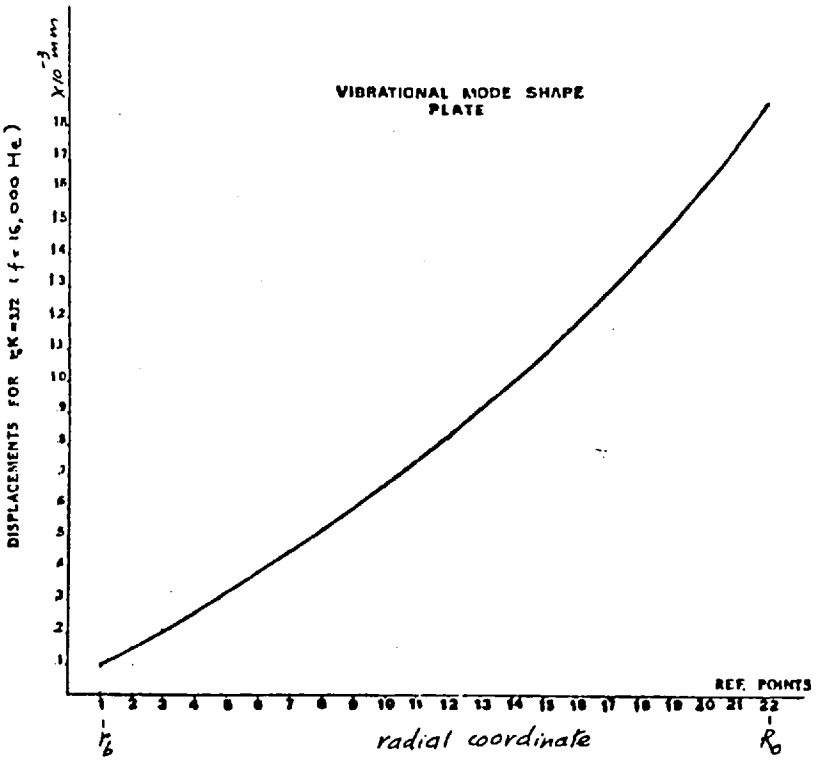

FIG. 3.4 Disc mode shape (from radius r_b to R_o).

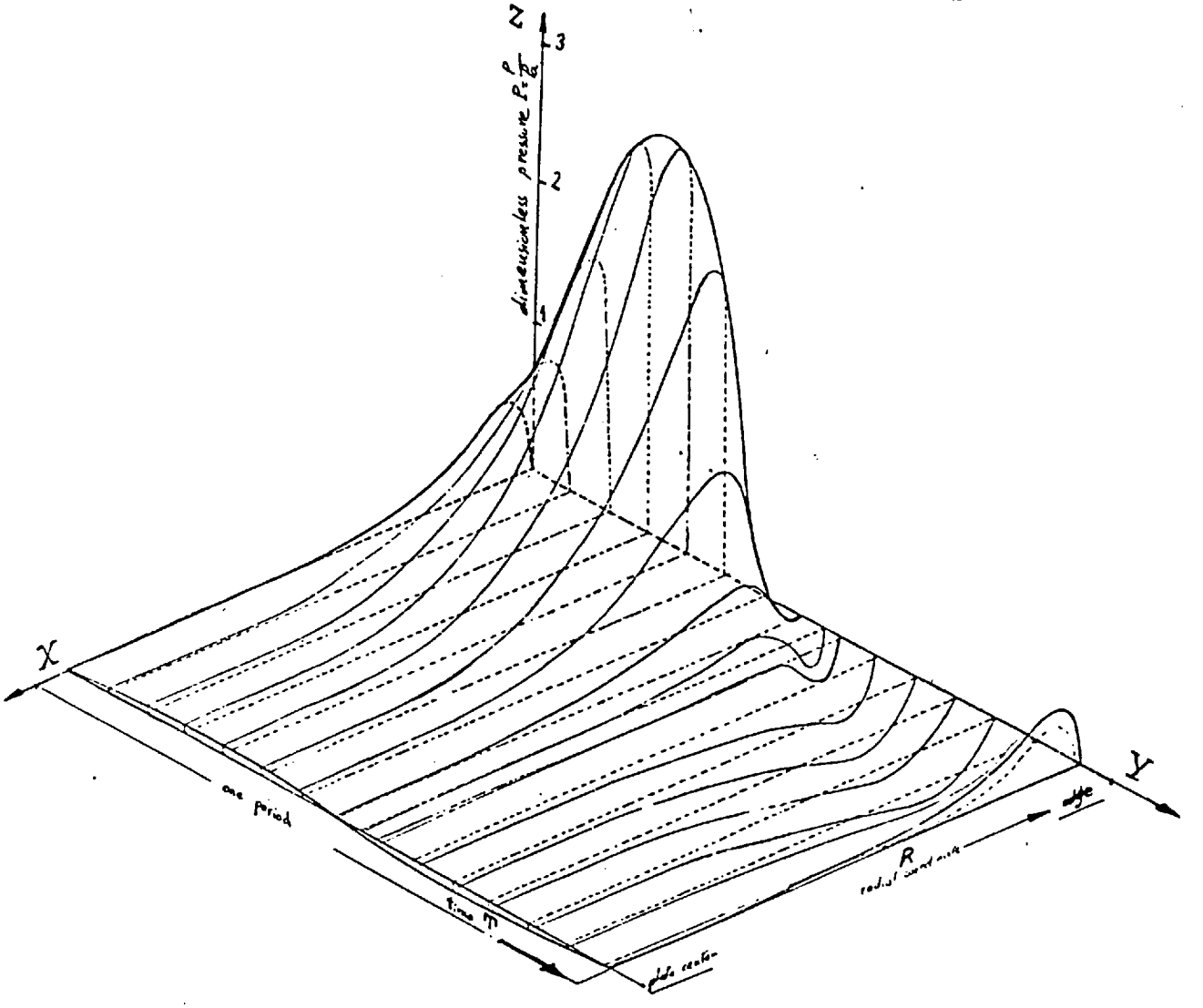

FIG. 3.5 Pressure distribution for disc plate - non-uniform excursion ratios.

h_o - assumed mean gap between bearing surfaces

$= 25.4 \times 10^{-4}$ mm

f - squeeze motion frequency = 16 KHz.

The disc was assumed to have an uniform amplitude of vibration from the centre to the radius r_b = 17.2 mm. The reason for this assumption is better explained in Chapter 7 dealing with disc thrust bearings.

From the radius r_b to the edge the plate mode shape is represented in Fig. 3.4.

The pressure distribution obtained for one period is shown in the 3-axial representation of Fig. 3.5. The X and Y axis represent respectively the radial coordinate and the time interval. The Z axis represents the pressure values. It is evident the non-symmetrical behaviour of the pressure curve in respect to the time. The maximum and minimum are verified near the edge with a steep "smoothing" to the atmospheric pressure.

For this same case a comparison of adimensional load capacity was established against that of uniform excursion. Both curves are represented in Fig. 3.6.

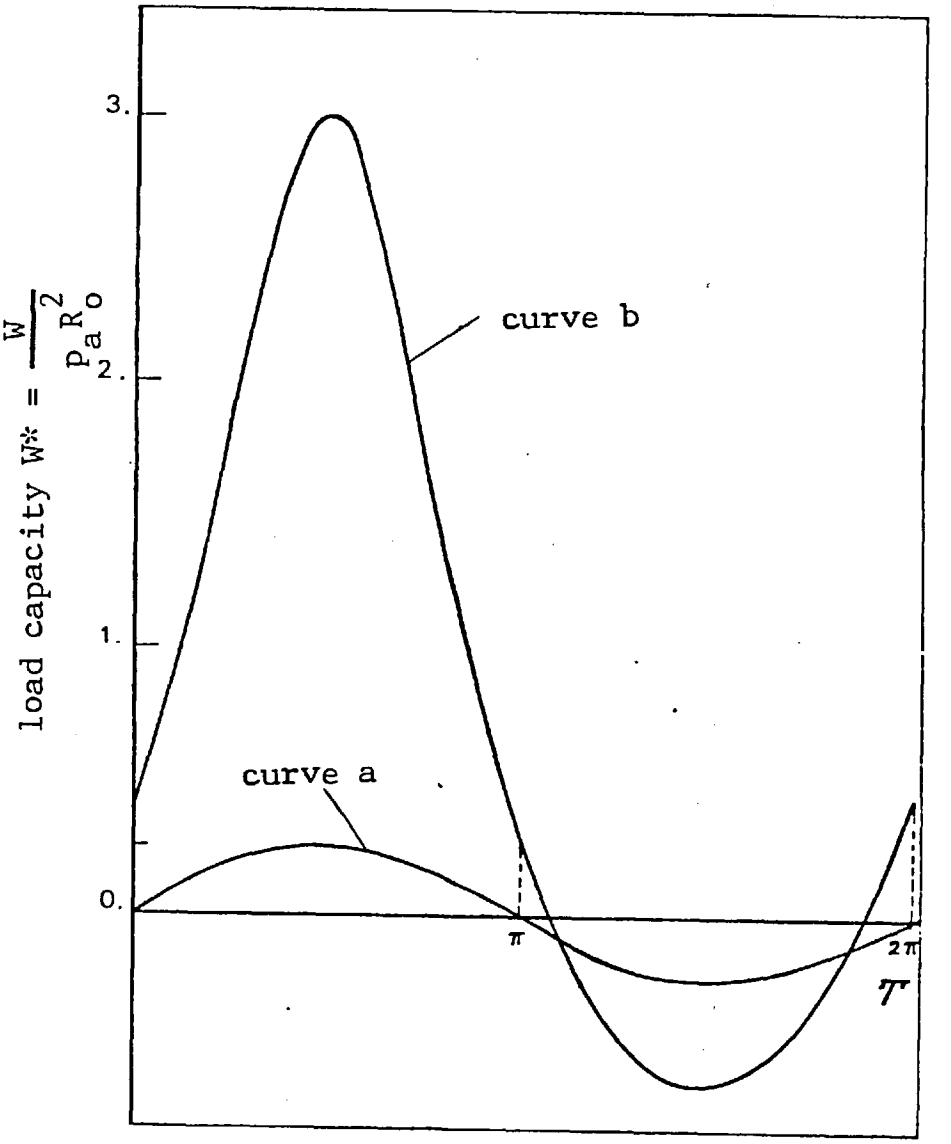

FIG. 3.6 Load capacity for one period of time for disc bearing:
Curve a - uniform excursion ratio,
Curve b - non-uniform excursion ratio.

3.4 CONCLUSIONS

Use of Boyle's Law provides only a rough calculation of the pressure distribution for uniform excursion. From PH = cte can be implied that the pressure ($P \alpha 1/H$) is

dependent on the time along the all surface bearing. This does not agree with the boundary condition $P = 1$ (corresponding to $p = p_{atm}$).

The analytical solution has the attraction of deriving analytical expressions for the solution of the Reynolds equation. In most of the practical cases the requirement for the squeeze number, σ, to be greater than 10^3 is satisfied. This enables one to calculate $\psi(X,T)$ as $\psi_\infty(X)$, neglecting terms of the order of $\frac{1}{\sqrt{\sigma}}$.

But, like Boyle's Law, the asymptotic solution does not satisfy the boundary condition (3.22). The boundary layer needs a special mathematical treatment (see equations (3.31)-(3.34)) and then the calculation of the $\lim \psi$ when the coordinate X tends to the boundary value. Actually this means that one uses a pseudo-boundary condition at an infinitesimal distance inside the true boundary (3.37). The width of this band bordering the ambient edge is of the order of $1/\sqrt{\sigma}$. The asymptotic theory has been extensively used by several authors for cases of uniform excursion.

For this case a relatively good agreement with numerical procedures is achieved, as Pan discussed in (10),

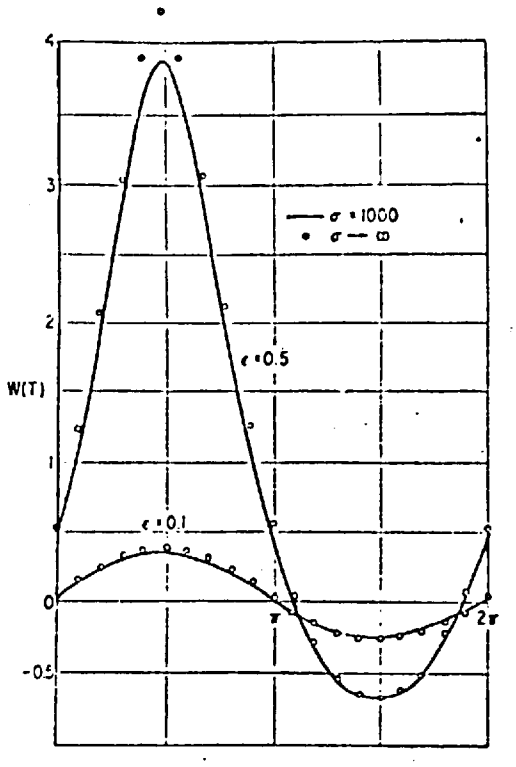

FIG. 3.7

Force variation for one period as predicted by the asymptotic theory ($\sigma \longrightarrow \infty$) and by numerical approximation (σ = 1000) for flat discs (Ref. 10).

see Fig. 3.7. When it was experimentally realised that the excursion had to be considered as non-uniform along the bearing surface a significant amount of complexity was introduced in the asymptotic theory,(13) and (29), to cope with the influence of this parameter. These analytical extensions of this theory still proved to be very limited on the allowable variation for this parameter. This seems to be one of the greatest drawbacks of the asymptotic theory.

The numerical methods are apparently more laborious than the asymptotic theory, though they present the

advantage of obtaining increased accuracy, as a function of the size of time steps. In a practical case there must be a compromise between the accuracy requirement and computing time. However, the greatest advantage of the numerical methods is the possibility of consideration of any case of modal shape of the bearing surface.

Calculating the bearing modal shape at working frequency and for a given mean clearance it is possible to know the film thickness at each instant for arbitrary points of the bearing surface. Then, these values are introduced as data in the numerical procedure. This will give the pressure distribution during one period of the squeeze motion.

To obtain the load capacity a double integration for one period of time and for the space coordinate interval is required.

An evaluation of the characteristics of the numerical methods was performed by Michael [5]. For a case where the analytical solution is known he performed several computing experiments. This enabled him to compare the error made in each case. His results are summarised in Fig. 3.8, Fig. 3.9 and Fig. 3.10. The error curves are traced for different spatial coordinate values, X = .25,

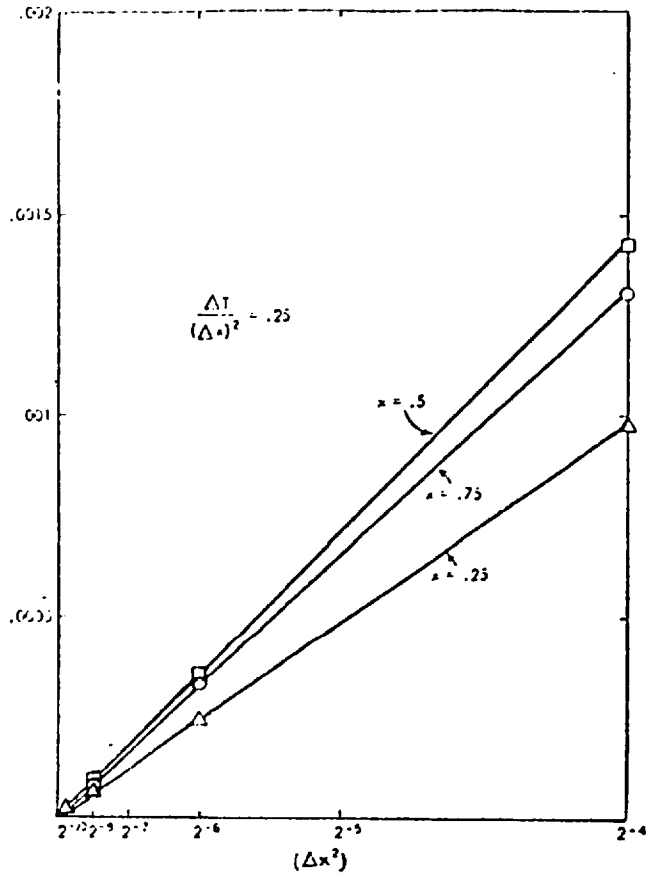

FIG. 3.8 Total error for explicit method.

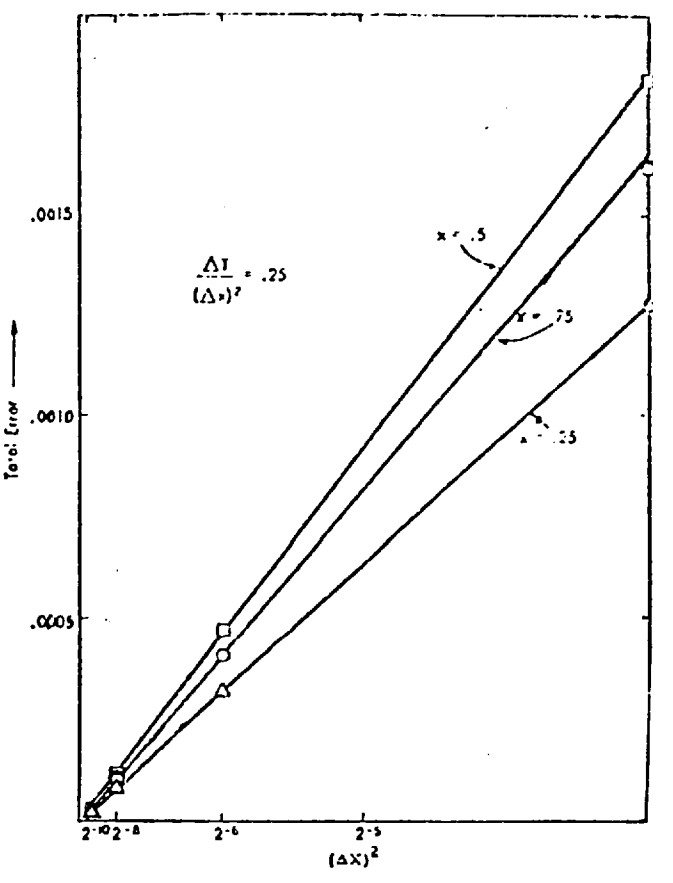

FIG. 3.9 Total error for Lees' formula.

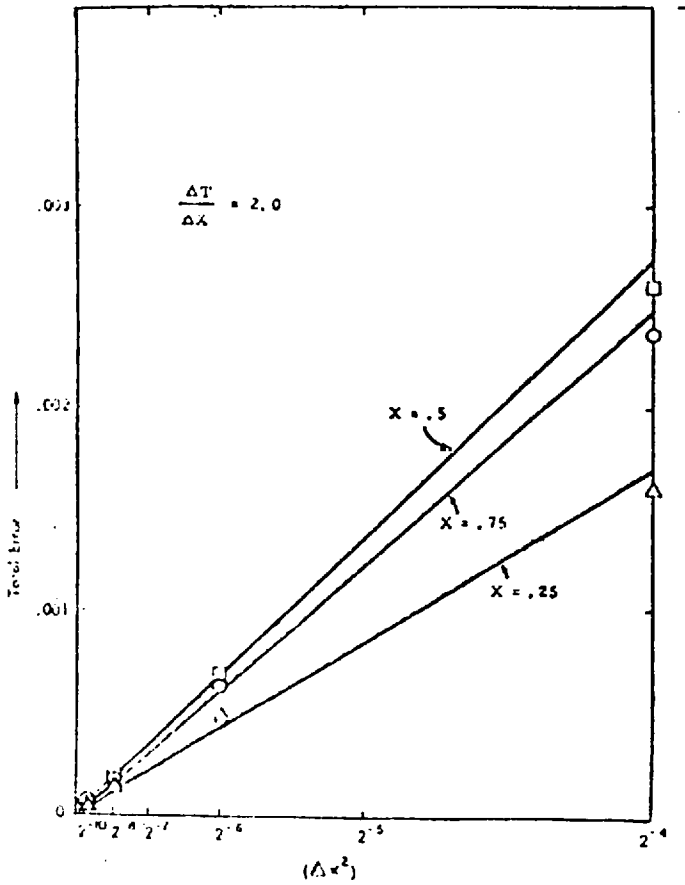

FIG. 3.10 Total error for Crank-Nicolson method.

TABLE 3.1 Maximum absolute error and computing time comparison.

ΔT	No of time steps	Maximum absolute error: Explicit formula	Lees formula	Crank-Nicolson formula
2^{-14}	4096	0.0[illegible]0002	0.0[illegible]0003	0.[illegible]
2^{-12}	1024	0.0[illegible]02	0.0[illegible]03	0.0[illegible]
2^{-10}	256	unstable	0.0[illegible]06	0.0[illegible]
2^{-8}	64	unstable	0.0[illegible]017	0.0[illegible]
2^{-6}	16	unstable	0.0[illegible]	0.0[illegible]
2^{-4}	4	unstable	0.0[illegible]	0.0[illegible]

ΔT	No. of time steps	Computing time, sec: Explicit formula	Lees formula	Crank-Nicolson formula
2^{-14}	4096	184	205	216
2^{-12}	1024	46	51	61
2^{-10}	256	unstable	12.8	15.4
2^{-8}	64	unstable	3.2	5.1
2^{-6}	16	unstable	.8	1.3
2^{-4}	4	unstable	.2	0.32

Note: Figures and Table from Ref. 5.

$X = .5$, and $X = .75$. The coordinate interval had the value $X = 1/32$ and ΔT was varied from 2^{-1} to 2^{-10}. As ΔT was increased it is apparent from the Figs. cited that the accumulated error (truncation error plus rounding) of the Lees formula increased steadily while the Crank-Nicholson formula increased very little.

The explicit method was unstable to values of ΔT of 2^{-10}. For the same time step the error of the Lees formula was smaller than that of the Crank-Nicholson when the time step is 2^{-14}. This suggests the use of the Lees formula when an extremely good accuracy is desired regardless of the computing time, or when the working frequency is very high. The Crank-Nicholson method, however, gave very good results even for relatively large time steps.

CHAPTER 4

EXPERIMENTAL PRELIMINARIES

4.1 THE OPTICAL MEASUREMENT SYSTEM

4.1.1 Introduction

The prediction of the pressure generated through the squeeze film effect requires the knowledge of the film thickness between the two bearing surfaces.

For an initial mean clearance and if it is assumed a stationary condition for the supported member, this film thickness is only a function of the lower moving member. When this member is considered as rigid, the gap will also be uniform at all points and only one amplitude measurement is sufficient to define it. However, in case of a flexible bearing support, the film thickness is also a function of the radial coordinate (considering only axi-symmetric vibrations). In this case we have to obtain local values for the film thickness and therefore for the motion amplitude. As the bearing size is usually relatively small (in our case, O.D. = 60 mm.), the physical size of the sensing element used for the evaluation of the motion amplitude is an important factor. Another significant condition is that the frequency response of the measuring

equipment must be good at high frequencies as in case of the conical shapes, the interesting frequencies can go as high as 20 KHz. For these two reasons, accelerometers are not suitable for this application. Fortunately an optical system called the Fotonic Sensor, and developed by Mechanical Technology Incorporated, satisfies these requirements and was used for the amplitude measurements.

4.1.2 Principle of operation

4.1.2.1 The fibre optic system:

Consider a light source and a light receiver, both near a moving reflecting surface, as in Fig. 4.1. When the sending and receiving elements are in contact with the surface, no light is reflected to the receiving element. As the distance increases, the cone of light from the transmitting element illuminates an increasingly larger area on the work surface. When this light is reflected by the surface the receiving element gets an increasing amount of this light and the relationship between surface displacement and receiver illumination is essentially linear. If the complete surface of the receiving element is illuminated by the reflected light this function ceases to be linear and reaches a peak, as shown in Fig. 4.2, and thereafter the

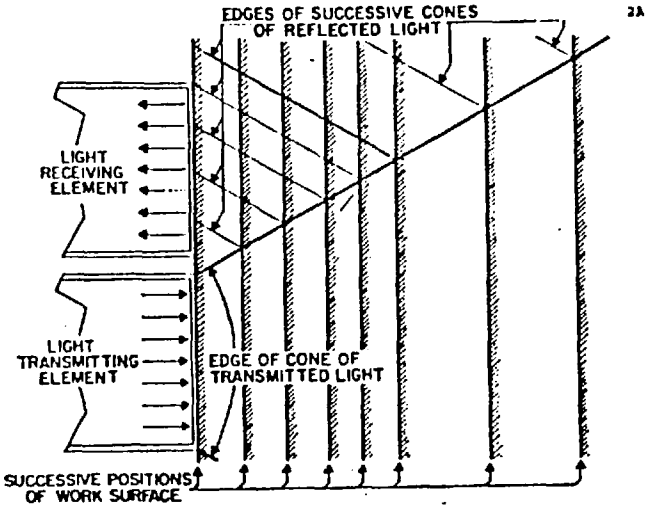

FIG. 4.1 Principle of operation for optical displacement measurements (Ref. 40).

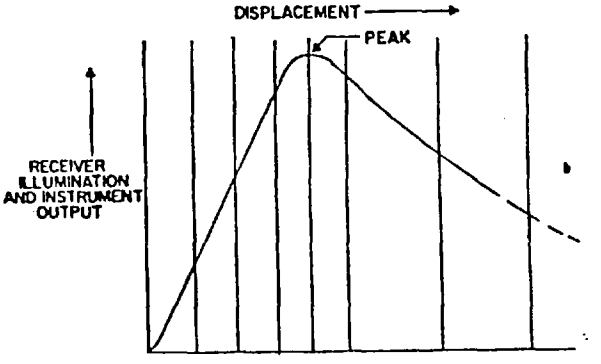

FIG. 4.2 Fotonic sensor response curve (Ref. 40).

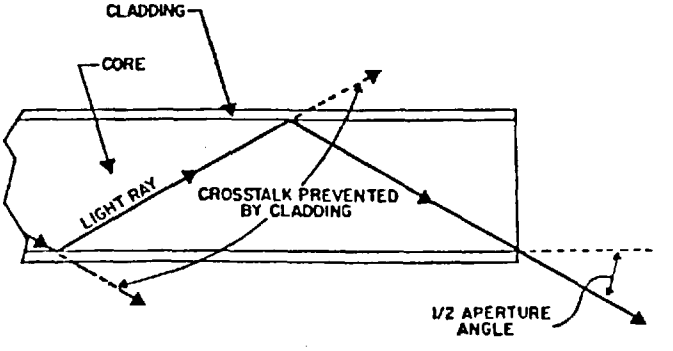

FIG. 4.3 Detail of light transmission through the glass fibres.

illumination decreases in an approximate inverse proportion to the square of the distance. Using a large number of fibre optics as sending and receiving elements, a steep response curve is obtained.

These glass fibres, numbering about 600, are the main components of the Fotonic Sensor probe. The receiver uses a photo diode to generate a current dependent on the intensity carried by the receiving branch. In the case of the KD-45 model, the one used in the experiments reported, the light source and the photocell are located in a remote cartridge connected to the control unit by a multicore cable.

Major advantages of this technique are the reduced size of the sensing element, flexibility of positioning and no contact with the moving surface.

4.1.2.2 Design characteristics:

The sensitivity of this instrument is dependent on the fibre bundle and the numerical aperture of the individual fibres. Another influencing factor is the effectiveness of the fibre cladding in preventing crosstalk. The cladding is obtained using glass with a refractive index smaller than

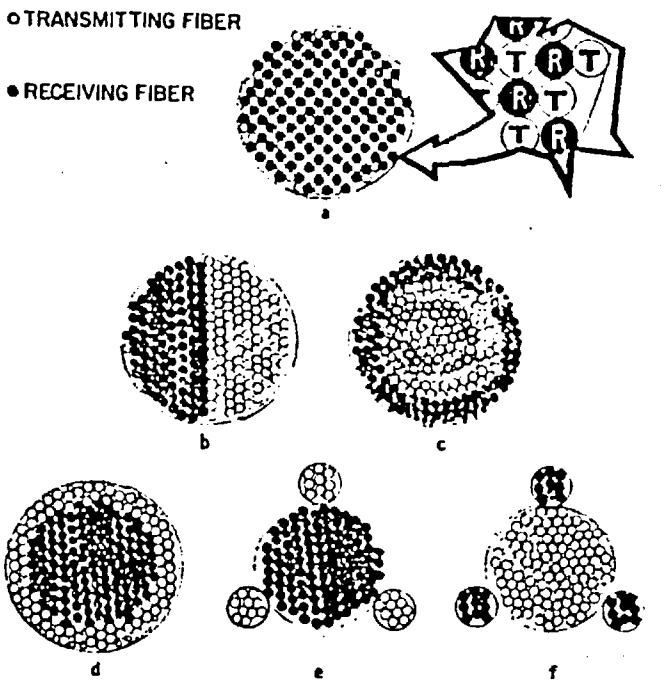

FIG. 4.4 Glass fibre arrangements.

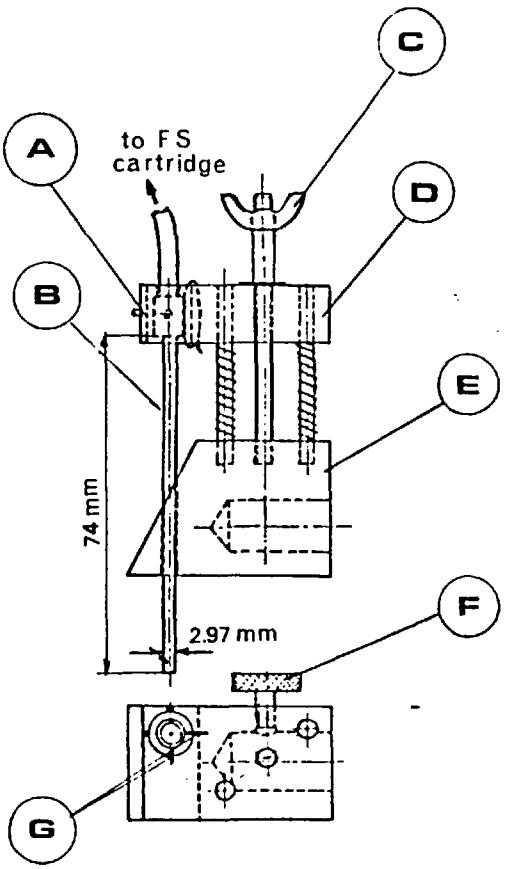

FIG. 4.5 Fotonic sensor probe support.

the core, which is in flint glass. This index difference defines the maximum angle of internal reflection and therefore the fibre aparture angle (usually 60^{o}).

The distribution of the fibres, controls the displacement range and the slope sensitivity of the probe. The optimum arrangement for the steepest response curve requires the surrounding of each receiving fibre with four transmitting fibres, Fig. 4.4. This is the configuration that enables more receiving fibres to be affected by the light emanated from one emitting fibre as the distance between probe and work surface increases. Unfortunately, this is very expensive and in practice it is a random distribution of the fibres that is used. The specification set for this case requires that no visible grouping of adjacent transmitting or receiving fibres should be seen (40). Other types of distribution are represented in the same figure. During the light transmission there is some light loss (between 50% and 80%) and this is a function of the bundle length. A compromise with the required working handling capability gives a maximum length of 3 feet.

4.1.3 Application to amplitude measurements

One of the requirements for the correct use of this equipment is for the probe to be normal to the moving

surface. For adjustment purposes and proper support of the probe, a stand (see Fig. 4.5) was built. The main parts are:

A. probe positioning, fine adjustment,

B. Fotonic Sensor probe,

C. vertical adjustment,

D. moving support,

E. static base,

F. stand fixing screw,

G. probe positioning springs.

After ensuring proper vertical alignment, it is necessary to compensate for different values of surface reflectivity. This is done using the Intensity Control in the Fotonic Sensor. Changing the meter sensitivity, a full scale meter deflection is achieved at the peak setting.

This corresponds to 2 volts DC output voltage. The linear range, as can be seen in Fig. 4.6, is obtained for meter readings between 20% and 60%. Because for low amplitudes and high frequencies the use of a high pass filter is recommended, a sound and vibration analyser was employed (from General Radio) for measurement of Fotonic Sensor output. This apparatus enabled a more accurate voltage measurement,

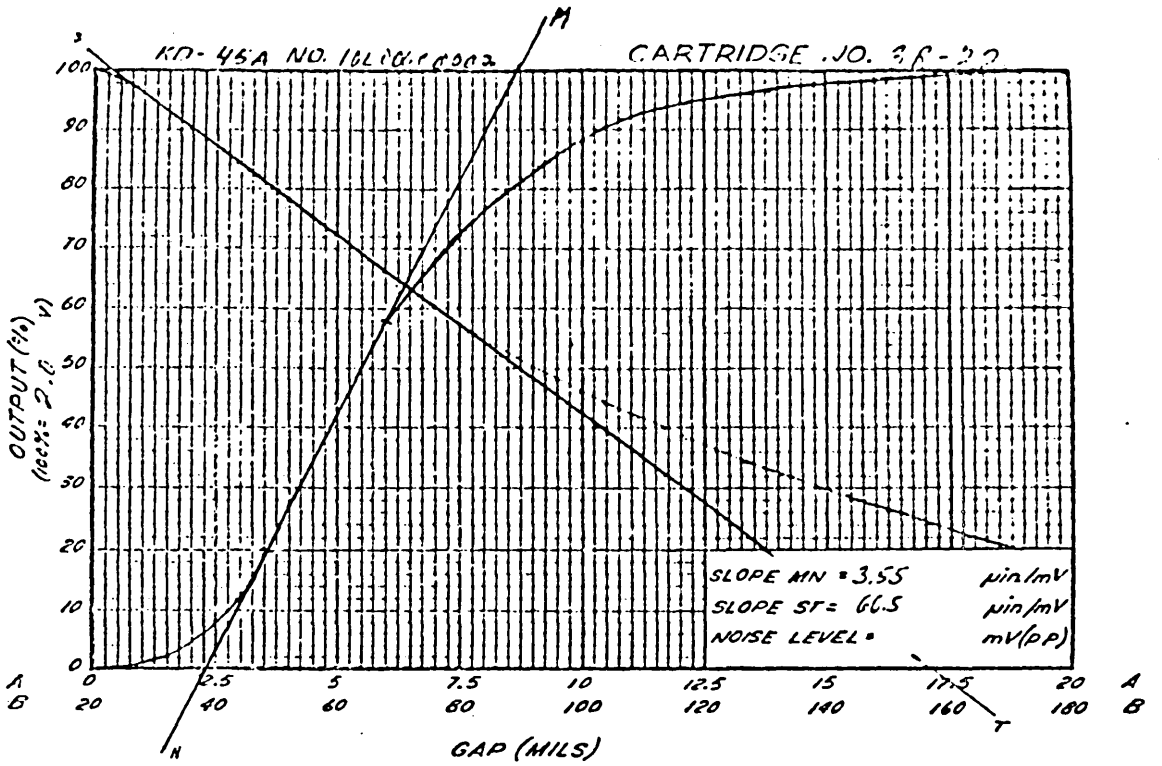

FIG. 4.6 Fotonic sensor calibration curve - for cartridge assembly 3R-22

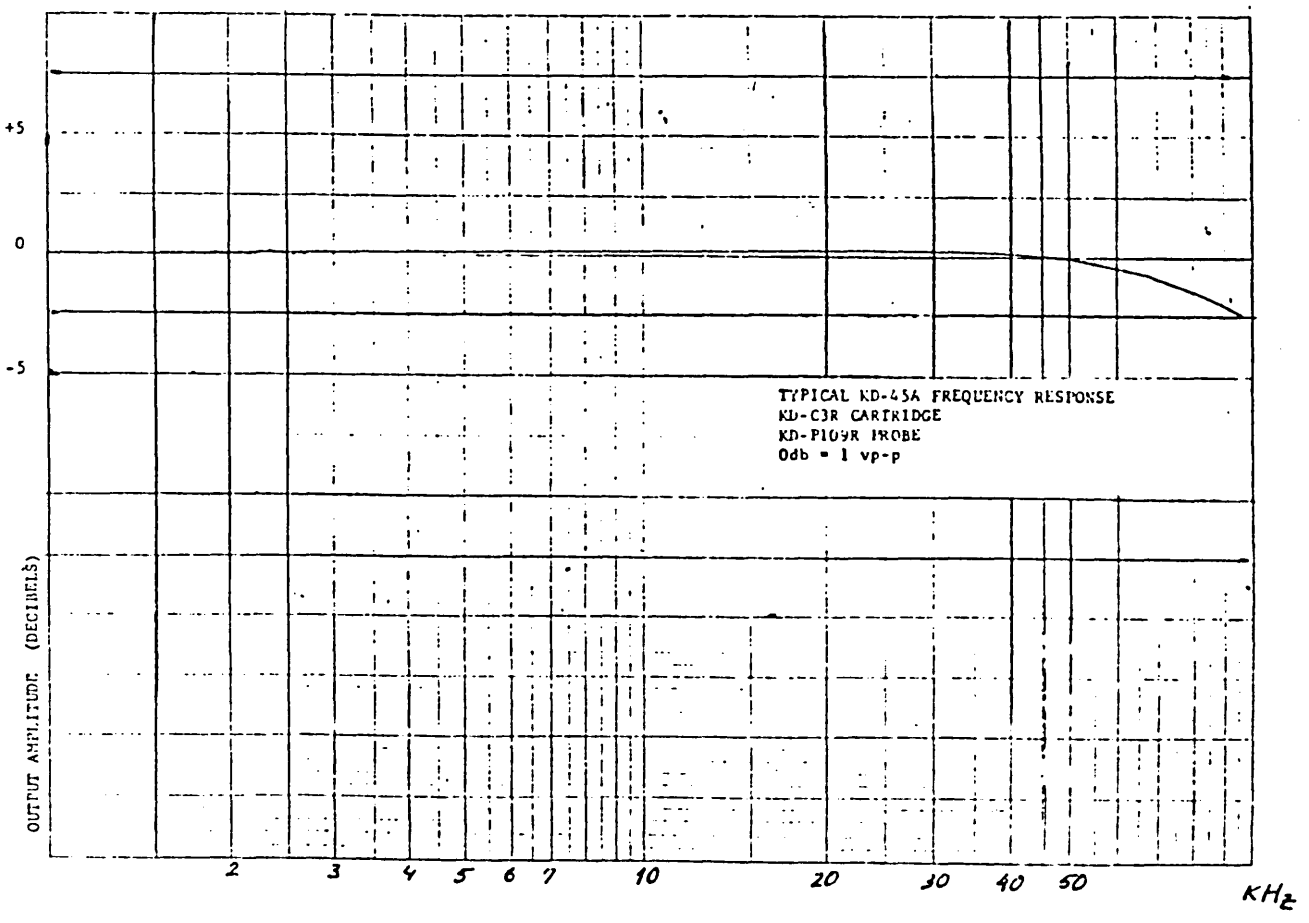

FIG. 4.7 Fotonic sensor frequency response

using at the same time its filtering capability. According to checks previously made, the filter unit is loss compensated. These checks consisted of comparing a reference signal displayed in an oscilloscope with the signal reached by the vibration and sound analyser, using the same reference signal intput at several frequencies.

4.2 CALIBRATION OF THE FOTONIC SENSOR

4.2.1 Manufacturer's calibration

The conversion of the Fotonic Sensor signal output to displacement units requires a sensitivity curve. Every cartridge is calibrated by M.I.T. and the values of output plotted in a graph for that individual cartridge. The frequency response curve is also tested. Both curves are represented in Fig. 4.6 and Fig. 4.7, respectively.

The calibration procedure used by Mechanical Technology Incorporated is as follows:[41]

4.2.1.1 Static calibration:

The probe or sensor is fixed. A highly polished reference surface is then moved to several positions. This motion is accurately controlled through an arrangement (similar to the rotating knob of a micrometer)

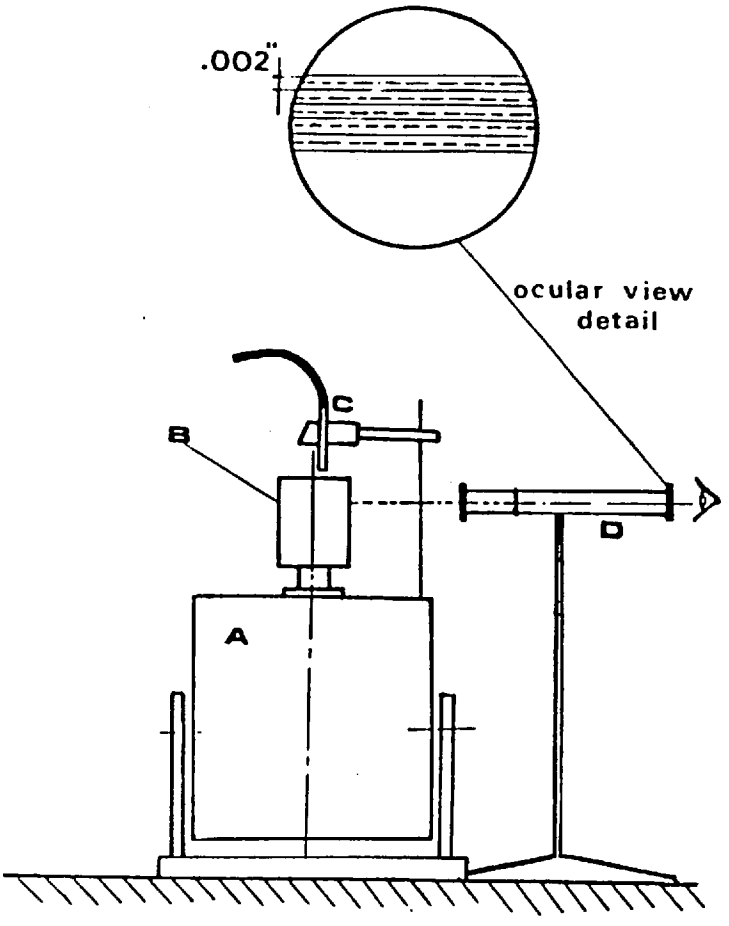

FIG. 4.8 Experimental arrangement for Fotonic sensor dynamic response checking.

Frequency c.p.s.	Half band value in.	Motion Amplitude		Fotonic sensor setting
		Voltage reading mV (r.m.s)	Peak values in.	
70	.001	250 250 220	.0012 .0012 .0011	24
80	.002	410 450 420	.0021 .0023 .0022	34

TABLE 4.1

that provides a direct reading of 10^{-4} inch. This equipment (KD-CM III calibration fixture) is also used for calibration of Wayne Kerr displacement transducers.

4.2.1.2 Dynamic calibration:

In this case there is not what can be considered as a typical dynamical calibration, but the measurement of the F.S. output variation with the frequency. The Fotonic Sensor probe is aligned with a LED (light emitting diode) light source that is amplitude modulated over the frequency range of 10 Hz to 2 MHz by connecting it to a signal generator. An oscilloscope is used to monitor the LED current drive and the resultant analog output of the Fotonic Sensor.

4.2.2 Laboratory Calibration

This section concerns the calibration made here. The equipment used is mainly intended for accelerometers so that this is then a true dynamic calibration.

Fig. 4.9 shows the experimental set-up used for this purpose. The Fotonic Sensor probe, C, is positioned over the top of the metallic block, B. The block is vibrated using a Derritron VP5 type vibrator, A. The

motion amplitude is varied by acting on the amplifier driving the vibrator.

On the metallic block are engraved the marks shown in the figure detail. These marks are spaced at intervals of 2, 4, 10 and 20 thou.

When it is apparent that due to the amplitude of vibration two lines seem to coincide with, respectively, the next upper and lower ones, it means that the block mass is moving with amplitude equal to half the distance between the marks. The results obtained are expressed in Table 4.1.

4.2.3 Comment on Calibration Procedures

The original calibration system (from M.I.T.) can be criticised due to the fact that there is no direct dynamic calibration but just a frequency response check. On the other hand, the laboratory procedure is a true dynamic calibration but had two major limitations. One of these is the impossibility of running the experiments at the range of frequencies to be used in the actual tests (5-20 KHz). This is caused by the performance of the vibrator which deteriorates at higher frequencies, with a first resonance at 7 KHz. The other factor affecting these results is the difficulty in noting the visual

superimposition of the engraved lines. A third factor that should be mentioned is the accuracy of the readings of the voltmeter, upon which depend the amplitude calculations. The values obtained with the Fotonic Sensor are slightly higher than nominal (defined by the marks). The error varies from +5 to +20%. A possible explanation for this lies in the inaccuracies referred to above. The use of the other marks, at .010 and .020 in. (.254 and .508 mm.), was not considered. Their superimposition would correspond to .005 in. (.127 mm.) and 0.010 in. (.254 mm.), respectively. From the calibration curve, Fig. 4.6, it is seen that the linear length of the curve (defining the slope MN) is 2.5 thou (.064 mm) from 3.5 thou to 6 thou. And for the half band of 5 thou the sensitivity cannot be taken then as constant. The other possibility considered was the use of the falling side of the curve. But for this branch the sensitivity (defined by the slope ST) is about twenty times more than that of the upward branch and no improvement in accuracy would be obtained.

CHAPTER 5

PIEZOELECTRIC CERAMIC ANALYSIS

5.1 PROPERTIES OF PIEZOELECTRIC MATERIALS

5.1.1 Introduction

We described briefly the phenomenon of piezoelectricity in Chapter 2. The piezoelectric effect is generally dependent upon the orientation of the applied force or the electric field with respect to the axes of the piezoelectric material. For natural piezoelectric materials such as quartz, these axes were established by crystallographers (Fig. 5.1). For piezoelectric ceramics, the axes have been designated with reference to the direction of the electric poling field, Fig. 5.2. This direction is taken as the Z axis of a right-hand orthogonal axial set X, Y, Z.

Since the properties are not variable in the plane perpendicular to this axis the senses chosen for X and Y are not important. It is usual practice (42) to relate the ceramic properties with subscripts, where the axes X, Y and Z are represented respectively by 1, 2 and 3 and the shear about these axes as 4, 5 and 6, Fig. 5.2.

5.1.2 Characteristic Constants

The relevant constants for piezoelectric materials are of three types:

i) Elastic Constants

ii) Electric Constants

iii) Piezoelectric Constants

5.1.2.1 Elastic Constants:

The most important elastic constant is the compliance defined as strain/stress. In order to identify the direction of the strain we use the first subscript, whilst the second subscript gives the direction of stress. As the constants differ slightly with the conditions at the ceramic electrodes, we use a superscript. Thus, if the electrodes of say a bar of piezoelectric material are connected together the bar displays higher compliance than when the electrodes are not connected. If the electric field is held constant by short circuiting the electrodes we use the subscript E. For an open circuit at the electrodes the superscript used is D. As an example, S_{33}^{E} is the strain to stress ratio in the 3 direction at a constant electric field (E = 0), with the condition that all other external stresses are constant. The symbol S_{44}^{D} is the shear strain to shear stress ratio at

constant electric displacement (D = 0) for shear strain around the axis 1 to shear stress around the 1 axis.

5.1.2.2 Electric Constants:

Notation similar to that used in the previous section can be applied to the dielectric constant (dielectric displacement/electric field). In this case the first subscript refers to the direction of the electric field and the second subscript denotes the direction of the electric displacement. In most of the piezoelectric materials used, the field along one axis results in dielectric displacement only along the same axis. For this reason, the two subscripts are the same, and one can be omitted; e, ε_3 means ε_{33}. In piezoelectric materials not only do the mechanical properties depend on the electrical conditions but the electrical properties also depend on the mechanical constraints. In fact, when a piezoelectric material is completely free the dielectric constant is higher than when the body is mechanically constrained. To define these mechanical boundary conditions, the subscripts S or T are used. The superscript T denotes the condition of constant stress, with no mechanical restraint. For constant strain, the superscript S is used.

5.1.2.3 Piezoelectric Constants:

The piezoelectric constants are actually electro-mechanical constants. The most commonly used are the coupling constant K_{ij}, the strain constant d_{ij}, and the stress constant g_{ij}. The coupling constant is related to the ability of the material to transmit mechanical energy to electrical energy and vice versa. The square of coupling is equal to the transformed energy divided by the total energy input. As before, subscripts are used, the first indicating the direction of electric field and the second the direction of stress or strain. The d_{ij} constant represents the ratio of the strain developed along or around a specified axis, to the field applied parallel to another specified axis, when all other external stresses are constant. The g_{ij} constants express the relation between the field developed along a specified axis to the stress applied along or around a specified axis when all other external stresses are constant. A very important constant that should also be mentioned, even if not belonging to one of these groups, is the frequency constant. The frequency constant N_{ij}, is the product of the mechanical resonant frequency (under specified electrical boundary conditions) and the dimension relevant to the type of vibration. Other important constants are the dissipation

factor and the mechanical Q. When an elastic body is deformed, not all the energy applied is stored as elastic energy. Part of this energy is dissipated as heat due to "molecular friction". The mechanical losses are expressed in terms of mechanical Q, which is the ratio of mechanical stiffness reactance to the impedance at resonance. The electrical losses are expressed as a dissipation factor, tan δ.

The units usually used for these constants, and their numerical values for the PZT ceramic series, are given in Tables 5.1 and 5.2.

5.1.3 Resonance Frequency of PZT-4 Ceramics

For future calculations one must know at least approximately, the value of the first resonant frequency of the ceramic disc (PZT-4 ceramic) used in these experiments. For this purpose we employ two methods. The first uses the definition of the frequency constant N_{3t} (Section 5.1.2). In this case, considering the thickness dilatational mode, the relevant dimension is the ceramic thickness, $t_c = 6.3 \times 10^{-4}$ m. The value of N_{3t}, from Table 5.2, is $N_{3t} = 2{,}000$ cycle meter s^{-1}. As

$$N_{3t} = f_c \times t_c \qquad (5.1)$$

the resonant frequency is $f_c = \frac{N_{3t}}{t_c} = 317$ KHz.

The other calculation procedure is based on a method by Onoe[43] and Lawson[44].

The basic equation for the resonance frequencies of a thickness mode piezoelectric resonator is:

$$\tan \Phi = \frac{\Phi}{K_t^2} \qquad (5.2)$$

where: $\Phi = \frac{\omega t_c}{2V_c}$, ω being the frequency, t_c the ceramic thickness, and V_c the phase velocity of the elastic wave motion and K_t is the coupling factor related to this mode of vibration. This equation was also derived by Stephenson[45], for longitudinal vibrations of bar shaped resonators. Tiersten[46] has shown that the same basic frequency equation could be applicable to the case of ceramic plates vibrating in thickness-dilatational and thickness-shear modes. Using the values of the roots of the frequency equation tabulated in (43), the resonance frequency of a crystal can be obtained in a straightforward way from equation (5.2):

$$\omega = \frac{2 V_c \Phi}{t_c} \qquad (5.3)$$

In our case $K_t = 0.51$. For $K_t = 0.5$ and a mode number n = 1 (first frequency) the Table 5.3 gives the value of 1.3932. The value of V_c obtained from (43) is $V_c = 2.4340$ Km/s.

TABLES FOR PIEZOELECTRIC PROPERTIES

TABLE 5.1

PIEZOELECTRIC PROPERTIES: SYMBOLS AND UNITS

ϵ_0 = dielectric constant of free space = 8.85×10^{-12} farads/meter.

ϵ^T/ϵ_0 = relative dielectric constant, free.

ϵ^S/ϵ_0 = relative dielectric constant, clamped.

$\tan \delta = \frac{1}{Q_E}$ = dissipation factor at 1 kcps, low electric field.

k_p = planar coupling factor.

k_{31} = transverse or lateral coupling factor.

k_{33} = longitudinal coupling factor.

k_{15} = shear coupling factor.

k_t = thickness coupling factor (laterally clamped).

d = piezoelectric constant, strain/field at constant stress or charge density /stress at constant electric field, 10^{-12} meters/volt.

g = piezoelectric constant, electric field/stress at constant charge or strain/charge density at constant stress, 10^{-3} volt meters/newton.

s^E = elastic compliance at constant electric field, 10^{-12} meter^2/newton.

s^D = elastic compliance at constant charge density, 10^{-12} meter^2/newton.

Q_M = mechanical Q. This is dependent upon configuration, and is given here for a thin disc.

N_1 = frequency constant of a thin bar, $f_R.\ell$, cycle meters/second.

N_{3a} = frequency constant of a long slender bar electroded on ends, $f_a.\ell$, cycle meters/second.

N_{3t} = frequency constant of a thin plate, $f_R.t$, cycle meters/seconds.

v_3^D = velocity of a compressional wave parallel to polar axis $\{c_{33}^D = (v_3^D)^2 \rho\}$, meters/second.

v_4^D = velocity of a shear wave perpendicular to polar axis with wave polarization parallel to polar axis $\{c_{44}^D = (v_4^D)^2 \rho\}$, meters/second.

v_4^E = velocity of a shear wave parallel to polar axis, $\{c_{44}^E = (v_4^E)^2 \rho\}$, meters/ second.

ρ = density, 10^3 kg/m^3.

ϕ = temperature, °C.

P = polarization, 10^{-6} coulomb/cm^2 (10^{-2} coulomb/m^2).

α = thermal expansion, 10^{-6}/°C.

TABLE 5.2

CONSTANTS DATA FOR CERAMICS OF PZT SERIES
(room temperature)

		Ceramic B	PZT-4	PZT-5A	PZT-5H	Preliminary data PZT-8
At one kcps*	$\epsilon_{33}^T/\epsilon_o$	1200	1300	1700	3400	1000
	$\epsilon_{33}^S/\epsilon_o$	910	635	830	1470	600
	$\epsilon_{11}^T/\epsilon_o$	1300	1475	1730	3130	—
	$\epsilon_{11}^S/\epsilon_o$	1000	730	916	1700	—
	tan δ	0.006	0.004	0.02	0.02	0.004
	k_p	−.33	−.58	−.60	−.65	−.50
	k_{31}	−.194	−.334	−.344	−.388	−.295
	k_{33}	.48	.70	.705	.752	.62
	k_{15}	.48	.71	.685	.675	—
	k_t	.384	.513	.486	.505	—
	k_{i3}	.491	.715	.715	.754	.63
	d_{31}	−58	−123	−171	−274	−93
	d_{33}	149	289	374	593	218
	d_{15}	242	496	584	741	—
	d_h	33	43	32	45	.32
	g_{31}	−5.5	−11.1	−11.4	−9.11	−10.5
	g_{33}	14.1	26.1	24.8	19.7	24.5
	g_{15}	21.0	39.4	38.2	26.8	—
	s_{11}^E	8.6	12.3	16.4	16.5	11.1
	s_{33}^E	9.1	15.5	18.8	20.7	13.9
	s_{44}^E	22.2	39.0	47.5	43.5	—
	s_{12}^E	−2.6	−4.05	−5.74	−4.78	−3.7
	s_{13}^E	−2.7	−5.31	−7.22	−8.45	−4.8
	s_{11}^D	8.3	10.9	14.4	14.05	10.1
	s_{33}^D	7.0	7.90	9.46	8.99	8.5
	s_{44}^D	17.1	19.3	25.2	23.7	—
	s_{12}^D	−2.9	−5.42	−7.71	−7.27	−4.5
	s_{13}^D	−1.9	−2.10	−2.98	−3.05	−2.5
	Q_M	400	500	75	65	1000
	N_1	2290	1650	1400	1420	1700
	N_{3t}	2740	2000	1890	2000	—
	N_{3a}	2530	2060	1845	1930	2000
	ρ	5.55	7.5	7.75	7.5	7.6
	Curie Point	115°C	328°C	365°C	193°C	300°C

k		f_n/f_M	k		f_n/f_M
	N=1			N=3	
0.00	1.5708	1.0000	0.00	7.8540	5.0000
0.05	1.5692	0.9989	0.05	7.8536	4.9997
0.10	1.5644	0.9959	0.10	7.8527	4.9991
0.15	1.5563	0.9907	0.15	7.8511	4.9981
0.20	1.5449	0.9835	0.20	7.8488	4.9967
0.25	1.5299	0.9740	0.25	7.8460	4.9949
0.30	1.5113	0.9621	0.30	7.8425	4.9926
0.35	1.4886	0.9477	0.35	7.8383	4.9900
0.40	1.4617	0.9305	0.40	7.8335	4.9869
0.45	1.4301	0.9104	0.45	7.8281	4.9835
0.50	1.3932	0.8869	0.50	7.8220	4.9796
0.55	1.3504	0.8597	0.55	7.8152	4.9753
0.60	1.3008	0.8281	0.60	7.8079	4.9706
0.65	1.2431	0.7914	0.65	7.7998	4.9655
0.70	1.1760	0.7486	0.70	7.7911	4.9600
0.75	1.0969	0.6983	0.75	7.7818	4.9540
0.80	1.0027	0.6383	0.80	7.7718	4.9476
0.85	0.8875	0.5650	0.85	7.7611	4.9409
0.90	0.7408	0.4716	0.90	7.7498	4.9337
0.95	0.5355	0.3409	0.95	7.7378	4.9260
	N=2			N=4	
0.00	4.7124	3.0000	0.00	10.9956	7.0000
0.05	4.7118	2.9996	0.05	10.9953	6.9998
0.10	4.7102	2.9986	0.10	10.9946	6.9994
0.15	4.7076	2.9969	0.15	10.9935	6.9986
0.20	4.7038	2.9945	0.20	10.9919	6.9976
0.25	4.6990	2.9915	0.25	10.9898	6.9963
0.30	4.6932	2.9877	0.30	10.9873	6.9947
0.35	4.6862	2.9833	0.35	10.9844	6.9929
0.40	4.6782	2.9782	0.40	10.9810	6.9907
0.45	4.6690	2.9724	0.45	10.9771	6.9882
0.50	4.6587	2.9658	0.50	10.9727	6.9854
0.55	4.6473	2.9586	0.55	10.9680	6.9824
0.60	4.6348	2.9506	0.60	10.9627	6.9791
0.65	4.6212	2.9419	0.65	10.9570	6.9754
0.70	4.6064	2.9325	0.70	10.9508	6.9715
0.75	4.5904	2.9223	0.75	10.9442	6.9673
0.80	4.5733	2.9114	0.80	10.9371	6.9627
0.85	4.5550	2.8998	0.85	10.9295	6.9579
0.90	4.5356	2.8874	0.90	10.9215	6.9528
0.95	4.5151	2.8744	0.95	10.9130	6.9474

TABLE 5.3 ROOTS OF FREQUENCY EQUATION AND FREQUENCY RATIOS TABULATED AS FUNCTIONS OF COUPLING FACTOR FOR n = 1, 2, 3, 4 (REF. 43)

Then:

$$\omega = \frac{2\, v_c\, \Phi}{t_c} = \frac{2 \times 4.340 \times 1.392 \times 10^3}{6.3 \times 10^{-3}}$$

$$= 3.6 \times 10^6 \text{ c.p.s.} = 306 \text{ Kps}$$

Comparing with the value obtained using the frequency constant (317 KHz) the agreement is quite good. Even assuming a reduction of the coupling factor which affects Φ, and a smaller value of the phase velocity, the value of resonant frequency is still substantially higher than the working frequency of the bearing unit (as considered in Section 5.3).

5.2 CERAMIC-BEARING ARRANGEMENT TYPES

The way the bearing surface is fixed to the driving element (the ceramic) is important. Use of ceramics as direct bearing members presents two major disadvantages: the mechanical instability and the tendency of ceramics to be easily damaged during operation.

For some types of ceramics it was found by Pan[47] that vibration amplitudes in excess of 10^{-4} in. (peak to peak) per inch of bearing diameter can cause dangerously high stresses in the piezoelectric material and increase rapidly the power dissipation. This means that one must use very small mean bearing gaps. Increasing appreciably the

vibration amplitude would, however, allow a corresponding increase in the mean bearing gap without loss in performance. This has resulted in the use of concentrators and wave extenders. Concentrators (Fig. 5.3a) are mechanical transformers which can amplify the motion of the bearing surface without affecting significantly the resonant frequency. Gradually varying cross sections with conical, Fourier, Catenoidal and exponential laws, and stepped concentrators are mentioned by Pan[12]. Using theory by Merkulov[48,49], Pan obtained gains of amplitude of vibration of the order of 15 to 20. Unfortunately concentrators had to be abandoned due to space and weight limitations. The wave extenders (Fig. 5.3b) act in a different way from that of the concentrators as the system frequency is different from that of the driver (the separate free resonator). The results obtained were not very favourable and these did not have much application either.

For a cylindrical ceramic operating at its longitudinal resonance (Fig. 5.4), Chiang[8] designed several arrangements of ceramic-conical bearings for gyroscopes. In his study he considered three designs for the elastic coupling between the bearings and the driven section. These configurations are represented in Fig. 5.5 (configuration "A"), Fig. 5.6 (configuration "B") and in Fig. 5.7

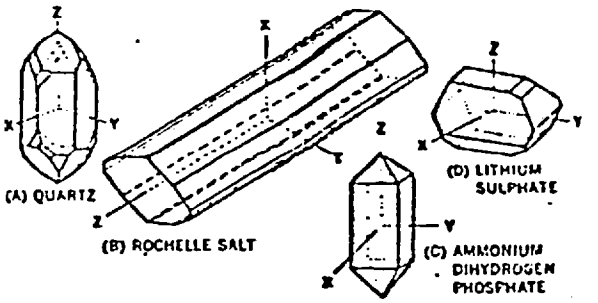

FIG. 5.1 Axes for natural piezoelectric materials.

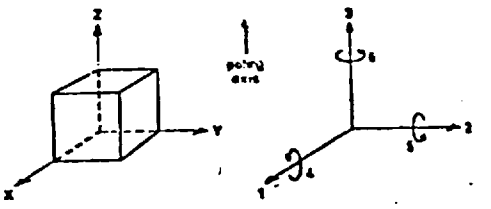

FIG. 5.2 Axes notation for ceramics.

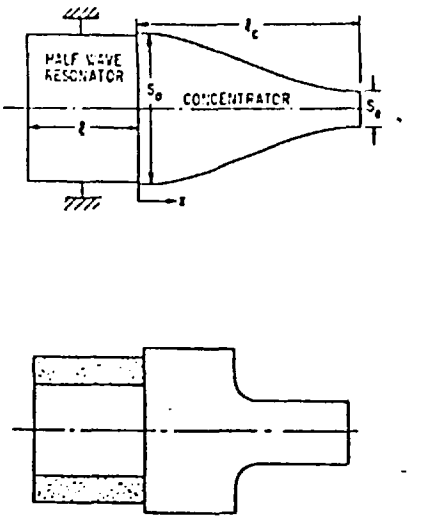

FIG. 5.3 Wave extenders-gradually varying and stepped concentrators(Ref. 12).

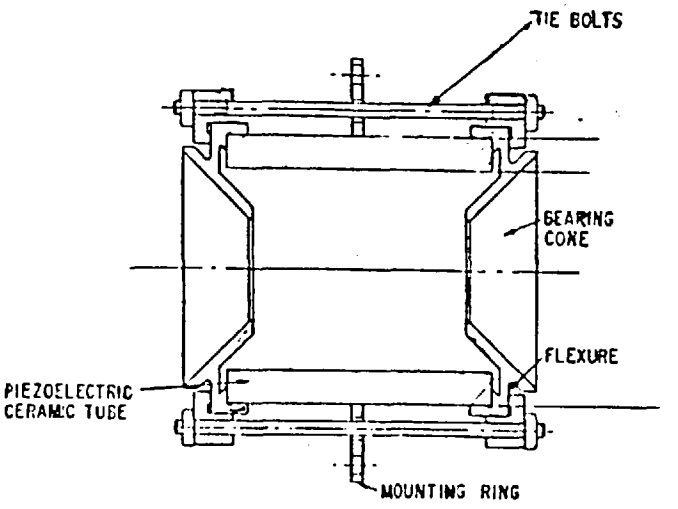

FIG. 5.4 Experimental conical bearing driven by ceramic tube (Ref. 9)

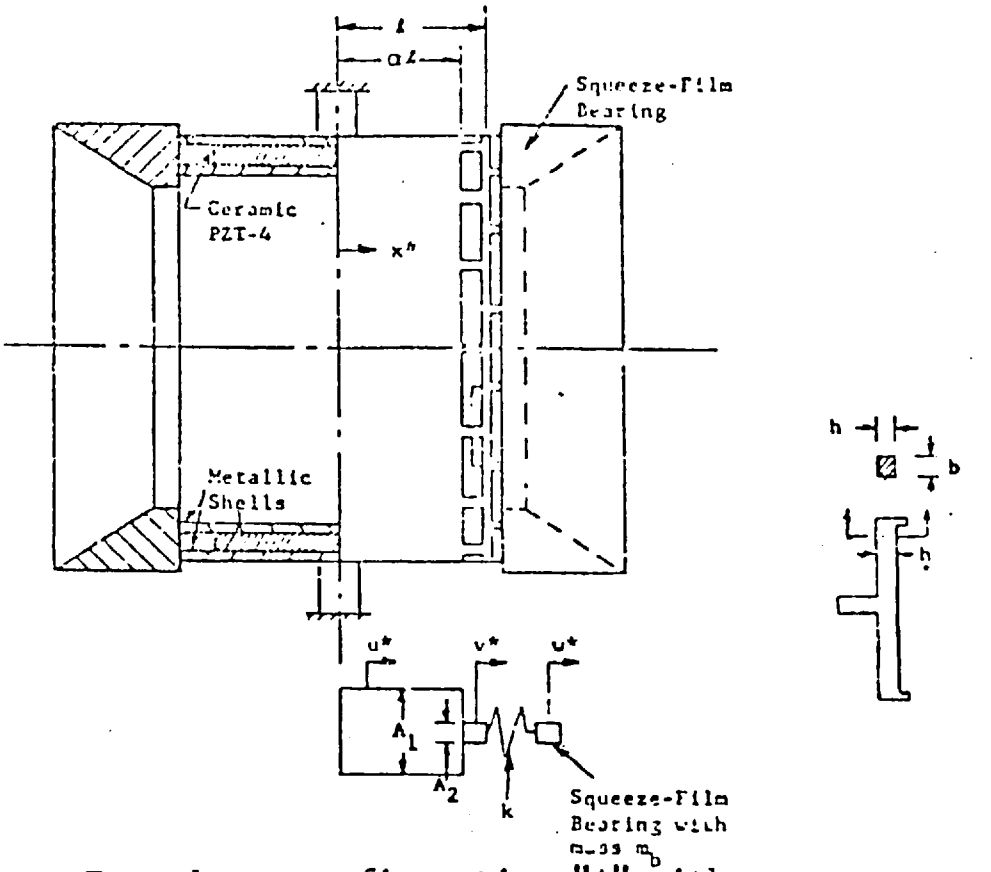

FIG. 5.5 Transducer configuration "A" with mechanical equivalent (Ref. 8).

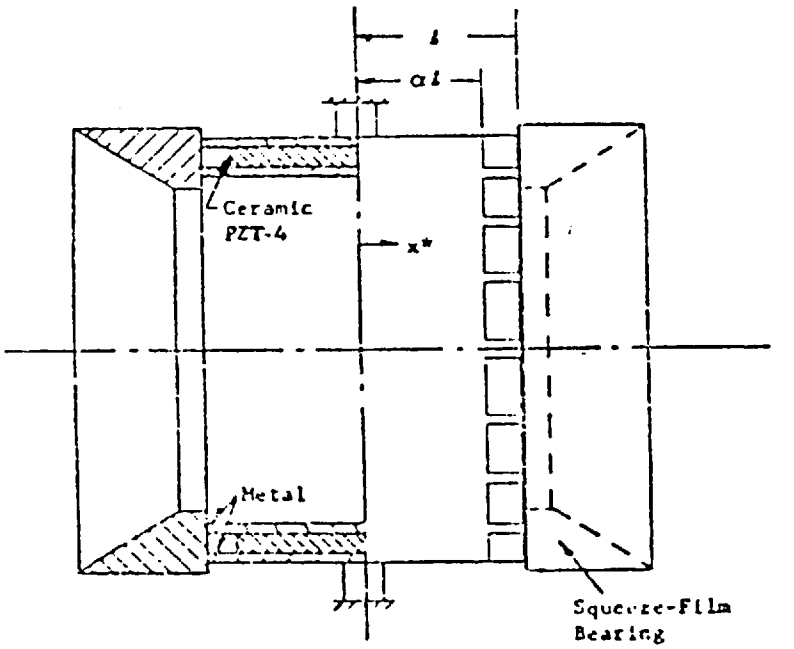

FIG. 5.6 Transducer configuration "B" (Ref. 8).

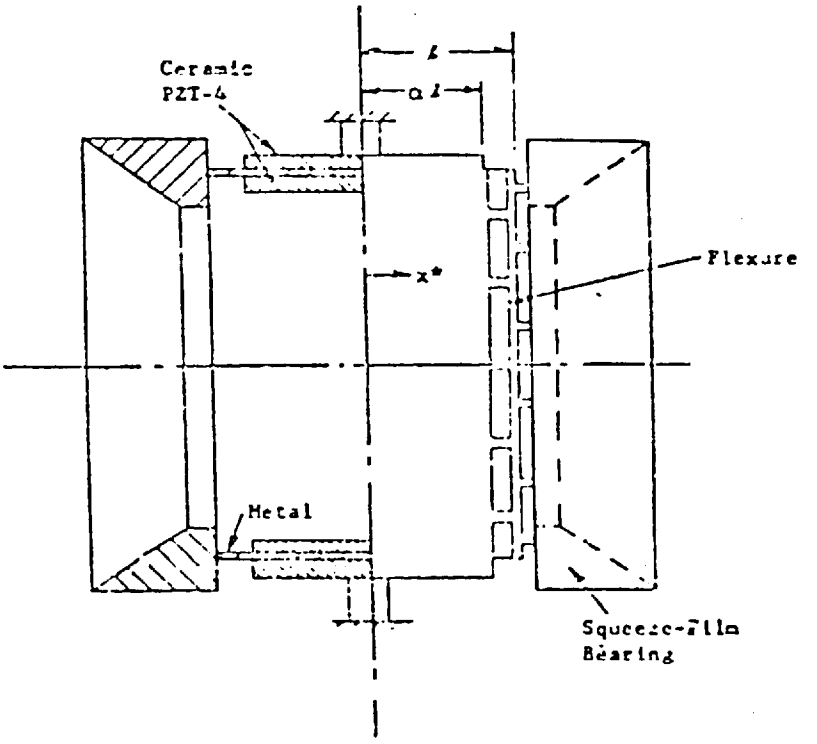

FIG. 5.7 Transducer configuration "C" (Ref. 8).

(configuration "C"). Molybdenum and Invar were used to provide a good matching for the thermal coefficient of expansion of the ceramic. Configurations "A" and "B" differ in the design of the flexible part of the driver and configuration "C", similar to "A", has a different metal-ceramic arrangement, with a double wall around the ceramic.

The aim of Chiang's work was to compare theoretically the performance of the configurations quoted. For this purpose he considered the end flexure region as a simple spring with its mass lumped into two points. Half the mass is attached to the bearing and the other half to the flexure location at $x = \ell$. The dynamic model is also represented in Fig. 5.5. The ceramic-metal assembly is

considered as a composite cylinder with the ceramic treated as a simple elastic material. The equations of motion are established for the assembly for the displacements u* and v*, as indicated in Fig. 5.5. These equations are:

for $0 < x^* < \alpha\ell$

$$\frac{E_1}{\rho_1}\frac{\partial^2 u}{\partial x^{*2}} = \frac{\partial^2 u^*}{\partial t^2} \tag{5.4}$$

and for $\alpha\ell < x^* < \ell$

$$\frac{E_2}{\rho_2}\frac{\partial^2 v^*}{\partial x^{*2}} = \frac{\partial^2 v^*}{\partial t^{*2}} \tag{5.5}$$

where: u^*, v^* - local displacements,

A_c - cross sectional area of ceramic cylinder,

A_m - cross sectional area of metallic cylinder,

E_m - metal Young modulus,

E_c - ceramic Young modulus,

ρ_c - metallic cylinder density,

$A_2 = A_m A_c + {}_m A_m / A_1$,

$\rho_2 = \rho_m$ - density of metallic cylinder,

$E_1 = E_c A_c + E_m A_m / A_1$,

$\rho_1 = \rho_c A_c + \rho_m A_m / A_1$,

$\rho_2 = \rho_m$.

To these equations the following boundary conditions are applied:

i) - the central plane is fixed in space

$$(u^*)_{x^* = \ell} = 0 \tag{5.6}$$

ii) - compatability of motion

$$(u^*)_{x^*=\alpha\ell} = (v^*)_{x^*=\alpha\ell} \tag{5.7}$$

iii) - force balance

$$(A_1E_1 \frac{\partial u^*}{\partial x^*})_{x^*=\alpha\ell} = (A_2E_2 \frac{\partial v^*}{\partial x^*})_{x^*=\alpha\ell} \tag{5.8}$$

For the bearing surface the equation of motion is:

$$-K\left[(w^*-v^*)_{x^*=\ell}\right] = (m_b + \frac{m_s}{2})\frac{\partial^2 w^*}{\partial t^{*2}} \tag{5.9}$$

with an additional boundary condition:

iv) - force balance

$$-A_2E_2(\frac{\partial v^*}{\partial x^*})_{x=\ell} - K\left[(v^*)_{x^*=\ell} - w^*\right] = \frac{m_s}{2}\frac{\partial^2 r^*}{\partial t^{*2}}\ _{x^*=} \tag{5.10}$$

The solution of equations (5.4) and (5.5) gives the following expressions:

$$u(x) = G \sin (\omega\ell \sqrt{\frac{\rho_1}{E_1}}\ X) \tag{5.11}$$

$$v(x) = C_2 \sin\omega\ell\sqrt{\frac{\rho_2}{E_2}}\ (X-X_o) \tag{5.12}$$

where: $\omega_1 = \frac{\pi}{2\ell}\sqrt{\frac{E_1}{\rho_1}}$

and $\omega_2 = \frac{\pi}{2\ell}\sqrt{\frac{E_2}{\rho_2}}$ (5.13)

C_1 and C_2 are the amplitudes of excursion and ω_1

and ω_2 are characteristic frequencies of the respective sections; X_o is a phase angle.

The conclusions of Chiang's analysis can be summarised as follows:

i) For the same size of driver and the same displacement at $x = \alpha$, the configuration "A" provides larger excursion amplitude for the squeeze film bearing than configuration "B".

ii) The configurations "A" and "C" with a properly designed end flexure do provide larger amplitude amplification than configuration "C". Also, for each corresponding design configuration larger amplitude amplification can be achieved increasing the size of the driving section. Thus, increased excursion amplitude can be obtained at expense of configuration complexity.

iii) The referred configurations can be placed in ascending order of achievable amplitude as:

1. Configuration "B" without extended section ($\alpha = \ell$).

2. Configuration "B" with an extended section ($\alpha < \ell$).

3. Configuration "A".

4. Configuration "B".

The major criticism of this work is the lack of experimental verification of these conclusions. The chosen configurations were also restricted to Chiang's particular application (gyroscopes).

It should also be pointed out that the high electromechanical coupling requires the solution of the full piezoelectric equations, instead of the simplified elastic equations which are only applicable to materials with low coupling[46]. However, this is the only previous known work on the flexible bearing arrangement. It shows that great differences in amplitudes can be expected due to the ceramic-bearing arrangement alone, though it seems doubtful that the expressions obtained can stand for other than qualitative values.

5.3 THEORETICAL AND EXPERIMENTAL ANALYSIS OF BEARING ARRANGEMENT UNDER INVESTIGATION

In this section the arrangement used for the present investigation is analysed. Data from (42) shows the mechanical compliance (open circuit electrodes) for PZT-4 to be:

$$S_{33}^{D} = 7.9 \times 10^{-2} \text{ metre}^2/\text{Newton}.$$

Therefore, the calculated equivalent stiffness is:*

$$K_c = 2.28 \times 10^{11} \text{ Newton/metre}.$$

For confirmation of this theoretical value, two experiments were carried out:

i) Measuring the output ceramic signal when a sinusoidal force is applied to the base. As the ceramic is stressed there is a mechanical to electrical energy transformation within the ceramic. It is the inverse phenomenon that is used for driving the squeeze-film bearing.

ii) Measuring in a mobility test, the response of the unit for the frequency range of interest.

In both cases the external force was applied along the axis of symmetry of the unit.

The two procedures will now be detailed.

---

* $E = \frac{1}{S_{33}} = .1265 \times 10^{12}$ Newton/metre^2

and $E = \frac{\sigma}{\varepsilon} = \frac{\frac{F}{\pi d_c^2}}{\frac{4}{t}}$,

$K_c = \frac{F}{\Delta} = \frac{E\pi d_c^2}{4th_c} = 2.28 \times 10^{11}$ Newton/metre.

5.3.1 Output voltage measurement

The diagram for the experiment is represented in Fig. 5.8. A shaker (Derriton VPZ vibrator), A, used in a horizontal position, was linked to the bearing unit by a rod, B. An adaptor was used, as the vibrator and the bearing unit had different threads. The output signal was collected by two wires, one connected to the electrode plate, G, and the other to one of the tightening bolts. The signal was measured with a sound and vibration analyser with filtering capability. The unit under test consisted of two bases E, two piezoelectric ceramics D, (only one is visible in Fig. 5.8), a thin contact plate, G, and an insulating ring, F. The unit was suspended by a string passing through the holes in the ring-electrode plate. In the experiments an amplifier was connected to the shaker. The usable frequency range was extended to 25 KHz by means of the amplifier external drive. The output readings (r.m.s. values), Figs. 5.10 and 5.11, show a very clear peak between 2.0 and 2.5 KHz, with other minor peaks at 11 KHz. The exact frequency where the voltage peak occurs varied slightly with the bolt torque. The peak value decreased as the torque was increased. However, a good contact between ceramics was achieved with a low torque value. Further increase in torque only prevented the ceramic expansion, and

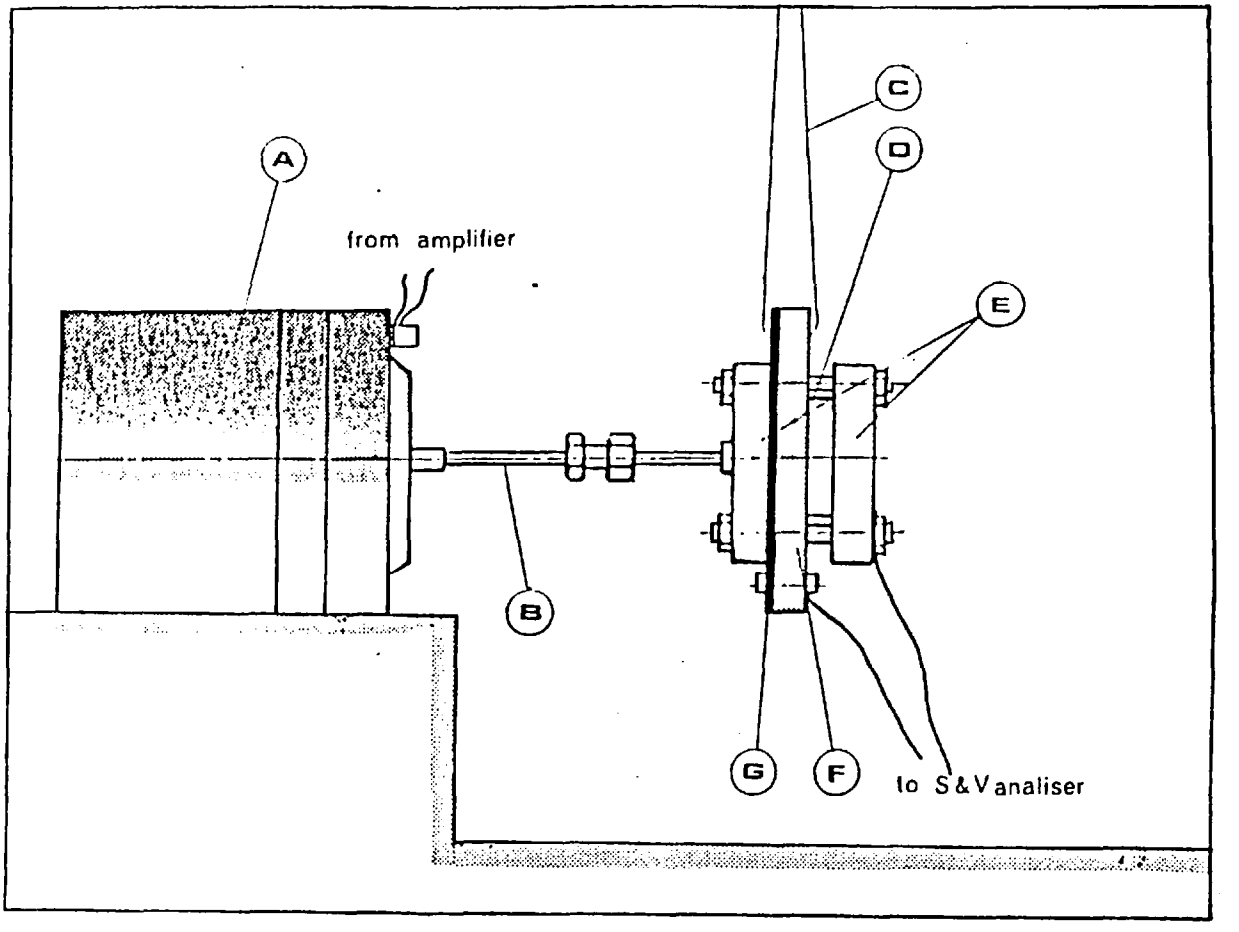

FIG. 5.8 Ceramic output measurement test.

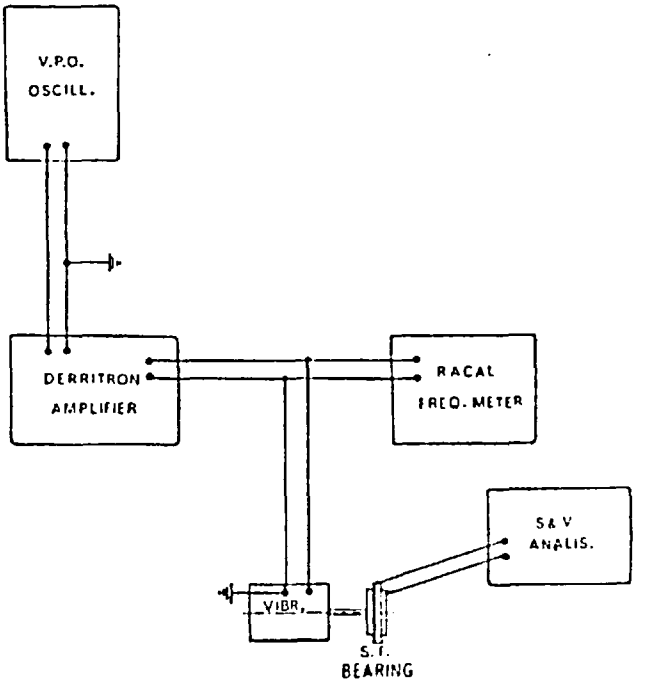

FIG. 5.9 Diagram of electrical arrangement for above test.

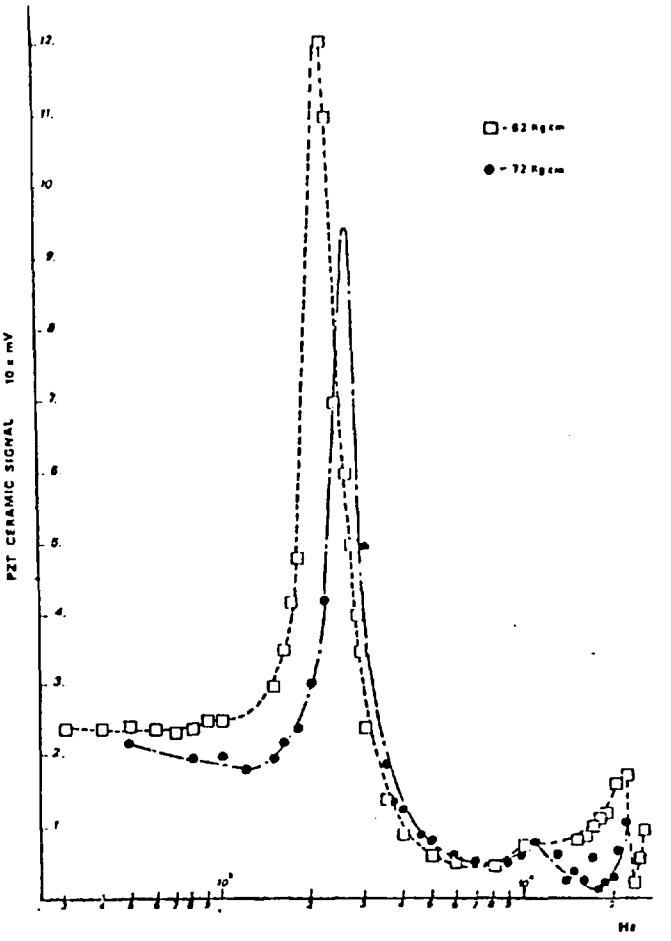

FIG. 5.10 and 5.11
Voltage signal produced by ceramic PZT-4.

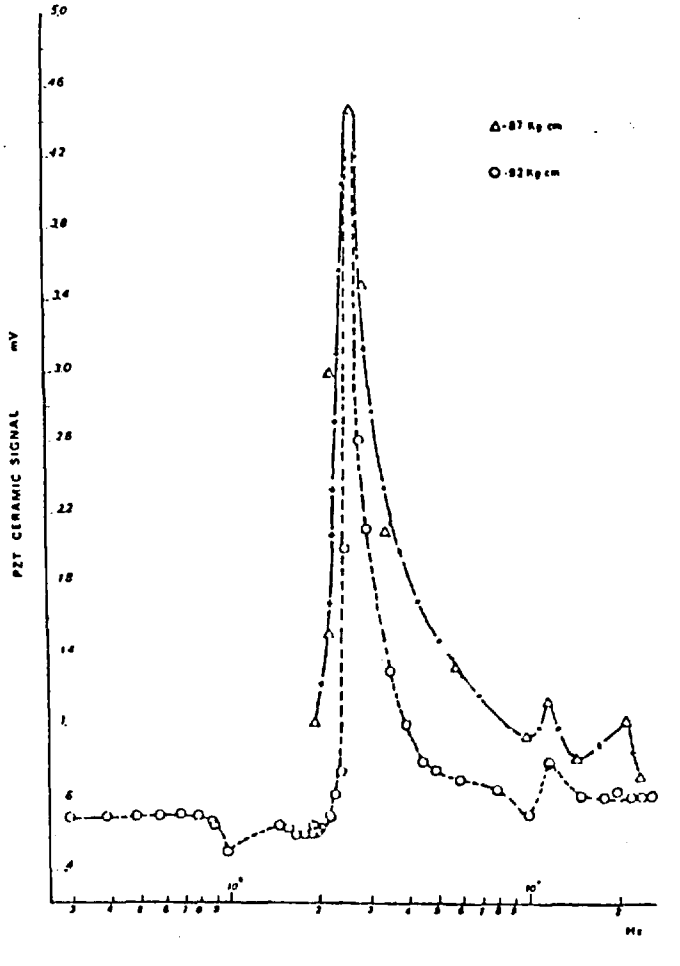

thus the associated developed charge. For this reason it seems advisable not to use torques higher than 60 Kg.cm in these arrangements.

5.3.2 Mobility response for base-ceramic

The mobility or admittance is defined as the ratio of velocity to applied force. If we consider the velocity measured at a point different from the point where the force is applied we have a transfer measurement. The point chosen for the velocity evaluation was the centre of one of the base plates, as in Fig. 5.12, by means of an accelerometer I. A force gauge F, was interposed between the vibrator table, A, and the excitation point. The whole assembly was suspended as in Section 5.3.1 with the aim of creating, as far as possible, free-free conditions.

The experiment was carried out using the mechanical impedance of the Vib. Lab. of Imperial College, which includes a PDP 8/E Mini Digital Computer coupled to impedance measuring equipment. Using the existing plotting facilities the mobility curve of Fig. 5.13 was obtained. Similarly, the phase angle curve (force leading velocity) was drawn, Fig. 5.14.

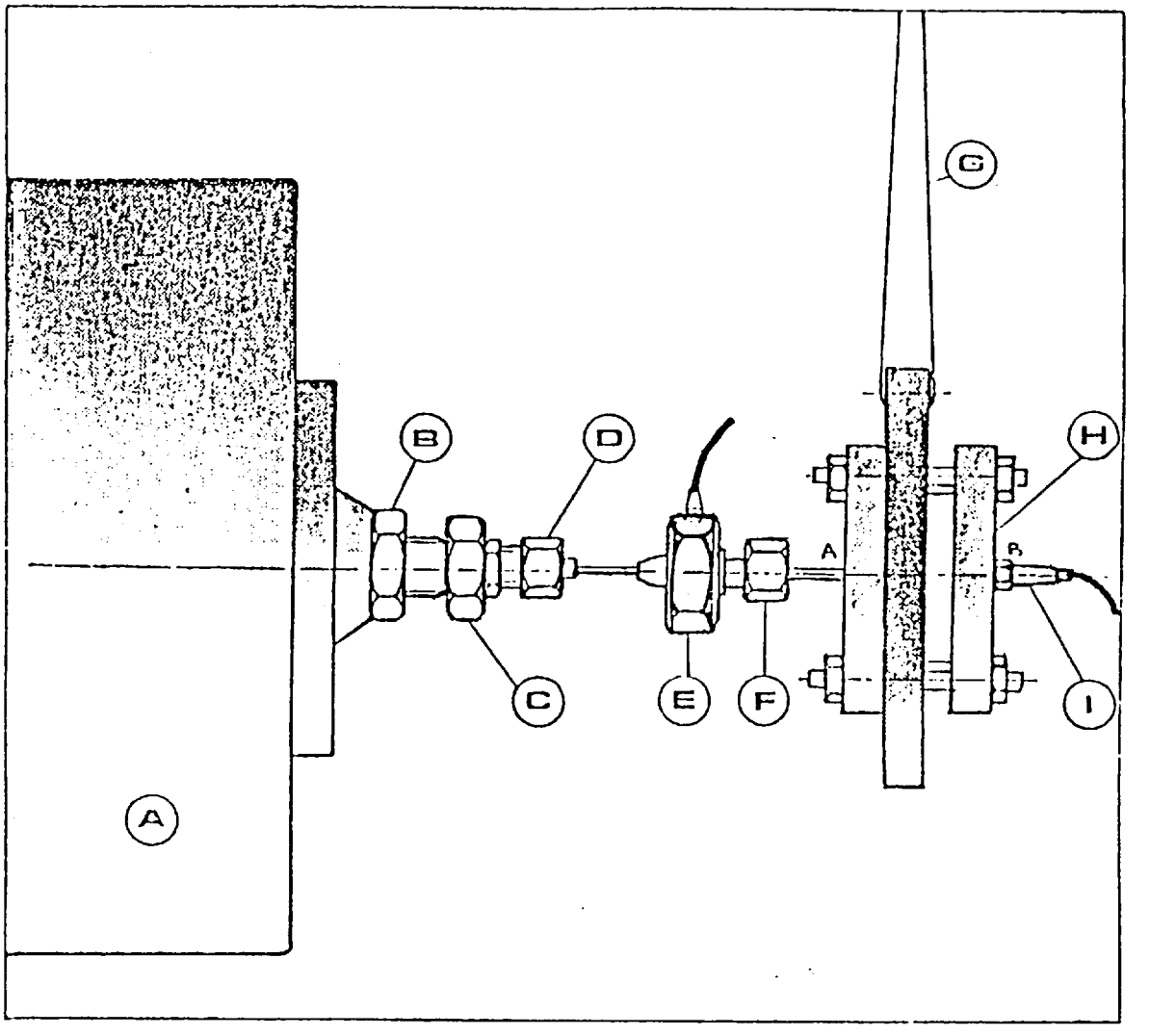

FIG. 5.12 Experimental set-up for mobility measurement.

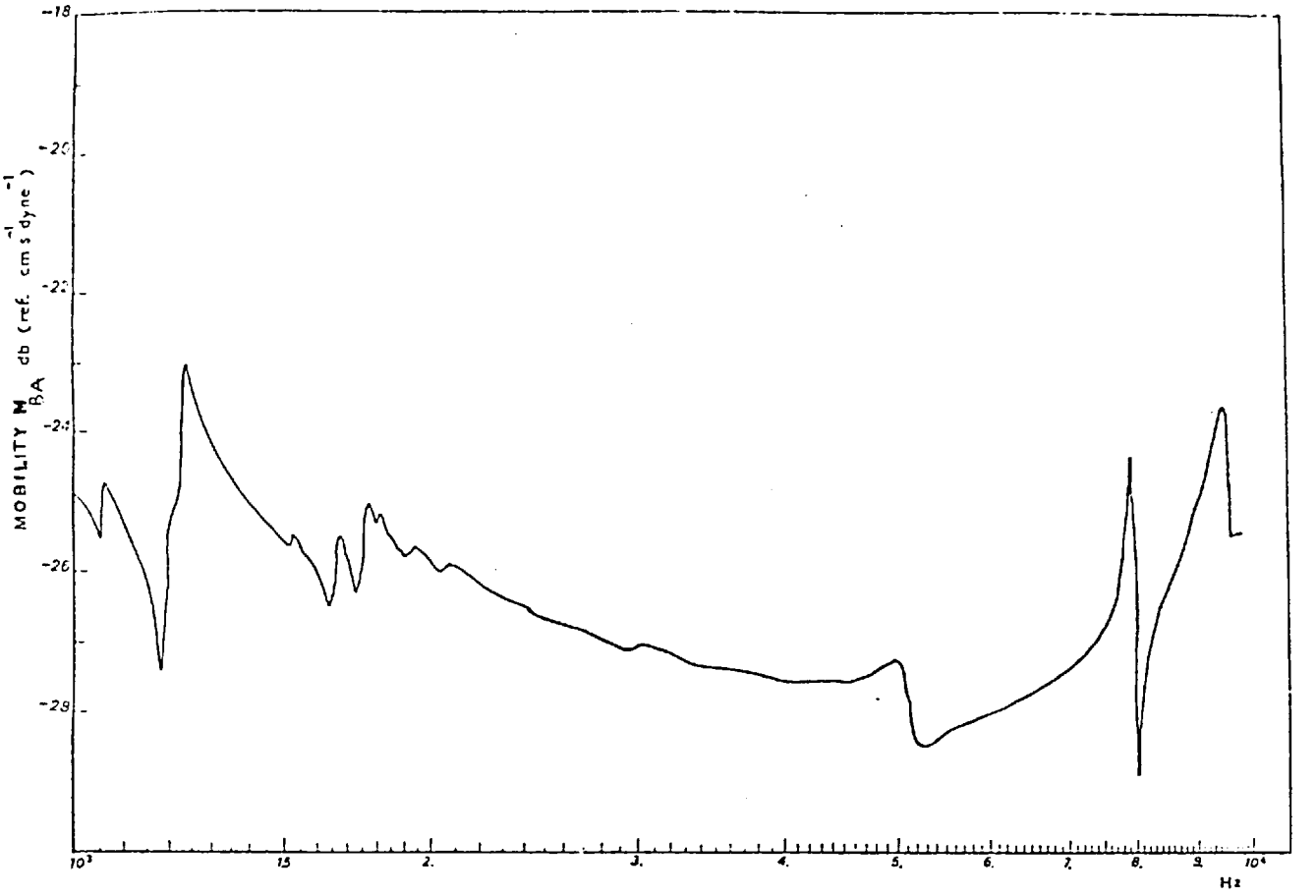

FIG. 5.13 Mobility curve for base-ceramic unit.

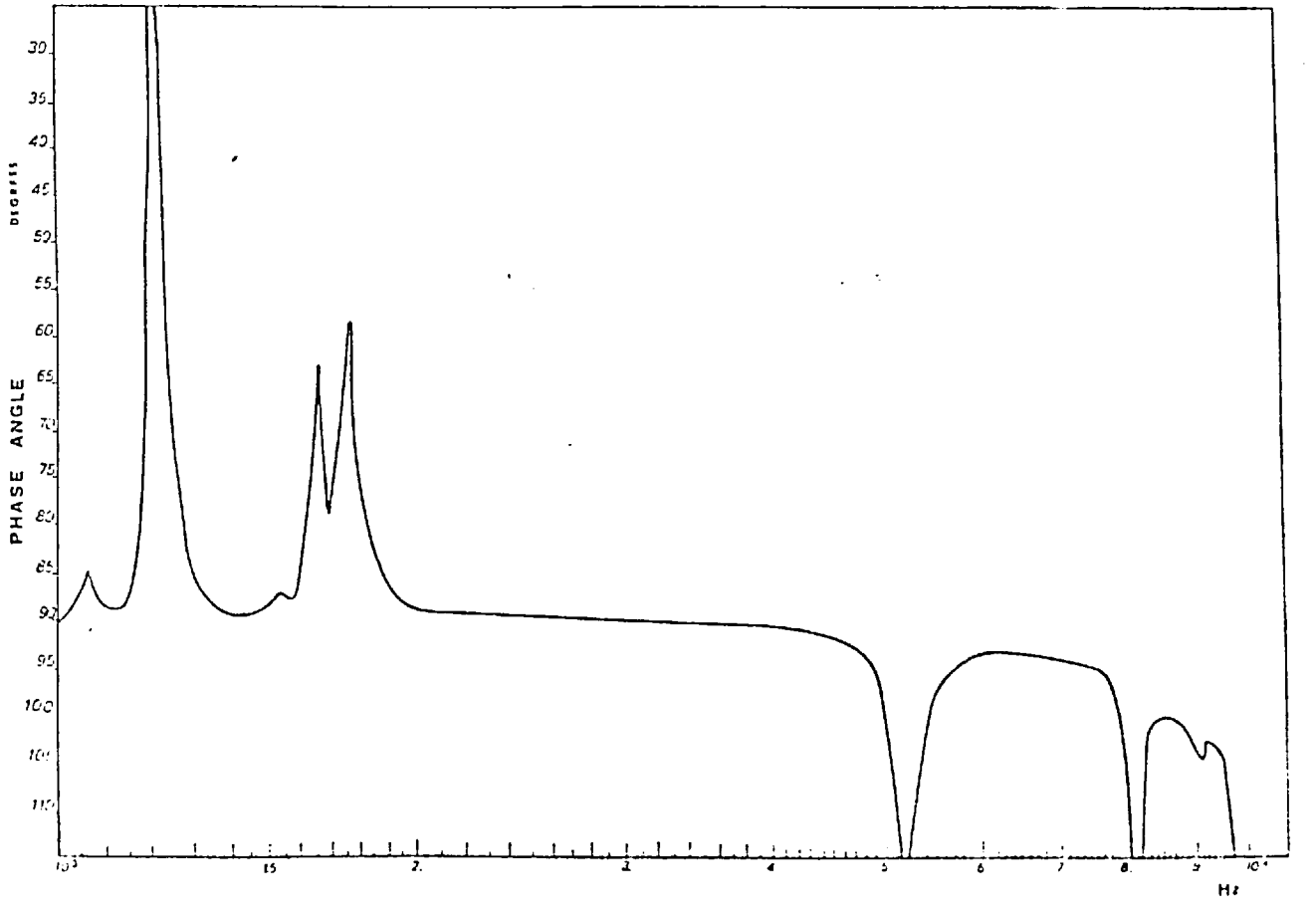

FIG. 5.14 Phase angle (force leading vel.) for the same unit .

5.3.3 Discussion of Results

The comparison of the results obtained with the experimental procedure of the previous sections requires the following comment:

The arrangement of Fig. 5.8 can be considered as that of two masses coupled by means of a spring. The first resonance occurs when the two masses are in a symmetric position but with maximum displacement from the rest position. The centre point in the electrode plate G, is stationary, it is an "apparent fixed point". This mode corresponds to maximum compression and expansion of the ceramics acting as a spring. The frequency where the peak occurs and that of the resonant frequency of the system do not exactly match. The maximum voltage signal is at 2.5 KHz and that from the mobility response is lower, at 1.25 KHz. A possible reason for this difference is the influence of the push-rod arrangement, C, D, F in Fig. 5.12. This influence is probably also the cause of other small peaks in the mobility curve.

Considering the higher frequency value from the two experiments to be the resonant frequency ω, from the expression

$$\omega = \sqrt{\frac{K_c}{m}} \qquad (5.15)$$

one obtains the value of the crystal stiffness in this arrangement. This expression applies to each of the crystal-base units in the symmetric arrangement of Fig. 5.12. K_c is the ceramic stiffness and m is the mass of each base plus the equivalent* mass of the ceramic.

Considering the less favourable condition where $f \simeq 3$ KHz, the value obtained for K_c is 7.73×10^{10} dynes/cm (7.73×10^{7} N/m). The theoretical value, from the compliance constant, was, in c.g.s. units, 2.28×10^{14} dynes/cm (2.28×10^{11} N/m). Using the same expression, (5.15), but now determining the resonant frequency of the assembly with the theoretical value of K_c, f_c = 53.5 KHz, much higher than the experimental values (1.3 and 2.5 KHz).

The main conclusions from these results are:

i) There is a minimum torque value that assures good contact between ceramic and base.

ii) Use of torque higher than this value affects the amplitude of vibration of the crystal, but only very slightly the frequency of resonance of the assembly.

---

* The equivalent mass is one-third of the actual mass of the ceramic.

iii) The actual stiffness of the ceramic when assembled with the other bearing elements is considerably smaller than the value predicted from the ceramic data. This fact has also been reported by Chiang[8] and is caused by the increased compliance in the base-ceramic and ceramic-central plate contact areas.

CHAPTER SIX

CONICAL SQUEEZE FILM BEARINGS

6.1 THE ADMIRALTY COMPASS OBSERVATORY MODEL

The Admiralty Compass Observatory main interest in squeeze film bearings has been in their use as gyro gimbal bearings. These should replace the angular contact ball bearings, normally used. The possible geometries of these bearings are conical and spherical. It is the first shape that is considered here.

The operational arrangement of a conical squeeze film bearing is shown in Fig. 6.1. The key to this figure is as follows:

1. Lower (supporting) member.
2. Upper (supported) member.
3. Supporting member base.
4. Element symmetric to (1).
5. Element symmetric to (3).
6. Piezoelectric ceramic crystal.
7. Fixing bolts.
8. Standing base (cylinder).
9. Connecting leads.
10. Bearing fixing bolts.

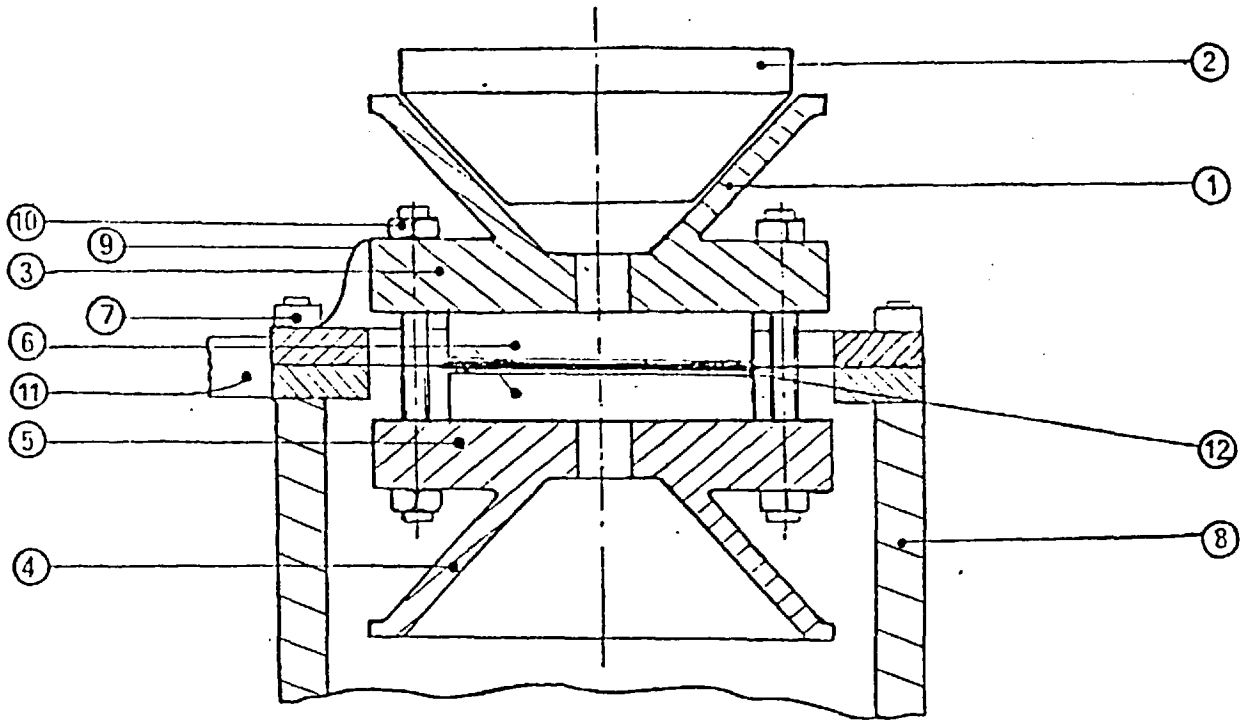

FIG. 6.1 Admiralty (A.C.O.) conical S.F. bearing model as used in test.

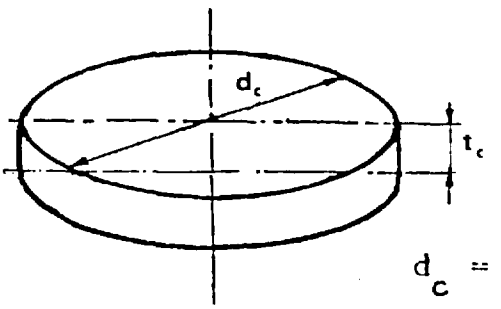

$d_c = .038$ m

$t_c = .006$ m

FIG. 6.2 Piezoelectric ceramic disc dimensions.

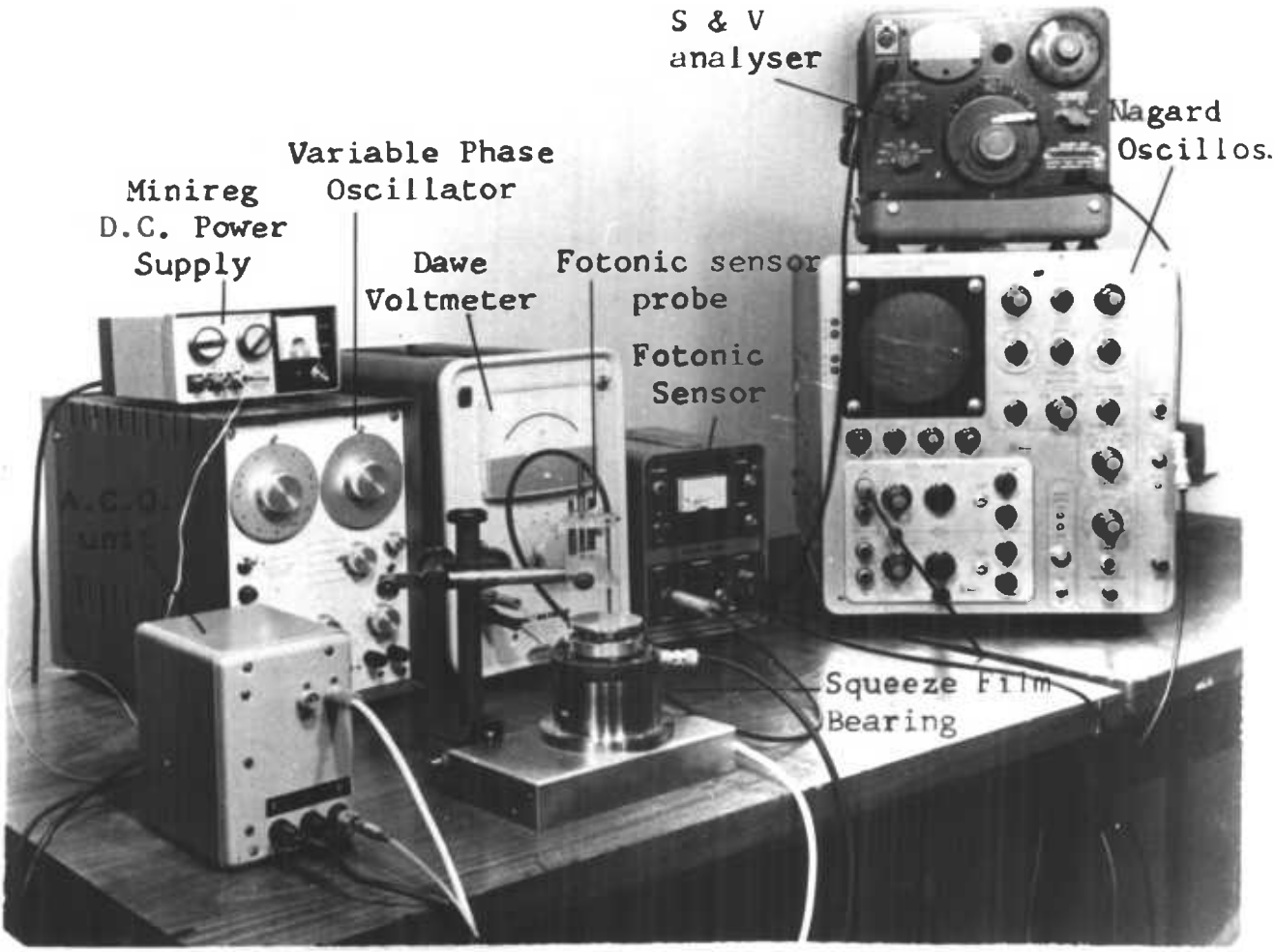

FIG.6.3 General view of the testing equipment.

11. Electrical input.

12. Central electrode.

13. Insulating rings.

This is a double arrangement with just one of the bearing surfaces actually being used. The reason for this is to guarantee, as far as possible, that the central electrode plate remains stationary. In a gyroscope application this arrangement would not be the most practical. However, for investigation purposes this arrangement is adequate. Parts (2) and (3) are of one piece in Dural (aluminium alloy). The standing base (8) is of steel. Part (2) is the "floating", supported bearing surface and in a gyroscope application should be part of the gyro gimbal. The cone and bearing axes are coincident, taking both thrust and radial loads. The ceramics (6) are of PZT-4 material, whose characteristics are described in Table 5.1. They are the same as used in experiments of Chapter Five, with the shape and dimensions shown in Fig. 6.2. The electric signal is applied to the ceramics through a socket (11), with one contact for the electrode plate (12), and the other for the base (8). A further connection from the bolts (7) is used to make contact with parts (1) and (9) that act as electrodes for the piezoelectric ceramics.

When an electric signal is applied to the ceramic it undergoes successive expansions and compressions with the same frequency as the input signal. This causes the supporting bearing surface to vibrate. The air between the two surfaces is subjected to a change of volume. For reasons already explained, this is the cause of the bearing load carrying capacity. The vibration of the bearing surface, conical in this case, is not only a rigid body motion but a more complicated modal shape.

In order to establish a possible relationship between this vibrational behaviour and the performance of the bearing, experiments using the set up of Fig. 6.3 were carried out. However, the theoretical analysis of the vibration of conical shells will be considered first.

6.2 VIBRATION OF CONICAL SHELLS

The vibration of plates, discs, cylinders and spheres has been extensively studied. Conical shells have not attracted as much attention. Only recently they have been analysed. The reason for this recent interest is mainly related to the study of loudspeakers and rocket "noses".

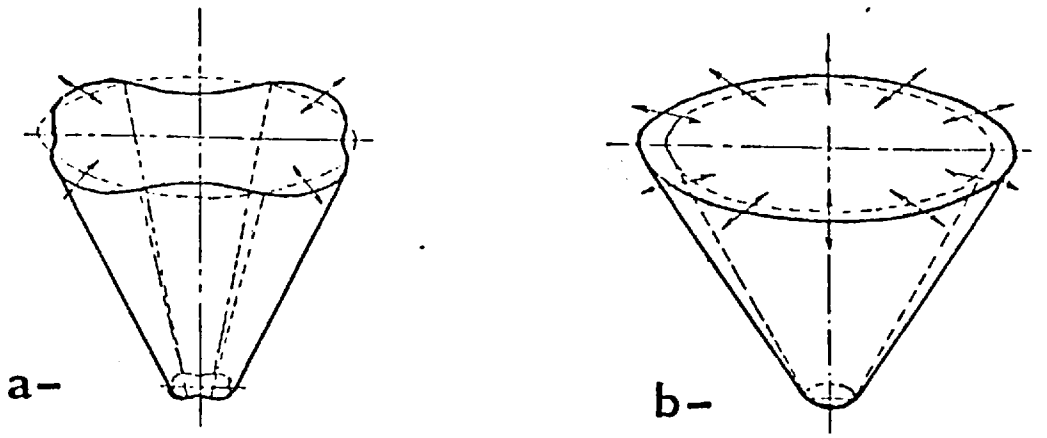

FIG. 6.4 Inextensional vibrations (a), and extensional vibrations (b) of conical shells.

6.2.1 Extensional and Inextensional Vibrations

Strutt (51) was one of the first to study conical shells. He considered only the case of inextensional vibrations. These are also called flexural vibrations and occur when the shell flexes. In this case the modal shapes have nodal lines coincident with the generators, Fig. 6.4(a). If the middle surface of the shell undergoes extension the vibrations are called extensional, Fig. 6.4(b). In general both classes of vibration will occur. The inadequacy of the inextensional theory to satisfy the boundary conditions of a completely restrained cone edge was demonstrated by Van Urk (52), in his experiments to verify the accuracy of the Strutt's formula (51). This problem was later investigated

by Federhofer (53) who derived a frequency expression for a truncated cone with one edge rigidly restrained and the other partially restrained. The calculation was based on an energy method of Rayleigh, with assumed mode shapes in the form of power series.

Conical, or cylindrical shells can only deform inextensionally if the generators remain straight. For very thin shells vibration will be predominantly inextensional if the associated deformations are compatible with the edge conditions. These conditions require that the edges are completely unrestrained, or restrained in a manner similar to that of a hinged joint. All the other edge conditions cause bending of the axial generators which then require some stretching of the shell middle plane.

As an illustration of what has been said we will refer the case of a spherical shell as discussed by Love (54). For a complete shell, all the modes of vibration are extensional. For an open spherical shell or bowl, there are two cases to consider. If the aperture is small, or the spherical surface is nearly complete, the vibrations approximate to those of a complete spherical shell. When the opening in the spherical shell is large, the vibrations approximate to those of a plate with displacements normal

to the plane of the plate (inextensional), together with displacements parallel to the plane of the plate (extensional).

For our purpose, the inextensional vibrations are undesirable, as the amplitude of vibration would also be a function of the angular coordinate. They would produce tangential gas flow due to pressure gradients in that direction. These vibrations are also considered a bad effect in loudspeaker cones, when a flange is often used to stiffen the large edge.

6.2.2 Solution of the Motion Equations by the Marcus-Goldberg Method

The solution of the equations of motion for the combined extensional and inextensional vibrations have been first studied by Sanders et al (55)(56). This method was also used by Platus (57). The latter has also compared the results with experiments. Both assumed polynomial mode shapes. In his work Platus also postulated that the kinetic energy was the same for the extensional and inextensional cases. Even so, and for the single case of a fixed-free cone, the analysis is complex.

As this study is only concerned with axisymmetric modes it benefits from simplifications. In the following analysis we start considering the forces and moments applied to the element. The forces and moments are herewith referred to as per unit length. Because of symmetry, there are no shearing forces at the lateral boundaries of the element of the shell (Fig. 6.5). At the upper and lower edges there are no circumferential shear forces either. These edges are only subjected to the normal forces N_z and the shear forces Q per unit length normal to the generators. The normal forces N_θ and the moments M_θ act at these lateral boundaries, and the moments M_z are applied at the upper and lower edges (Fig. 5.6). In this figure the system of coordinates chosen is also shown with the z axis coinciding with the generators that define the element. The z axis is positive from the cone apex (Fig. 6.5).

A cone generator and a section of the respective element and the forces acting in the vertical plane of this generator are also shown in Fig. 6.7a. All these forces and moments are considered per unit of length of the area where they are applied. In the following expressions ρ_s is the density of the material of the shell and h_s the thickness. The coordinates z and θ are defined in Fig. 6.5,

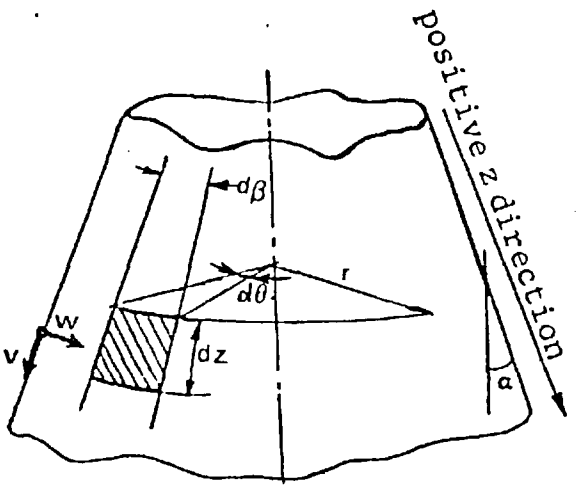

FIG. 6.5 Typical conical shell element.

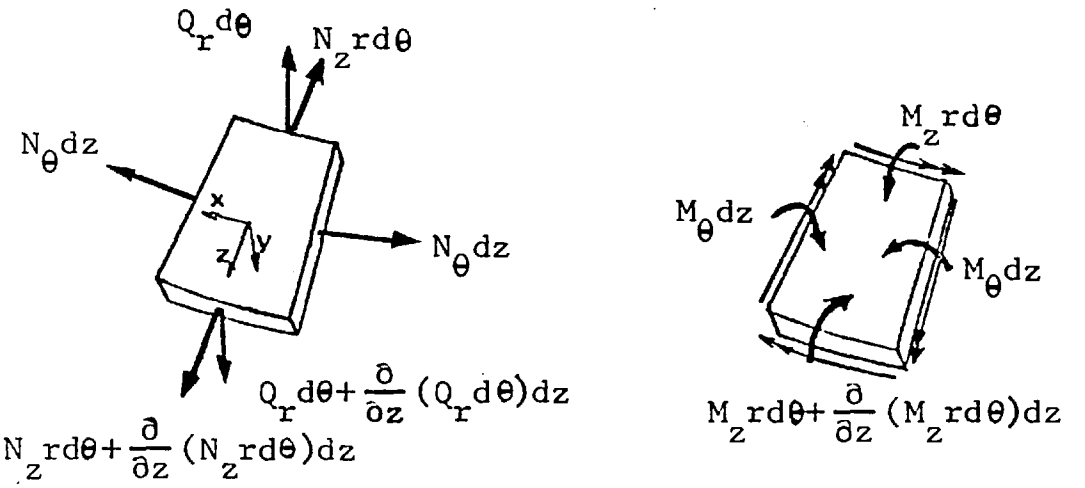

FIG. 6.6 Forces and moments acting on shell element.

and r is the distance from the element to the cone axis. The cone semi-vertical angle is α. The forces acting on the element must be in equilibrium. The components in the y-direction are:

(i) $Q\,r\,d\theta$ and $\left[Q\,r\,d\theta + \frac{\partial}{\partial z}(Q\,r\,d\theta)dz\right]$.

(ii) The components of the normal forces $N_\theta dz$. These two forces can be combined as in Fig. 6.7b. The resultant is $2\,N_\theta\,dz \sin\frac{d\theta}{2}$. For small $d\theta$, $\sin(\frac{d\theta}{2})$ can be replaced by $\frac{d\theta}{2}$, and it follows that the sum of these forces in the y-direction is:

$$2\,N_\theta\,dz\,\frac{d\theta}{2}$$

(iii) The inertia forces $\rho_s h_s \frac{\partial^2 w}{\partial t^2} r\,d\theta\,dz$.

For equilibrium:

$$\frac{\partial}{\partial z}(Qrd\theta)dz + N_\theta dzd\theta\cos\alpha = \rho_s h_s \frac{\partial^2 w}{\partial t^2} rd\theta dz \qquad (6.1)$$

As, $$r = z\sin \qquad (6.2)$$

$$\frac{\partial}{\partial z}(Qz)\sin\alpha + N_\theta\cos\alpha = \rho_s h_s \frac{\partial^2 w}{\partial t^2} z\sin\alpha \qquad (6.3)$$

or, $$\frac{\partial}{\partial z}(Qz) + N_\theta\,\mathrm{cotg}\,\alpha = z\,\rho_s h_s \frac{\partial^2 w}{\partial t^2} \qquad (6.4)$$

For the components acting in the z-direction we have:

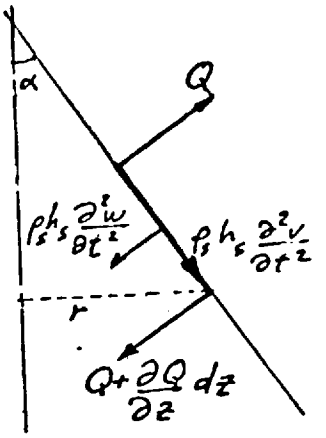

FIG. 6.7a Shell element cross-section and inertia and shear forces acting on this element.

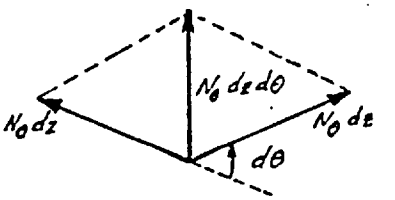

FIG. 6.7b Vectorial sum of normal forces N_θ.

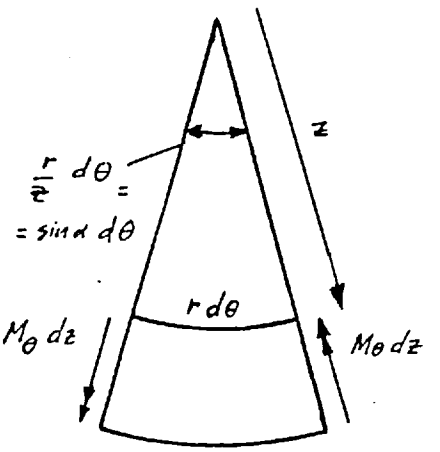

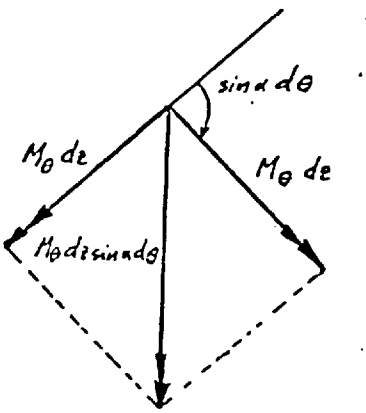

FIG. 6.7c Resultant of moments N_θ.

FIG. 6.7

(i) The normal forces $N_z\, r\, d\theta$ and $\left[N_z\, r\, d\theta + \frac{\partial}{\partial z}(N_z + d\theta)\right]$.

(ii) The components in the z-axis of the normal forces $N_\varphi dz$.

(iii) The inertia forces $\rho_s h_s \frac{\partial^2 V}{\partial t^2} r\, d\theta\, dz$. The equilibrium in this case requires:

$$-\frac{\partial}{\partial z}(N_z\, r\, d\theta)dz + N_\theta\, dz\, d\theta \sin\alpha = \rho_s h_s \frac{\partial^2 V}{\partial t^2} r\, d\theta\, dz \quad (6.5)$$

Using expression (6.2) and simplifying:

$$\frac{\partial}{\partial z}(z\, N_z) - N_\theta = z\, \rho_s h_s \frac{\partial^2 V}{\partial t^2} \quad (6.6)$$

Considering now the moments with respect to the x-axis, we have:

(i) The moments $M_z\, r\, d\theta$ and $\left[M_z r d\theta + \frac{\partial}{\partial z}(M_z r d\theta)dz\right]$.

(ii) The moment due to the forces Q. Neglecting terms of second order, this is equal to $Qrd\theta dz$.

(iii) The resultant of the moments $M_\theta dz$. These vectors make an angle of $\pi - \sin\alpha d\theta$ (Fig. 6.7c). The total moment is $M_\theta dz \sin\alpha\, d\theta$.

The equilibrium of these moments yields the following equation:

$$Q\, r\, d\theta\, dz - \frac{\partial}{\partial z}(M_z\, r\, d\theta)dz - M_\theta dz \sin\alpha d\theta = 0 \quad (6.7)$$

or, simplifying:

$$Q_z = -\frac{\partial}{\partial z}(M_z z) - M_\theta = 0 \qquad (6.8)$$

These internal forces are also related to the displacements of the middle surface.

The stresses σ_z and σ_θ can be expressed in terms of the strain, ε_z, ε_θ, by:

$$\sigma_z = \frac{E}{1-\nu^2}(\varepsilon_z + \nu\varepsilon_\theta) \qquad (6.9)$$

$$\sigma_\theta = \frac{E}{1-\nu^2}(\varepsilon_\theta + \nu\varepsilon_z) \qquad (6.10)$$

where σ_z is the stress in the z-direction, σ_θ is in the θ direction and ε_z and ε_θ are the respective strains.

As N_z is the force due to the stresses σ_z:

$$N_z = \int_{-h/2}^{h/2} \sigma_z dz = \frac{Eh}{1-\mu^2}(\varepsilon_z + \nu\varepsilon_\theta) \qquad (6.11)$$

where ν is the Poisson coefficient.

Due to stresses σ_θ:

$$N_\theta = \int_{-h/2}^{h/2} \sigma_\theta dz = \frac{Eh_s}{1-\nu^2}(\varepsilon_\theta + \nu\varepsilon_z) \qquad (6.12)$$

because,

$$\varepsilon_\theta = \frac{V}{z} - \frac{w}{z}\cot\alpha \qquad (6.13a)$$

and, $$\varepsilon_z = \frac{\partial V}{\partial z} \qquad (6.13b)$$

Expressions (6.11) and (6.12) then become:

$$N_z = \frac{Eh_s}{(1-\nu^2)}\left[\frac{\partial V}{\partial z} + \nu\left(\frac{V}{z} - \frac{W}{z}\cot\alpha\right)\right] \qquad (6.14)$$

$$N_\theta = \frac{Eh_s}{(1-\nu^2)}\left[\frac{V}{z} - \frac{W}{z}\cot\alpha + \nu\frac{\partial V}{\partial z}\right] \qquad (6.15)$$

If $\bar{D}$ is the flexural rigidity:

$$\bar{D} = \frac{Eh_s^3}{12(1-\nu^2)} \qquad (6.16a)$$

Also let $$S = \frac{\partial w}{\partial z}. \qquad (6.16b)$$

It follows that the moment per unit length M_z caused by the stresses τ_z is:

$$M_z = -\bar{D}\left(\frac{\partial S}{\partial z} + \frac{S}{z}\right) \qquad (6.17)$$

Similarly,

$$M_\theta = -\bar{D}\left(\frac{S}{z} + \nu\frac{\partial S}{\partial z}\right) \qquad (6.18)$$

Q can be obtained from equations (6.7), (6.17) and (6.18), i.e.:

$$Q = -\bar{D}\left(\frac{\partial S^2}{\partial z^2} + \frac{1}{z}\frac{\partial S}{\partial z} - \nu\frac{1}{z^2}S\right) \qquad (6.19)$$

If the applied force varies harmonically with frequency ω, as in the case of squeeze film bearings driven

by piezoelectric ceramics, the solution of (6.3), (6.6) and (6.8) can be written in the form:

$$V(z,t) = V^{*}(z)\cos\omega t$$

$$W(z,t) = W^{*}(z)\cos\omega t$$

$$M_z(z,t) = M_z^{*}(z)\cos\omega t$$

$$M_\theta(z,t) = M_\theta^{*}(z)\cos\omega t$$

$$N_\theta(z,t) = N_\theta^{*}(z)\cos\omega t$$

and $$Q(z,t) = Q^{*}(z)\cos\omega t \qquad (6.20$$

where V^{*}, W^{*}, M_z^{*}, M_θ^{*}, N_θ^{*} and Q^{*} are the amplitudes of the variables, only dependent on the coordinate z.

By substituting equation (6.20) into equations (6.14) through (6.19), and using equation (6.16 b), it is possible to write the six equations below governing the displacement of a point on the cone middle plane.

$$S^{*} = \frac{\partial W^{*}}{dz} \qquad (6.$$

From equation (6.17):

$$\frac{dS^{*}}{dz} = \frac{M_z^{*}}{D} - \frac{\nu}{z}S^{*} \qquad (6.21)$$

From equations (6.4) and (6.15):

$$\frac{dQ^{*}}{dz} = -\frac{Q^{*}}{z} - \frac{Eh}{z}\cot\alpha(V^{*}-W^{*}\cot\alpha) - \nu\frac{\cot\alpha}{z}N_z^{*}$$

$$- \rho_s h_s \omega^2 W^{*} \qquad (6.22)$$

From equations (6.8) and (6.17):

$$\frac{dM_z^*}{dz} = -\frac{(1-\nu)}{z} M_z^* - \frac{(1-\nu^2)}{z^2} \bar{D} \frac{dW^*}{dz} + Q^* \qquad (6.23)$$

From equations (6.6) and (6.15):

$$\frac{dN^*}{dz} = \frac{Eh_s}{z}(V^* - W^* \cot \alpha) - \frac{1-\nu}{z} N_z^* - \omega^2 \rho_s h_s V^* \qquad (6.24)$$

where α, as referred to above, is the cone semi-vertical angle.

From equation (6.11):

$$\frac{dV^*}{dz} = \frac{1-\nu^2}{Eh_s} N_z^* - \frac{\nu}{z}(V^* - W^* \cot \alpha) \qquad (6.25)$$

These equations may now be integrated with assumed boundary conditions. The expression $S = \frac{\partial W^*}{dz}$ was added to this set of five equations. A numerical procedure by Goldberg and others (58) was used for this integration. Basically this consisted of the transformation of a two point boundary value problem to an initial value problem. These equations, (6.21) to (6.25), must be simultaneously integrated, and Goldberg suggestions that one designates each variable, V^*, W^*, S^*, M_z^*, N_z^* and Q^* by generic functions $Y_i(z)$. In this case the referred equations (6.21) to (6.25) and (6.16) can be written as:

$$\frac{dY_i}{dz} = \sum_{j=1}^{6} a_{ij} Y_j \qquad (6.26)$$

with a_{ij} being the variable factors multiplying the variables $V^*, W^*, S, M_z^*, N_z^*$ and Q^* in eq.(6.21) to (6.25). The functions Y_j are defined as:

$$Y_i(z) = \alpha_i(z) N_{z,a}^* + \beta_i(z)\, M_{z,a}^* + \gamma_i(z)\, Q_a^* \qquad (6.27)$$

$N_{z,a}^*$, $M_{z,a}^*$ and Q_a^* represent the values assumed by N_z^*, M_z^* and Q^* at the cone inner edge, where z = a. The variable coefficients $\alpha_i(z)$, $\beta_i(z)$ and $\gamma_i(z)$, which are functions of the coordinate z, are now the unknowns.

Substituting (6.27) in (6.26):

$$\frac{dY_i}{dz} = \frac{d\alpha_i(z)}{dz} N_{z,a}^* + \frac{d\beta_i(z)}{dz} M_{z,a}^* + \frac{d\gamma_i(z)}{dz} Q_a^* \qquad (6.28)$$

and noting that:

$$Y_j(z) = \alpha_j(z) N_{z,a}^* + \beta_j(z) M_{z,a}^* + \gamma_i(z) Q_a^* \qquad (6.29)$$

it is possible to write:

$$\frac{d\alpha_i(z)}{dz} N_{z,a}^* + \frac{d\beta_i(z)}{dz} M_{z,a}^* + \frac{d\gamma_i(z)}{dz} Q_a^* = \sum_{j=1}^{6} a_{ij} \left[\alpha_j(z) N_{z,a}^* + \beta_j(z)\, M_{z,a}^* + \gamma_j(z)\, Q_a^* \right] \qquad (6.30)$$

Now, equating coefficients of, respectively $N_{z,a}^*$, $M_{z,a}^*$ and Q_a^* in (6.30) we get:

$$\left.\begin{aligned} \frac{d\alpha_i(z)}{dz} &= \sum_{j=1}^{6} a_{ij}\alpha_j(z), \text{for coefficients of } N_{z,a}^* \\ \frac{d\beta_i(z)}{dz} &= \sum_{j=1}^{6} a_{ij}\beta_j(z), \text{for coefficients of } M_{z,a}^* \\ \frac{d\gamma_i(z)}{dz} &= \sum_{j=1}^{6} a_{ij}\gamma_j(z), \text{for coefficients of } Q_a^* \end{aligned}\right\} \qquad (6.31)$$

So, instead of integrating the equations (6.16) to (6.24), we have to integrate the set of equations (6.31) subjected to certain boundary conditions. The interval of integration remains, as before, from z = a (the cone small edge coordinate) to z = b (cone outer edge coordinate). The integration can be performed, for instance, using the Runga-Kutta method.

6.2.2.1 Integration of Equations of Motion

The equations of motion have been transformed in section 6.2.2 into the set of equations (6.31). In these equations, the variables $Y_i(z)$ designate any of the variables $W^*(z), S^*(z), V^*(z), M_z^*(z), N_z^*(z)$ and $Q^*(z)$ defined in (6.20). To perform now the integration of (6.31) we have to establish a correspondence between $Y_i(z)$ and these other variables. The choice for the variables $Y_i(z)$, that we adopted, to perform the integration is:

$$\begin{aligned} Y_1(z) &= W^*(z) \\ Y_2(z) &= S^*(z) \\ Y_3(z) &= M_z^*(z) \\ Y_4(z) &= Q^*(z) \\ Y_5(z) &= N_z^*(z) \\ Y_6(z) &= V^*(z) \end{aligned} \qquad (6.32)$$

We will drop now the use of stars and use the notation W as $W^*(z)$, V as $V^*(z)$, S as $S^*(z)$, M_z as $M_z^*(z)$, N_z as $N_z^*(z)$ and Q as $Q^*(z)$.

6.2.2.2 Boundary Conditions

To integrate the set of equations (6.31) we have to define three boundary conditions according to the kind of restraints existent at the cone small edge. If we assume a clamped condition at this edge, where z = a, this results in:

$$\begin{aligned} (W)_{z=a} &= 0 \\ (V)_{z=a} &= 0 \\ (S)_{z=a} &= 0 \end{aligned} \qquad (6.33)$$

Because we set in (6.32) W = Y, S = Y_2 and V = Y_6, the equations (6.33) can also be written as

$$\begin{aligned} (Y_1)_{z=a} &= \alpha_1(a)N_{z,a} + \beta_1(a)M_{z,a} + \gamma_1(a)Qa = 0 \\ (Y_2)_{z=a} &= \alpha_2(a)N_{z,a} + \beta_2(a)M_{z,a} + \gamma_2(a)Qa = 0 \\ (Y_6)_{z=a} &= \alpha_6(a)N_{z,a} + \beta_2(a)M_{z,a} + \gamma_6(a)Qa = 0 \end{aligned} \qquad (6.34)$$

$N_{z,a}$, $M_{z,a}$ and Q_a being arbitrary constants, the conditions (6.34) are verified if, at z = a:

$$\begin{aligned} &\alpha_1 = 0, \quad \beta_1 = 0 \text{ and } \gamma_1 = 0 \\ &\alpha_2 = 0, \quad \beta_2 = 0 \text{ and } \gamma_2 = 0 \\ &\alpha_6 = 0, \quad \beta_6 = 0 \text{ and } \gamma_6 = 0 \end{aligned} \qquad (6.35)$$

The moments and forces at the small edge boundary are not known. However, it is still possible to establish some more conditions for a_i, β_i and γ_i noting that, according to (6.32):

$$
\begin{aligned}
(M_z)_{z=a} &= Y_3(a) = \alpha_3(a)N_{z,a} + \beta_3(a)M_{z,a} + \gamma_3(a)Q_a \\
(Q)_{z=a} &= Y_4(a) = \alpha_4(a)N_{z,a} + \beta_4(a)M_{z,a} + \gamma_4(a)Q_a \\
(N_z)_{z=a} &= Y_5(a) = \alpha_5(a)N_{z,a} + \beta_5(a)M_{z,a} + \gamma_5(a)Q_a
\end{aligned}
\qquad (6.36)
$$

In these expressions, the moment M_z at the inner boundary $z = a$ is, in fact, represented in two ways: as a particular value of the variable M_z at the boundary $z = a$ and as an arbitrary constant $M_{z,a}$, thus $(M_z)_{z=a}$ and $M_{z,a}$ are only and the same variable. The different notation results from the previous designations of section (6.2.2.1). The same considerations could be extended to $(N_z)_{z=a}$ and $N_{z,a}$ and to $(Q)_{z=a}$ and Q_a. Then (6.36) requires that:

$$
\begin{aligned}
&\alpha_3(a) = 0, \quad \beta_3(a) = 1 \text{ and } \gamma_3(a) = 0 \\
&\alpha_4(a) = 0, \quad \beta_4(a) = 0 \text{ and } \gamma_4(a) = 1 \\
\text{and} \quad &\alpha_5(a) = 1, \quad \beta_5(a) = 0 \text{ and } \gamma_5(a) = 0
\end{aligned}
\qquad (6.37)
$$

If other boundary conditions were considered, a different set of values for α_i, β_i and γ_i at $z = a$ would result. But, in any case we would get nine constant values. With these constant values the set of equations (6.31) can now be integrated using a numerical procedure, by for instance, the Runga-Kutta method of fourth order(60). A programme, FRECON, using this method is detailed in Appendix 4. Basically, it enables the calculation of the values of α_i, β_i and γ_i at the outer boundary, where $z = b$ (see fig. 6.8). At this boundary we have a free edge and this provides another set of three conditions. At this edge all force and moment components must be zero:

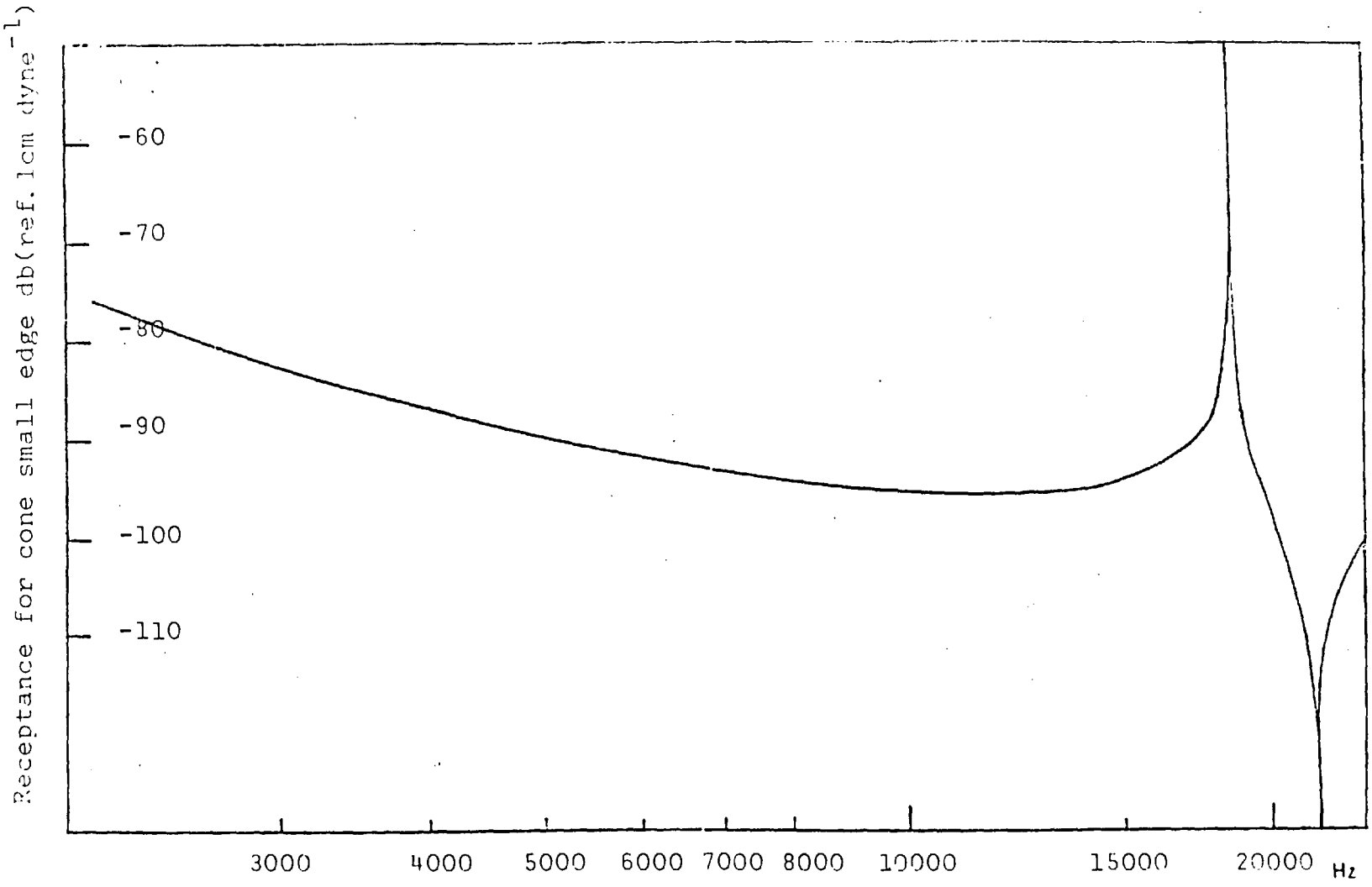

Fig. 6.9 Receptance curve obtained using the Goldberg-Marcus procedure

$$(M_z)_{z=b} = 0,$$
$$(N_z)_{z=b} = 0, \quad \text{and}$$
$$(Q)_{z=b} = 0 \tag{6.38}$$

Using the notation defined in (6.32):

$$(M_z)_{z=b} = Y_3(b) = \alpha_3(b)N_{z,a} + \beta_3(b)M_{z,a} + \gamma_3(b)Q_a$$
$$(N_z)_{z=b} = Y_4(b) = \alpha_4(b)N_{z,a} + \beta_4(b)M_{z,a} + \gamma_4(b)Q_a$$
$$(Q)_{z=b} = Y_5(b) = \alpha_5(b)N_{z,a} + \beta_5(b)M_{z,a} + \gamma_5(b)Q_a \tag{6.39}$$

Because $(M_z)_{z=b}$, $(N_a)_{z=b}$ and $(Q)_{z=6}$ are zero. and the programme FRECON provides the values of $\alpha_i(b)$, $\beta_i(b)$ and $\gamma_i(b)$ we can establish a set of three equations with three unknowns. These unknowns are the arbitrary constants $N_{z,a}$, $M_{z,a}$ and Q_a. Solving this system, it is now possible to calculate the values of these constants and, replacing them in (6.27), to find any value of $Y_i(z)$.

For the cone used later in the experiments, shown in Fig. 6.1, a calculation of the displacement component W^* at the inner boundary, z = a, was performed. In this case we assumed a sliding condition at this boundary. This assumption is suggested by the fact that the cone moves, at this edge, upwards and downwards, due to the force applied by the piezo-electric effect in this area.

The integration of the motion equations was made between $z = a = 8.5 \times 10^{-3}$m and $z = b = 36 \times 10^{-3}$m. Additional data used is indicated in Fig. 6.8. If one considers a unit

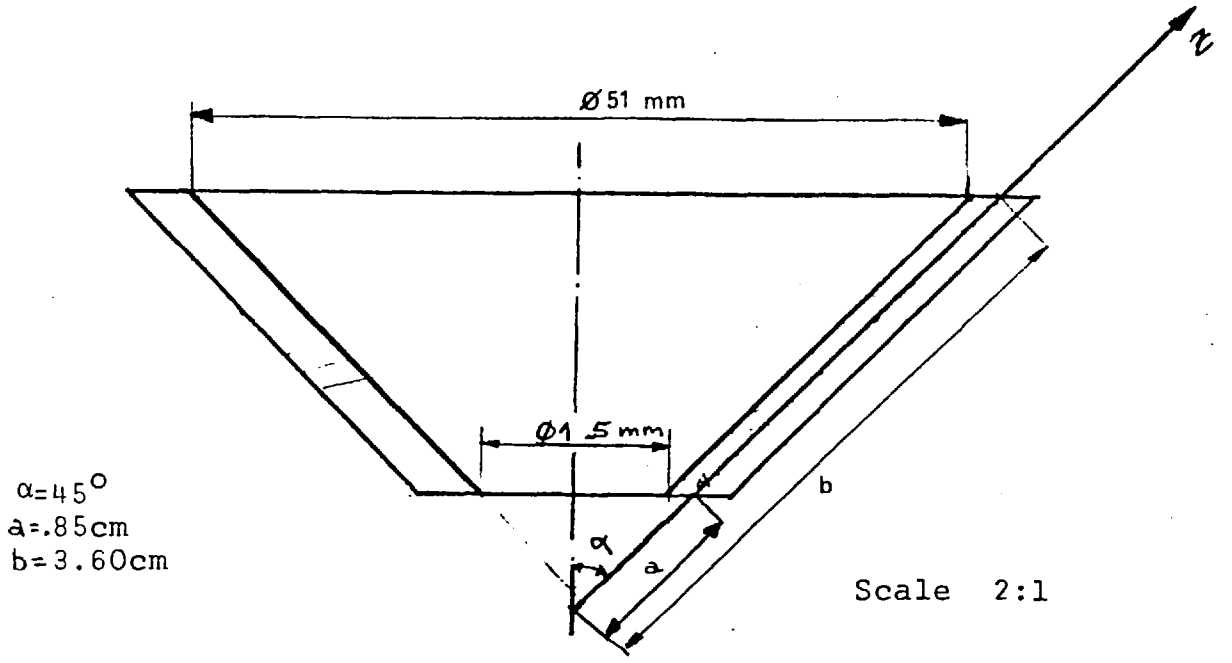

Fig. 6.8 Geometry data for the aluminium cone as used in Experiments

of supplied force the correspondent values of the displacement are also the receptance valves. These receptances were calculated and are plotted in Fig. 6.9. The maximum value of receptance occurs at a frequency of 17,700 Hz, with a minimum at a frequency of 20,500 Hz. The maximum response of the system (cone) corresponds to its resonance. At low frequencies the shell behaves mainly as a mass. Then, the system becomes more elastic as the frequency increases. The determination of the frequency of resonance of the shell is of first importance for the reasons explained in 6.1. In order to compare this theoretical result with the actual dynamic behaviour of the cone, the experiments described in 6.3 were performed.

6.3 Experimental Amplitude Measurements

To identify the first resonant frequency and to measure the amplitudes of vibration, the Fonotic Sensor equipment, analysed in Chapter 5, was used. The optical probe was positioned at several points along one of the cone generators. The relative position of these points is shown in Fig. 6.10, and the actual distances of these stations to the cone small edge are indicated in Table 6.1. The experiments were performed with different voltages across the ceramic from 50 volts to 70 volts (in some cases only 50 and 60 volts). For each voltage the force generated by the piezoelectric ceramic is constant with the frequency. Therefore the maximum amplitude of vibration at any point corresponds to a maximum receptance at the considered point. The signal measured by the Fonotic Sensor was converted to amplitude of displacement using the sensitivity curve of Fig. 4.6 and the results plotted for the various points and different frequencies. These response curves are shown from Figs. 6.11 to 6.15. In these curves two values of maximum are apparent. One at 18.550 KHz and other at about 19.5 KHz. The second peak is explained by the actual nonsymmetry of the bearing arrangement. As shown in Fig. 6.1, the bearing is supposed to be symmetrical in relation to the electrode plate (12). In practice this did not occur and there was a slight difference in the resonant frequencies of the two units.

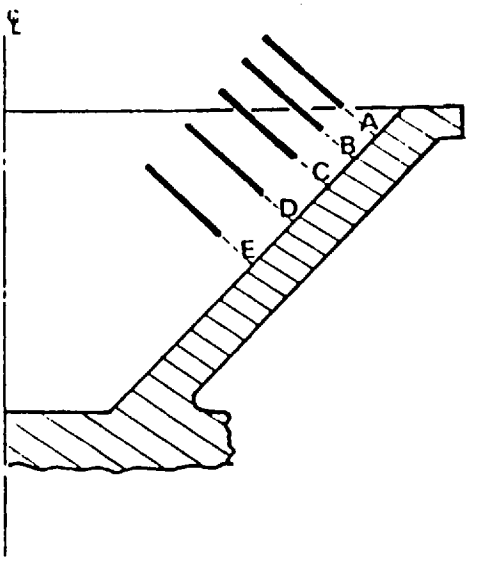

Fig. 6.10 Amplitude measuring points along the cone generator

The maximum amplitudes decrease considerably from the outer edge to the inner edge (Fig. 6.16). For the point E the data obtained became very scattered and it is impossible to draw a curve for each of the applied voltages.

An interesting point to note is that the amplitudes measures at point B are higher than at point A. This is most probably caused by the stiffening effect of the ring at the cone outer edge.

Comparing the value of the resonant frequency obtained experimentally, w_{exp}, and the theoretical one, w_{theor}, as calculated in 6.2.2 the experimental exceeds the theoretical about 1 KHz. If we assume the experimental value as correct, the relative error of the predicted value is

$$\text{error (\%)} = \frac{w_{exp} - w_{theor}}{w_{exp}} \times 100\% = \frac{18550-17700}{18550}$$

$$= 4.58\%$$

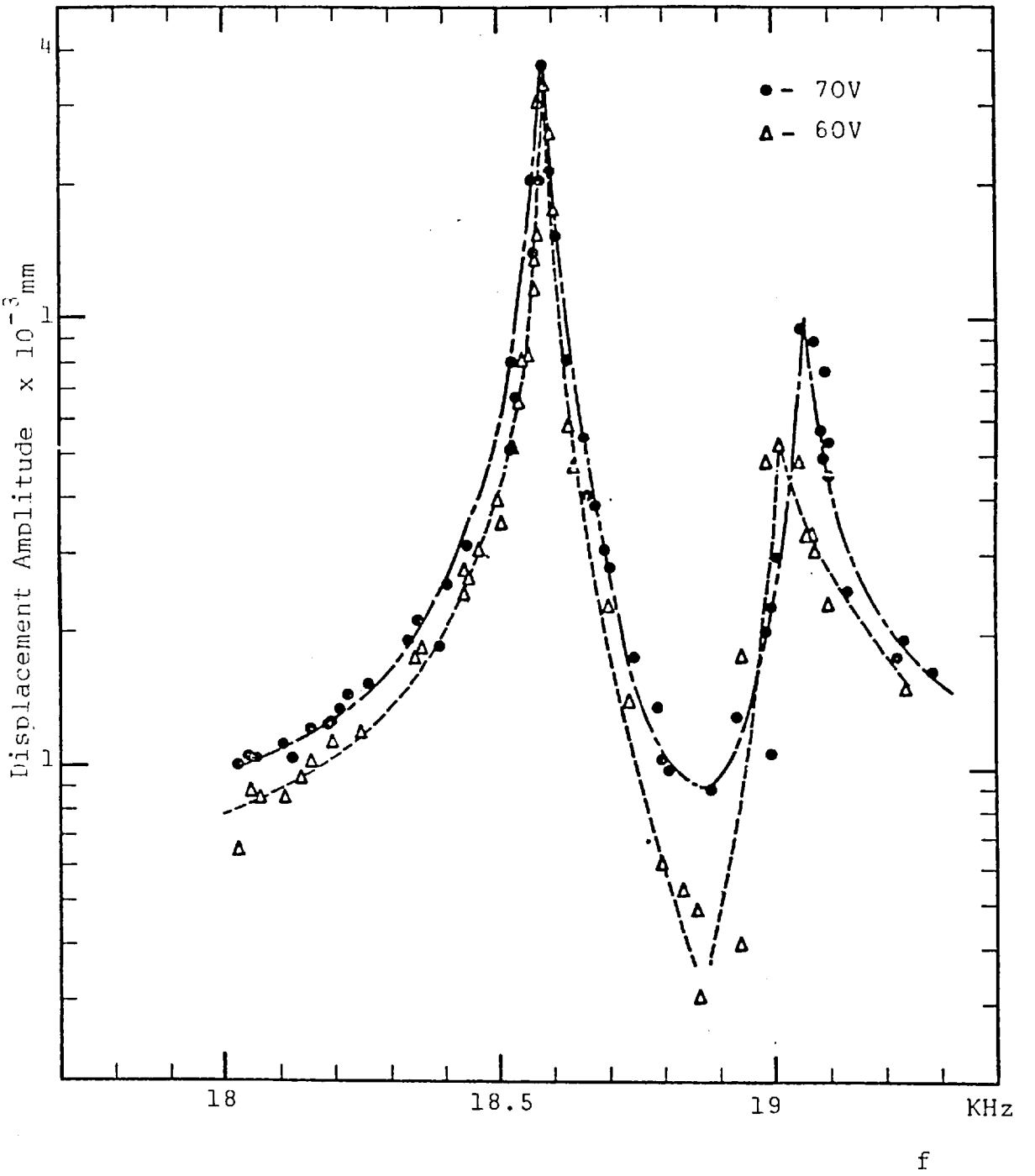

Fig. 6.11 Displacement amplitude measurements for probe position A

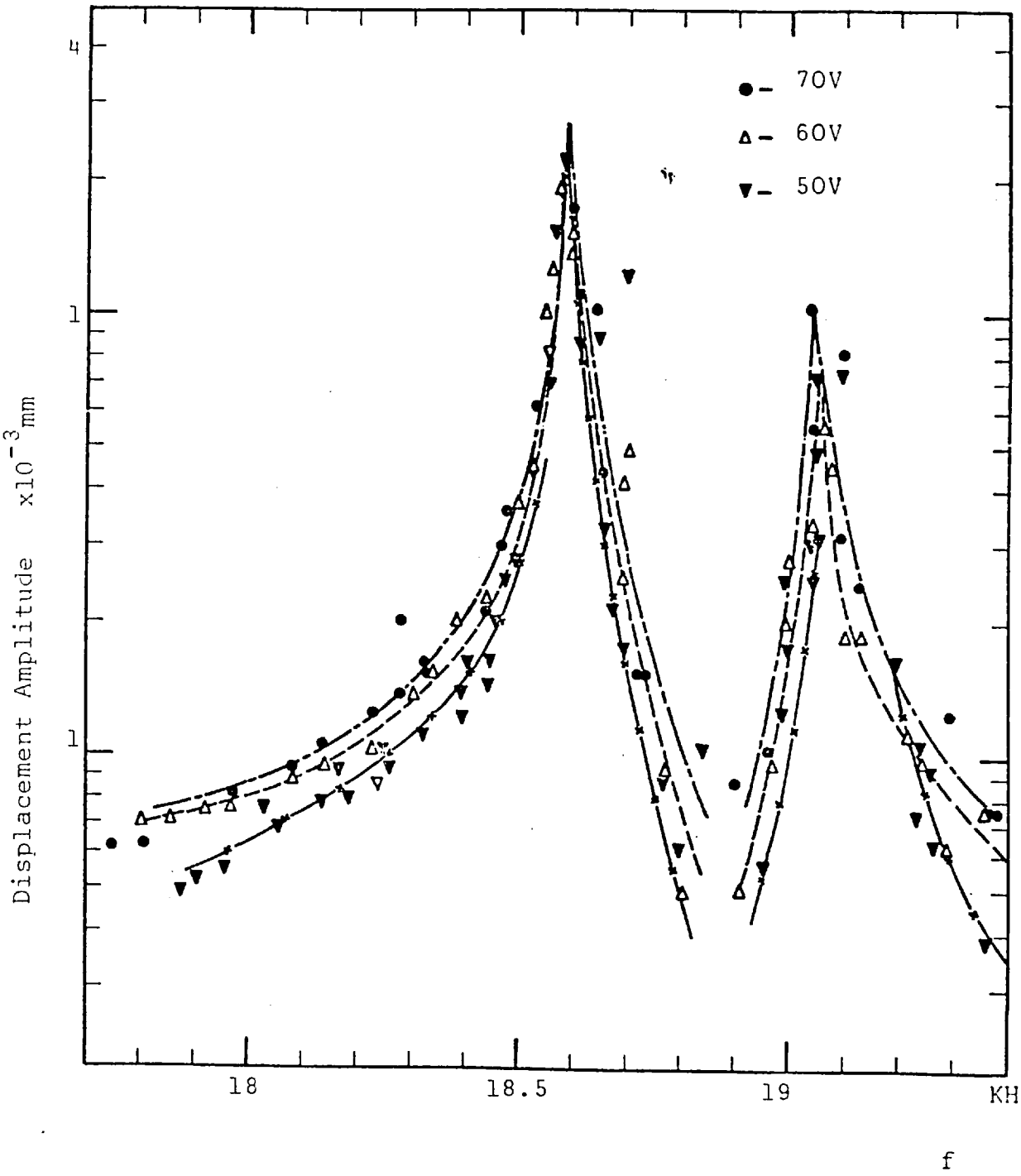

Fig. 6.12 Displacement amplitude measurements for probe position B

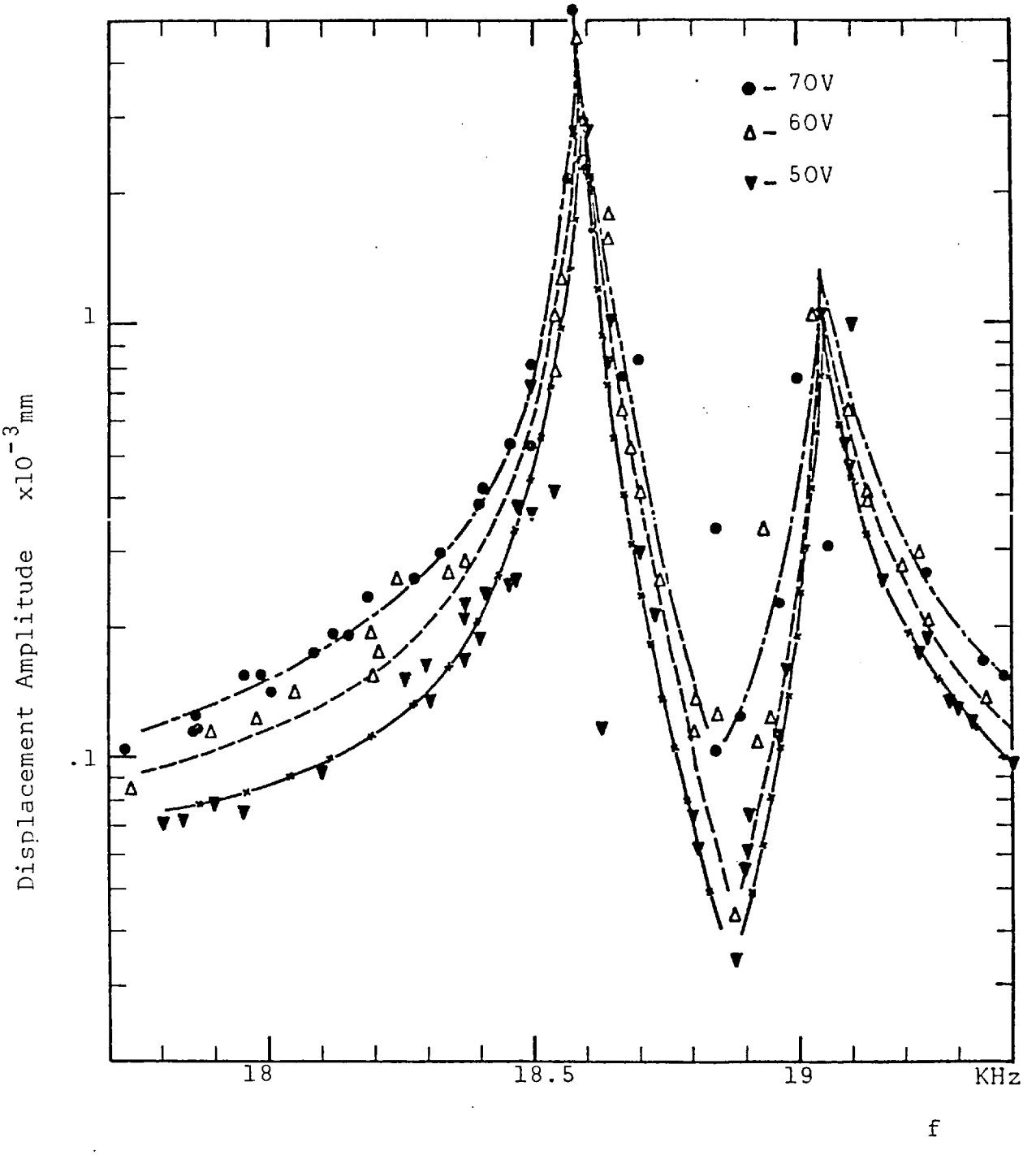

Fig. 6.13 Displacement amplitude measurements for probe position C

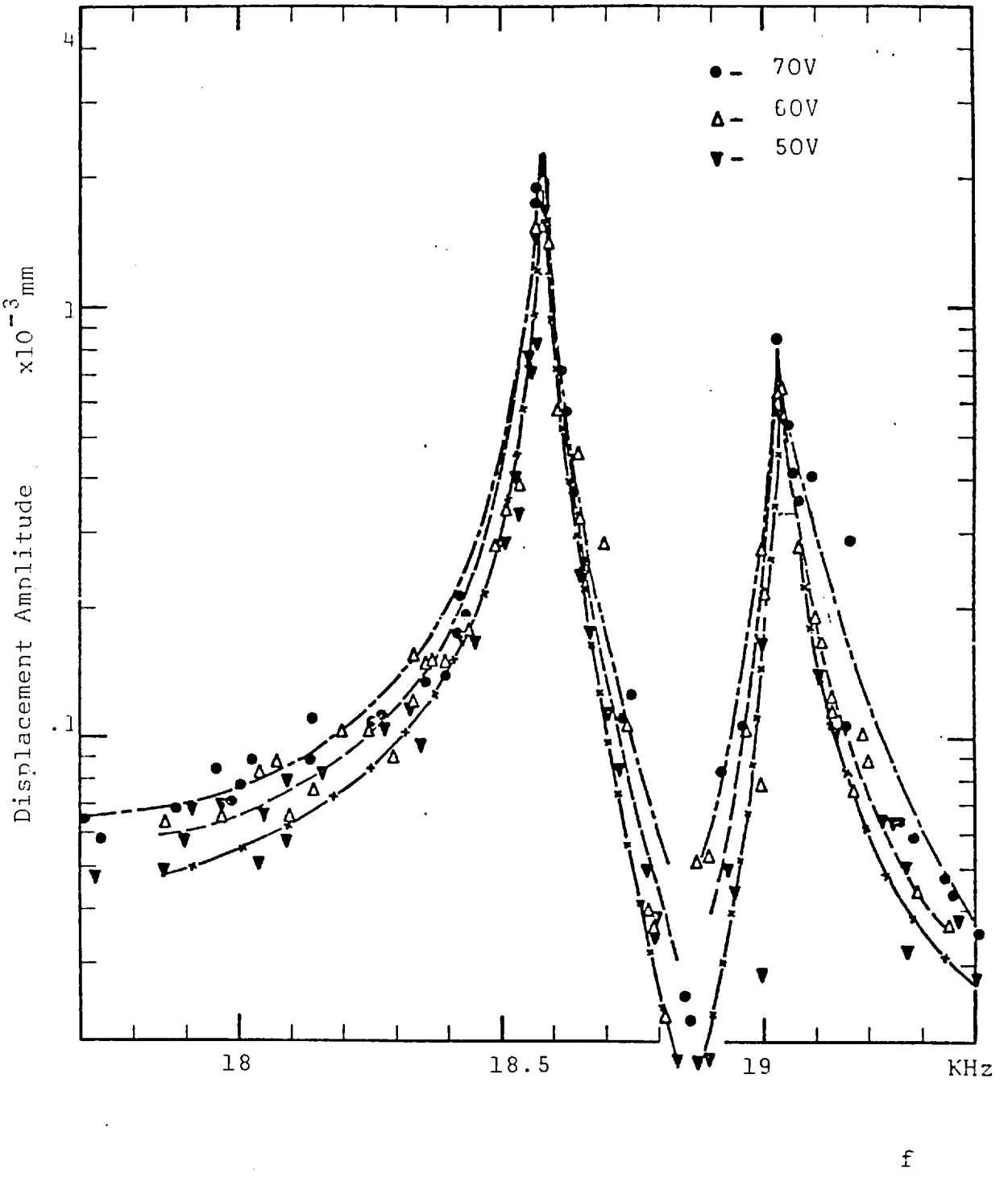

Fig. 6.14 Displacement amplitude measurements for probe position D

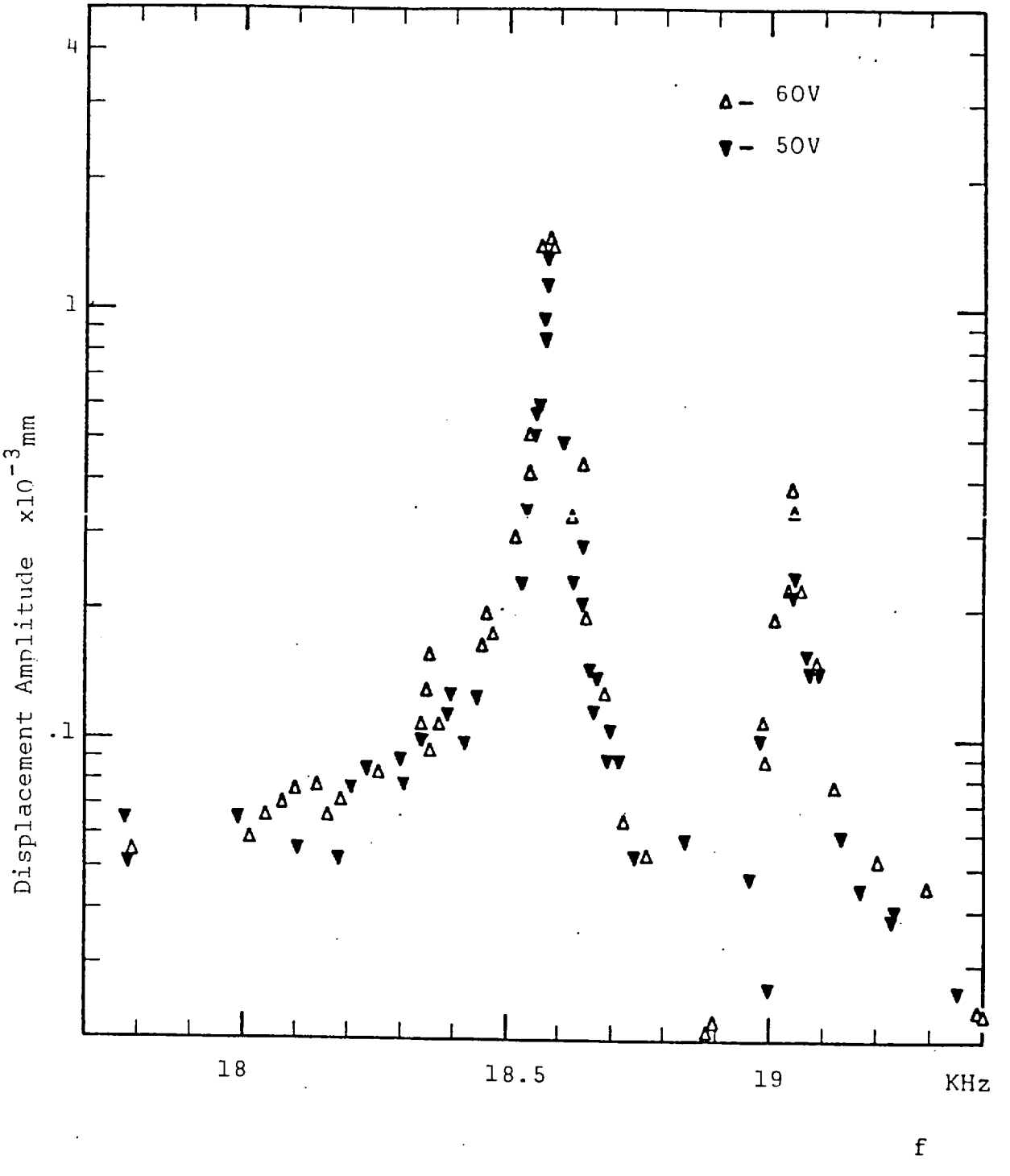

Fig. 6.15 Displacement amplitude measurements for probe position E

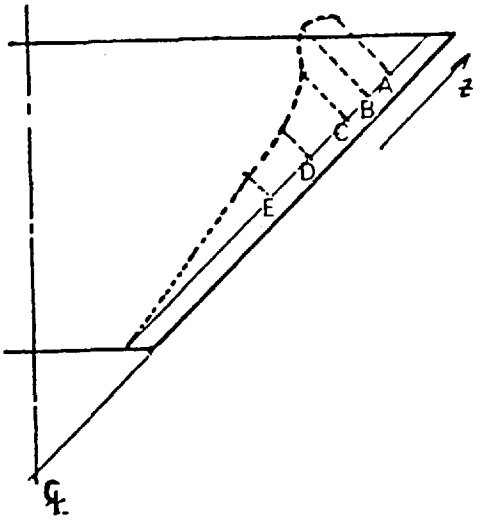

Fig. 6.16 Cone mode shape at experimental resonant frequency f_v = 18550 Hz

It is possible that part of this error is due to the fact that the boundary condition at the small edge actually will not be pure sliding. This condition should also include the rotation of the generators at this point. Therefore, we have a composite sliding and pinned condition, although this rotation is very small because it requires local deformation of the base at this edge.

6.4 Load Capacity

All known applications of squeeze film bearings have so far been for cases where load capacity is relatively small (about 1 pound per 1" projected area). However, it seems to be of interest to complete this study with the determination of the actual load capacity of the bearing used.

The two major problems associated with this evaluation are the disturbance caused by the application of load, and the simultaneous measurement of load and lift. The loading of the bearing has to be slow and symmetrical enough to prevent unbalance and shock of the supported member and, if possible there should be the possibility of a continuous variation of this load. For this purpose an auxiliary externally pressurised gas bearing was built. The complete apparatus is shown in Fig. 6.17 and it illustrates a metallic structure supporting this gas bearing(4). The gas bearing produced a downwards force on a lever arrangement(5). This lever, also shown in Fig. 6.18, transmitted the force to the supported member(3) of the squeeze film bearing(2). As this equipment was also intended to be used with disc squeeze bearings, a journal bearing, also externally pressurised, was associated with the loading bearing. The load applied to the squeeze film bearing was regulated by the inlet air pressure to the auxiliary bearing. The measurement of this load was obtained reading the pressure at the bearing recess(B). A calibration curve relating this pressure to the load applied to the bearing, at point (E) was previously obtained using a load cell. This curve, design calculations and drawings for the auxiliary bearings, are presented in Appendix 1. To measure the gas gap existing at each value of applied load a Wayne-Kerr capacitance probe(6) was placed over the supported member. The supported member had one hole in it with a sphere attached to the lever bearing against the hole edge (Fig. 6.18). This ensured uniform load distribution on the supported member.

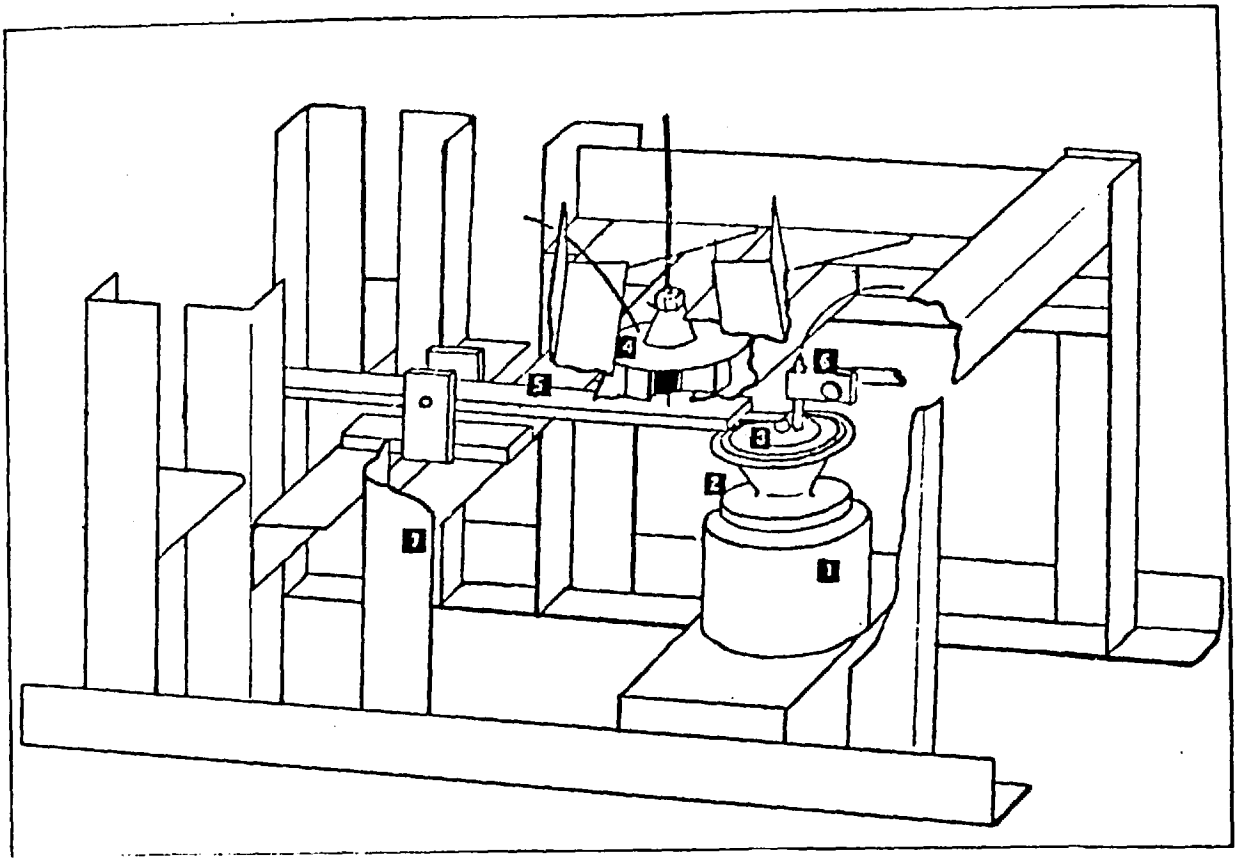

FIG. 6.17 Device built for measuring the load capacity of S.F. conical bearing.

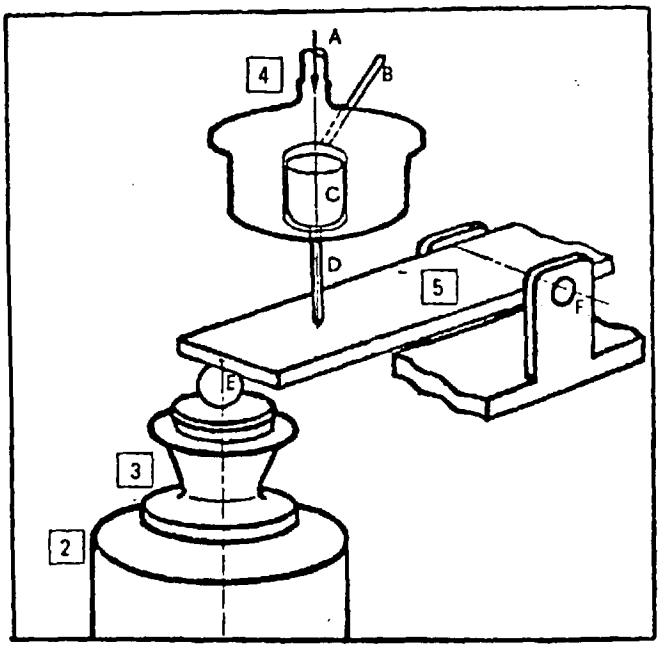

FIG. 6.18 Detail showing the lever arrangement and the auxiliary e.p. gas bearing

All the measurements were taken at a frequency of 18,596 Hz. The power input used was very low (maximum power was .146 watts for a voltage applied to the ceramic of 90 volts), and that was the only frequency at which the lift of the floating (Upper member) was verified. For very little changes in frequency (of about $\pm$ 5 Hz) the bearing showed complete loss of load capacity. When this happened, the two bearing surfaces came into contact with considerable resistance to the rotational motion. The measured values of film mean gap, load capacity and voltage applied to the piezoelectric ceramic are presented in Table 6.2. The dimensionless load $F^* = \frac{F}{\pi p_a r_b^2}$ is plotted against the dimensionless film gap $H^* = \frac{h}{h_o}$ in Fig. 6.19. In these expressions F is the load applied to the upper member, p_a is atmospheric pressure, r_b is the cone bigger edge and h_o is the initial vertical gap between bearing surfaces. The variable h represents, as before, the instantaneous mean film thickness.

6.5 Results and Discussion

The numerical procedure (Marcus Goldberg) is satisfactory in predicting the resonant frequency to within 5% of the experimental value. The only other application of this theory that is known is from Goldberg himself(58). For a much larger cone (254×10^{-3}m for the cone larger diameter) Goldberg indicates fifteen intervals for the z coordinate as giving excellent results for calculating the three first frequencies. In our case, fifteen intervals were also

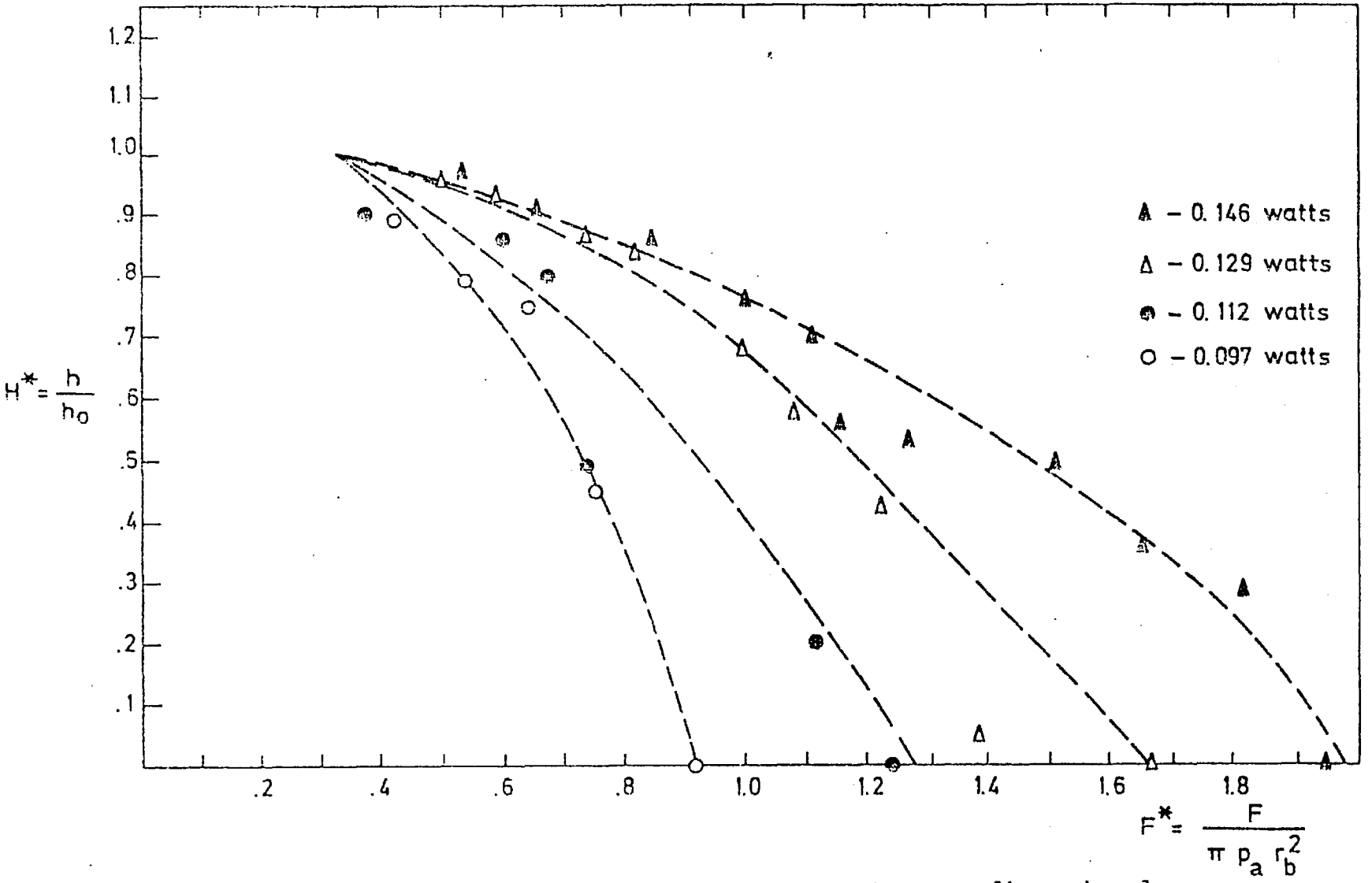

Fig. 6.19 Nondimensional load capacity versus nondimensional film thickness

used. However, it is possible that better results can be obtained by increasing the number of intervals. Another possible cause for the higher experimental value of the resonant frequency is the effect of a ring near the cone big edge. This change in geometry cannot be included in this theory. This fact and the imperfect knowledge of the exact boundary conditions at the inner edge can be taken as a possible explanation for the difference verified on the prediction of the resonant frequency. Besides the effect on the frequency, the ring also causes a decrease of the amplitude of vibration at the edge. This fact has also been verified by Huxley(31), in a similar arrangement to ours (Fig 6.20).

Regarding the amplitudes of vibration, the following conclusion can be drawn:

(i) increasing the power input to the bearing causes an increase in amplitude of vibration , as expected; but this relation is not linear and is limited by the impedance of the cone;

(ii) the existence of the stiffening ring produces a reduction of the amplitudes near the edge;

(iii) comparing the frequency where lift occurs (f_1=18,596 Hz) and the resonance frequency obtained experimentally in Section 6.3, (f_r = 18,550 Hz), it is permissible to conclude that the two frequencies seem to be intimately connected. This would mean that, in fact, the amplification of the vibrational

amplitudes verified at resonance of the shell, benefits the bearing load capacity.

From statement (iii) two practical implications can be drawn:

(a) For systems where the available power is very limited, the prediction of the resonant frequency of the bearing unit is of primary importance because it works best at this frequency.

(b) In systems where the input power does not create a problem, the operation of the bearing at or very near the resonant frequency would product a noticeable increase of load capacity.

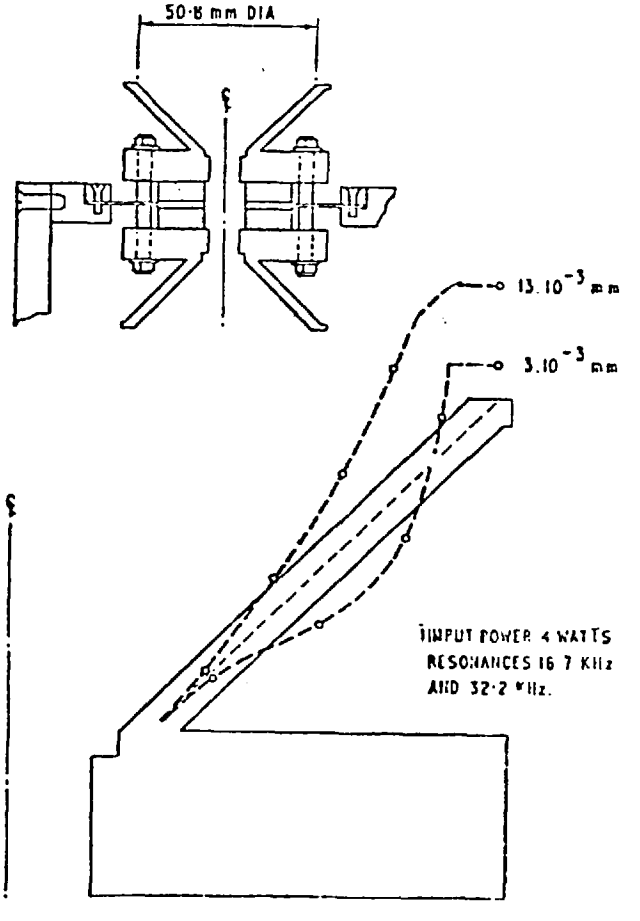

Fig. 6.20 Huxley experimental results using a conical bearing (Ref. 31)

CHAPTER SEVEN

DISC SQUEEZE-FILM BEARING

7.1 INTRODUCTION

In all the experiments described in the previous Chapters the geometry of the conical bearing was the same in every case. However, Huxley (31) suggested that changes occur in the resonant frequency of similar bearing arrangements when the geometry of the small base of the cone was modified. This base is in direct contact with the supporting member base (item 3 in Fig. 6.1). Therefore, this suggests a dynamic study of a squeeze film bearing having different geometries.

Because a disc bearing is easier to manufacture with satisfactory geometrical accuracy than a conical one it was decided to use in this study several disc specimen. The bearing arrangement being basically the same as that of the conical bearing, but the conical shell is now replaced by a simple disc, as shown in Fig. 7.1.

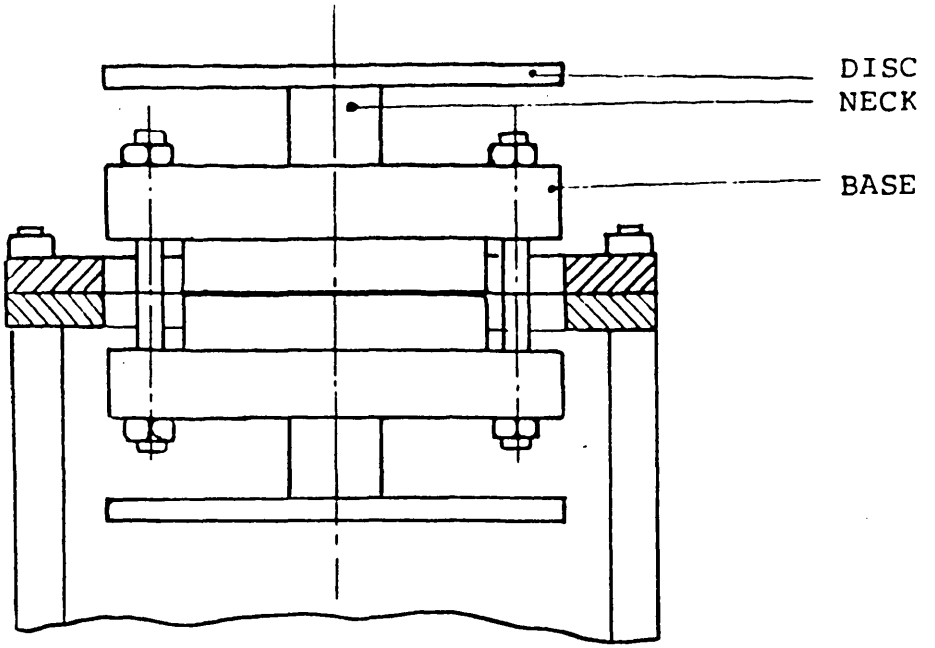

FIG. 7.1 - Disc squeeze film bearing arrangement.

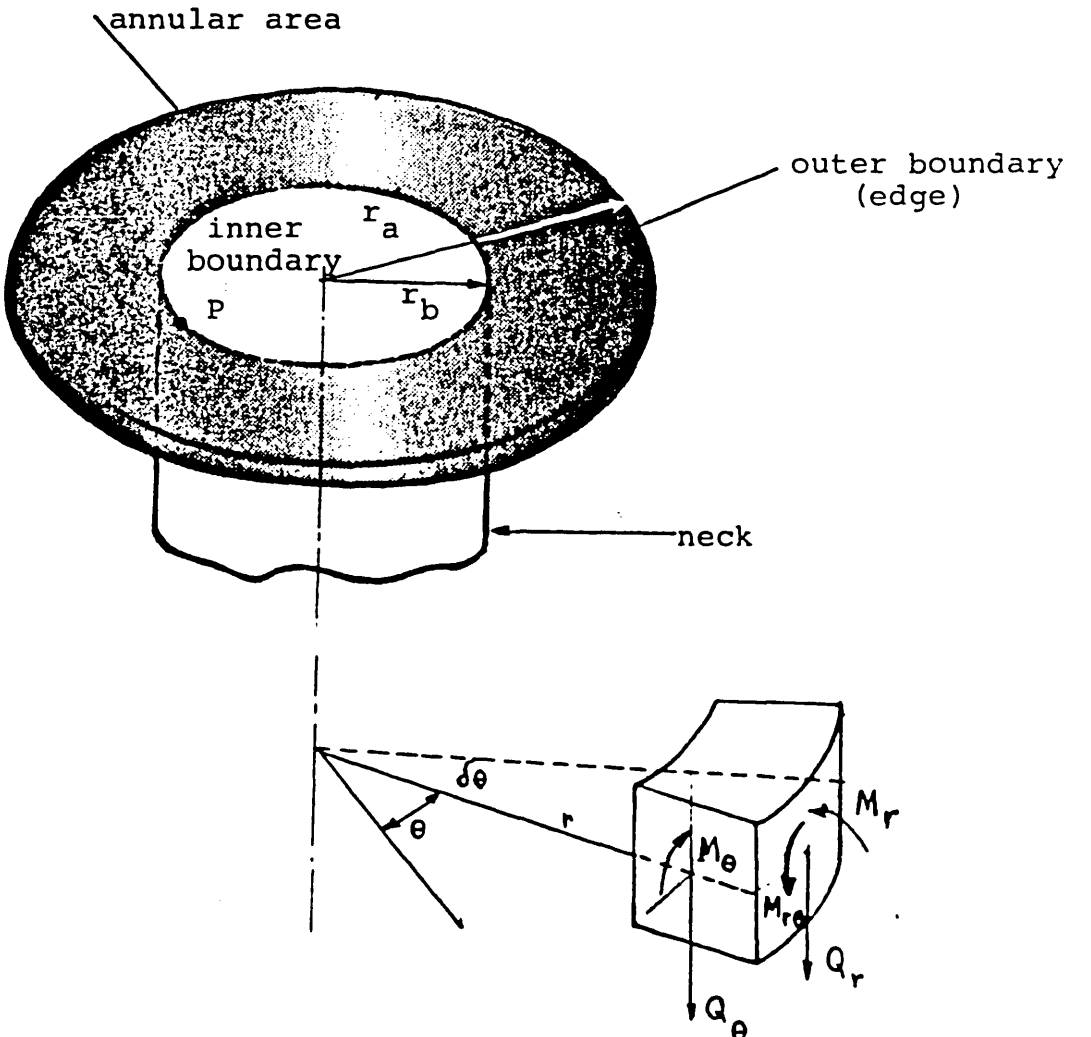

FIG. 7.2 - Bearing surface showing the annular area and the "neck". On the corner is also shown a detail of a plate element and forces and moments acting on it.

7.1.2 DISC CHARACTERISTICS

7.1.2.1 Geometry

The disc diameter chosen is the same as the larger base of the cone. This ensures that the projected bearing area of the cone equals that of the disc.

A change in geometry was thus obtained by variation of the radius of the small cylinder joining the supporting member to the base (designated as NECK in Fig.7.1).

This cylinder provides the required clearance for the bolt nuts and also the space for the insertion of a thightening wrench (shown in Appendix 2). The existence of this neck is then indespensable for this type of arrangement. Its height was considered constant for the different cases, and equal to $h_n = 10^{-2}$ m.

Our initial assumption in this study is that the change of the neck radius (r_b) can produce considerable variation of the resonant frequency of the supporting member. This change should cause various resonant frequencies, according to the value of r_b, there being no modification of the bearing surface size or shape.

The different neck sizes are characterised in this study by the ratio of its radius, r_b, to the bearing radius, r_a, and this ratio will be hereafter designated as neck coefficient.

A detail of the Fig. 7.1 is shown in Fig. 7.2. This detail indicates the two areas, these being an external area, with the geometry of an annulus, separated from a central area at a boundary of radius, r_b. This radius is the same as that of the neck.

The possible changes in the resonant frequency of the bearing member, due to a variation in the value of r_b, and the establishment of a possible correlation between the values of these frequencies and that of optimum performance of the bearing are the subject of the following sections.

7.1.2.2 Bearing Materials

The materials used for the supporting member in the present study are mild steel and an aluminium alloy, dural. The choise of this materials is dictated by availability and ease of machining.

The relevant data for these materials is as follows:

Young's modulus - E

- steel: 207×10^9 (N/m^2)
- aluminium: 68.9×10^9 (N/m^2)

Density - ρ

- steel: 7,850 (Kg/m^3)
- aluminium: 2,720 (Kg/m^3)

Poisson's Coef. - ν

- steel: .3
- aluminum: .3

7.1.2.3 Surface Texture

For all the (disc) specimen used in experiments a ground finish was specified for the bearing surfaces. An exception was made for two of the aluminum discs for which lapped surfaces were defined.

The surface texture of the different specimens was measured with a Talysurf instrument. The data obtained is shown in Table 7.1. Tests to determine the flatness of this surface by interference methods were also carried out. Unfortunately, the characteristics of reflectivity of the surfaces were not good enough to obtain a clear fringe patterns; this procedure consisted of comparison of the interference bands on the workpiece (the bearing disc) with a platen in the interferometer.

The results of the texture measurements are shown in Table 7.1.

MATERIAL	COEFFICIENT	C.L.A. (μ in.)
STEEL	.2	15.0
STEEL	.4	4.0
STEEL	.5	12.0
DURAL	.2	7.0
DURAL	.4	1.0
DURAL	.5	1.6

TABLE 7.1

7.2 VIBRATION OF CIRCULAR PLATES

7.2.1 Plate Equations and Boundary Conditions

As stated before, the disc thrust bearing assumed to be a circular annulus and an inner region to which the "neck" is attached.

The vibrations of annular discs have been treated by Bishop and Mc Leod (62) and their analysis is used in this Chapter. However it should be mentioned that it is also possible to apply the Goldberg method (used in Chapter 6) to this problem as a particular case of a cone with half apex angle, α, equal to 90 degrees.

Bishop and McLeod's procedure results in a simpler analytical treatment.

The general equation of motion of a plate in polar coordinates is:

$$\left(\frac{\partial^2}{\partial r^2} + \frac{1}{r}\frac{\partial}{\partial r} + \frac{1}{r^2}\frac{\partial^2}{\partial \theta^2}\right) \times \left(\frac{\partial^2 w}{\partial r^2} + \frac{1}{r}\frac{\partial w}{\partial r} + \frac{1}{r^2}\frac{\partial^2 w}{\partial \theta^2}\right) + \frac{\rho h_d}{\bar{D}}\frac{\partial^2 w}{\partial t^2} = \frac{q}{\bar{D}} \qquad (7.1)$$

In this expression r is the radial coordinate and θ is the angular coordinate. The displacement component normal to the plate surface is represented by w. The

transverse force, per unit of perimeter is q. The plate thickness is h_d and ρ is the plate material density. The constant $\bar{D}$ $(=\frac{E\, h_d^3}{12\,(1-\nu^2)})$ is the flexural rigidity and ν represents the Poisson's coefficient.

Considering an element of the shell and its equilibrium, Fig. 7.2, it is possible (62) to establish the following expressions:

- for the shear force components:

$$Q_r = -\bar{D}\left[\frac{\partial w^3}{\partial r^3} + \frac{1}{r}\frac{\partial^2 w}{\partial r^2} - \frac{1}{r^2} - \frac{\partial w}{\partial r} + \frac{1}{r^2}\frac{\partial w^3}{\partial r \partial \theta^2} - \frac{2}{3}\frac{\partial w}{\partial \theta^2}\right] \tag{7.2}$$

$$Q_\theta = -\bar{D}\left[\frac{1}{r}\frac{\partial^2 w}{\partial r^2\ \partial \theta} + \frac{1}{r^2}\frac{\partial^2 w}{\partial r\ \partial \theta} + \frac{1}{r^2}\frac{\partial^2 w}{\partial \theta^2}\right] \tag{7.3}$$

- for the bending moments:

$$M_r = -\bar{D}\left[\frac{\partial w^3}{\partial r^3} + \frac{1}{r}\frac{\partial^2 w}{\partial r^2} - \frac{1}{r^2}\frac{\partial w}{\partial p} + \frac{1}{r^2}\frac{\partial w^3}{\partial r \partial \theta^2} - \frac{2}{3}\frac{\partial^2 w}{\partial \theta^2}\right] \tag{7.4}$$

$$M_\theta = -\bar{D}\left[\frac{1}{r}\frac{\partial w}{\partial r} + \frac{1}{r^2}\frac{\partial^2 w}{\partial \theta^2} + \nu\frac{\partial^2 w}{\partial r^2}\right] \tag{7.5}$$

- for the twisting moment:

$$M_{r\theta} = (1 - D)\,\bar{D}\left[\frac{1}{r}\frac{\partial^2 w}{\partial r \partial \theta} - \frac{1}{r}\frac{\partial w}{\partial \theta}\right] \tag{7.6}$$

To solve the equation of motion (7.1) it is

necessary to name two more boundary conditions at each edge. The boundary conditions that can be assumed are four:

- clamped
- sliding
- pinned, and
- free

In the example quoted the disc outer edge is free to move. For the inner boundary of the annular area at radius r_b, the free conditions can not be used only the three other conditions need to be considered. At the inner edge r_b, the actual boundary condition is very difficult to establish. The reason is that the annulus and the neck are both elements of the same body, considered as two for the analytic simplicity (as explained in 7.1.1), so, several hypothesis must be analized:

For a pinned edge:

$$\begin{cases} W = 0 & (7.7) \\ M_\theta = 0 & (7.8) \end{cases}$$

At a clamped edge the the slope and the displacement are zero:

$$\begin{cases} W = 0 & (7.9) \\ \frac{\partial w}{\partial r} = 0 & (7.10) \end{cases}$$

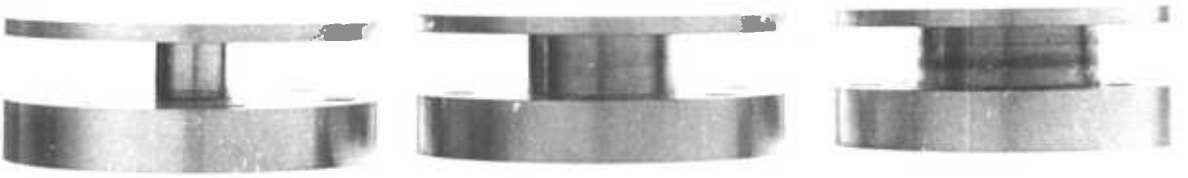

coef. .2 coef. .4 coef. .5

FIG. 7.3 Disc-shaped squeeze film bearing supporting members as used in experiments.

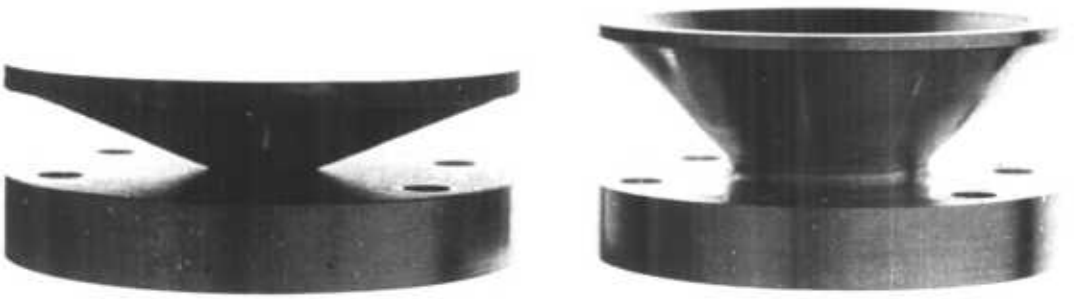

FIG. 7.4 Ribbed disc and conical squeeze film supporting members.

Before discussing these boundary conditions, the solution of the equation of motion will be solved for the case of symmetrical vibrations:

7.2.2 SYMMETRICAL VIBRATIONS

7.2.2.1 Solution of Equation of Motion

The flexural vibrations of circular plates can occur in two ways:

- if the deflection at any point is a function of the radius and time alone these are called symmetrical vibrations and have nodal circles. There is no dependence on the angular coordinate.

- if the deflection is not symmetrical with respect to the disc center, the vibrations are nonsymmetrical and the nodal points are situated along diameters. These vibrations are usually due to nonuniformly applied forces or to nonsymmetrical boundary conditions.

In our case the only type of vibrations likely to occur are of the first type, the symmetrical ones, also called "umbrella" modes, when all applied forces and conditions are symmetrical. These vibrations correspond to the extensional vibrations of cones, referred in 6.2.1. For these vibrations the equation of motion simplifies to:

$$\left(\frac{\partial^2}{\partial r^2} + \frac{1}{r}\frac{\partial}{\partial r}\right)\left(\frac{\partial^2 w}{\partial r^2} + \frac{1}{r}\frac{\partial w}{\partial r}\right) + \frac{\rho h_d}{\bar{D}}\frac{\partial^2 w}{\partial t^2} = 0 \quad (7.11)$$

If we assume a harmonic vibration with the frequency ω, the displacement w can be written as:

$$w = W^*(r) \sin(\omega t) \quad (7.12)$$

$W^*(r)$ is a function of the radial coordinate alone. Thus, equation (7.11) can be written as:

$$\left(\frac{d^2}{dr^2} + \frac{1}{r}\frac{d}{dr}\right)\left(\frac{d^2}{dr^2} + \frac{1}{r}\frac{d}{dr}\right) W^* - k^4 W^* = 0 \quad (7.13)$$

In this equation t is the time coordinate and k is a parameter, called the <u>frequency parameter</u>. The parameter k is:

$$k = \left(\frac{\rho h_d \omega^2}{\bar{D}}\right)^{1/4} \quad (7.14)$$

The equation (7.13) can also be written in the form of a Bessel equation:

$$(\nabla^2 + k^2)(\nabla^2 - k^2) W^*(r) = 0 \quad (7.15)$$

with $\nabla^2 = \frac{d^2}{dr^2} + \frac{1}{r}\frac{d}{dr}$, the Laplatian operator.

The solution of this equation is:

$$W^*(r) = AJ_o(kr) + BY_o(kr) + CI_o(kr) + DK_o(kr) \quad (7.16)$$

A, B, C and D are constants dependent on the boundary condition and J_o, Y_o, I_o, K_o are Bessel functions*.

Using this expression in equations (7.2) to (7.5) results in:

- for the slope

$$\frac{dW^*}{dr} = - k\left[AJ_1(kr) + BY_1(kr) - CI_1(kr) + DK_1(kr)\right] \qquad (7.17)$$

- for the shear force:

$$Q_r = \bar{D}\, k^3 \left[AJ_1(kr) + BY_1(kr) + CI_1(kr) - DK_1(kr)\right] \qquad (7.18)$$

- for the radial moment:

$$M_r = \bar{D}\, k^2 \left[A\left\{J_o(kr) + \frac{\nu-1}{kr} J_1(kr)\right] + B\left\{Y_o(kr) + \frac{\nu-1}{kr} Y_1(kr)\right\} + C\left\{I_o(kr) + \frac{\nu-1}{kr} I_1(kr)\right\} - D\left\{K_0(kr) - \frac{\nu-1}{kr} K_1(kr)\right\}\right] \qquad (7.19)$$

Where J_1, Y_1, I_1, K_1 are also Bessel functions*

---

* $J_o(kr)$ is a Bessel function of first kind, zero order

$Y_o(kr)$ is a Bessel function of second kind, zero order

$I_o(kr)$ is a Modified Bessel function of first kind, zero order

$K_o(kr)$ is a Modified Bessel function of second kind, zero order

7.2.2.2 Frequency Equation

Putting all possible boundary conditions in equations (7.17) to (7.19) (always free at the outer edge), leads to four alternative equations. The frequency equation can then be found equating to zero the determinant of the matrix formed by the coefficients of the constants A, B, C and D.

Let us assume that we have an annular plate with outer radius, r_a, and inner radius, r_b. The determinants obtained for each pair of boundary conditions are the following[62]:

i) Clamped condition at r_b
Free condition at r_a

$$\Delta_{C-F}=\begin{vmatrix} J_o(kr_b) & Y_o(kr_b) & I_o(kr_b) & K_o(kr_b) \\ J_1(kr_b) & Y_1(kr_b) & -I_1(kr_b) & K_1(kr_b) \\ J_1(kr_a) & Y_1(kr_a) & I_1(kr_a) & -K_1(kr_a) \\ J_{o1}(kr_a) & Y_{o1}(kr_a) & I_{o1}(kr_a) & K_{o1}(kr_a) \end{vmatrix} \qquad (7.20)$$

---

*

$J_1(kr)$ is a Bessel function of first kind, first order

$Y_1(kr)$ is a Bessel function of second kind, first order

$I_1(kr)$ is a Modified Bessel function of first kind, first order

$K_1(kr)$ is a Modified Bessel function of second kind, first order

Δ_{C-F} represents the determinant that must be equated to zero to find the natural frequencies for a clamped-free condition. The functions $J_{o1}(kr_a)$, $Y_{o1}(kr_a)$, $I_{o1}(kr_a)$ and $K_{o1}(kr_a)$ result from combinations of the Bessel functions already defined and presented on page 166 .

ii) Sliding condition at r_b
Free condition at r_a

$$\Delta_{s-F}= \begin{vmatrix} J_1(kr_b) & Y_1(kr_b) & -I_1(kr_b) & K_1(kr_b) \\ J_1(kr_b) & Y_1(kr_b) & I_1(kr_b) & -K_1(kr_b) \\ J_1(kr_a) & Y_1(kr_a) & I_1(kr_a) & -K_1(kr_a) \\ J_{o1}(kr_a) & Y_{o1}(kr_a) & I_{o1}(kr_a) & K_{01}(kr_a) \end{vmatrix} \quad (7.21)$$

iii) Pinned condition at r_b
Free condition at r_a

$$\Delta_{p-F}= \begin{vmatrix} J_o(kr_b) & Y_o(kr_b) & I_o(kr_b) & K_o(kr_b) \\ I_{o1}(kr_b) & Y_{o1}(kr_b) & I_{o1}(kr_b) & K_{o1}(kr_b) \\ J_1(Kr_a) & Y_1(kr_a) & I_1(kr_a) & -K_1(kr_a) \\ J_{o1}(kr_a) & Y_{o1}(kr_a) & I_{o1}(kr_a) & K_{o1}(kr_a) \end{vmatrix} \quad (7.22)$$

ir) Free condition at r_b
Free condition at r_a

$$\Delta_{F-F}= \begin{vmatrix} J_1(kr_b) & Y_1(kr_b) & I_1(kr_b) & -K_1(kr_b) \\ J_{o1}(kr_b) & Y_{o1}(kr_b) & I_{o1}(kr_b) & K_{o1}(kr_b) \\ J_1(kr_a) & Y_1(kr_a) & I_1(kr_a) & -K_1(kr_a) \\ J_{o1}(kr_a) & Y_{o1}(kr_a) & I_{o1}(kr_a) & K_{o1}(kr_a) \end{vmatrix} \quad (7.23)$$

with

$$J_{ol}(kr_i) = J_o(kr_i) + \frac{\nu-1}{kr_i} J_1(kr_i)$$

$$Y_{ol}(kr_i) = Y_o(kr_i) + \frac{\nu-1}{kr_i} Y_1(kr_i)$$

$$I_{ol}(kr_i) = - I_o(kr_i) - \frac{\nu-1}{kr_i} I_1(kr_i)$$

$$K_{ol}(kr_i) = - K_o(kr_i) + \frac{\nu-1}{kr_i} K_1(kr_i) \qquad (7.24)$$

At resonance, the determinants (7.20 - (7.23) are zero. Considering several values of the frequency, and for given values of r_a and r_b it is possible to establish the behaviour of these determinants.

Considering a free outer boundary and four different conditions at the inner boundary the determinant curves are plotted in Figs. 7.5 and 7.6. The range of frequencies vary from 0 to 13 KHz and the absolute value of the determinant, Δ, is considered between 0 and 2.

The numerical values used for plotting these curves were obtained from expressions (7.20) to (7.23) and computed with the programme FREDIS, shown in Appendix 4. Both aluminium and steel disc plates show very close values of the first natural frequency, for each boundary condition. The clamped-free conditions gives the lowest frequency, for

either aluminium or steeel discs. The value of this first frequency increases with the value of the Neck coefficient, as would be expected. For aluminium plates, only the sliding-free and clamped conditions were considered (Fig.7.7). These two conditions are the most realistic for a squeeze--film bearing unit.

7.2.3 Receptance expressions

Also for interest is the prediction of the amplitudes of vibration of the disc annulus when a force is applied to the inner boundary. For a force uniformly distributed along the boundary the amplitude of vibration of any point will be dependent on the boundary conditions. The amplitude of displacement caused by a unit of applied force is called the receptance. The total displacement will obviously be the product of the receptance times the force. If the point is situated at a distance r from the center of the annulus and the force applied at a point located, for instance, at the inner boundary r_b, the receptance will be designated by α_{rb}. Bishop and Mc Leod[62] derivated expressions for receptance for different boundary conditions and for uniformly distributed forces or single forces. For uniformly distributed applied force the receptance expressions are as follows:

i) Clamped-Free boundary conditions:

applied force not possible.

ii) Sliding-Free boundary conditions:

$$\alpha_{rb} = \frac{1}{\bar{D}\, k^3\, 2\pi\, \Delta_{S-F}\, r_b} \left[-\Delta_A J_o(kr) + \Delta_b Y_o(kr) - \Delta_C I_o(kr) + \right.$$

$$\left. + \Delta_D K_o(kr) \right] \qquad (7.25)$$

iii) Pinned-Free boundary conditions:

applied force not possible

iv) Free-Free boundary conditions:

$$\alpha_{rb} = \frac{1}{\bar{D}\, k^3\, 2\pi\, \Delta_{F-F}\, r_b} \left[\Delta_A J_o(kr) - \Delta_B Y_o(kr) + \Delta_C I_o(kr) - \right.$$

$$\left. - \Delta_D K_o(kr) \right] \qquad (7.26)$$

The values of Δ_{S-F} and Δ_{F-F} are given by (7.21) and (7.23) respectively. The symbols $\Delta_A, \Delta_B, \Delta_C$ and Δ_D also represent determinants whose value is given in Appendix 5 for each example of boundary conditions.

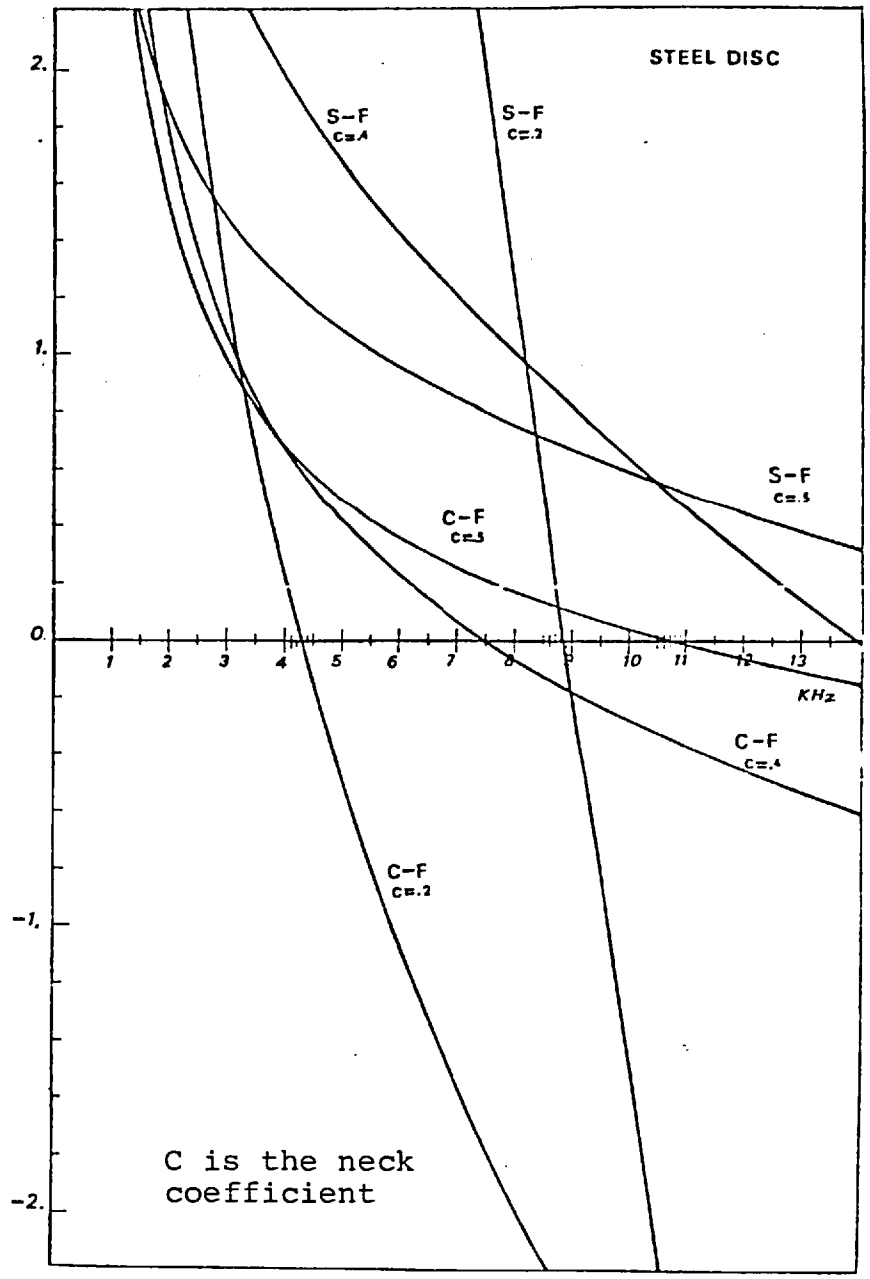

FIG. 7.5 Determinant curves for clamped-free (C-F) and sliding-free (S-F) boundary conditions - steel disc annulus.

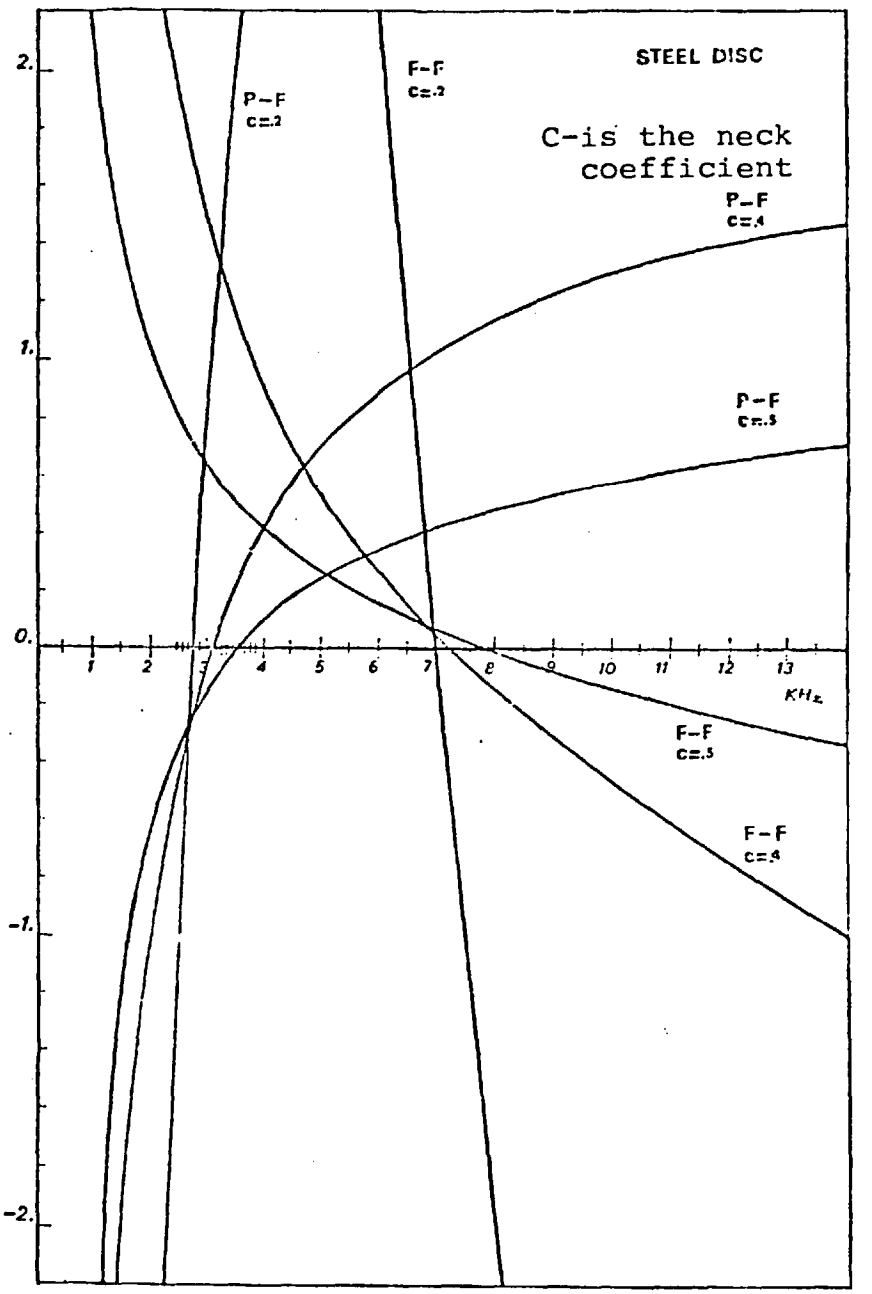

FIG. 7.6 Determinant curves for pinned-free (P-F) and free-free (F-F) boundary conditions - steel disc annulus.

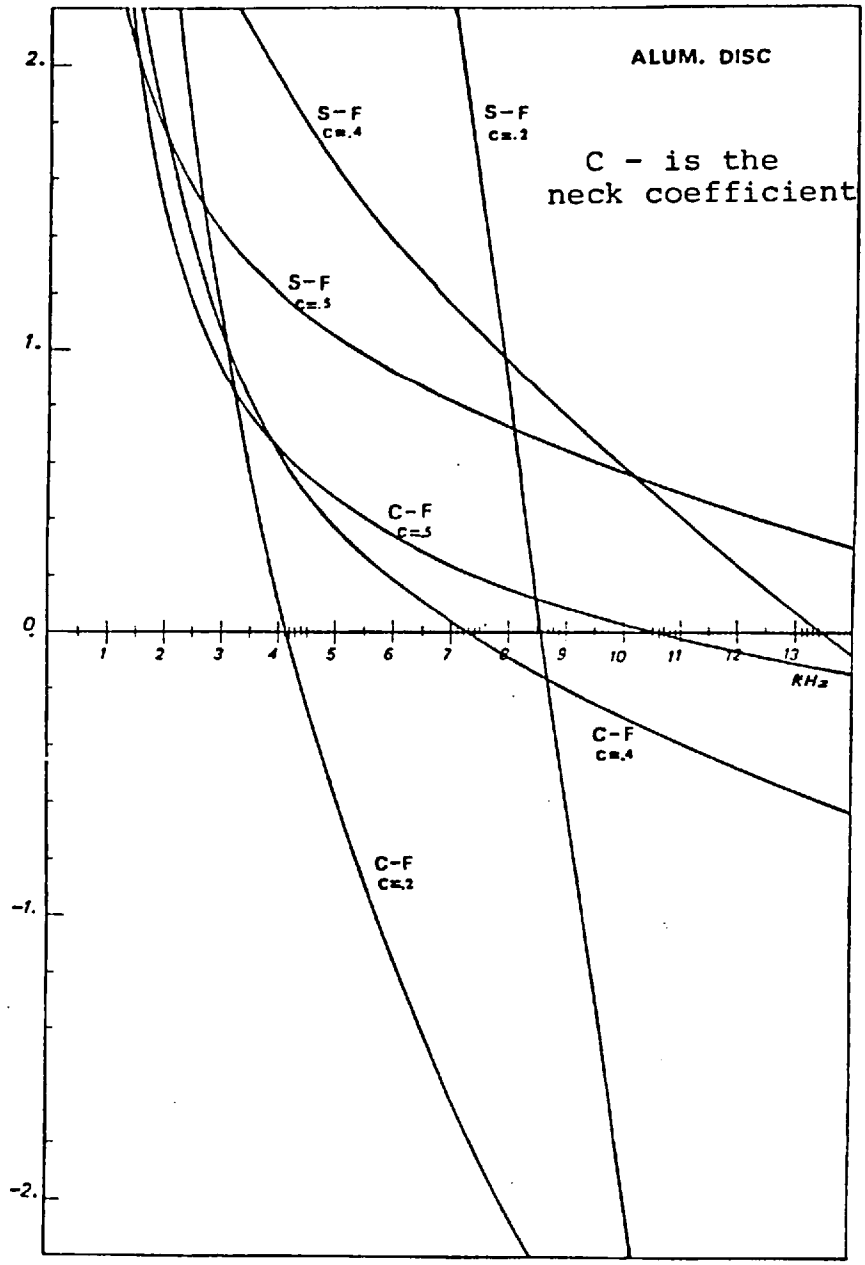

FIG. 7.7 Determinant curves for clamped-free (C-F) and sliding-free (S-F) boundary conditions - aluminium disc annulus.

7.2.4 Disc Mobility Analysis

Not all the applied force produced by the exciter is used to vibrate the disc annulus. Part of it is applied to the ceramic itself. The other part is applied to the base and "neck". Fig. 7.8 shows a schematic diagram of the bearing unit. In this figure F_t represents the total force generated by the ceramic. The symbols F_c, F_b and F_d are used for the components of this force for the parallel arrangement shown. F_c is the force applied to the crystal which we assume to behave as a spring. The base and neck behave mainly as a mass, and the force acting on them is F_b. The force component considered as applied to the disc is F_d, so that:

$$F_t = \Sigma F_i = F_c + F_b + F_d \qquad (7.27)$$

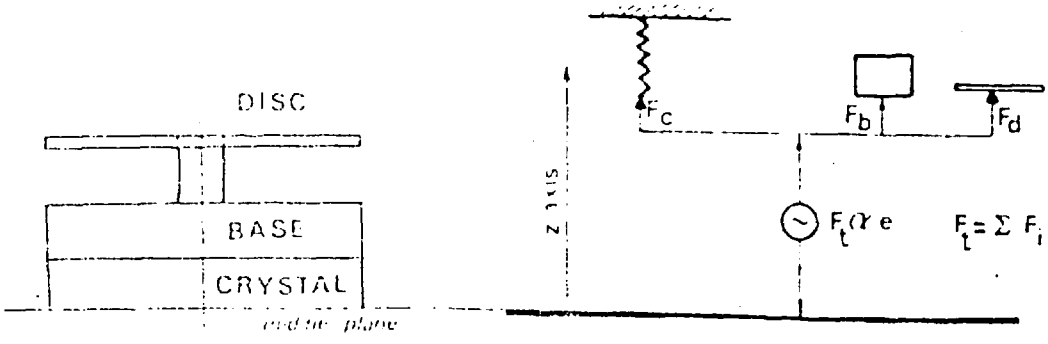

Fig. 7.8 - Schematic diagram of the bearing u

F_t - Total force
e_o - voltage applied to the ceramic
F_b - force applied to the base
F_d - force applied to the disc
F_c - force applied to the ceramic

The receptance (displacement caused by one unit of applied force) has, for each of these elements, the following expressions:

i) <u>for a spring</u> with stiffness k_c (piezoelectric ceramic)

$$\alpha_c = \frac{1}{k_c} \tag{7.28}$$

ii) <u>for a mass</u> m_b (base and neck)

$$\alpha_b = -\frac{1}{\omega^2 m_b} \tag{7.29}$$

ω being the angular frequency of the motion

iii) <u>for an annular disc</u> the receptance expression is shown in 7.2.3. In our case we are interested in calculating the displacements at the inner boundary. The receptance, according to 7.2.3, should be designated by α_{bb}. For simplicity we will use α_d instead, the subscript d referring to disc.

For the model represented in Fig. 7.8, because it is a parallel arrangement, the total force F_t and the forces applied to each element are related by the expression (7.27).

The total displacement, w, is the same for all elements so,

$$F_d = \frac{w}{\alpha_d} ,$$

$$F_c = \frac{w}{\alpha_c} \tag{7.30}$$

$$F_b = \frac{w}{\alpha_b}$$

Because,

$$F = \Sigma F_i = \left(\frac{1}{\alpha_b} + \frac{1}{\alpha_c} + \frac{1}{\alpha_d}\right) w \tag{7.31}$$

or,

$$F = \frac{w}{\alpha_{tot}} \tag{7.32}$$

where

$$\alpha_{tot} = \frac{1}{\frac{1}{\alpha_b} + \frac{1}{\alpha_c} + \frac{1}{\alpha_d}} \tag{7.33}$$

The receptance expression relating the total force applied to the body and displacement of the point P (as indicated in Figs. 7.9, 7.10 and 7.11) can be written as:

$$\alpha_{tot} = \frac{1}{k_c - \omega^2 m_b + \frac{1}{\alpha_d}} \tag{7.34}$$

This expression and the fact that the displacement and velocity are related to each other, enable us to work with a more usual variable of dynamic analysis: the mobility. The mobility of a point of a body is defined as the ratio between the velocity of this point and the force applied to the body.

The modulus of mobility for a point at the radius

r_b is, then:

$$\left|M_{tot}\right| = \left| \frac{\omega}{k_c - \omega^2 m_b + \frac{1}{\alpha_d}} \right| \qquad (7.35)$$

Using the expression (7.35) it is possible to observe where the maximum velocity response of the system occurs.

The value of mass m_b will be affected by the material used for the base due to variation of density.

The disc material also affects the value of α_d due to variation of $\bar{D}$ (flexural rigidity).

The value of k_c depends mainly on the ceramic type and dimensions. For a more complete study of the influence of the material properties, besides the two cases of disc and base in steel and disc and base in aluminium, two other possibilities for the mobility calculations are also considered. One is the base (and neck) in aluminium (dural) and the annular disc in steel; the other is the base (and neck) in steel and the disc in aluminium. The four possibilities of combination, can be summarized as follows:

CASE A { BASE: STEEL
DISC: STEEL

CASE B { BASE: ALUMINIUM
DISC: ALUMINIUM

CASE C { BASE: STEEL
DISC: ALUMINIUM

CASE D { BASE: ALUMINIUM
DISC: STEEL

Using the expression (7.25) for the disc receptance it is assumed that a sliding condition at the inner edge is the hypothesis more likely to interpret the actual condition at this boundary. The mobility curves for these four s are plotted in Figs. 7.9, 7.10 and 7.11. In these calculations the ceramic stiffness is taken as being $k_c = 7.73 \times 10^7 N/m$, from experiments (see section 5.3.3). The mass of the base, in expression (7.36) also includes the mass of the neck and it varies of course, with the material and the value of coefficient. The mobility is expressed in these graphs in d_b with reference to 1 dyne x cm x s^{-1}. At the resonant frequency, the mobility reaches a maximum and it is possible from these curves to determine the resonance of the unit.

The all aluminium unit (case B) has a higher resonant frequency than the steel one (case A), decreasing slightly (from 5.2 KHz to 4.85 kHz) with the increase of the coefficient (coef.) value.

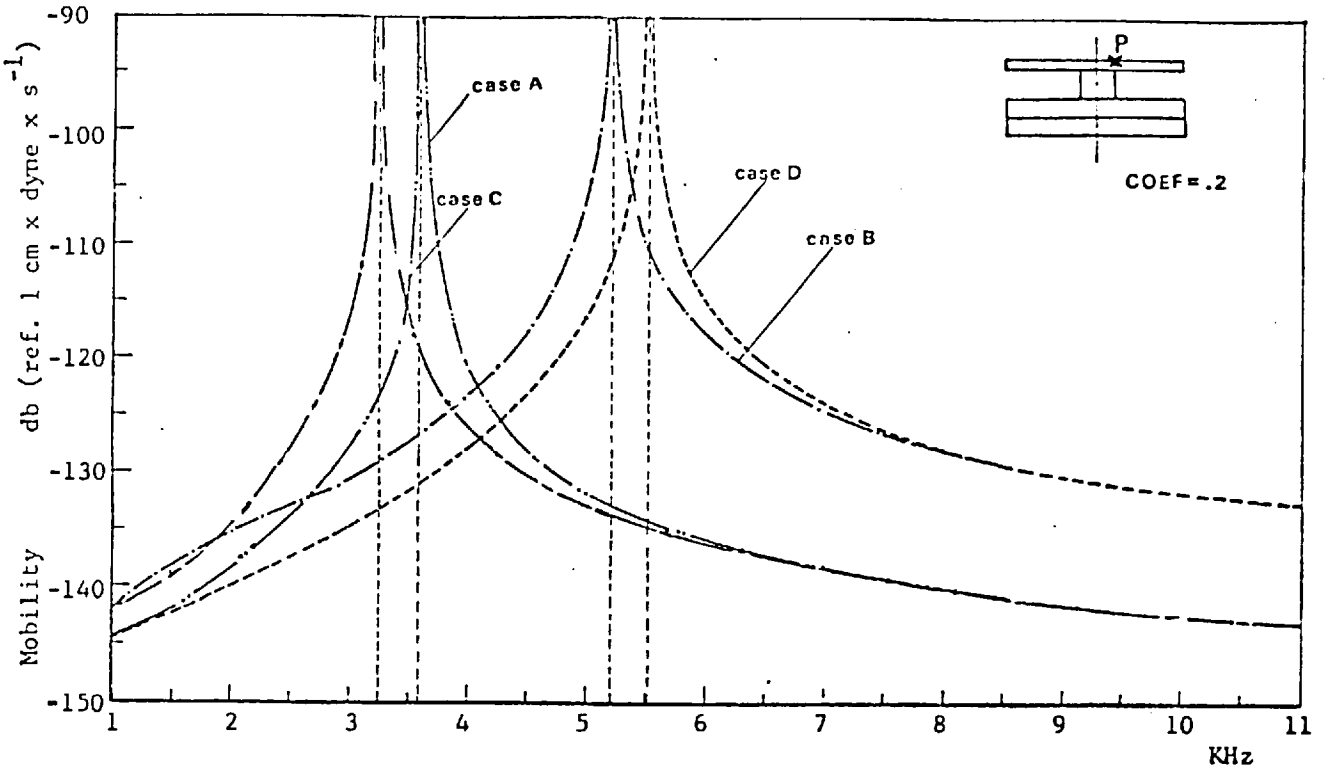

FIG. 7.9 Mobility at point P for coeff. = .2.

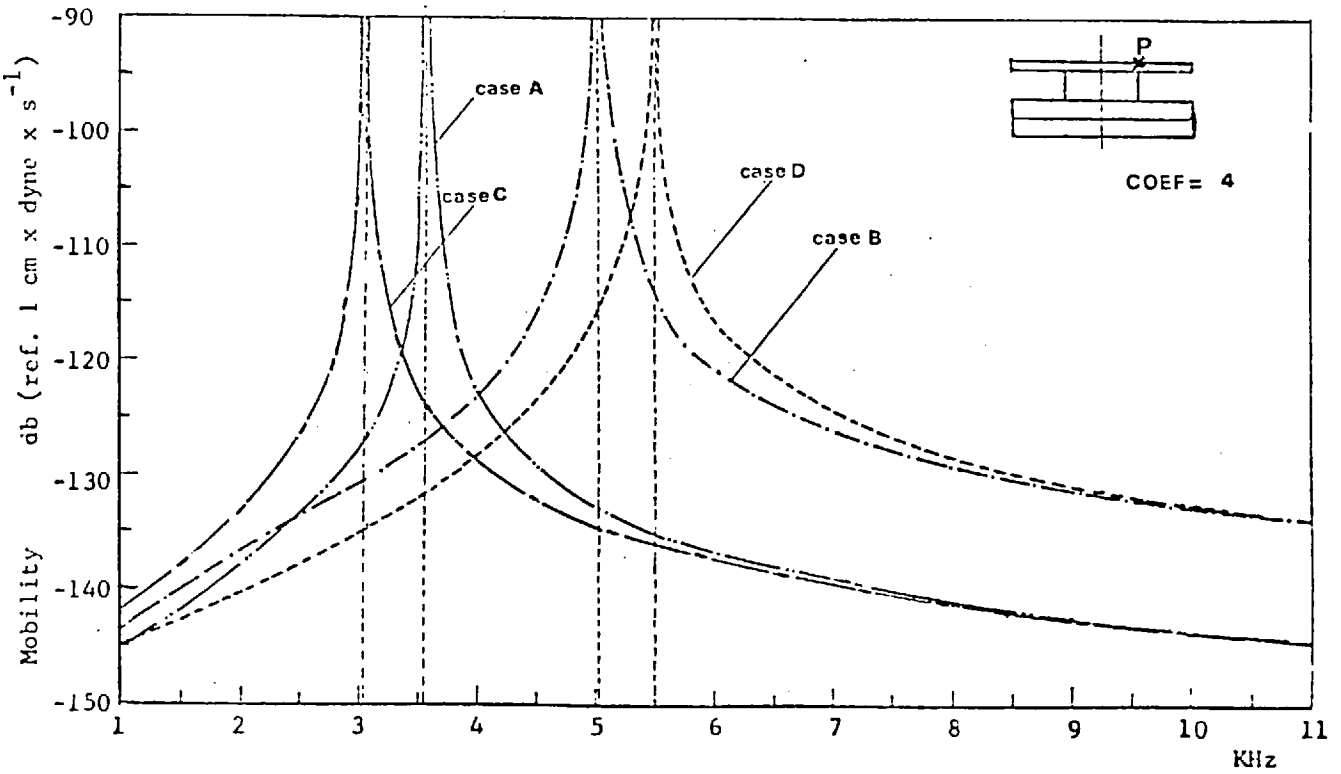

FIG. 7.10 Mobility at point P for coeff. = .4.

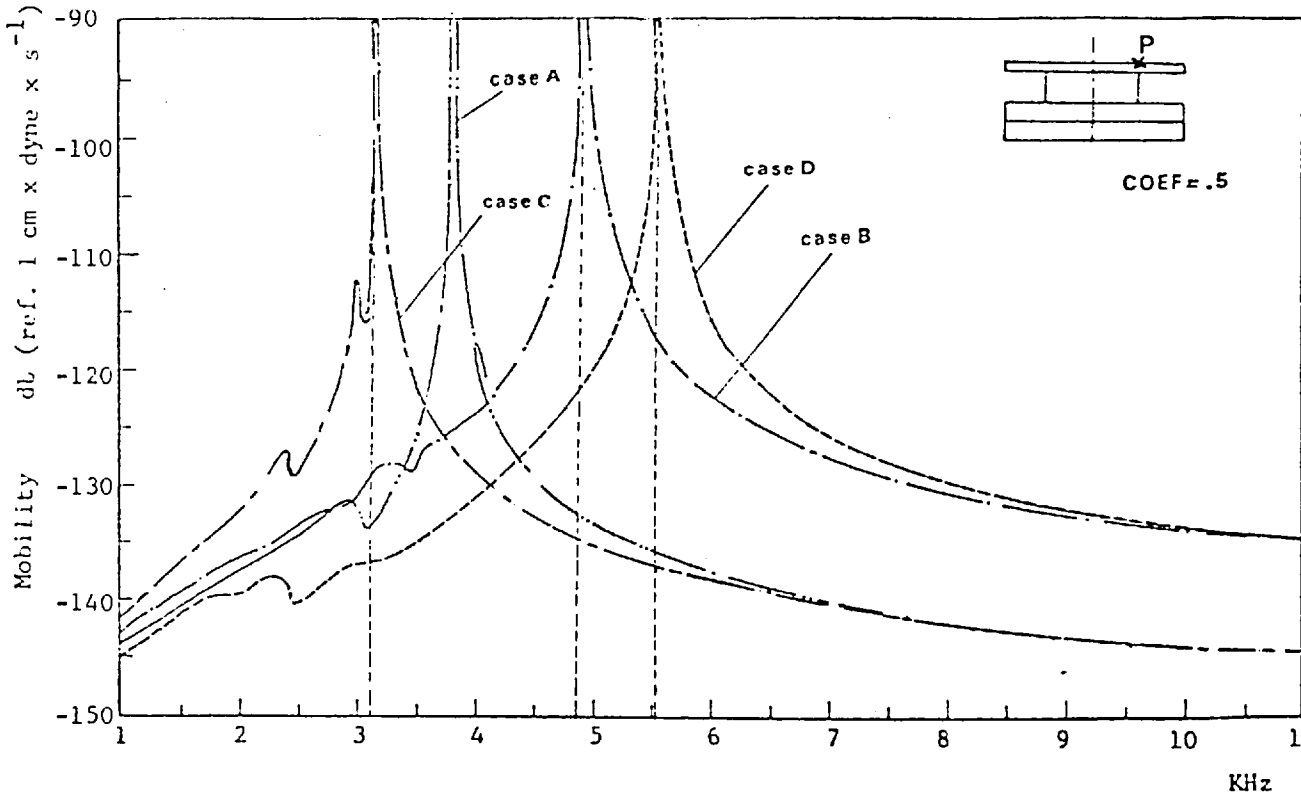

FIG. 7.11 Mobility at point P for coeff. = .5.

The lowest frequency is verified for case C, the aluminium disc with steel base. The highest frequency is verified for case D, steel disc with aluminium base.

From these graphs it is also evident that:

- The use of a steel base (cases A and C) brings the frequency down, compared with the aluminium one (cases B and D).

- The influence of the material of the disc is not so significant, and for the same base, the differences (cases A and C and cases B and D respectively) are of the order of 300 Hz to 600 Hz. The greatest difference is verified for the large value of the coefficient (.5).

- When the coefficient value increases the resonance frequency becomes lower for cases of aluminium base. For the cases of a steel base the behaviour is somewhat unexpected with the lowest value for coef =.4. Both. coef =.2 and coef =.5, present slightly higher values than coef .4 for the resonance frequency.

- The cases C and D, when <u>different materials are used for the base (and neck) and the annular disc</u>, are purely ideal in the sense that it is assumed that the contact between the two materials is a perfect bonding. This type of

contact is very difficult to obtain in pratical models and the interface effect must be taken into account.

- It is also interesting to notice that, as predicted in section 7.2.2.2, the aluminium disc (that has by itself a lower resonance than the steel disc) also lowers the frequency of the whole unit (disc plus base and neck).

In section 7.2.2 it is shown how the neck coefficient (ratio between inner and outer radius of the annular disc) affects definetely the frequency of resonance. For the unit comprising now the ceramic, base and neck this parameter still affects this variable, but the material of the base and the characteristics of the ceramic also influence the resonance of the unit. Therefore, according to each coefficient, one should use the material that provides the best compatibility of the two resonances, that of the disc and the total unit frequency.

In order to compare these results with the actual performance of the bearing some experiments described in the next sections were carried out. In these experiments only one piece units are used, and so, only cases A and Б will be considered.

7.3 EXPERIMENTS WITH FLAT CIRCULAR DISCS

7.3.1 AMPLITUDE MEASUREMENTS

In a similar way to that described in Chapter 6 for conical shells, measurement for disc motion amplitudes was performed. The Fotonic Sensor was used for these measurements with the probe placed normal to the disc surface as shown in Fig. 7.12.

(a) Steel discs

The first experiments were conducted using discs in mild steel, represented in Fig. 7.3 The values of coefficient choosen are .2, .4 and .5*.

For coefficient .2 two values of voltage were applied to the piezoelectric ceramic, 90 volts and 120 volts.

The probe positions are identified in the next figures by the letters *A* to *H* with *0* for the disc center.

For coefficients .4 and .5, two radial directions were considered, Figs. 7.13 and 7.14. Reading in these two directions were taken to confirm the axisymetry of the vibration amplitudes.

In every case bearing unit was driven (oscillated) in the range of frequencies 0 to 20 KHz. The resonant frequency was determined when the maximum amplitude occured for all the points along the discs.

---

* These particular values were choosen arbitrary.

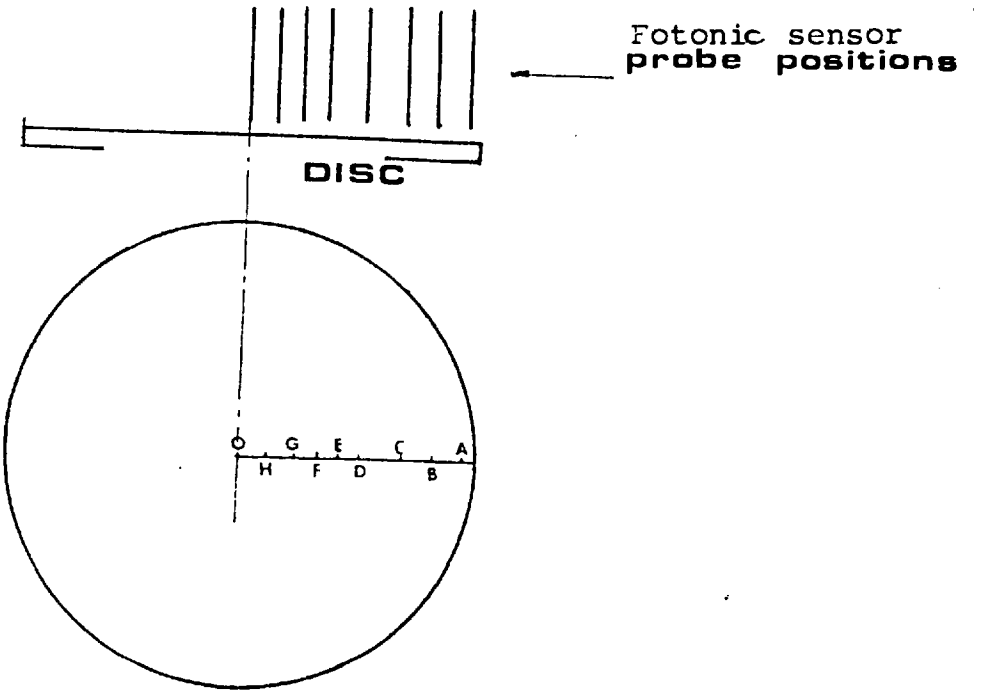

Fig. 7.12 - Probe positions for steel disc with coefficient

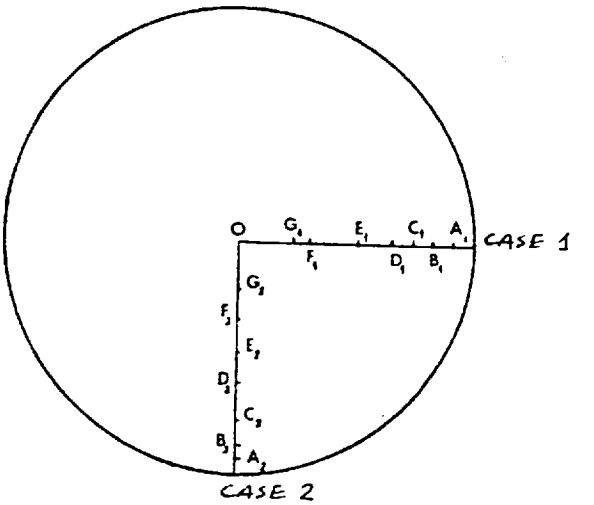

Fig. 7.13 - Probe positions for steel disc with coefficient

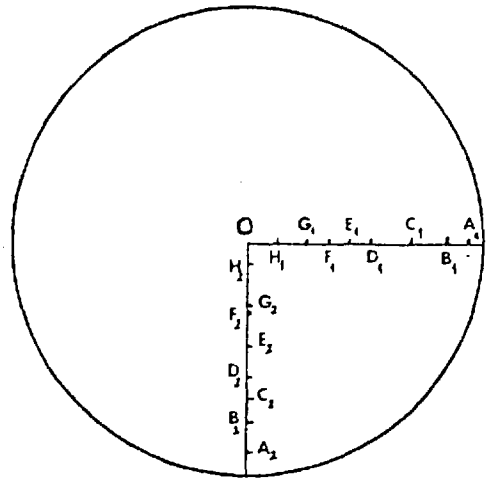

Fig. 7.14 - Probe positions for steel disc with coefficient .5

For coefficient .2 the resonance was verified at 4002 Hz. For coefficient .4 this value was 6176 Hz and for coefficient .5, 8567 Hz. The amplitude measurements are displayed in tables 7.2, 7.3 and 7.4.

Voltage	Freq. c.p.s	PROBE POSITION								
		A	B	C	D	E	F	G	H	O
		MOTION AMPLITUDE ($\times 10^{-4}$ mm)								
90 volts	3982	8.3	5.1	4.1	2.2	1.1	0.6	0.5	1.0	1.1
	3987	10.8	6.5	5.1	2.5	1.4	0.8	0.7	1.4	1.7
	3992	16.7	7.6	7.6	4.3	1.9	1.1	1.0	2.0	2.7
	3997	28.0	15.3	15.3	9.6	3.2	2.2	2.2	4.3	6.6
	4002	68.7	44.6	38.2	15.3	9.6	5.1	5.1	8.3	8.3
	4007	25.5	16.6	15.3	5.1	3.8	2.0	2.3	3.3	4.0
	4012	14.0	7.6	7.6	3.2	2.3	1.2	1.0	2.0	2.1
	4017	8.9	5.1	5.1	2.2	1.2	0.5	0.8	1.4	1.7
120 volts	3950	3.8	3.4	2.2	1.5	0.9	-	0.3	0.3	0.4
	3960	4.4	4.5	2.7	2.0	1.1	-	0.4	0.4	0.5
	3970	6.4	6.1	3.7	2.5	1.3	-	0.5	0.5	0.6
	3975	7.0	7.1	4.5	2.8	1.5	0.3	0.6	0.6	0.8
	3980	8.3	8.5	5.2	3.4	1.6	0.3	0.7	0.7	0.9
	3982	10.2	7.6	7.6	3.6	1.5	0.7	0.7	0.7	1.5
	3987	12.7	10.2	9.5	4.7	1.8	1.0	0.9	0.9	2.2
	3992	20.4	14.0	14.0	7.6	3.0	1.5	1.7	1.7	3.6
	3997	43.3	29.3	28.0	5.3	5.2	2.8	3.9	3.9	6.5
	4002	89.1	72.5	66.2	30.5	1.1	5.6	7.0	7.0	12.7
	4007	29.3	25.5	22.9	10.2	4.4	2.8	2.3	2.3	5.6
	4012	17.8	14.0	12.7	4.4	2.3	1.5	1.3	1.3	3.2
	4017	11.5	10.2	8.9	2.5	1.4	1.0	1.0	1.0	2,0
Distance from centre (mm)		28.4	25.0	21.0	15.4	12.8	10.3	7.7	3.9	0.0

TABLE 7.2 Amplitude Measurements for Steel Disc Bearing (coeff. = .2).

If he had made the exper 6181 + core 1.
theory + exper would have coincided!

	Voltage	Freq. c.p.s.	PROBE POSITION							
			A_1	B_1	C_1	D_1	E_1	F_1	G_1	$\underline{O}$
			MOTION AMPLITUDE ($\times 10^{-4}$ mm)							
CASE 1	90 volts	6166	57.3	57.3	31.8	28.0	12.7	0.9	0.6	0.6
		6171	108.1	133.6	95.5	76.4	38.2	2.3	1.3	1.2
		6176	190.1	178.2	120.9	101.8	40.7	1.5	0.6	0.4
		6181	101.8	101.8	63.6	50.9	20.4	1.5	0.3	0.3
		6186	68.7	63.6	40.7	31.8	12.7	0.5	0.4	0.8
		6191	43.3	45.8	25.5	17.8	7.6	1.1	1.0	0.8
	Distance from centre (mm)		27.5	25.0	22.0	20.0	15.0	9.0	7.0	0.0

	Voltage	Freq. cps	PROBE POSITION							
			A_2	B_2	C_2	D_2	E_2	F_1	G_2	$\underline{O}$
			MOTION AMPLITUDE ($\times 10^{-4}$ mm)							
CASE 2	90 volts	6166	95.5	63.6	63.6	30.5	15.3	2.8	0.6	0.6
		6171	280.0	114.5	299.1	78.9	30.6	8.9	1.4	1.4
		6176	254.6	203.6	152.7	82.7	33.1	5.1	0.6	0.8
		6181	152.7	127.3	101.8	40.7	16.5	2.5	0.4	0.4
		6186	103.1	89.1	70.0	38.2	15.3	1.5	0.8	0.6
		6191	63.6	52.2	35.6	17.8	8.3	1.8	1.1	0.8
		6196	31.8	24.2	19.1	14.0	4.1	1.1	0.6	0.5
	Distance from centre (mm)		28.0	26.0	23.0	18.0	14.0	10.0	6.0	0.0

TABLE 7.3 Amplitude Measurements for Steel Disc Bearing (coeff.=.4).

	Voltage	Freq. c.p.s.	PROBE POSITION - (RADIUS 1)								
			A_1	B_1	C_1	D_1	E_1	F_1	G_1	H_1	O
			MOTION AMPLITUDE (mm x 10^{-4})								
CASE 1	90 volts	8552	10.8	9.2	5.3	-	0.4	0.6	0.7	0.9	1.0
		8557	14.0	12.7	7.1	0.5	0.5	0.9	1.0	1.1	1.5
		8562	25.5	20.4	12.7	0.8	0.9	1.5	1.9	2.0	2.7
		8567	70.0	57.3	33.1	1.7	2.4	3.6	4.5	4.8	5.9
		8572	31.8	-	19.1	0.9	1.4	2.2	2.2	2.4	3.2
		8577	20.3	17.8	8.9	0.5	0.8	1.3	1.1	1.7	1.9
	Distance from centre (mm)		28.4	25.0	21.0	15.4	12.8	10.3	7.7	3.9	0.0

	Voltage	Freq. c.p.s.	PROBE POSITION - (RADIUS 2)								
			A_2	B_2	C_2	D_2	E_2	F_2	G_2	H_2	O
			MOTION AMPLITUDE (mm x 10^{-4})								
CASE 2	90 volts	8552	7.6	5.7	5.3	-	1.5	0.8	-	0.9	0.9
		8557	10.2	7.6	7.1	0.7	0.9	1.1	-	1.4	1.3
		8562	19.1	14.0	12.7	1.1	1.4	2.3	-	2.2	2.3
		8567	57.3	38.2	33.1	2.9	3.8	5.7	-	5.7	5.1
		8572	34.4	20.4	19.1	1.5	2.2	3.0	-	3.1	3.1
		8577	17.8	11.5	8.9	0.8	1.3	1.8	-	1.8	1.8
	Distance from centre (mm)		27.0	23.0	20.0	17.0	13.0	9.0	8.0	2.5	0.0

TABLE 7.4 Amplitude Measurements for Steel Disc Bearing (coeff. = .5).

To compare the different modal shapes the amplitudes for each resonnance are plotted in graphs, Fig. 7.15, Fig. 7.16 and Fig. 7.17. In every case the amplitudes at the free edge are higher than at the center of the plate (about 10 times) with a node near the connection neck-annular plate. The increase in voltage caused an increase in amplitudes too, but the reduced number of voltages didn't provide the establishement of any precise relationship between the voltage applied and these displacements. It is possible, nevertheless, to say that their law of variation is almost linear in the range studied.

almost as .6 slope ~ 0 at edge of disc!

Theor. res freqn was 7500 which would have given a much higher angle

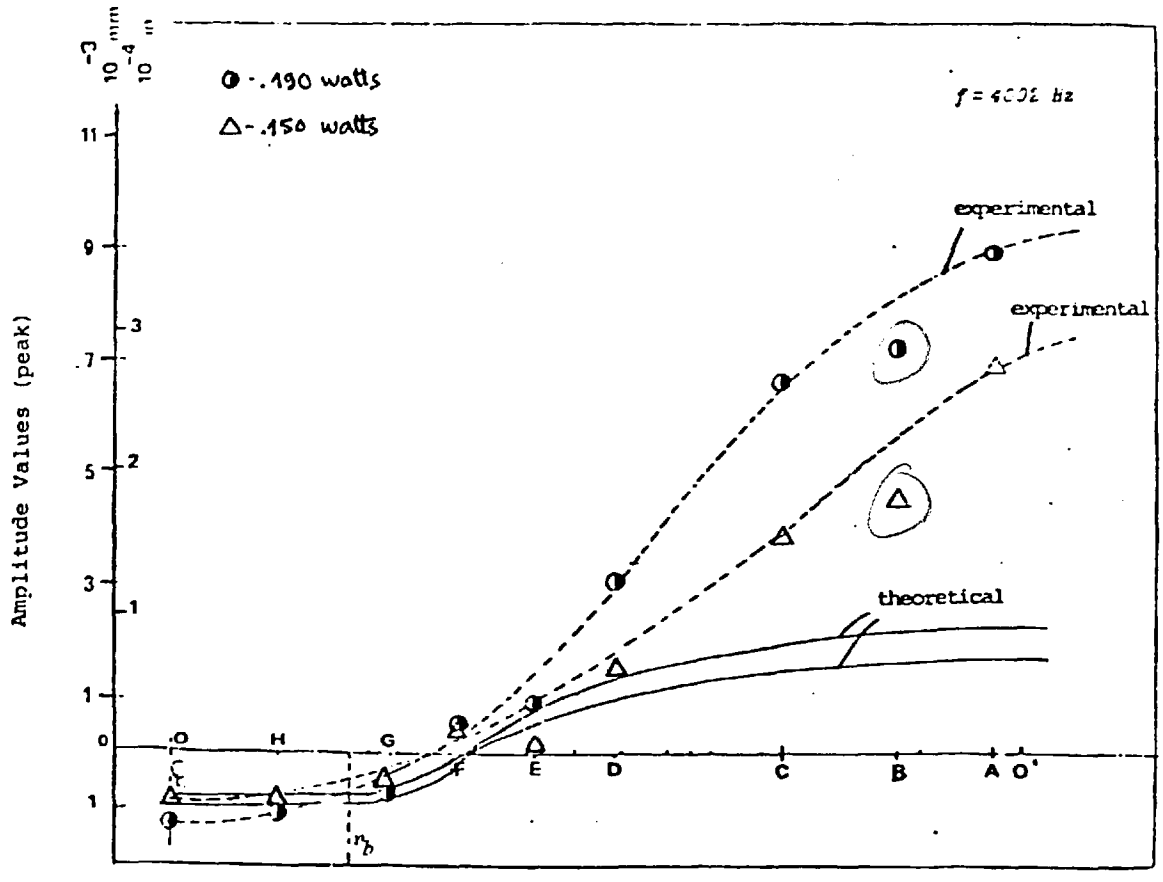

Fig. 7.15 - Experimental and Theoretical Mode Shapes for Steel Disc Bearing (coeff. .2)

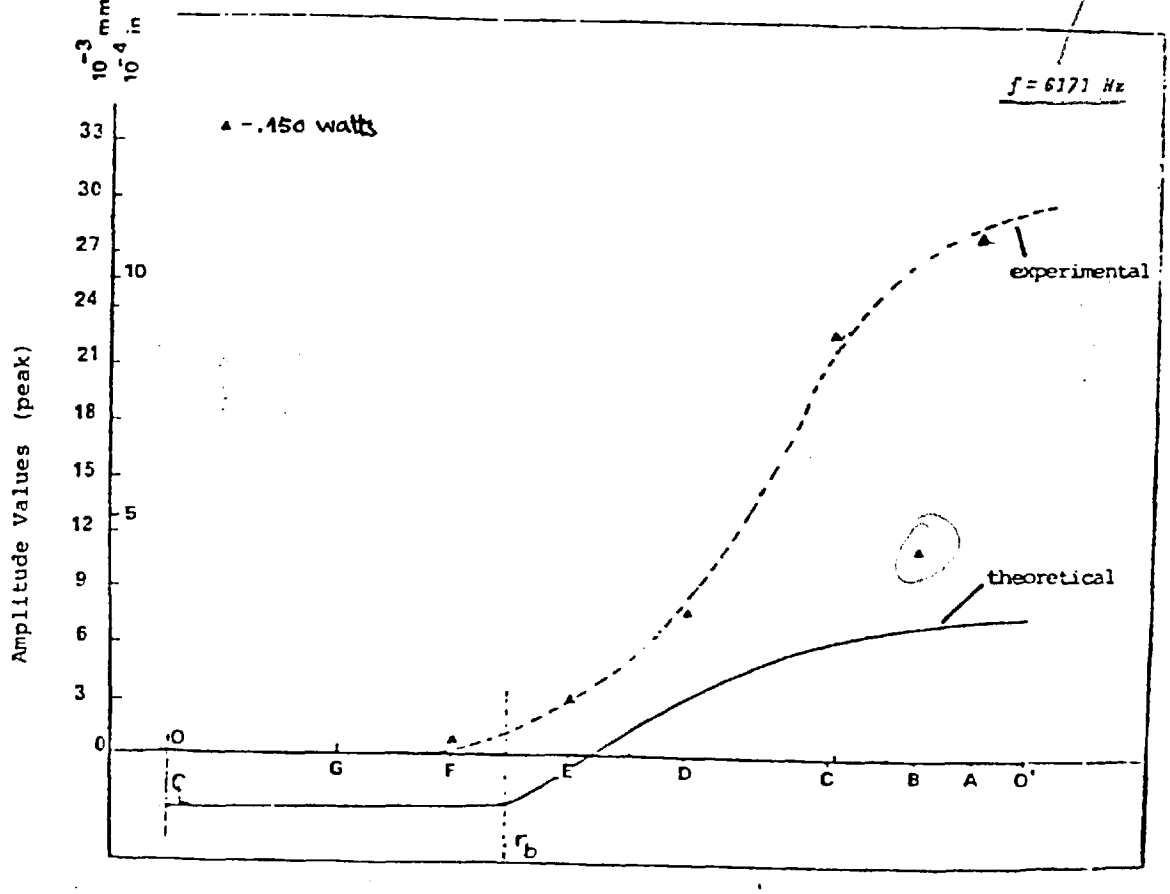

Fig. 7.16 - Experimental and Theoretical Mode Shapes for Steel Disc Bearing (coeff. .4) - case 2

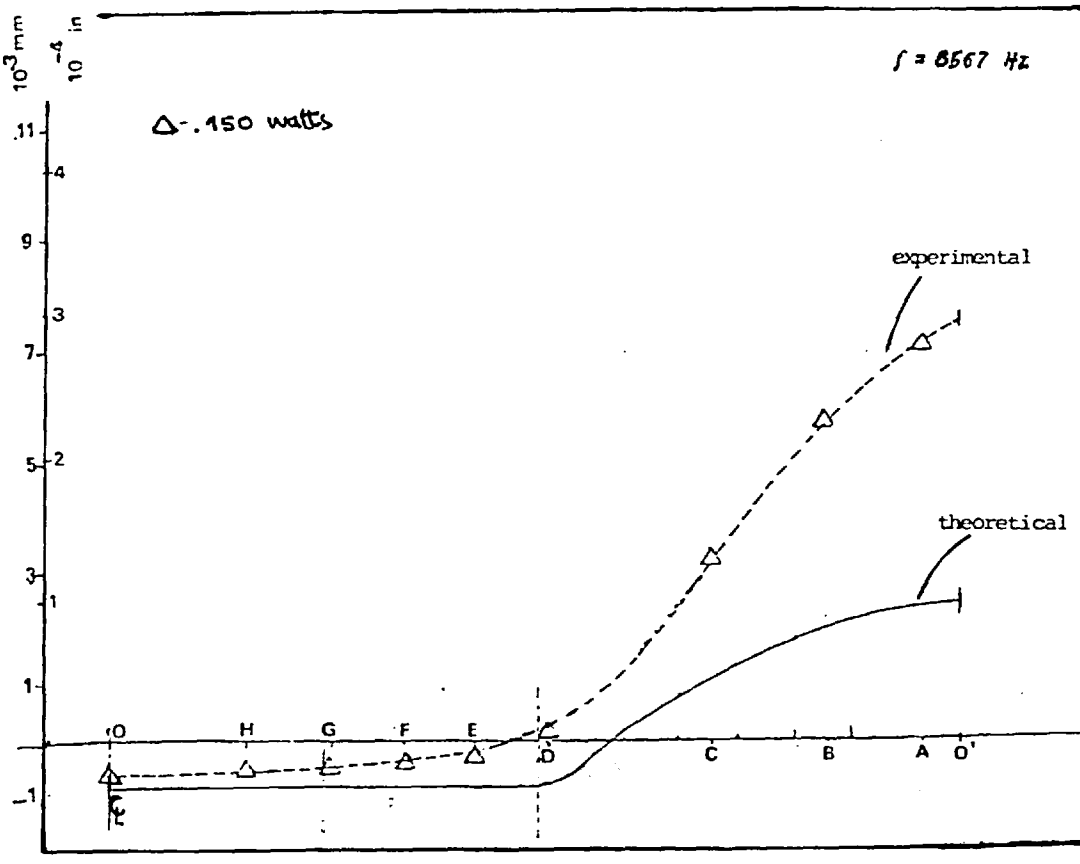

Amplitude Values

Fig. 7.17 - Experimental and theoretical Mode Shapes for Steel Disc Bearing (coeff. .5)

b) Aluminium Discs

For the aluminium discs the geometry was maintained, with the same neck coefficients: .2, .4 and .5. So, only the material was different. The squeeze film bearing arrangement was also identical to that used with steel discs.

Because for this material the resonnance curves were much smother, it was possible to take a greater number of frequency readings within the capabilities of the equipment. The use of a digital oscillator also enabled to set the frequency more accurately. The amplitudes obtained for the several frequencies and coefficients are shown in Tables 7.5, 7.6 and 7.7. The respective probe stations are also presented, in Fig. 7.18, Fig. 7.19 and Fig. 7.20.

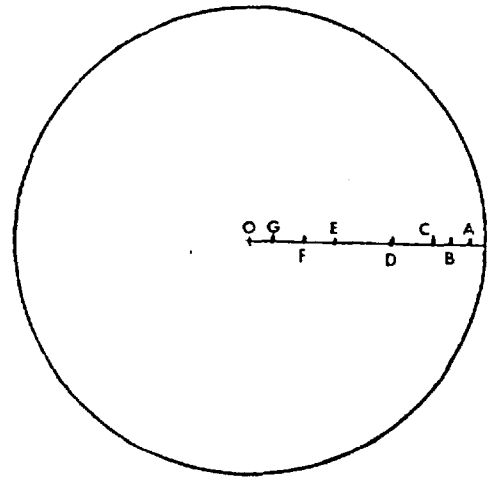

Fig. 7.18 - Probe positions for aluminium disc with coefficient .2

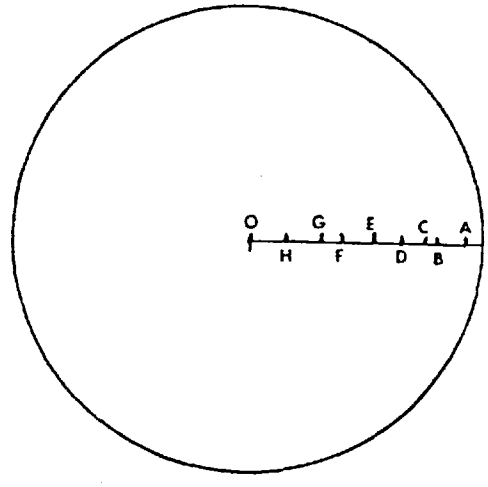

Fig. 7.19 - Probe positions for aluminium disc with coefficient .4

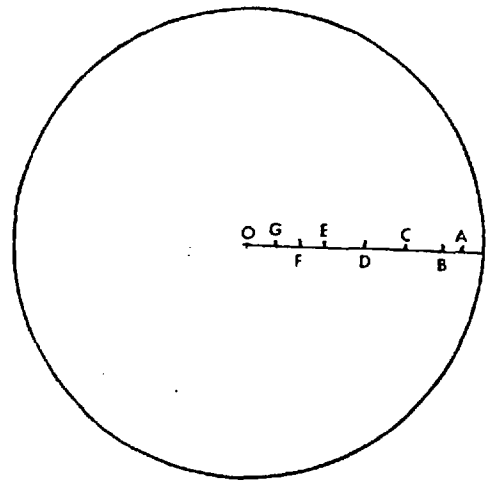

Fig. 7.20 - Probe positions for aluminium disc with coefficient .5

Voltage	Freq. c.p.s.	PROBE POSITION							
		A	B	C	D	E	F	G	O
		MOTION AMPLITUDE ($\times 10^{-4}$ mm)							
70 volts	4111	12.8	10.5	11.5	6.4	1.3	0.8	1.3	1.3
	4119	25.5	23.0	20.4	14.0	2.8	1.8	2.9	2.6
	4120	29.3	25.5	25.5	15.3	3.2	2.2	3.8	3.3
	4121	35.7	28.0	30.6	19.1	3.8	2.3	3.8	3.8
	4122	52.6	33.2	38.3	21.7	4.5	2.6	4.6	4.1
	4123	44.6	42.1	44.6	25.5	4.5	3.2	5.1	4.5
	4124	48.5	44.6	49.7	26.8	5.1	3.4	5.4	5.1
	4125	53.7	43.4	44.6	25.5	5.0	3.3	5.1	4.6
	4131	25.5	21.7	23.0	12.8	2.6	2.0	2.8	2.3
	4141	11.5	9.6	10.2	6.0	1.0	1.0	1.3	1.2
	4146	8.9	7.3	8.3	4.5	0.8	0.8	1.3	0.9
	4151	7.7	6.3	7.7	3.8	0.6	0.7	1.0	0.8
	4156	-	5.1	5.6	3.1	0.6	0.6	0.8	0.7
	4161	5.1	4.5	5.1	2.7	0.5	0.5	0.8	0.6
	4166	-	3.8	4.5	2.3	0.3	0.5	0.6	0.6
	4171	4.5	3.6	4.3	2.0	0.3	0.4	0.6	0.5
	4176	-	3.3	3.8	1.9	0.3	0.4	0.5	0.5
	4181	3.8	2.8	3.6	1.8	0.3	0.4	0.5	0.5
	4186	-	2.6	3.2	1.5	0.3	0.4	0.5	0.5
	4191	3.2	2.4	3.1	1.4	-	0.4	0.5	0.4
	4196	2.8	2.3	2.6	1.3	-	0.3	0.4	-
Distance from centre (mm)		28.5	26.0	24.0	18.0	11.0	7.0	3.0	0.0

TABLE 7.5 Amplitude Measurements for Aluminium Disc Bearing (coeff. = .2).

Voltage	Freq. c.p.s.	PROBE POSITION								
		A	B	C	D	E	F	G	H	O
		MOTION AMPLITUDE ($\times 10^{-4}$ mm)								
70 volts	6231	51.0	47.2	47.2	35.7	17.9	7.0	1.4	0.6	0.9
	6236	186.0	127.5	114.8	66.3	-	19.1	2.4	1.4	9.5
	6239	306.0	293.3	229.6	178.5	53.6	15.3	1.8	1.9	5.1
	6240	306.0	242.3	255.1	114.8	57.4	9.5	1.5	1.6	5.8
	6241	293.3	178.3	153.0	82.9	38.3	8.9	1.3	-	1.7
	6242	165.8	146.7	102.0	76.5	33.2	8.9	1.0	1.4	-
	6243	127.5	114.8	82.9	57.4	25.5	7.7	0.9	1.3	1.4
	6244	114.8	99.5	76.5	51.0	24.2	6.4	0.6	1.2	1.3
	6245	89.3	82.9	70.2	38.3	23.0	5.7	0.5	1.1	1.2
	6246	95.6	76.5	58.7	31.9	19.1	5.1	0.4	1.0	1.1
	6251	53.6	42.1	40.7	28.1	11.5	3.8	0.4	0.8	0.9
	6256	30.0	30.6	29.3	20.4	8.9	2.6	-	0.8	0.8
	6261	28.0	24.2	21.7	17.9	7.5	2.3	-	0.5	0.7
	6266	22.9	19.1	17.8	12.8	6.0	1.8	-	0.5	0.6
	6271	17.8	16.6	14.0	11.5	-	-	-	0.4	0.5
	6276	15.3	14.0	12.8	10.2	4.1	1.3	-	-	0.5
	6281	14.0	12.8	10.8	8.3	3.8	1.0	-	-	0.4
	6286	11.5	10.2	8.3	7.7	3.3	0.9	-	-	0.4
	6291	10.2	9.6	7.0	6.4	2.9	0.8	-	-	-
	6301	8.3	7.7	5.8	4.1	2.4	0.6	-	-	-
Distance from centre (mm)		28.0	24.5	23.0	20.0	16.0	12.0	10.0	5.0	0.0

TABLE 7.6 Amplitude Measurements for Aluminium Disc Bearing (coeff. = .4).

Voltage	Freq. c.p.s.	PROBE POSITION							
		A	B	C	D	E	F	G	O
		MOTION AMPLITUDE ($\times 10^{-4}$ mm)							
70 volts	8700	5.4	5.2	2.3	-	-	0.4	0.4	0.5
	8705	6.5	6.4	2.8	1.0	0.4	0.5	0.5	0.6
	8710	8.3	7.7	3.3	1.3	0.5	0.6	0.6	0.6
	8715	12.1	10.3	5.2	1.1	0.6	0.8	0.8	1.0
	8720	17.9	14.0	7.7	1.3	1.0	1.1	1.3	1.4
	8724	25.5	23.0	10.8	-	1.4	2.0	1.8	2.3
	8725	34.4	25.5	12.1	1.3	1.5	2.3	2.2	2.4
	8726	35.1	29.3	14.0	1.4	1.8	2.4	2.4	2.8
	8727	35.7	30.6	15.3	1.4	2.2	2.8	2.7	2.9
	8728	38.3	33.2	17.9	1.5	2.3	2.9	3.1	3.2
	8730	34.4	30.6	19.1	-	2.3	2.8	2.8	2.9
	8735	23.0	25.5	14.0	1.0	1.5	1.9	1.8	1.8
	8740	15.3	15.3	8.9	1.0	1.0	1.3	1.3	1.3
	8745	11.5	11.5	6.4	0.9	0.8	0.9	1.0	1.0
	8750	8.3	9.6	5.1	-	0.6	0.8	0.8	0.8
	8755	7.7	7.7	4.1	-	0.5	0.6	0.6	0.6
	8760	6.4	6.4	3.3	-	0.5	0.5	0.5	0.5
	8765	5.1	5.5	2.8	-	-	0.5	0.4	0.5
Distance from centre (mm)		27.5	25.0	20.5	15.0	10.0	7.0	4.0	0.0

TABLE 7.7 Amplitude Measurements for Aluminium Disc Bearing (coeff. = .5).

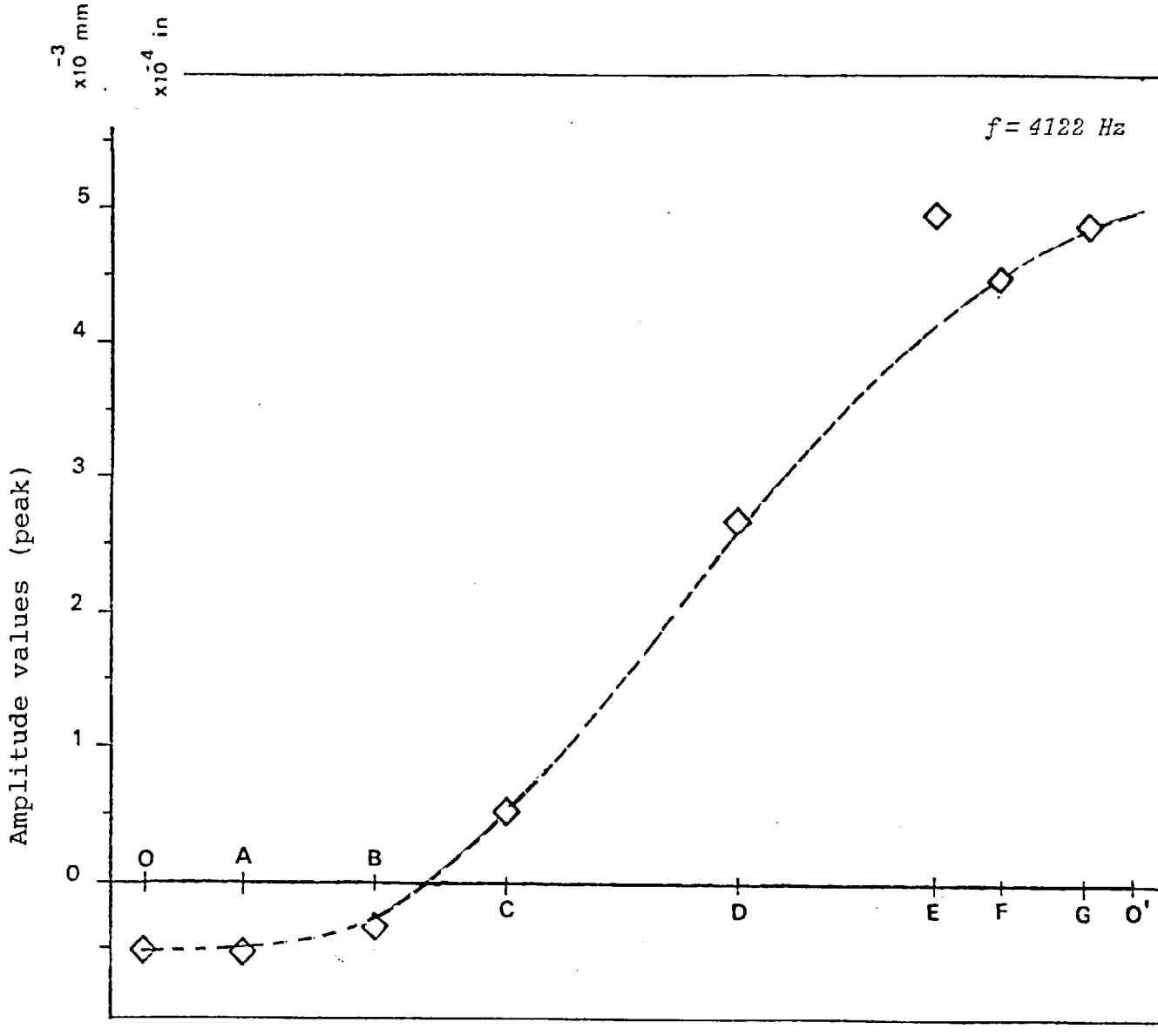

Fig. 7.21 - Experimental Mode Shape for Aluminium Disc Bearing (coeff. .2)

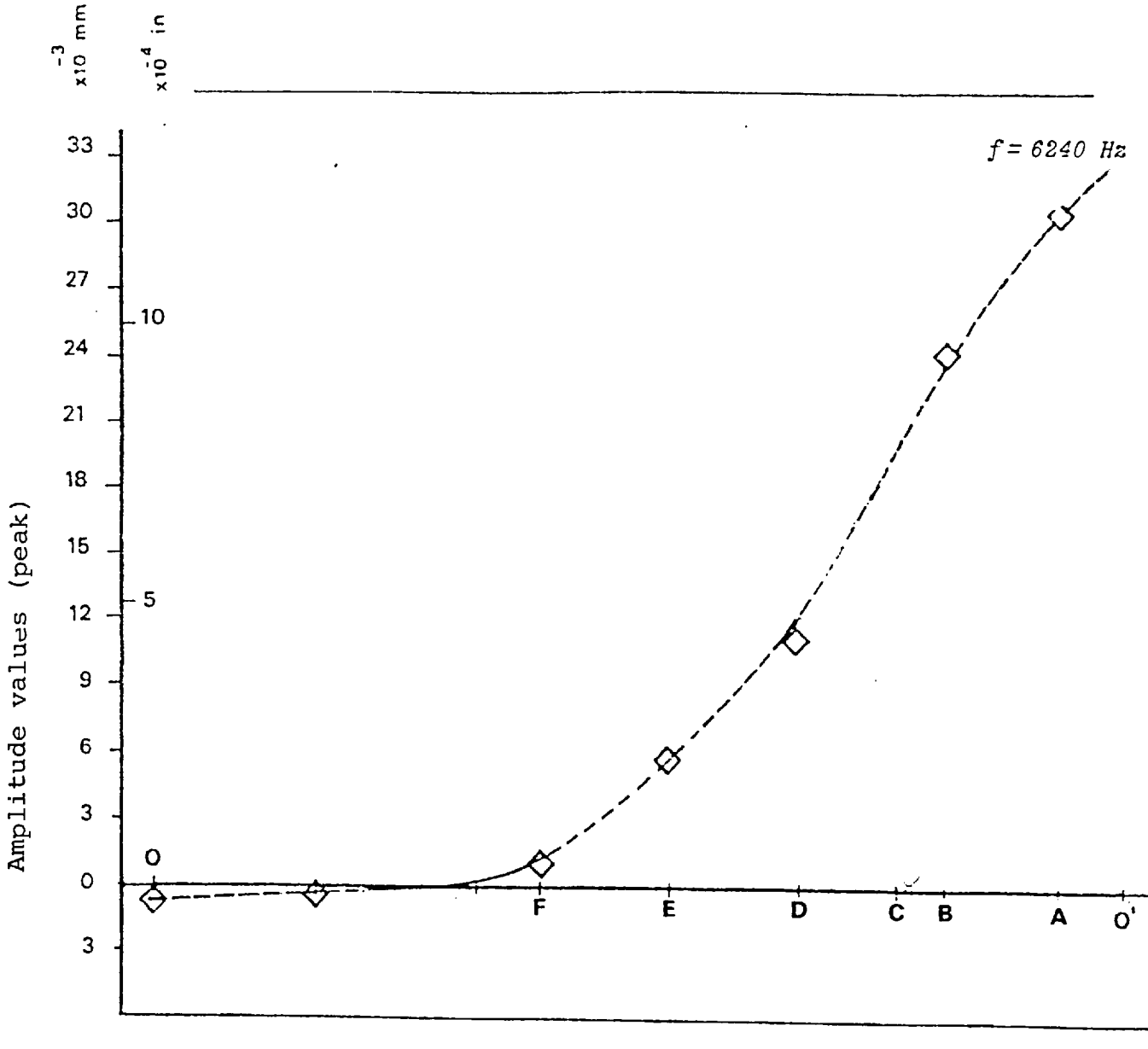

Fif. 7.22 - Experimental Mode Shapes for Aluminium Disc Bearing (coeff. .4)

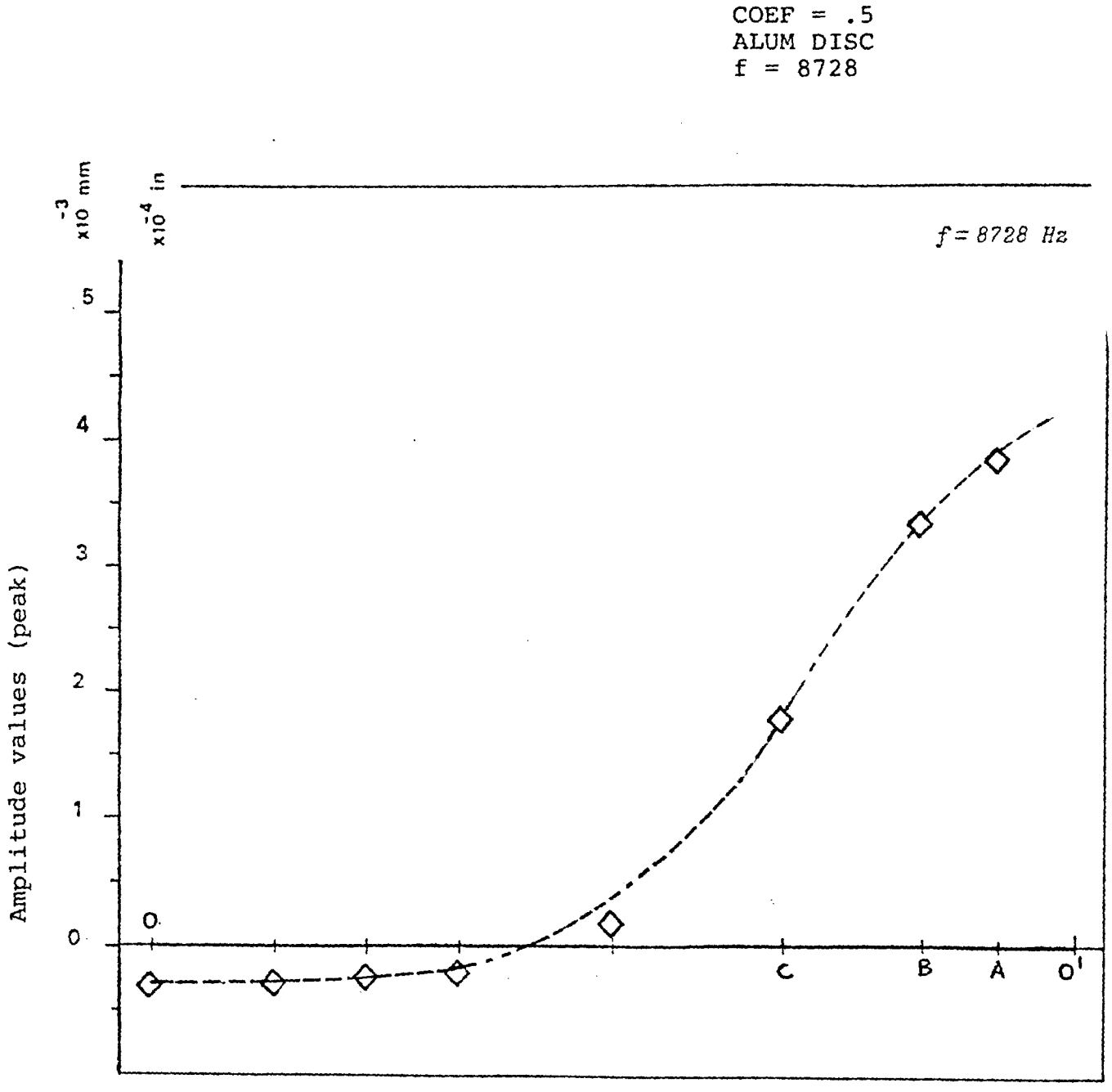

Fig. 7.23 - Experimental Mode Shapes for Aluminium Disc Bearing (coeff. .5)

7.3.2 Loss Factor

The specimen used in experiments come from different batches of material. It was considered that this fact could be correlated with the dynamic behaviour observed. For this reason the loss factor, η, was calculated for each case. The loss factor is defined as

$$\eta = \frac{1}{Q_{mech}} = \frac{W_{static}}{W_{resonance}} \qquad (7.37)$$

where:

Q_{mech} - (already refered in chapter 5) representing the mechanical Q factor of the disc material

W_{static} - represents the static deflection of the system (bearing unit plus ceramic)

$W_{resonance}$ - represents the amplitude of vibration at resonance.

Assuming a symetrical response curve (amplitudes plotted against frequency) it is possible to calculate the loss factor of the material using the half power point bandwith . The procedure is described next :

The energy dissipated by the system during a cycle of motion is ΔE. For an amplitude W_1, so that:

$$W_1 = \frac{W_{resonance}}{\sqrt{2}} , \qquad (7.38)$$

The energy dissipated is related with ΔE by:

$$\Delta E_{W_1} = \frac{1}{2} \Delta E \qquad (7.39)$$

Defining the variable $\bar{\gamma} = \frac{\omega}{\omega_r}$, designating to ω a particular value of frequency and to ω_r the angular frequency at resonance it is possible to establish the following relationship:[50]

$$W = \frac{F}{k'} \quad \frac{1}{\sqrt{(1-\bar{\gamma}^2)^2 + \eta^2}} \qquad (7.40)$$

Where W is the amplitude of vibration of the system, F is the applied force and k' the stiffness of the system. After some manipulation the following expression is obtained (50):

$$\eta = \frac{\omega_2 - \omega_1}{\omega_r} \qquad (7.41)$$

In expression (7.41) ω_1 and ω_2 are frequencies corresponding to amplitudes related to the resonant amplitude by expressions like (7.38).

This last expression gives a method of calculation of the loss factor if the response curve of the system is known.

The main difficulty associated with this procedure

is the determination of the exact value of ω_{res}. Using data from Tables 7.1, 7.2 and 7.3 the response curves for different neck coefficients W could be plotted, and the values of ω_1 and ω_2 were graphically obtained. This permitted the calculation of η. The values of η are represented in Table 7.7.

TABLE 7.7

NECK	POINT	$\eta \times 10^{-3}$
.2	A	1.25
	B	.99
	C	1.24
	D	1.08
.4	A	.89
	B	1.07
	C	.92
	D	1.42
.5	A	.55
	B	.62
	C	.62
	D	-

These values respect, as mentioned, mild steel discs. From Table 7.7 it is possible to conclude on the higher loss coefficient of .2 neck coefficient case, η decreasing with increasing neck coefficient values. Because the higher amplitudes were obtained, as seen in section 7.3, for coefficient .2, this seems to dismiss the hypothesis of the amplitude variation being caused by the material properties of a particular batch. The variation of the loss coefficient must actually be due to a different contact between the disc specimen and the ceramic disc. The fluctuactions, of η for different points, are probably caused by the error on the determination of the correct value of ω_{res} (frequency of resonance).

7.4 COMPARISON OF THEORETICAL AND EXPERIMENTAL MODAL SHAPES FOR DISCS.

The modal shape of the bearing discs is obviously a function of the force applied to these discs. Using the expression (7.25) and assuming, as before, a sliding-free condition for the annulus inner boundary, it is possible to predict these mode shapes. For this calculation it is necessary to know this force.

Because all the bearing elements (annular disc, base and ceramic) are associated in parallel (see Fig. 7.8) the total displacement W_b will be the same for points at radius r_b. The force applied to the disc alone, F_d, can be calculated knowing the disc receptances at these points, from (7.42):

$$F_d = \frac{W_b}{\alpha_d} \qquad (7.45)$$

In this expression α_d is the same variable as α_{bb} (receptance of a point at a radius b, due to a force at the same radius). The notation α_d is used instead of α_{bb}, as explained in 7.2.4. The force F_d varies with frequency, the neck coefficient (because of the influence of α_d), and obviously with the voltage applied to the ceramic. Using the expression (7.45) the table 7.9 was built for several cases of coefficient and voltage. The coefficients choosen, .2, .4 and .5 are the same as considered in experiments referred in 7.3.1 and 7.3.2. The same criterium was used for the voltages. The frequencies considered were those of the resonance (for each coefficient) and also when the lift of the upper member ocurred. If the theoretical resonance frequencies were taken instead, the values of the receptance would be infinite because in the expressions of

displacement, W, for a point at a distance b from the center of the disc is then:

$$W_b = \alpha_{rb} \; F_d \tag{7.42}$$

The force F_d is the force applied at the disc inner boundary. To calculate this force one needs to know the total force F_t, which is related to the voltage across the piezoelectric ceramic by the constant g_{33} (see section 5.1.2.3). The subscripts used in this constant indicate that both the generated force and the applied electrical field have the same direction (the z axis, defined in chapter 5). For a PZT - 4 ceramic, the value of this constant is (Table 5.2):

$$g_{33} = 26.1 \times 10^{-3} \text{ volt meter/Newton}$$

Designating by e_o the voltage applied to the ceramic, t_c the ceramic thickness and A_c the ceramic area normal to the direction of the electrical field, F_t is:

$$F_t = \frac{\frac{e_o}{t_c}}{\frac{g_{33}}{A_c}} \tag{7.43}$$

For the ceramics used in this work the thickness, t_c, and diameter, d_c, are (fig. 6.2)

$$t_c = 6 \times 10^{-3} \text{ m} \qquad \text{and}$$

$$d_c = 38 \times 10^{-3} \text{ m}$$

Substitution of this values in 7.43 results in:

$$F_t = 7.2 \ e_o \qquad (7.44)$$

In (7.44) F_t is expressed in Newtons and e_o is expressed in volts . Table 7.8 shows the values of the force F_t for the voltages used in experiments:

Voltage, e_o (volts)	Force, F_t (N)
60	432
70	505
90	649
120	866

TABLE 7.8

Generated force due to voltage applied to the ceramic

Because all the bearing elements (annular disc, base and ceramic) are associated in parallel (see Fig. 7.8) the total displacement W_b will be the same for points at radius r_t. The force applied to the disc alone, F_d, can be calculated knowing the disc receptances at these points, from (7.42):

$$F_d = \frac{W_b}{\alpha_d} \qquad (7.45)$$

In this expression α_d is the same variable as α_{bb} (receptance of a point at a radius b, due to a force at the same radius). The notation α_d is used instead of α_{bb}, as explained in 7.2.4. The force F_d varies with frequency, the neck coefficient (because of the influence of α_d) and obviously with the voltage applied to the ceramic. Using the expression (7.45) the table 7.9 was built for several cases of coefficient and voltage. The coefficients choosen, .2, .4 and .5 are the same as considered in experiments referred in 7.3.1 and 7.3.2. The same criterium was used for the voltages. The frequencies considered were those of the resonance (for each coefficient) and also when the lift of the upper member ocurred. If the theoretical resonance frequencies were taken instead, the values of the receptance would be infinite because in the expressions of

the receptance the determinant of the natural frequencies appears as a factor in the denominator (see section 7.2.3). As it is zero at resonance the receptance becomes infinite. One advantage of using the experimental values of the frequency is to provide a straight comparison of the predicted mode shapes with those obtained experimentally, i.e., the displacements in both cases respect the same frequencies. With the values of F_d and calculating the receptances for several points along the disc radius (programme FREDIS) the curves of Figs. 7.15, 7.16 and 7.17 are obtained for steel discs. For aluminium discs a completely similar procedure can be used. For this case the theoretical mode shapes are plotted in Figs. 7.21, 7.22 and 7.23.

Coefficient, COEF.	frequency, f (c.p.s)	voltage, e_o (volts)	total receptance, α_t (10^{-8}m/N)	disc receptance, α_d (10^{-8}m/N)	motion amplitude, W_b (10^{-5}m)	Force applied to the disc F_d (N)
.2	3879+	120	1.82	.88	1.57	1784
	4002*	90	35	1.03	.67	774
		120			.89	1.029
.4	6176	90	.39	1.8	.25	138.9
		120			.31	184 7
	6260+	90	.34	3.3	.22	66.7
		120			.29	87.8
.5	8567*	90	.13	3.4	.08	23.5

NOTES: + lifting frequency
* resonant frequency

TABLE 7.9 - Summary of results for theoretical modal shapes.

7.5 ALTERNATIVE DISC BEARING DESIGNS

7.5.1 Ribbed Steel Disc

One disc type also investigated is represented in Fig. 7.24. Basically it is a disc with a central neck with coefficient .2 (equivalent to a 12 x 10^{-3} m diameter), but with ribs of thickness equal to 3 x 10^{-3} m spaced at 90º degrees. This disc is fixed with a central screw to a base.

Amplitude measurements were performed spaced of 5 degrees. The maximum amplitude value was registered at a frequency of 8242 Hz. The voltage input was 70 volts. The amplitude varied in this case with the angular coordinate θ from a point at middle distance between ribs (point M) to a point situated corresponding to a rib (point R). All the intermediate points and the two referred extreme points were located at 27.5 x 10^{-3}m from the center. The amplitudes measured at all the points were very small but they increased from the point R to the point M. For this reason this model is not suitable for use in squeeze-film bearings, at least for this rib thickness. This corresponds to a non-axisymmetric mode of vibration caused by the

existence of this ribs. The frequency of resonance is much higher than for the disc without ribs (f_r = 4002 Hz). The effect obtained by use of the ribs, change in the frequency of resonance, can not be properly used because the amplitudes are very small compared with those obtained for the same coefficient and with a nonribbed disc. The main reason for this occurence is the existence in this model of a new interface between the ribbed disc and the base. Unless all the unit (disc and base) is obtained by casting this interface will always be present. From the results obtained it is possible to infere two major conclusions. First, the shape associated with the bearing surface presents, even for small differences, significant changes of the resonant frequency. Secondly, any asymetry of the geometry must be discarded as the amplitudes of vibration will reflect this asymetry. If the amplitudes of vibration are not radially symmetric, radial flow occurs and this is not benefitial in terms of load capacity.

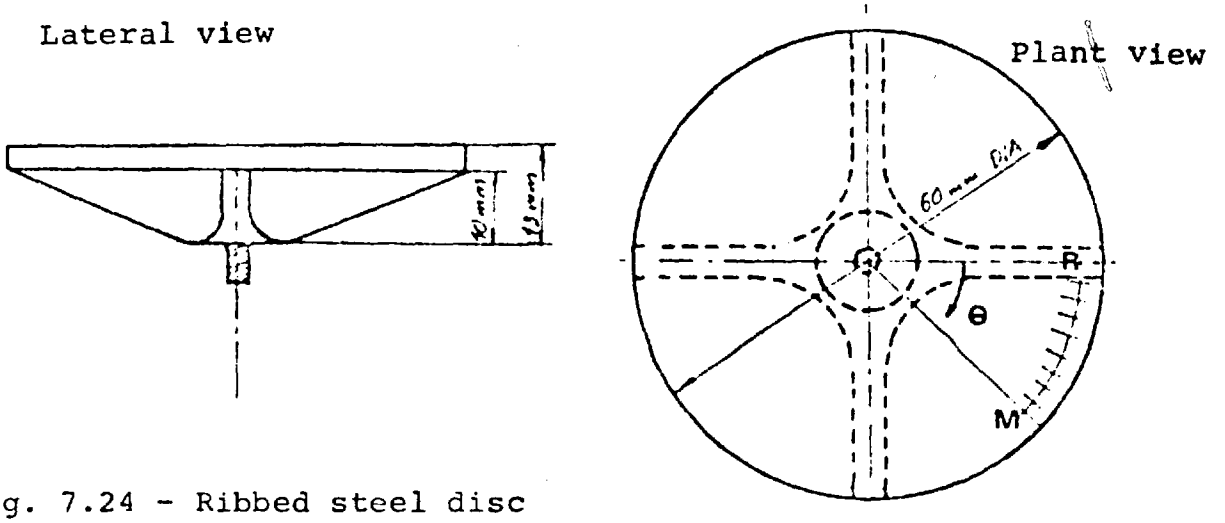

Fig. 7.24 - Ribbed steel disc

7.5.2 Solid Base Prototype

The experimental bearing configuration is illustred by Fig. 7.25. This general arrangement was dictated by the following objectifs:

i) use of electrical power available for maximum rigid body vibration amplitude.

ii) best amplification of the amplitude at the outer edge.

iii) correct positionning of the ceramic

The aims expressed by i) and ii) are easily understandable from the point of view of the bearing performance, as they respect the excursion ratio. The condition iii) is determined from the necessity to guarantee good ceramic-base contact and prevent the ceramic deterioration, referred in Chapter 5. A minor requierement to be satisfied was the immobilisation of the non acessible nuts (G) of the tie rods used to thighten the ceramic.

To satisfy the conditions referred in i) and ii) two ceramics (C) were used acting on only one supporting member (A) . The supporting member being a disc unit with

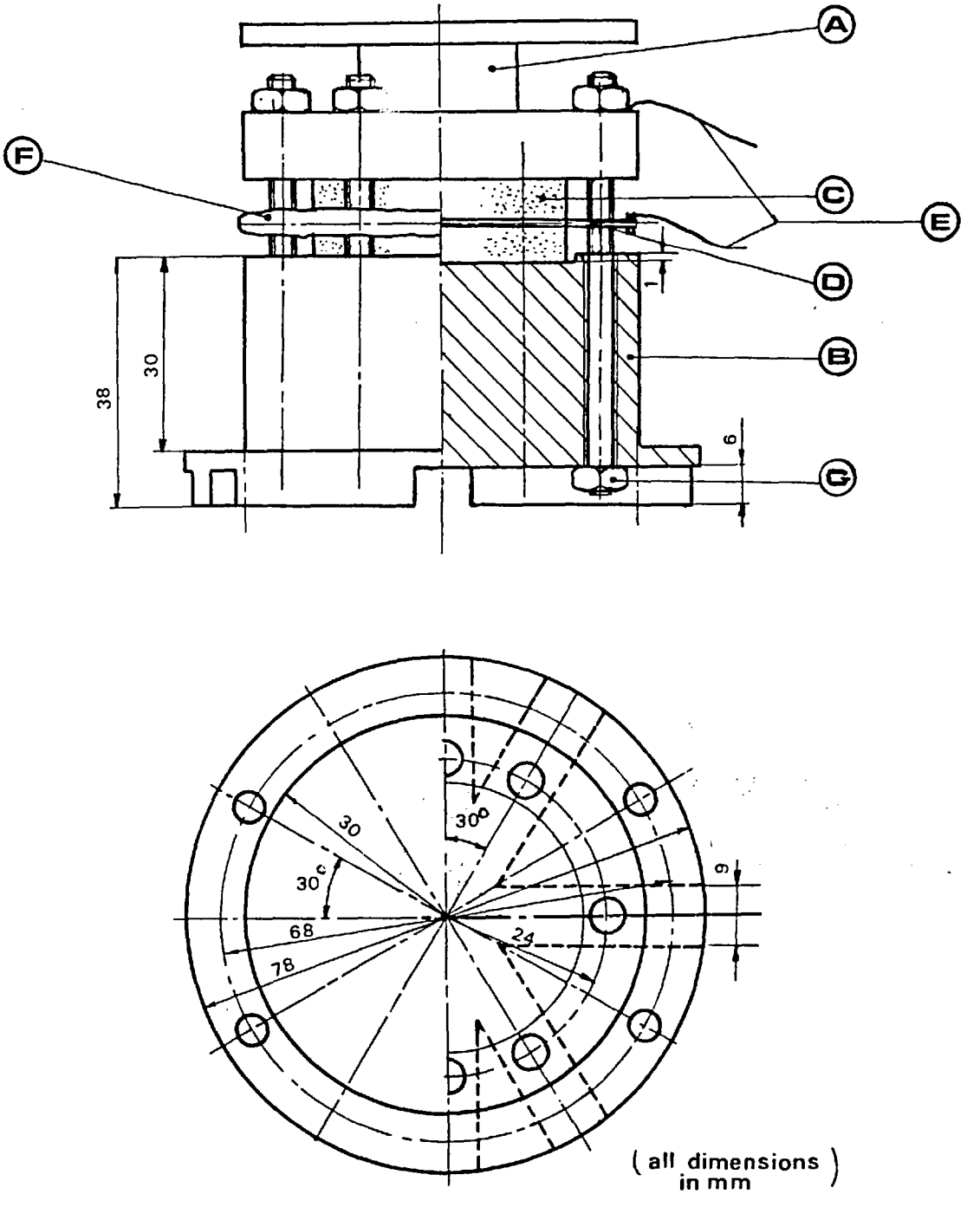

FIG. 7.25 - Prototype thrust S.F. bearing - solid base.

coefficient .4. This value of coefficient was choosen because it gave the best results in experiments detailed in the previous sections. Whenever a solid base is referred it means the steel cylinder (B) where piezoelectric ceramics and disc bearing (A) are fixed to.The electrical signal is applied to the ceramics through the wires (E) connected to the disc bearing and to the central electrode (D) , insulated by the rubber strip (F) .

Underneath the cylinder three slots were machined providing immobilisation of the nuts (G) which are not accessible.

A recess was designed on the upper base of the cylinder to locate the lower ceramic disc. A similar recess in the supporting member would provide the same function for the upper ceramic. It was verified in previous experiments that ceramics tended to slide as the bolts were thighten up. Special care was requered to prevent the ceramics to get damaged when in contact with the bolts threads. However no alteration was done to the supporting member to maintain the same overall.

7.5.2.1 ANALYSIS OF THE CYLINDRICAL BLOCK

The steel block supporting the bearing can be analised using simple theory. One pretends to know a first approximation of the resonance frequency of the block. It must be stressed that this is only a rough approximation justifiable for its simplicity. Actually, this theory only applies to a long thin rod vibrating axially, and where the ratio length to diameter is not greater than .6 - in our case this ratio is 1. A more accurate analysis requires the use of a finite element approach. However, the complexity involved by this method justifies this simple analysis bearing in mind that the results represent only, as referred, a first approximation.

Considering a bar subjected to a steady axial force any cross section of this bar is subjected to a compressible or tensile stress. When this force varies with time and for any element defined by two planes normal to the axis of the bar we can establish the following governing equation:

$$E \frac{\partial^2 u}{\partial x^2} + \frac{f}{A} = \rho \frac{\partial^2 u}{\partial t^2} \qquad (7.48)$$

with the nomenclature:

E - Young modulus

u - longitudinal displacement

f - external force

A - bar cross sectional area

x - axial coordinate

The basic approximation involved in the derivation of this equation respects the non existence of displacements normal to the bar axis. Because the cylinder is fixed to the ground we also assume a clamped condition at this end. For the other end a free condition will be considered. The expression of the natural frequencies is:

$$\omega_r = \frac{2(r - 1)\ \pi a}{2L} \qquad (7.49)$$

The subscript r indicates the order of the mode. The variable L represents the length of the bar (cylinder); a is equal to $\sqrt{\frac{E}{\rho}}$; E is the Young modulus and ρ is the density.

For the dimensions of Fig. 7.27 one obtains:

$$f = 44.767 \text{ KHz}$$

Even taking this frequency as an approximated value it is sufficiently high to guarantee that the steel base (cylinder) is not affected at squeeze film bearing working frequencies.

7.5.2.2 AMPLITUDE MEASUREMENTS

Amplitude measurements were made using, as before, the Fotonic Sensor (described in Chapter 4). The probe was positioned as for the case of the aluminium disc with coefficient .4 (section 7.3.1). The Table 7.11 shows the results obtained. For case a), the disc had a small cone frustrum at the outer edge, Fig. 7.28. In a pratical application this shape would provide some radial support. The frequency of maximum amplitude, 7598 Hz, is higher than for the previous experiments (for disc of coef. .4 the frequency was 6239 Hz). For the same disc, referred in 7.3.2, with coefficient .4, the resonant frequency with this arrangement was verified at 6170 Hz and this case is indicated in Table 7.11 as case b). In this case the amplitudes are smaller than in the case a). For these two experiments the electrode used had a thickness of 10^{-3} m and was in copper. Another experiment using an electrode in steel with a thickness of 5.1×10^{-3} m is considered in Table 7.11 as case c).

In all these tests the amplitudes verified are smaller than with double arrangement. The possible reason for these lower amplitudes is that part of the force is spent

Model	Frequency (c.p.s.)	PROBE POSITION								
		A	B	C	D	E	F	G	H	O
		MOTION AMPLITUDE ($\times 10^{-4}$ mm)								
a)	7583	-	-	57.4	31.9	24.2	5.4	-*	0.4	0.6
	7593	-	-	140.3	63.8	35.7	7.7	-*	0.4	0.7
	7598	-	-	-	89.3	-	-	-*	-	-
	7603	-	-	102.2	63.8	38.3	8.9	-*	1.1	1.2
	7613	-	-	53.6	51.0	17.9	4.5	-*	0.8	0.9
	7623	-	-	31.9	30.6	11.5	2.8	-*	0.6	-
b)	6130	-	-	10.2	10.2	4.1	-*	0.6	-	-*
	6140	-	-	14.0	12.7	5.4	1.1	0.7	-	-*
	6150	-	-	17.9	16.6	6.4	1.2	0.8	0.5	-*
	6160	-	-	21.7	21.7	7.7	1.4	0.9	0.4	-*
	6170	-	-	23.0	23.0	7.9	1.5	0.8	0.4	-*
	6180	-	-	21.7	21.7	7.0	1.3	0.7	-	-*
	6190	-	-	20.4	18.5	6.4	1.1	0.5	-	-*
	6200	-	-	15.3	15.3	6.0	0.8	-*	-	-*
c)	6155	-	-	26.0	-	8.9	-	-	-	-*
	6165	33.2	-	29.3	16.6	10.8	2.2	-	-	-*
	6175	38.3	-	31.9	20.4	12.7	2.9	-	-	-*
	6180	38.3	-	35.7	30.6	15.3	3.1	-	-	-*
	6185	37.0	-	31.9	21.7	13.1	2.6	-	-	-*
	6190	34.4	-	38.3	18.5	11.5	2.3	-	-	-*
	6195	31.9	-	28.0	19.1	10.8	2.2	-	-	-*
	6205	28.0	-	25.5	15.3	9.6	1.8	-	-	-*
Distance from centre (mm)		28.0	24.5	23.0	20.0	16.0	12.0	10.0	5.0	0.0

* NOTE: Measurement values of order of equipment noise level.

TABLE 7.11 Amplitude Measurements for Prototype S.F. Bearing.

on elastic deformation of the cylinder block. This seems to be confirmed by the results obtained with the different electrodes, cases b) and c). In fact the copper electrode provided smaller amplitudes than the steel one. The performance of the disc of case a) is somehow unexpected as the resonant frequency is higher than in cases b) or c).

The conclusions from this experiments can be resumed by the following points:

i - Although the arrangement in study should enable all the power to be use by one bearing element alone the actual displacements are smaller than with the double arrangement.

The possible cause for these lower amplitudes is that part of the force is spent on elastic deformation of the cylinder block. This seems to be confirmed by the results obtained with the different electrodes, cases b) and c)*, with the copper thicker electrode providing smaller amplitudes than steel one. The performance of disc of case a) is somehow unexpected as the resonance being higher than b) or c) the amplitudes are also greater.

---

* cases b) and c) use the supporting-member shown.

7.6 DISCUSSION OF THEORY AND EXPERIMENTS FOR DISCS

7.6.1 INTRODUCTION

In this section we will discuss the theoretical and experimental results for discs. This discussion will be divided into two major sections:

a) The dynamic behaviour of the bearing supporting members (steel and aluminium discs).

b) The performance of the squeeze film bearing when enclosed in the supporting members mentioned in a).

Here, the performance of the squeeze film bearing, will be analysed by considering the relationship between load capacity and film thickness for the various neck coefficients.

7.6.2 DYNAMIC BEHAVIOUR OF THE SQUEEZE FILM BEARING SUPPORTS

a) Resonant Frequency

The results of dynamic experiments performed with discs and the corresponding theoretical results are shown overleaf in Tables 7.12a) and 7.12b).For each of the two disc materials, three neck ratios, *ra/rb*, have been considered: 0.2, 0.4 and 0.5. For the 0.2 ratio a special design (a ribbed version detailed in section 7.5.1.) is also presented. These neck ratio values were arbitrary chosen.

To obtain the experimental values of the frequency at resonance (shown in column 3 of Table 7.12 a) the Fotonic Sensor

Neck coeff. ratio $\frac{r_a}{r_b}$	Frequency at resonance (c.p.s.)		Freq. at Lift (c.p.s.)
	experimental	calculated	
.2	4002	4300	4125
.4 } .4	6175	7500	6260
.5	8567	10600	no lift *
.2 (ribbed)	8975	—	no lift

Table 7.12 a)

Comparison between the resonant frequency and the frequency at lift for steel discs.

Neck coeff. ratio $\frac{r_a}{r_b}$	LIFT	LOAD	ELECTRICAL INPUT	
	Recorded gap at lift. h_o *(mm)*	W *(kgf)*	power *(Watts)*	voltage *(Volts)*
.2	10.0×10^{-2}	6.65×10^{-2}	.190	120
.4	8.2×10^{-2}	6.65×10^{-2}	.150	90
	22.0×10^{-2}	6.65×10^{-2}	.190	120
.4	18.5×10^{-2}	13.30×10^{-2}	.190	120
.4	17.5×10^{-2}	15.30×10^{-2}	.190	120
.5	No lift *	—	.190	120
.2 (ribbed)	No lift	—	.190	120

* very unstable

Table 7.12 b)

Experimental relationship between load and lift for the squeeze film bearing using steel discs.

readings were used. The details of this evoluation are given in section 7.3. For comparison purposes the corresponding calculated frequencies are also shown in column 4. The calculation is presented in section 7.2.2.2. The resonant frequency varies with the neck coefficient ratio with ths highest value when the ratio is .5. The lowest value is when it is .2. The theoretical values follow the same pattern although they differ in magnitude from the experimental ones.

The fact that a considerable change in the resonant frequency of these discs is produced by variation in the neck coefficient seems to be very important, as it enables a simple way to control this frequency. The reason why the expected (calculated) values do not closely agree with the experiments is difficult to ascertain. It could be explained by an inexact boundary condition assumed in the theory for the disc inner radios (r_b).

A clamped condition was assumed there with $\frac{\partial w}{\partial r} = 0$, where w is the displacement.

Unfortunately it is not possible to introduce a more realistic condition in the existing theory. On the other hand no comparison has been made before by other workers between the theory used to obtain these frequencies and experimentals results. Therefore; it is rather difficult to state if this difference is

due to the theory itself or to the assumed boundary conditions. It should be noted that the discrepancy increases with the neck ratio, from 7.4% to 23.7%

It is not the purpose of this Chapter to repeat conclusions already presented but propably it was not well stressed that in all the experiments the disc thickness has been considered as constant ($e = 0,003\ m$), and this suggests the following comments : it is obvious that changes in the resonant frequency are to be expected if the thickness varies from specimen to specimen. The amplitudes of vibration will also be different, the thinner the disc the bigger the amplitude, if the input power to the piezoelectric ceramic is the same. The effect of thickness on the dynamic behaviour of squeeze film bearings should also be analysed. However, in this work, the influence of the neck coefficient was considered as more important. Actually, the neck size defines the working frequency of the bearing and also the allowable space for the bolts fixing the disc to the piezoelectric ceramic.

Comparison between amplitudes of cone and discs having the characteristics already referred to in Chapters 6 and 7, respectively, indicate :

i - Considering the same input power the greater amplitudes occur with discs, but for a cone with the same overall size

it has a much higher resonant frequency than a disc. In fact the highest resonant frequency of a disc (in this case with a neck coefficient of .5) was 8567 cps and the cone used in experiments resonated at 18 Kcps.

ii - The disc with a neck coefficient of .4 gave for both steel or aluminium cases the highest amplitude, for the same power input. This means that for a given piezoelectric ceramic there is one value of coefficient ratio for which the amplitudes obtained are maximum. Whilst no variation of the neck coefficient have been carried out for conical bearings, this suggests that a similar effect should be expected.

iii - Because the piezoelectric ceramics are part of the vibrating system their dynamic characteristics (mainly the stiffness) will defenitely affect the amplitude of vibration of the bearing member.

7.6.3 LOAD CAPACITY

The load capacity is some times of great significance for the user of this type of bearing. For the squeeze film bearing it has not been possible to exceed a mere 1/2 lb (aproximately 20 Newtons) for the size and power input considered in this work. The load capacity of the bearing is the total force that can be applied to the bearing supported member whilst maintaining the least film between this member and the supporting member. It

will be denoted by W in this work. Actually, we are dealing with a mean value of gap and this for several reasons. One is that the supporting member is vibrating, and the second is that the amplitudes of vibration are not the same for all radial points on the supporting member. The third reason is that the experimental measurements only read the mean gap as indicated by the lift of the load members.

Whilst this load capacity, W, is what the bearing user will need to know, it is necessary to introduce another variable, the instantaneous load capacity, W_{inst}.

To obtain the load capacity, , from the instantaneous load capacity, W_{inst}, an integration in time must be made. As the instantaneous pressure, p, varies with the disc radius the value of W_{inst} is obtained according to (7.45) :

$$W_{inst} = \int_0^{r_a} 2\pi\, p\, r\, dr \qquad (7.45)$$

Where p is the actual pressure value at a distance from the disc center, r, and r_a is the radius at the bearing (disc) outer edge, as shown in Fig. 7.2 .

Defining a nondimensional instantaneous load capacity, W^*_{inst} :

$$W^*_{inst} = \frac{W_{inst}}{Atmospheric\ load\ pressure} = \frac{W_{inst}}{\pi\, p_a\, r_a^2} \qquad (7.46)$$

then,

$$W^*_{inst} = \frac{2}{p_a r_a^2} \int_0^{r_a} p\, r\, dr \qquad (7.47)$$

or,

$$W^*_{inst} = \frac{2}{r_a^2} \int_0^{r_a} \frac{p}{p_a}\, r\, dr \qquad (7.48)$$

Defining a nondimensional pressure as $P = \frac{p}{p_a}$ and the nondimensional coordinate $R = \frac{r}{r_a}$,

$$W^*_{inst} = 2 \int_0^1 P\, R\, dR \qquad (7.49)$$

The time average of W^*_{inst} for one cicle of plate motion represents the nondimensional load capacity of the bearing, W^*. Using also the nondimensional variable $T = \omega t$, ω being the frequency of vibration of the supporting member, and integrating for one cycle :

$$W^* = \frac{1}{2\pi} \int_0^{2\pi} W^*_{inst}\, dT \qquad (7.50)$$

In terms of the actual load, W :

$$W = W^* \pi p_a r_a^2 \qquad (7.51)$$

The usable load capacity, W_u, being :

$$W_u = W - \pi p_a r_a^2 = (W^* - 1) \pi p_a r_a^2 \qquad (7.52)$$

For one of the discs used in the experiments a numerical calculation of W^*_{inst} was performed. The disc characteristics are as follows :

material . . . . . steel

coefficient (neck ratio) 4

frequency of resonance . . . . . 6171 cps

frequency used for the calculation . 6171 cps

The Reynolds equation (3.44) and the numerical procedure presented in 3.3.3 for its integration (Crank-Nicholson formulation) are used. The film thickness values are taken from the plain curve if Fig. 7.17 (theory), the increments $\Delta X = 1/36$ and $\Delta T = 1/31$. These values are choosen in accordance with the suggestions presented by Michael in (5). The corresponding computer programme is shown in Appendix 3.

To compare the pressure distribution with the dynamic behaviour of the disc, its modal shapes and the corresponding values are shown in the following pages, (Figs. 7.26 a) to 7.31 b)).

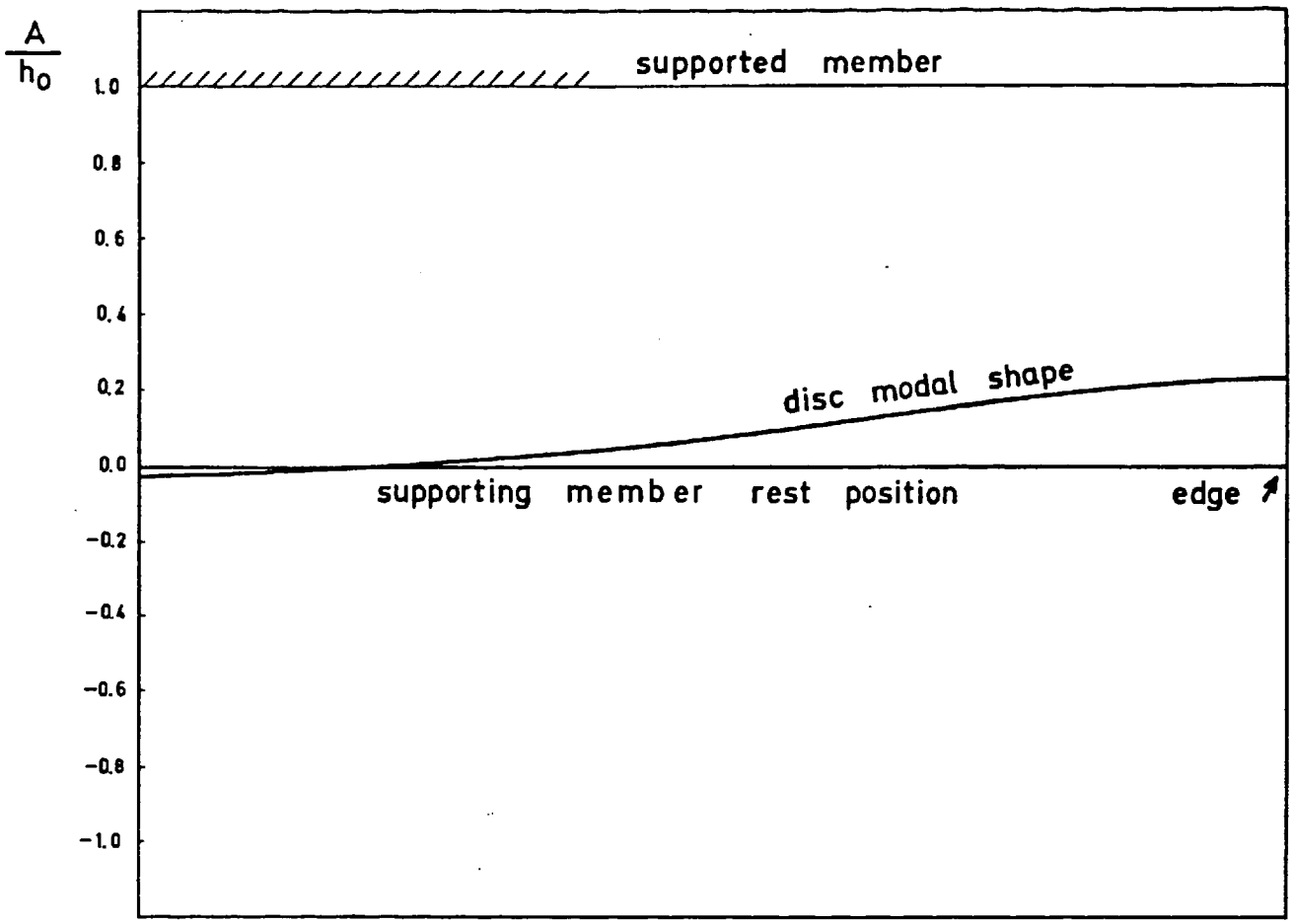

Fig. 7.26 a) disc modal shape for coeff. = .4 and f = 6171 Hz for T = 1.5 ΔT.

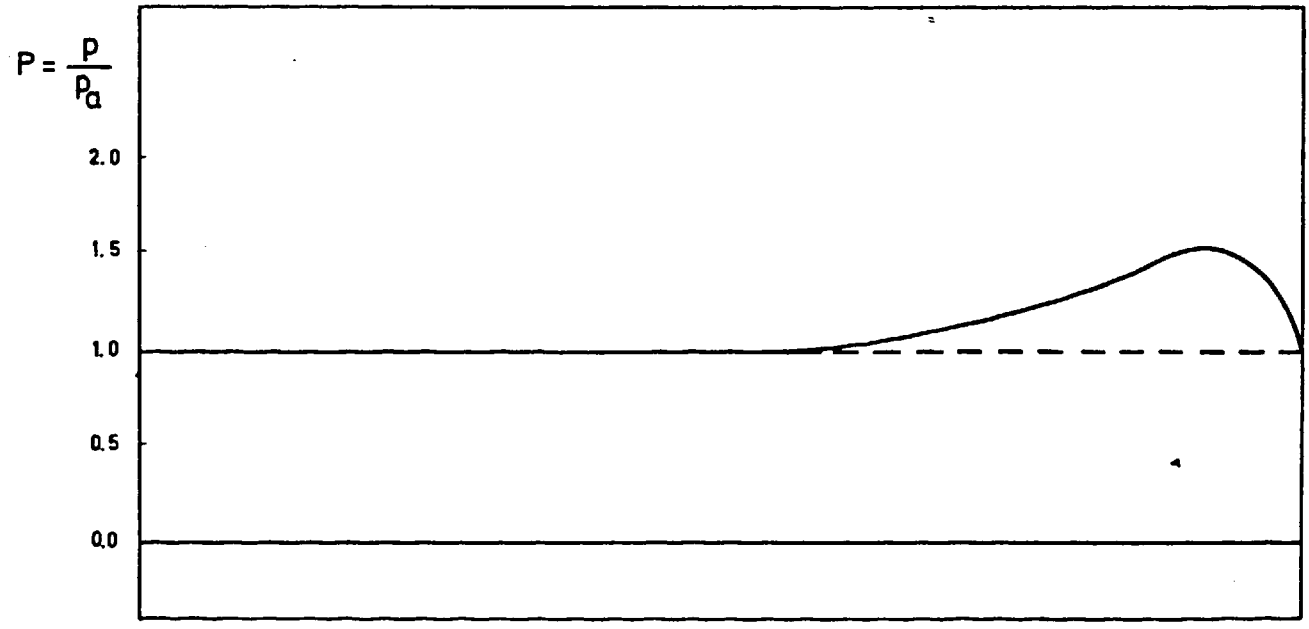

Fig 7.26 b) pressure distribution along radius corresponding to modal shape shown in Fig. 7.26 a).

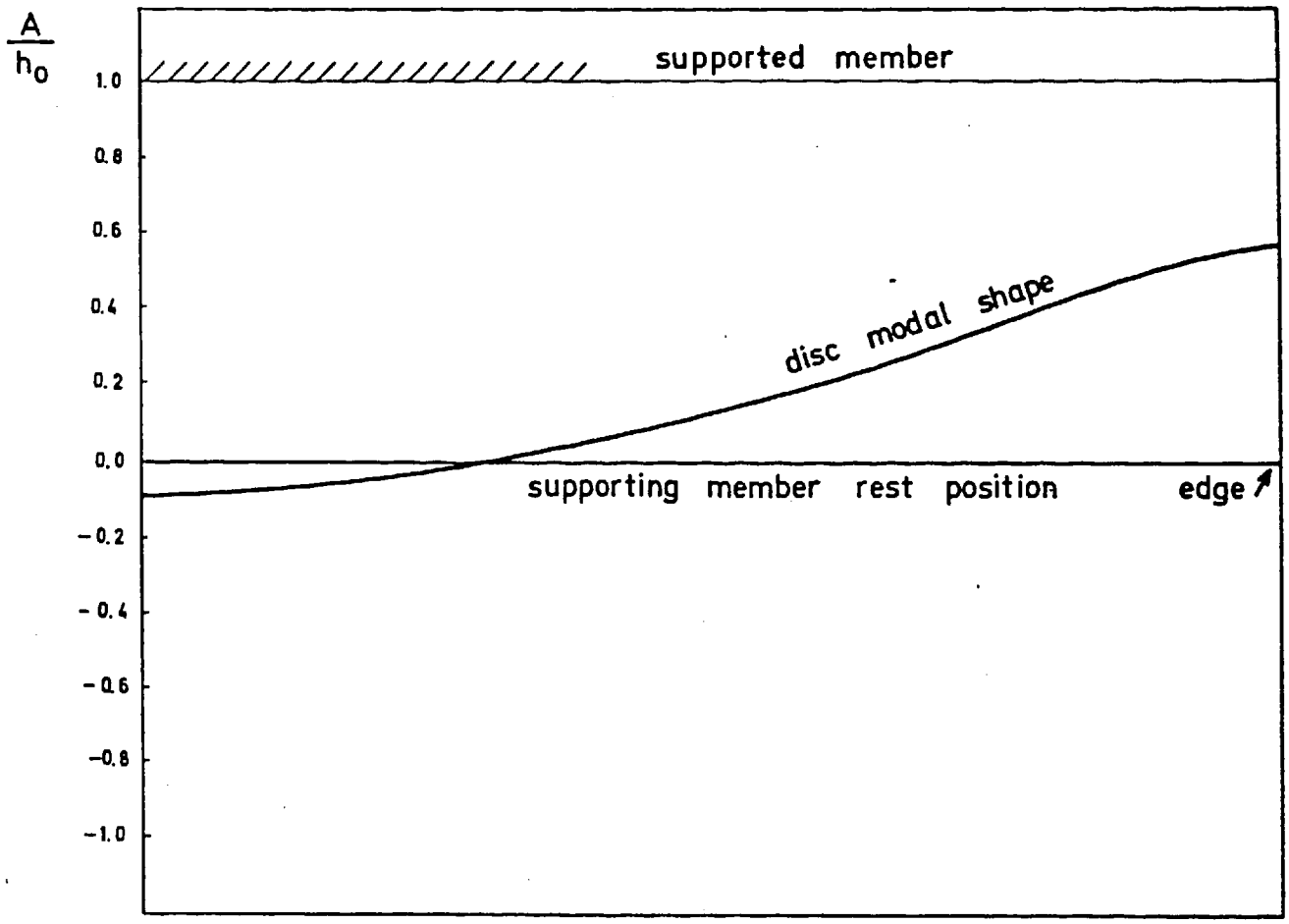

Fig. 7.27 a) disc modal shape for coeff = .4 and f = 6171 Hz for T = 4,5 ΔT.

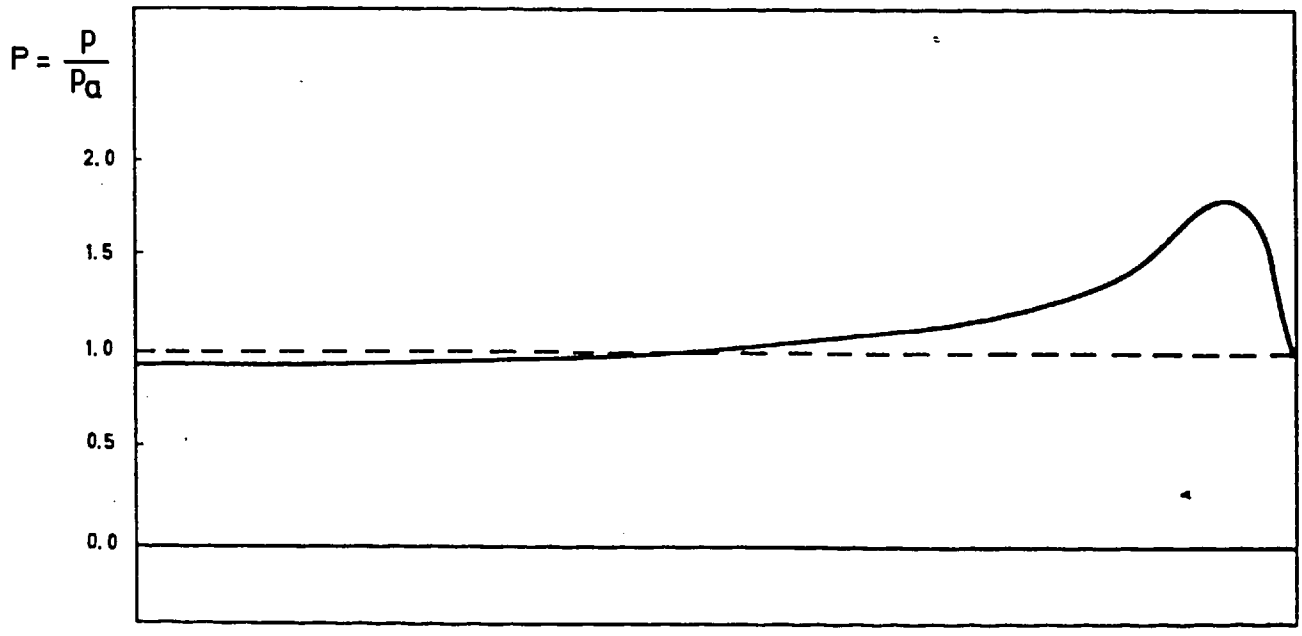

Fig. 7.27 b) pressure distribution along radius corresponding to modal shape shown in Fig. 7.27 a).

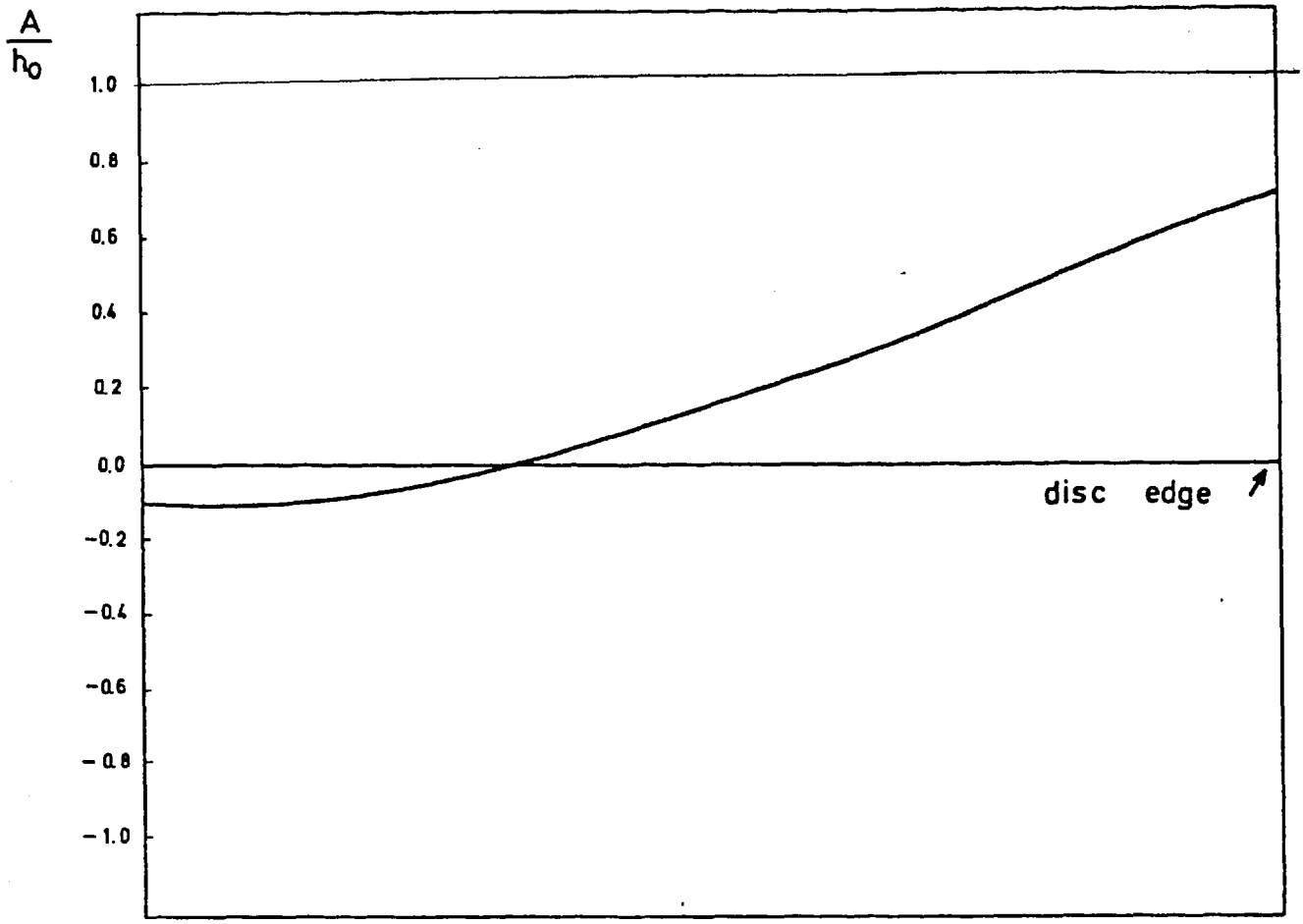

Fig. 7.28 a) disc modal shape for coeff = .4 and f = 6171 Hz, value T = 7.5 ΔT.

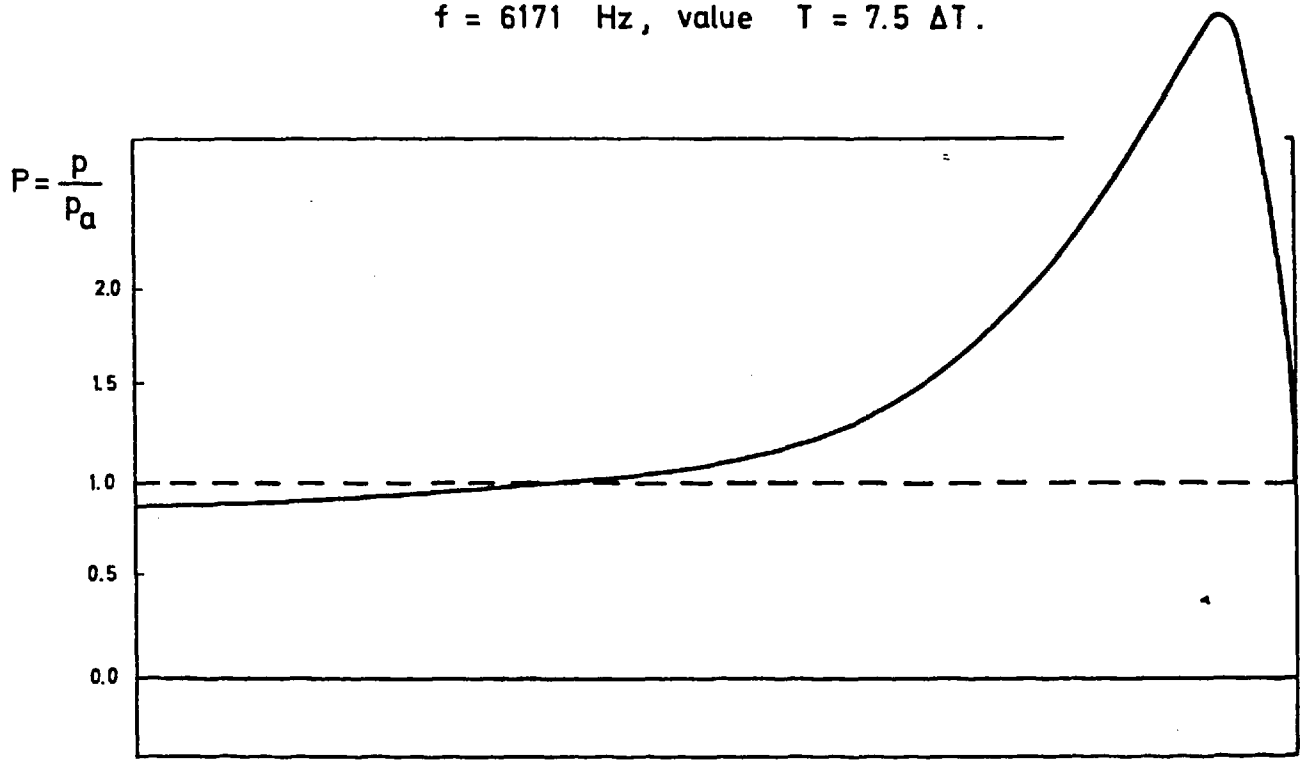

Fig. 7.28 b) pressure distribution along radius corresponding to modal shape shown in Fig. 7.28 a).

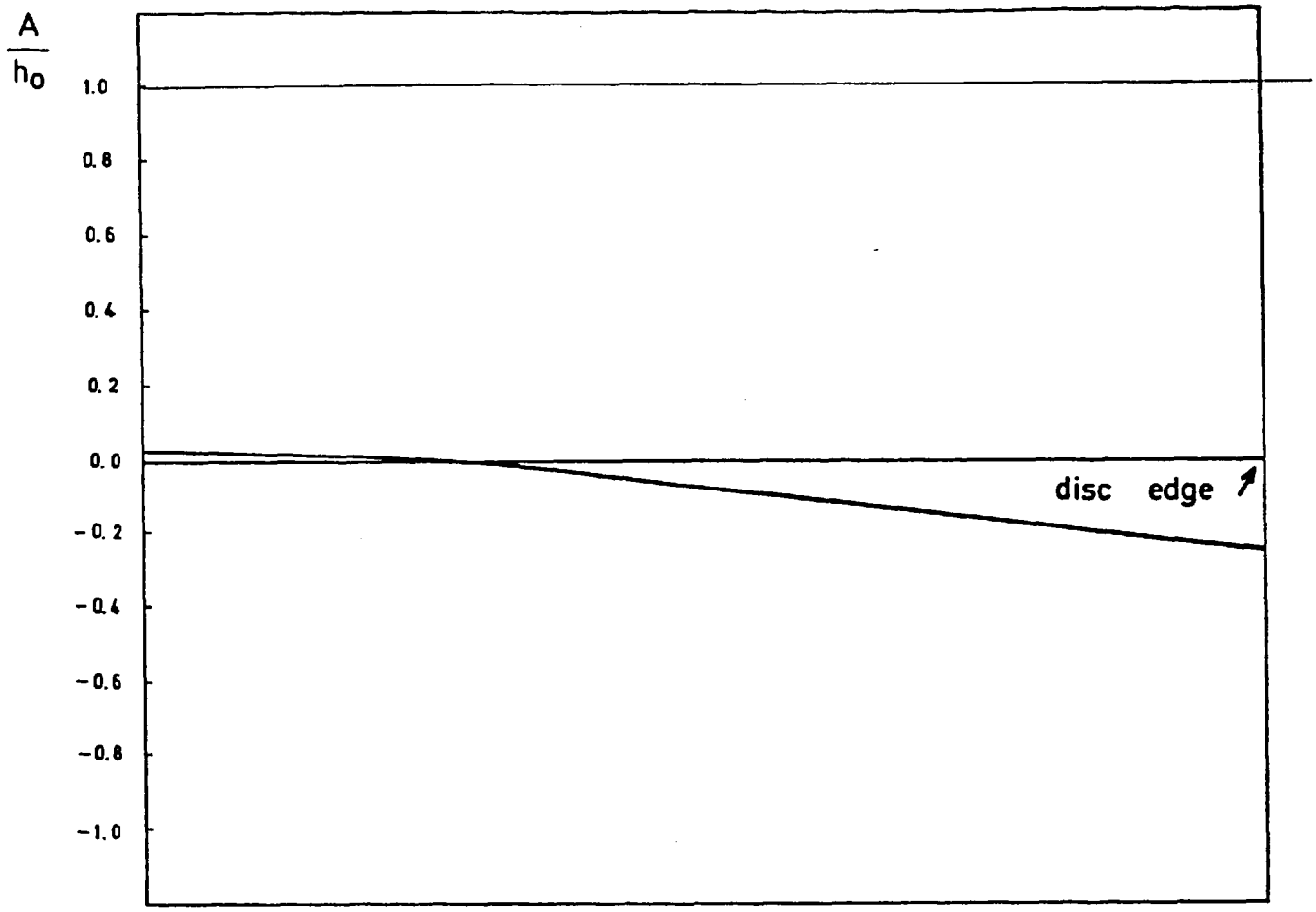

Fig. 7.29 a) disc modal shape for coeff = .4 and f = 6171 Hz, value of T = 16 ΔT .

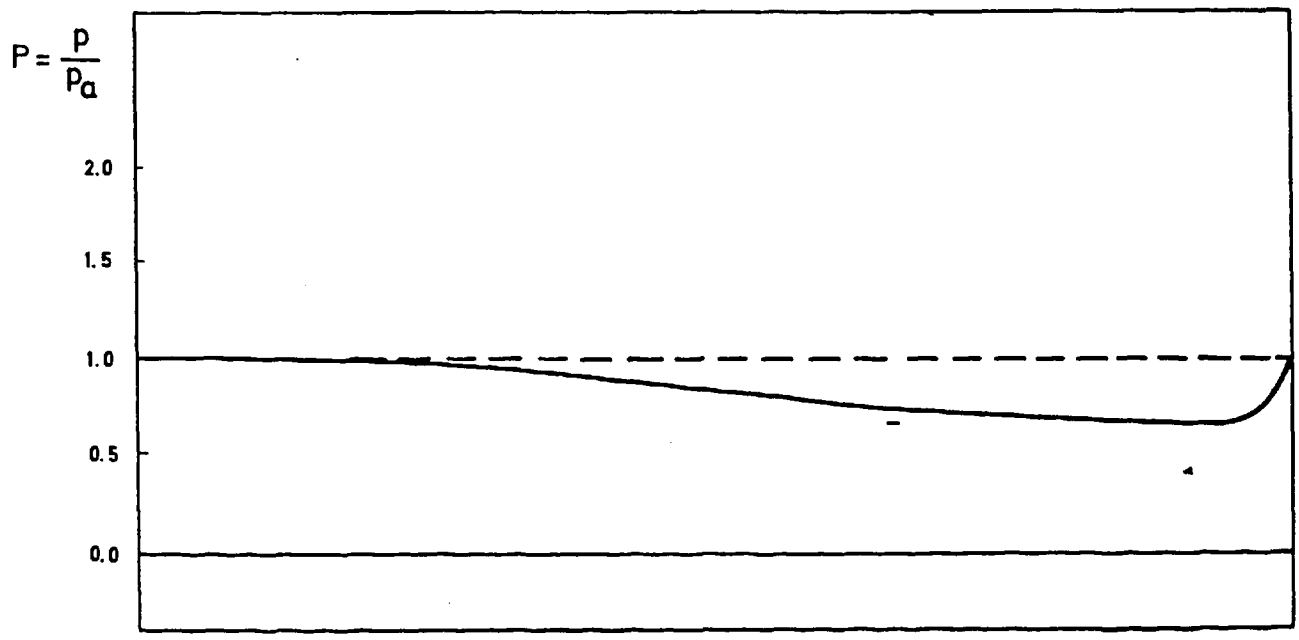

Fig. 7.29 b) pressure distribution along radius corresponding to modal shape shown in Fig. 7.29 a).

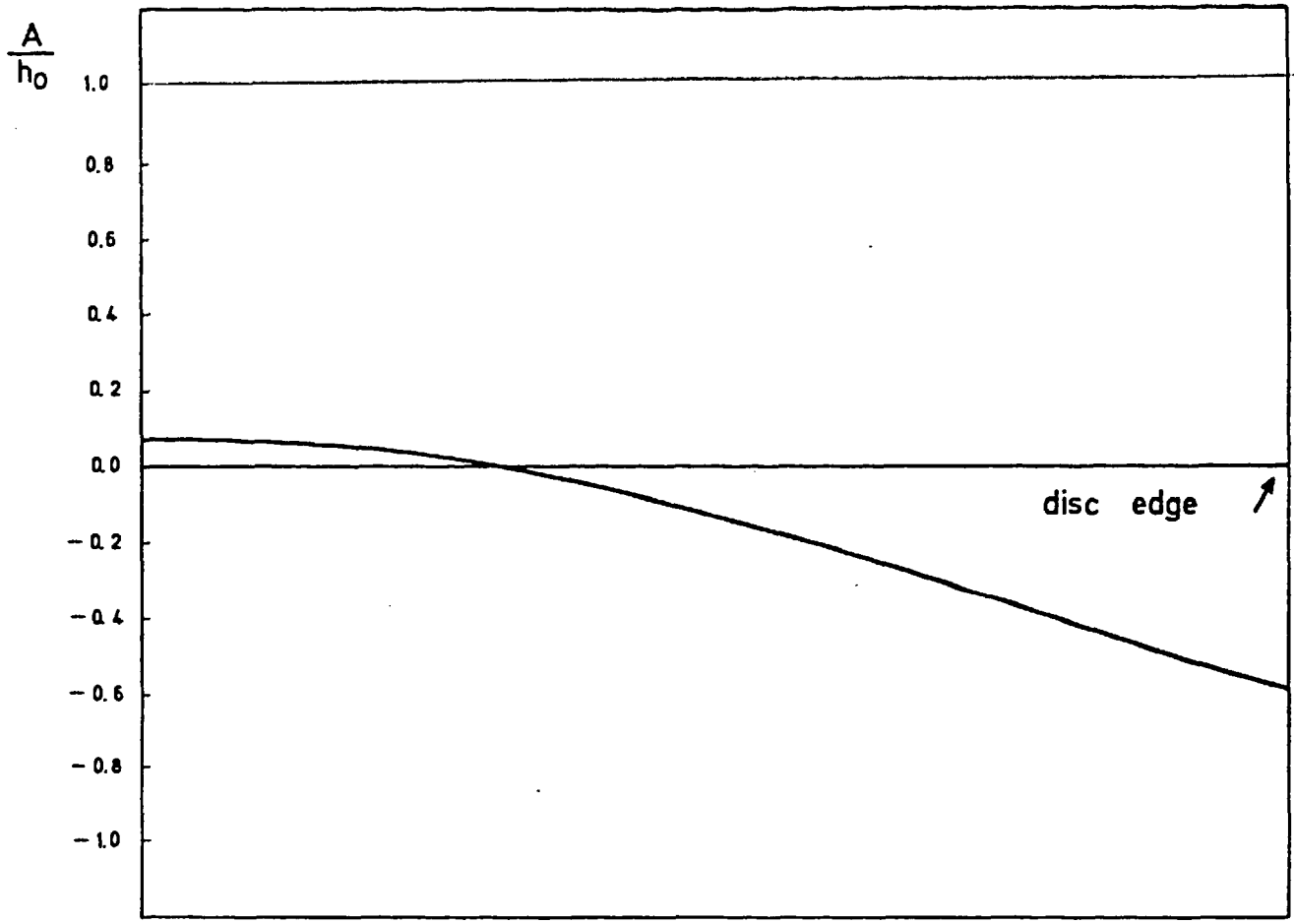

Fig. 7.30 a) disc modal shape for coeff = .4 and f = 6171 Hz, value of T = 19 ΔT.

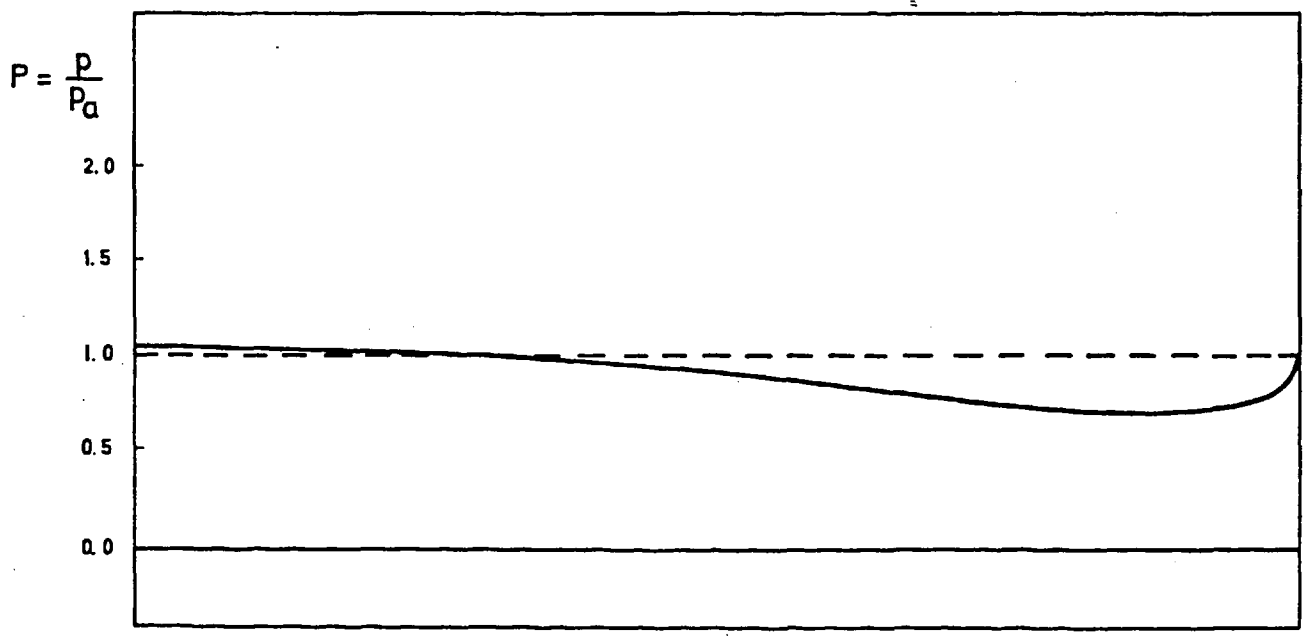

Fig. 7.30 b) pressure distribution along radius corresponding to modal shape shown in Fig. 7.30 a).

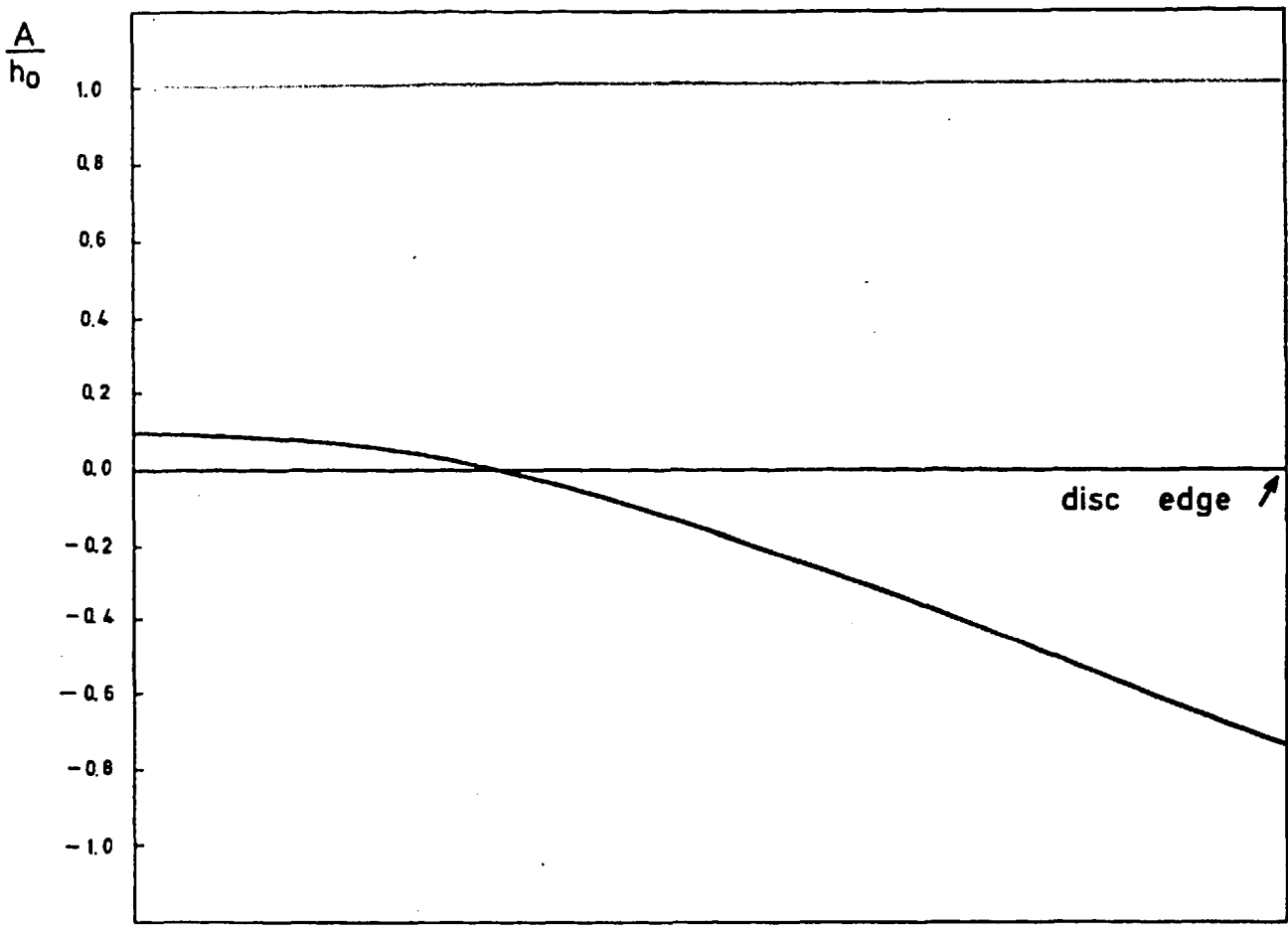

Fig. 7.31 a) disc modal shape for coeff = .4 and f = 6171 Hz, value of T = 22 ΔT.

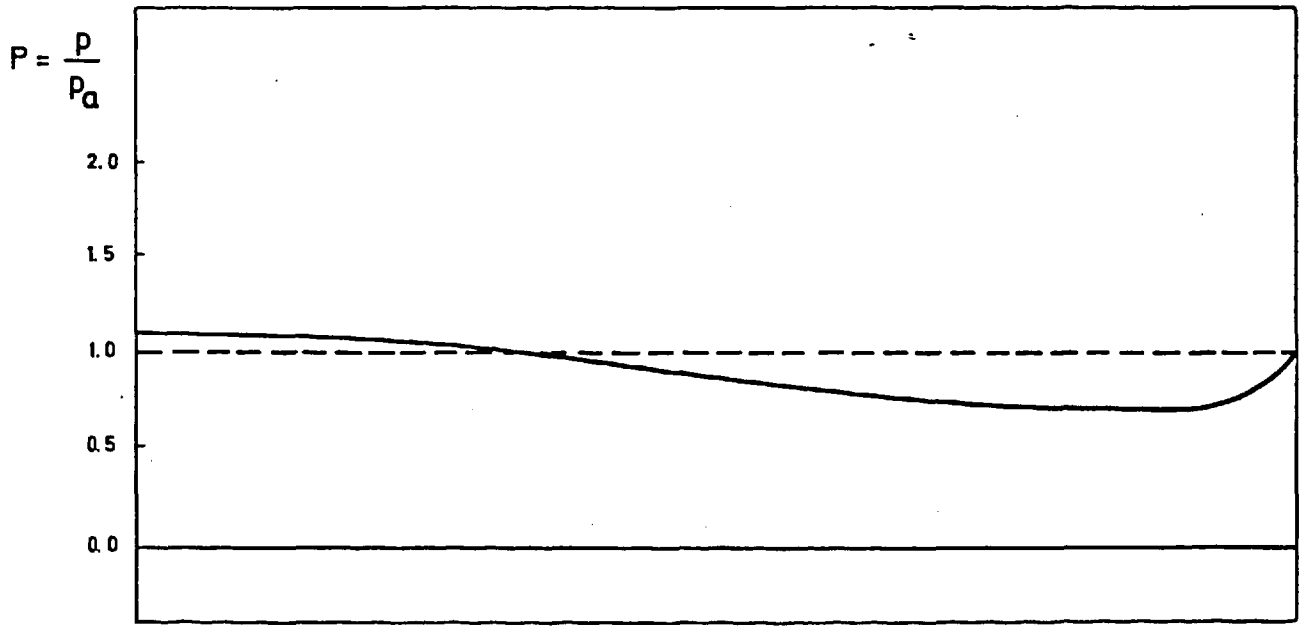

Fig. 7.31 b) pressure distribution along radius corresponding to modal shape shown in Fig. 7.31 a).

The figures shown at the top of these pages refer to the modal shapes. These graphs have a vertical axix graduated from -1.0 to 1.0 and the variable represented in this axix is a nondimensional amplitude $A^* = \frac{A}{h_o}$ where A is the actual amplitude of vibtration and h_o is the mean gap between the bearing members.

For the example analysed the value retained for h_o is , $h_o = 1. \times 10^{-3} m$. The figures at the bottom of each page represent the nondimensional pressure $P = \frac{p}{p_a}$ versus the nondimensional radius $R = \frac{r}{r_a}$ for the same dynamic conditions (frequency, material, coefficient ratio). The film thickness, h, is obtained from $h = h_o - A$, with the A values taken from the corresponding modal shapes in Figs. 7.24 a) to 7.29 a). Theses modal shapes are represented by the disc surface and show a node near the inner radius, r_b. At the center line (C.L.) the motion has an opposite phase angle to those of points of the annular area, from r_b to r_a. This means that when the neck center is moving down, for instance, the annular disc moves up and vice-versa.

The pressure values can be integrated for one cycle according to equation 7.47 thus calculating W^*_{inst}. Values of W^*_{inst} are plotted for the particular case shown in Fig. 7.32. This curve is similar in shape to that obtained

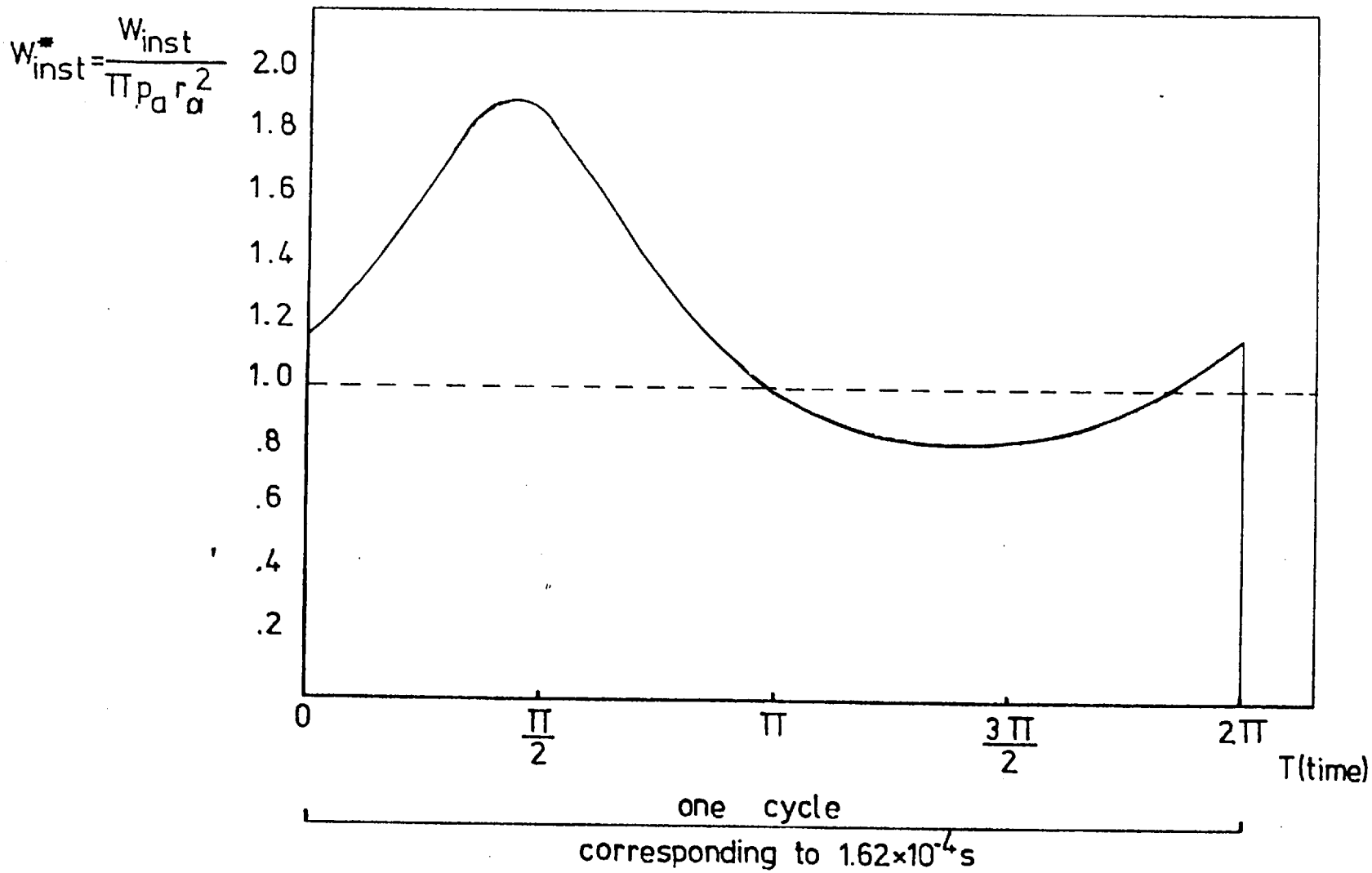
$W^*_{inst} = \frac{W_{inst}}{\pi p_a r_a^2}$
2.0
1.8
1.6
1.4
1.2
1.0
.8
.6
.4
.2
0
$\frac{\pi}{2}$
π
$\frac{3\pi}{2}$
2π
T(time)
one cycle
corresponding to 1.62×10^{-4}s

Fig 7.32

by other methods (discussed in Chapter 3) but it is more accurate as it accounts for the nonuniform excursion.

7.6.3.1 THEORETICAL RESULTS

The nondimensional load capacity, W^*, is, then, obtained through expression (7.50), as it is in fact the time average of W^*_{inst} during one cycle of the periodic motion. A simple Simpson's role method can be used to obtain the value of W^*. Of course, this value of W^* is related to a particular mean gap (clearance) between the supported ans supporting bearing members and the consideration of several values of this clearance will give corresponding values of W^*. As W^* does not take account of the load produced by the ambient atmosphere, the nondomensional variable $W^* = \frac{W_u}{\pi p_a r_a^2}$ is preferred for the following calculations with W_u, already defined in expression (7.52), and related to W^* by

$$W_u = (W^* - 1)\ \pi p_a r_a^2 \qquad (7.52)$$

The nondimensional variable W^*_u can be then expressed in terms of W^* by

$$W_u = W^* - 1 \qquad (7.53)$$

The variable h_o, which represents the mean gap between the bearing members can be nondimensionalised dividing by r_a, the disc outer radius. The two variables, W^*_u and

$H_o^* = \frac{h_o}{r_a}$, are plotted on one graph for the three disc examples studied with coefficient values equal to .2, .4 and .5 .

The disc amplitudes used to compute W^*, and therefore W_u^* are those of the experimental curves of Fig 7.15 (for coeff. .2) ; Fig 7.16 (for coeff. .4) and Fig 7.17 (for coeff. .5).

In all three cases W_u^* increased with reduction of H_o^*. This was predictable because a decrease of H_o^*, or h_o as r_a is a constant, gives higher values of the excursion ratio parameter, ε (defined in 2.2.3.1), and the load capacity increases with ε, as referred in (6).

The minimum allowable value for H_o^* is given in each case by the maximum amplitude of vibration of the disc, i.e., the value of h_o that equals A (A, being the maximum amplitude of vibration), when the bearing members will be in contact, as in Fig 7.33. This explains why for curve *a)* (for disc with coeff. .4) it is not possible, in this case, to assume values of H_o^* under 3×10^{-4}. If H_o^* is too large, the value of h_o will be much greater than the amplitudes of vibration . The compression effect is negligible and so it is the load capacity of the bearing, and values of W_u^* smaller than 2×10^{-3} are not represented. The usable region for each of the mentioned cases is then represented by the corresponding curve. It is interesting to notice that due to its vibrational characteristics the three disc have very

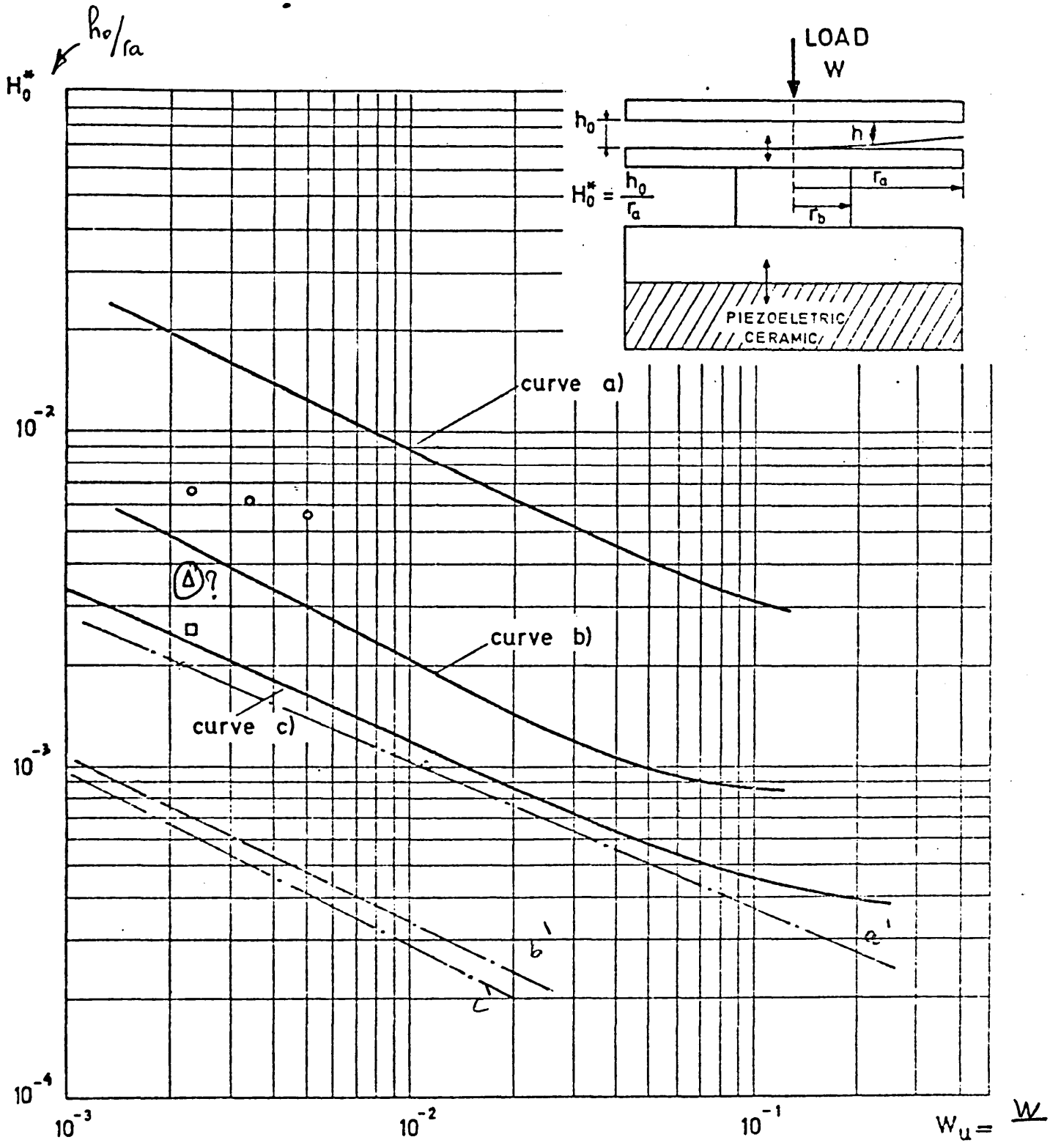

Fig. 7.33 Comparison between theoretical and experimental s.f. bearings.

THEORY
numerical work
- curve a)-neck coefficient .4 at frequency 6176 Hz
- curve b)-neck coefficient .5 at frequency 8567 Hz
- curve c)-neck coefficient .2 at frequency 4062 Hz

PAN'S THEORY
- curve a')-neck coefficient .4
- curve b')-neck coefficient .5
- curve c')-neck coefficient .2

EXPERIMENTS
- o - neck coefficient .4
- Δ - neck coefficient .5 (very unstable)
- □ - neck coefficient .2

different performances from the point of view of the load capacity. Obviously, it is possible to drive the piezoelectric ceramics with a smaller power input which will decrease the value of the allowable mean clearance, h_o , ie, without interference between the two bearing members due to their contact.

From the Fig. 7.32 the following conclusions can also be drawn :

i - If the load has an imposed value, which means that the value of W_u^* is fixed, instead of h_o , it is possible to conclude that the disc with 0.4 neck coefficient ratio will give the higher lift, i.e., the higher clearance between the bearing members. This is caused by the higher amplitudes of vibration for this particular neck coefficient which produce higher values of the excursion ratio, ε.

ii - Comparing now the bahaviour of the two other cases, discs with coefficient .5 and coefficient .2, whilst the first case presents slightly higher amplitudes and therefore higher excursion ratio values, the behaviour of the .5 case is better from this point of view. The only explanation for this fact is the higher working frequency.

iii - The experimental values of the load capacity, denoted by small triangles in Fig. 7.33, are lower than the theoretical ones for the same bearing clearance. One reason for this fact could be the damping effect of the air film on the disc amplitudes. Because the film thickness for the load capacity calculation is derived from the disc modal shapes, without the air film, and therefore the excursion ratio values result overestimated. This fact originates a higher load capacity than the actual one.

iv - Comparison these results with those forecasted for non flapping, rigid discs and computed with the Pan's asymptotic theory (11) can now be made using the curves $a`, b`$ and $c`$ of Fig. 7.33.

It was considered a uniform amplitude of vibration along the disc radius and equal to the disc center value, obtained, for each case, from Figs. 7.15, 7.16 and 7.17.

The relative position of the three curves is the same as with curves a, b, c, but for the same adimensional film thickness the corresponding load capacity is much lower than the theoretical values, or the experimental ones.

It is possible then to conclude that the flapping effect produces a better performance from the point of view of

the load capacity of the bearing. In practical cases it is also more realistic to use a nonuniform amplitude analysis because, depending on the dynamic characteristics of the member there will be always some degree of flapping.

7.6.3.2 EXPERIMENTAL RESULTS DISCUSSION

a) Steel Discs

The experiments to obtain the actual value of the load capacity of the disc bearing are similar to those of the conical bearing study detailed in section 6.4. The main difference is that a thin disc is now used as the upper, supported, member. For disc shaped bearings the load capacity is significantly lower than for the conical bearings. So, for the experimental arrangement used, it was only possible to impose a maximum of three different loads. In the case of the .5 coefficient disc it was not possible to obtain the lift of the supported member within the available power input to the piezoelectric ceramic. The disc with coefficient .2 produced the lift of the upper member at a frequency, (designated hereafter as the lifting frequency), of 4125 c.p.s., as shown in Table 7.12. When the load increases the gap between the supporting and the supported member decreases. Finally, the disc with a neck coefficient equal to .4 produced lift at 6260 c.p.s., i. e., a value slightly higher than the resonant frequency of the supporting disc ($f_r = 6176$ c.p.s.). For this specimen two values of power input were applied for a fixed load value, this load being the upper member's own weight ($6.65 \times 10^{-2} kg \sim 1.47 \times \times 10^{-1} lb$). With .190 watts of power input (corresponding to

120 volts across the piezoelectric ceramic, the lift, gap between the bearing members almost doubled that found with .150 watts (equivalent to 90 volts across the ceramic). The respective values of h_o were $15.24 \times 10^{-6} m$ and $8.15 \times 10^{-6} m$. These measurements where obtained with the Wayne Kerr capacitance probe described in section 6.4. All numerical values of the applied loads, corresponding lifts and the experimental conditions are presented in Table 7.12, page 220. The comparison between the results provided by theory presented in 7.6.3 and these experimental values is shown in Fig. 7.33. The theoretical results overestimate the lift but it should be mentioned that they don't refer to the same frequencies. The theoretical curves are obtained at the resonant frequency of the corresponding disc. So, for the coefficient .5 the frequency is 8567 c.p.s.; for coefficient .2, the frequency is 4062 c.p.s.; and for the disc with coefficient .4 the frequency is 6176 c.p.s.. The experimental values represented in the the same Figure are obtained at the lifting frequency of each disc. At these frequencies the amplitudes of vibration are much smaller than at the resonant frequency. To explain the non coincidence of the two frequencies, the lifting frequency and the resonant frequency, it should be remembered that the resonant frequency is for a free moving disc. In other words the resonant frequency

values are obtained without the upper member and the confined squeeze film. These two elements could cause a shifting of the resonant frequency of the order that is observed, i.e., 1.9% for .2 coefficient and 1.3% for .4 coefficient. For the .5 disc it was not possible, as already referred, to detect any situation of lift.

b) Aluminium Discs

These same experiments were prepared for the aluminium discs. However no lift occured for these bearings and two reasons can be advanced for this : the aluminium discs are more prone to surface distortion during grinding than the steel ones, whilst the same effect occurred with steel disc with .5 neck coeeficient; the other possible cause of poor performance of these discs is the deterioration of the piezoelectric ceramics, some surface damage being apparent after the operations of dismounting and reassembly of the bearing unit.

CHAPTER EIGHT

SUGGESTIONS FOR FUTURE RESEARCH

One of the greatest gaps in the investigation of squeeze film bearings is the simultaneous treatment of both theory and experiment, so that correlation of results can be obtained. Most of the theoretical analysis of gas behaviour is well treated and the contribution of COOKE (30) is very valuable in this respect. However, it is not possible to calculate the final performance of this type of bearing by assuming the gas to be confined in hypothetically positioned surfaces at each instant. The fact that the actual position of the supporting member surface varies at each instant causes the analysis of these bearings to be quite different from that used for externally pressurised gas bearings. The dynamic behaviour of the supporting surface must be known therefore. This makes it important also to study the vibrating piezoelectric ceramic characteristics.

Therefore the following suggestions are made as a continuation of this work :

Theoretical Work

i) A finite element approach for the dynamic analysis of the conical bearing. This study could be performed by considering the total cone as subdivided into several conical elements and then calculating the mass and stiffness matrices for the total cone as made up of these elements. Then, it is possible to include in these matrices the mass or stiffness of the base, neck and piezoelectric ceramic. This analysis also enables the ring,which is formed at the cone outer edge and referred to in Chapter Six to be considered.

Using this analysis it is possible to calculate the natural frequencies as well as the modal shapes.

ii) Using data from i), ie, the modal shapes of the conical shell, the load capacity for the same bearings could be calculated using a numerical method based on the Reynolds equation.

Experimental Work

i) One of possible improvements to the squeeze film bearings is to use glue to ensure contact between the ceramics and the electrodes. Therefore the amplitudes of vibration for discs considered in Chapter 7 can be investigated when employing a glue like Epoxy or an Araldite Type, discribed in Ref. 63.

ii) According to the values obtained in i) if they are more favourable (higher amplitudes) than those obtained using fixing bolts, an investigation of the lift, frequency and load capacity can be performed.

iii) Another possible ceramic arrangement is that shown in Fig. 8.2 with the piezoelectric crystal working in a shear mode. This arrangement is based on the recent application of this configuration to a new series of accelerometers by a well know manufacturer.

The response curves for the old type and the new series of accelerometers are shown in Fig. 8.3

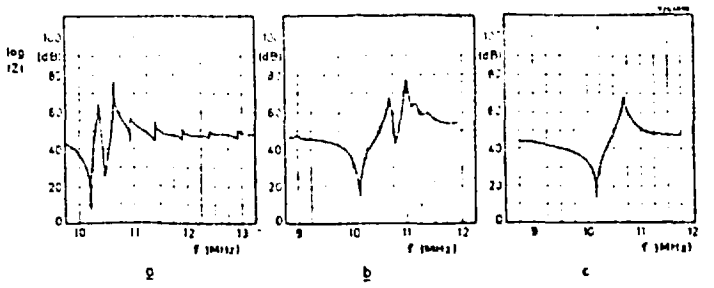

Fig. 8.1 - Influence of electrode diameter on the harmonic resonances of a thickness mode ceramic resonator.

a) electrode covering the entire area
b) electrode with 30% of ceramic diameter
c) electrode with 21,5% of ceramic diamete

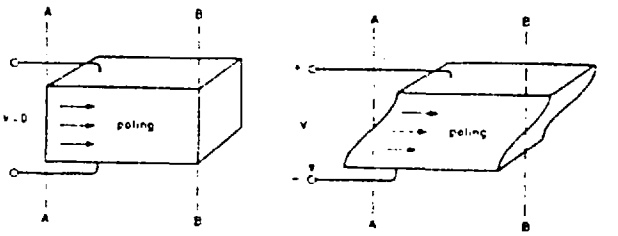

Fig. 8.2 - Transducer operating in a shear resonant mode (Ref.63)

and 8.4 a). The Fig. 8.4 b) shows a section detailing the accelerometer parts. Three slices of piezoelectric material are clamped between a central mass and seismic masses with a high radial force applied by a preloading ring. In a squeeze film bearing the central mass would be replaced by a neck associated with the base and the seismic masses could actually be fixed to the supporting surface. This system requires a very fine degree of flatness and dimensional accuracy for the areas in contact, but avoids the use of any adhesive in order to guarantee a good contact. The response curves obtained for this accelerometer show a displacement of the peak of about 10 KHZ for the new type, being about 5 db greater than the first one. It seems that it would be possible with this type of fitting to reduce considerably the loss at the piezoelectric ceramic interfaces.

iv) Using the same values of neck coefficient, ie. .2, .4 and .5, tests should be carried out to confirm the new arrangement referred to in ii)

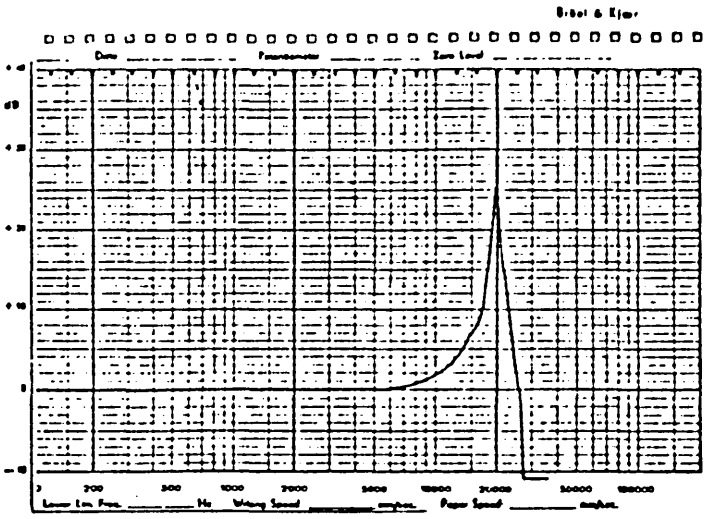

FIG. 8.3 Response curve for accelerometer (type 4332-4335) using a thickness mode operating ceramic.

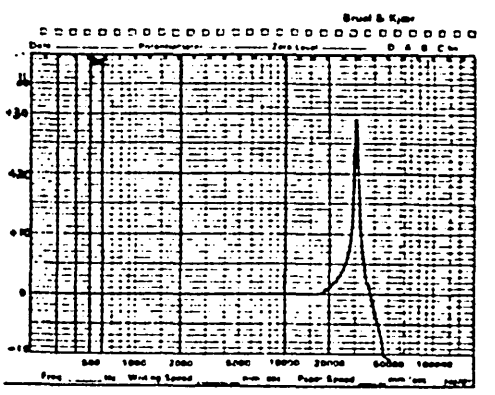

a)

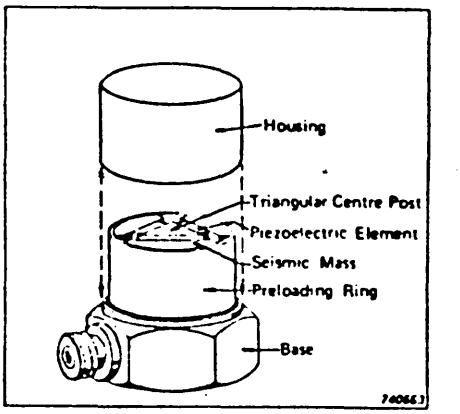

b)

FIG. 8.4 Response curve and arrangement diagram for identical accelerometer (series 4366, 4369)

and compare the results with those presented in this work.

v) For the values of the coefficient used, thinner discs (less than .003 m thick) should be used in experiments, similar to those performed in this study to verify the effect of disc thickness in both the amplitude of vibration and resonant frequency. Although disc supporting members can only provide axial load capacity this shape is recommended for these experiments. Discs are easy to manufacture and as shown, are sensitive to slight changes in geometry or arrangement of the support conditions.

A P P E N D I C E S

APPENDIX 1

APPENDIX 1

DESIGN OF SLAVE JOURNAL AND THRUST AIR BEARING

As mentioned in Chapter 6, this bearing is used to load the squeeze film bearing. One of the advantages of the use of this bearing is to vary the applied load continuously, if required. As it was also intended to measure load capacity for disc squeeze film bearings (Chapter 7), a journal bearing was also coupled to the thrust bearing arrangement, Fig. A.1.3. The journal bearing is used to prevent displacement of the disc in the horizontal plane.

a) Journal Bearing Design

As there is no applied load in the radial direction the design characteristics of this bearing were mainly dictated by size and manufacturing considerations. It was intended to have a reduced bearing size to give space to measuring equipment of the rig and a simple design for low cost.

The available air pressure could reach 90 p.s.i. but the bearing was designed for a supply pressure, p_s, of 64.7 p.s.i., so that the gauge pressure was 50 p.s.i. For this value of $p_s - p_a$ there is design data already available.

The journal bearing length was chosen to be L = 1 in. and the air jets placed in the middle plane, Fig. A.1.4, central admission. This gives a value of the distance from the jet to the edge of the bearing of $\ell^* = .5$.

The air jets used in these bearings can be of two types, recessed jets or plain jets as in Fig. A.1.1. Plain jets were chosen because they are easier to manufacture.

We assumed a diametral clearance between the bearing and the shaft**, $2C = 2 \times 10^{-5}$m (8×10^{-4} in.) and a bearing diameter, $L = 25.4 \times 10^{-3}$m (1 in.).

Another parameter used in design calculations is the bearing pressure factor, K_{go}, defined as:

$$K_{go} = \frac{p_{ds} - p_a}{p_s - p_a}$$

where p_{ds} is the pressure adjacent to jet and p_s and p_a are considered as before. For maximum load capacity and if $p_a > .0213$, Whitley[59] suggests that the value of K_{go} must be .4. Using design data from (33), for L/D = 1, $\ell/L = .5$ and number of jets, n = 8, the jet diameter is $d = 3 \times 10^{-3}$ in.

---

* ℓ is the distance from the jet position to the bearing edge.

** The shaft in this case is a small cylinder represented in Fig. A.1.1.

As we used four jets only, the value of d must be corrected. The diameter and number of jets are related by:

$$d \propto \frac{1}{n}$$

so, the corrected diameter is:

$$d_{co} = 2d = 6 \times 10^{-3} \text{ in.}$$

The calculated volume flow for this geometry is, from (30) and after correction:

$$v_{co} = 6.06 \times 10^{-5} \text{ m}^3/\text{s}.$$

b) Thrust Bearing Design

The thrust air bearing provides the force to be applied to the squeeze film bearing during the experiments referred to in Section 6.4.

As in case a) we assume a supply pressure p_s = 64.7 p.s.i. and a laboratory atmosphere, p_a = 14.7 p.s.i. In this case the clearance and the pressure force adjust to each other. The gas (air in this case) can be supplied through either a single jet or a ring of jets, Fig. A.1.3. Assuming one central jet and a clearance value of 10^{-3} in., the maximum bearing stiffness is obtained when bearing pressure factor, $K_g = .69$[33]. The bearing load capacity is proportional to K_g:

$$W = K_g(p_s - p_a) \frac{\pi(b^2 - a^2)}{2 \log_e (b/a)}$$

The optimum jet diameter (for central jet) using a ratio b/a = (.5/.2)in. = 2, is d = .02".

The calculated maximum load capacity using the expression is W = 16.49 lb_f

The journal-thrust bearing is shown in Fig. A.1.3. The bearing components are represented in Fig. A.1.4 (journal bearing), Fig. A.1.5 (thrust bearing), Fig. A.1.6 (bearing collar), Fig. A.1.7 (upper plate) and Fig. A.1.8 (lower plate). This design was slightly altered after test in the following manner:

1) Four small holes were made in the thrust air bearing plate (Fig. A.1.5), spaced at 90 degrees, providing more escape of air from the recess when this bearing is operating.

2) The cylinder represented in Fig. A.1.3 used only one pin to transmit the force to the squeeze film bearing as this seemed to be sufficient for proper location of Part 6.

3) An air intake to a manometer was provided in

the thrust air bearing to give direct load reasings after calibration.

c) Calibration of air thrust bearing

The air pressure existing in the thrust bearing recess was used for measurement of the load provided by this bearing. This pressure was read in an Hg manometer. In order to transform these pressure readings in the respective load values a calibration was necessary.

This consisted of using a load cell in place of the supported member of the squeeze film bearing. The load values were then plotted against the corresponding pressure readings, as presented in Fig. A.1.9.

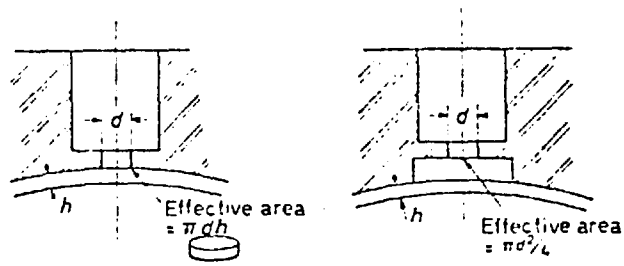

(a) Plain jet

(b) Jet with circular pocket

FIG. A.1.1 Type of jets used in air thrust bearings.

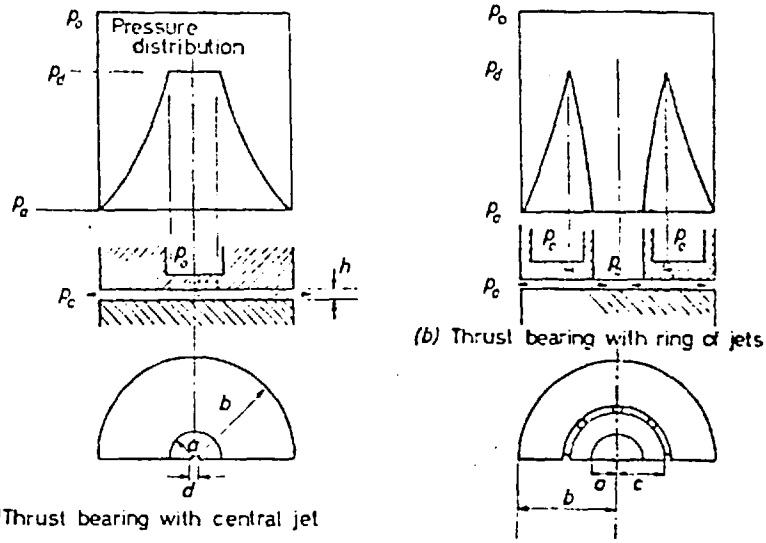

FIG. A.1.2 pressure distribution for jets represented in Fig. A.1.1

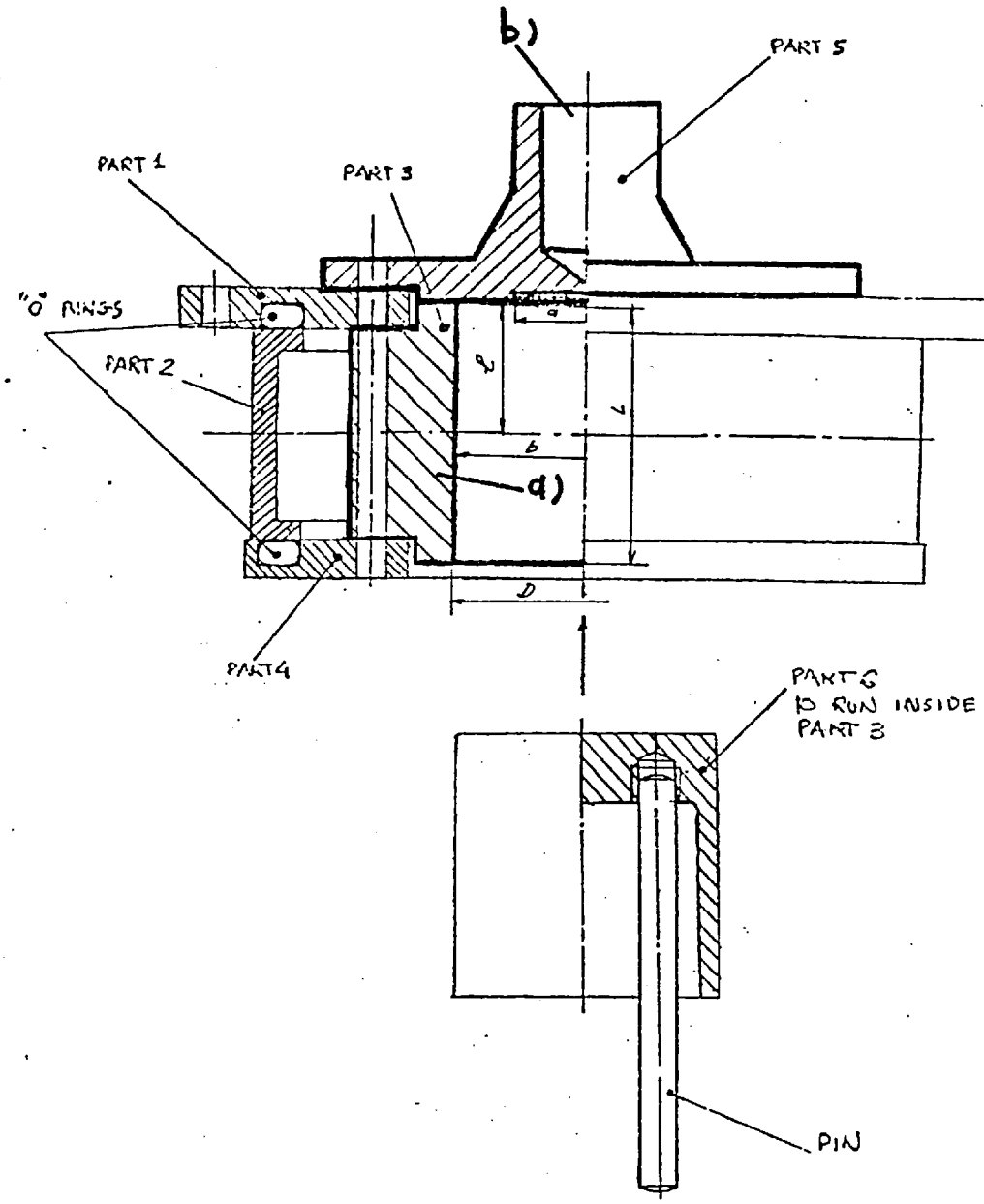

Fig. A.1.3 The journal-thrust bearing

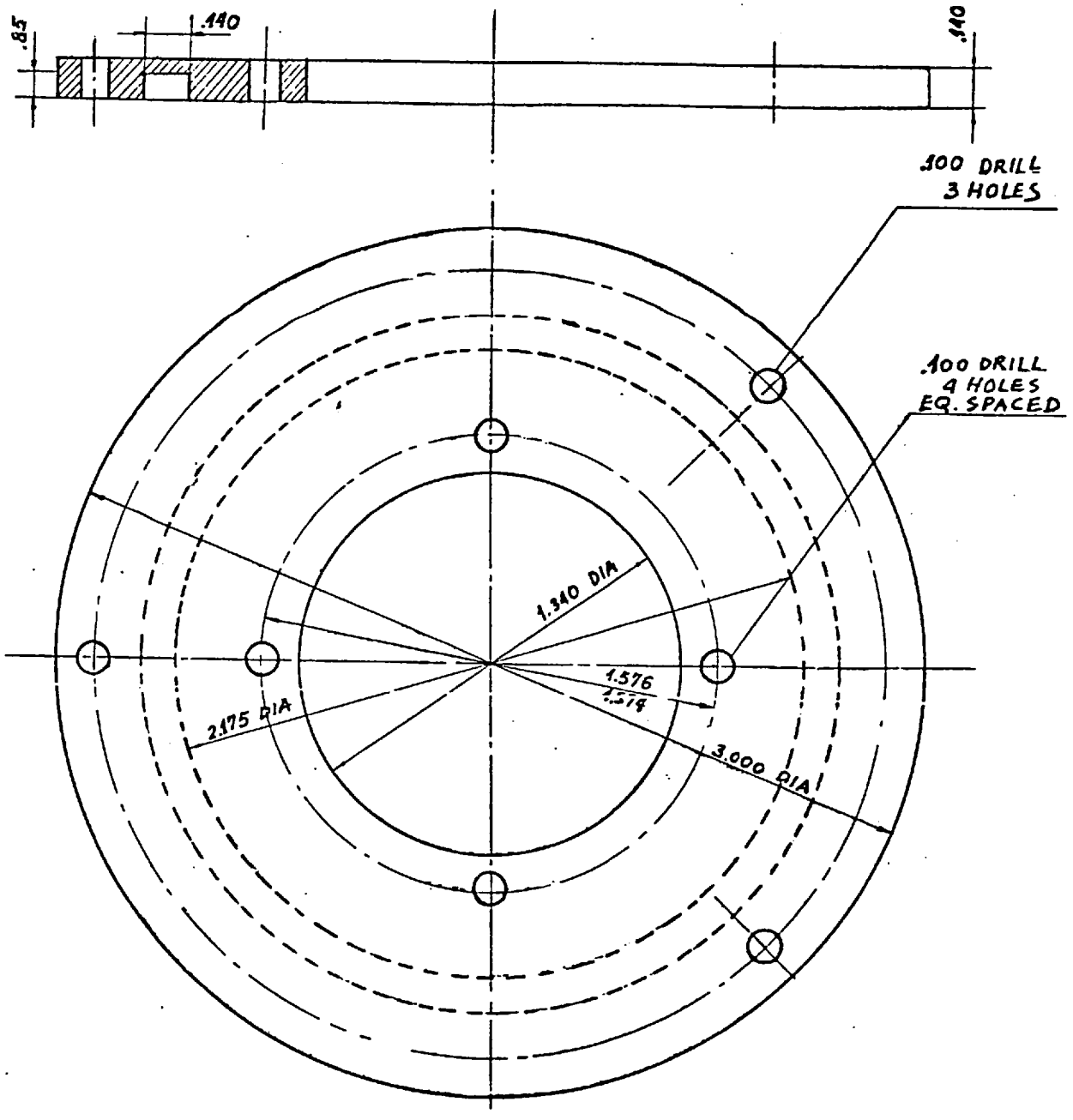

Component 1
Material - Steel

FIG. A.1.4 Bearing case upper plate.

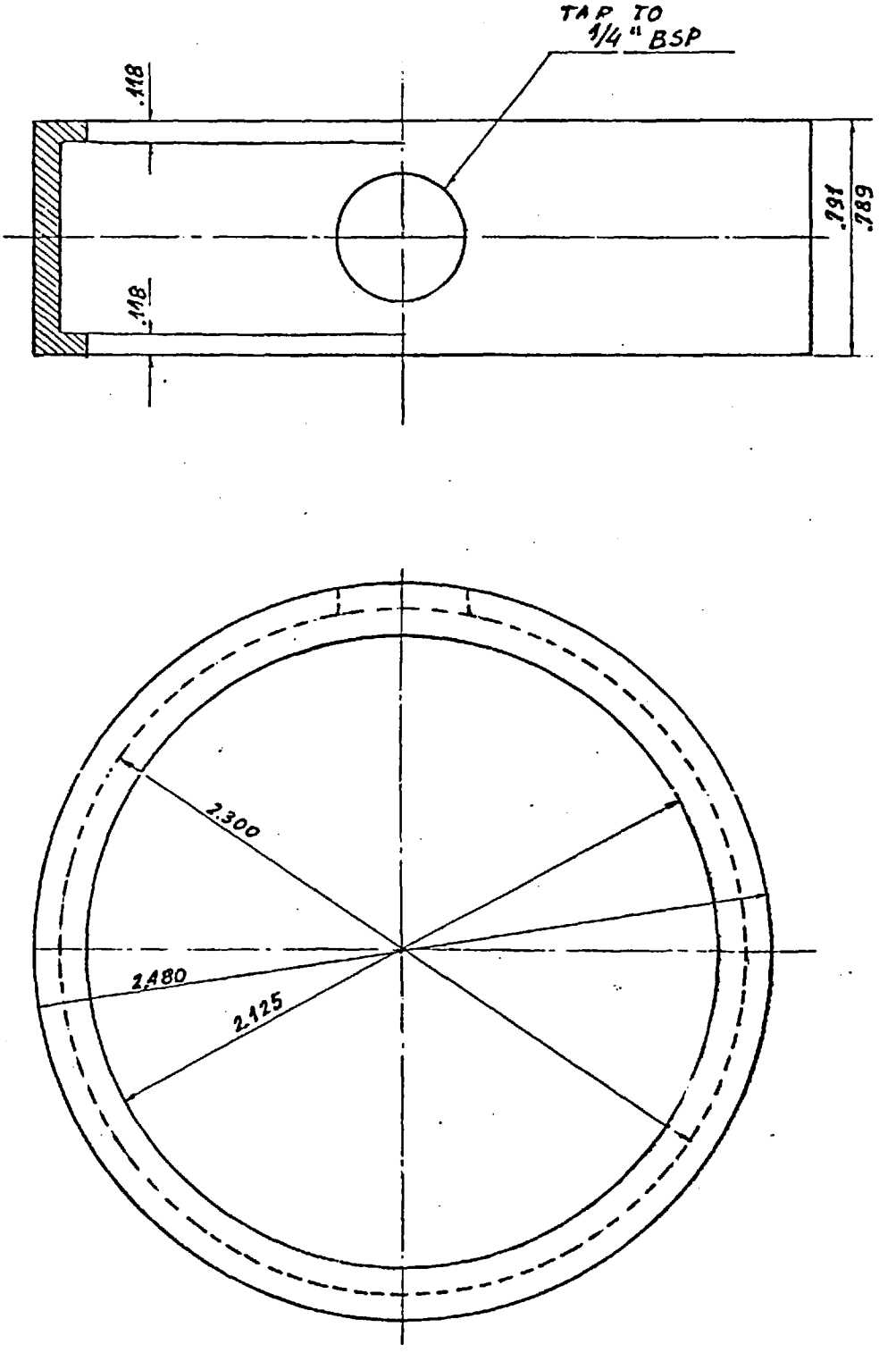

Component 2
Material - Steel

FIG. A.1.5 Journal bearing distribution collar.

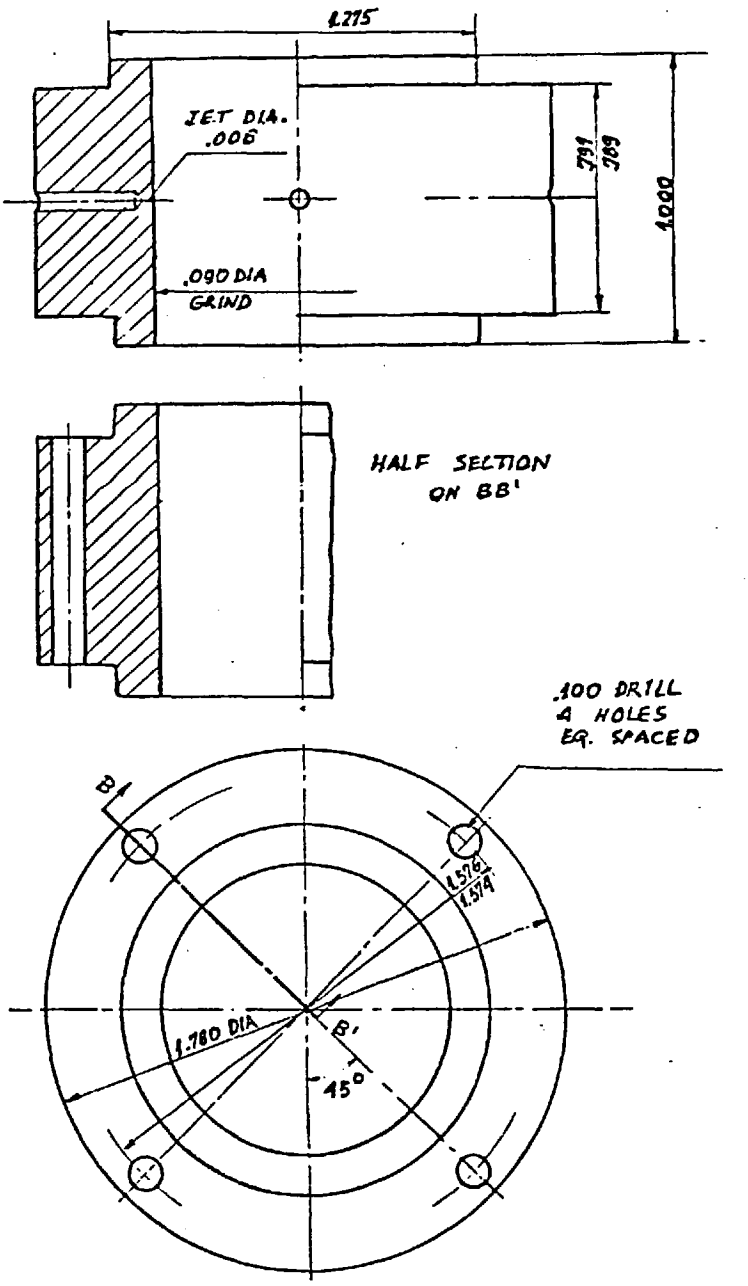

Component 3
Material - Steel

FIG. A.1.6 Journal Air Bearing.

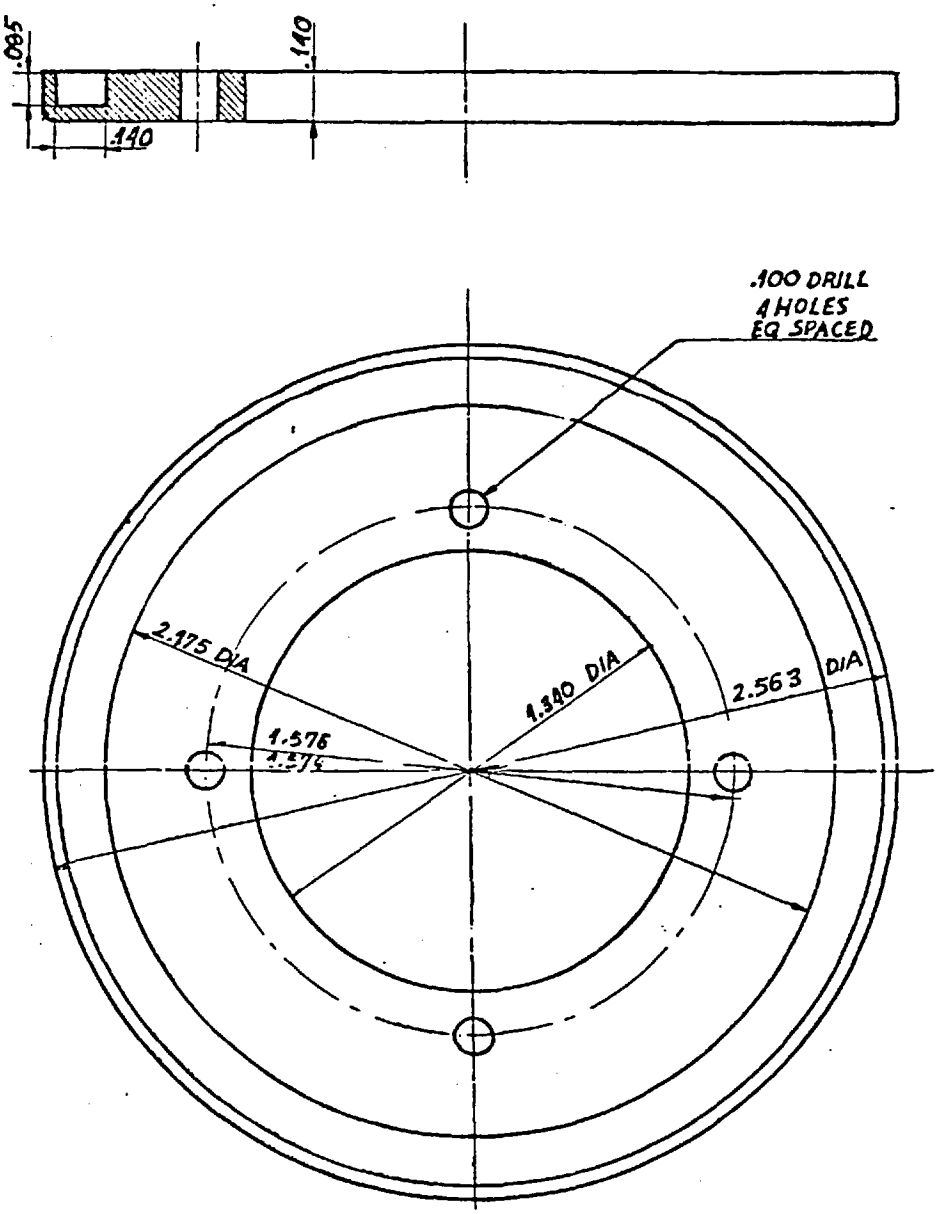

Component 4
Material - Steel

FIG. A.1.7 Bearing case lower plate.

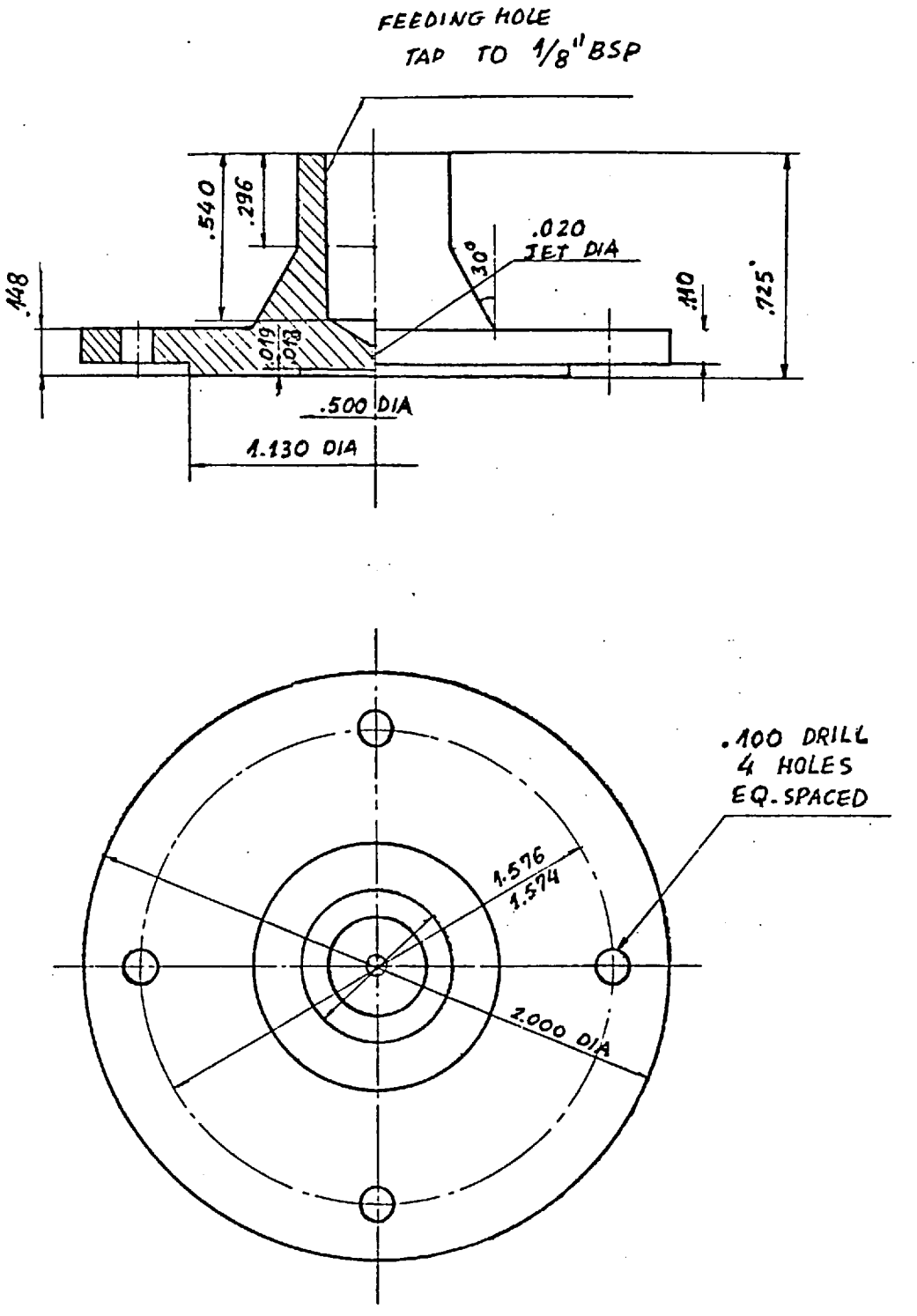

Component 5
Material - Steel

FIG. A.1.8 Thrust Air Bearing.

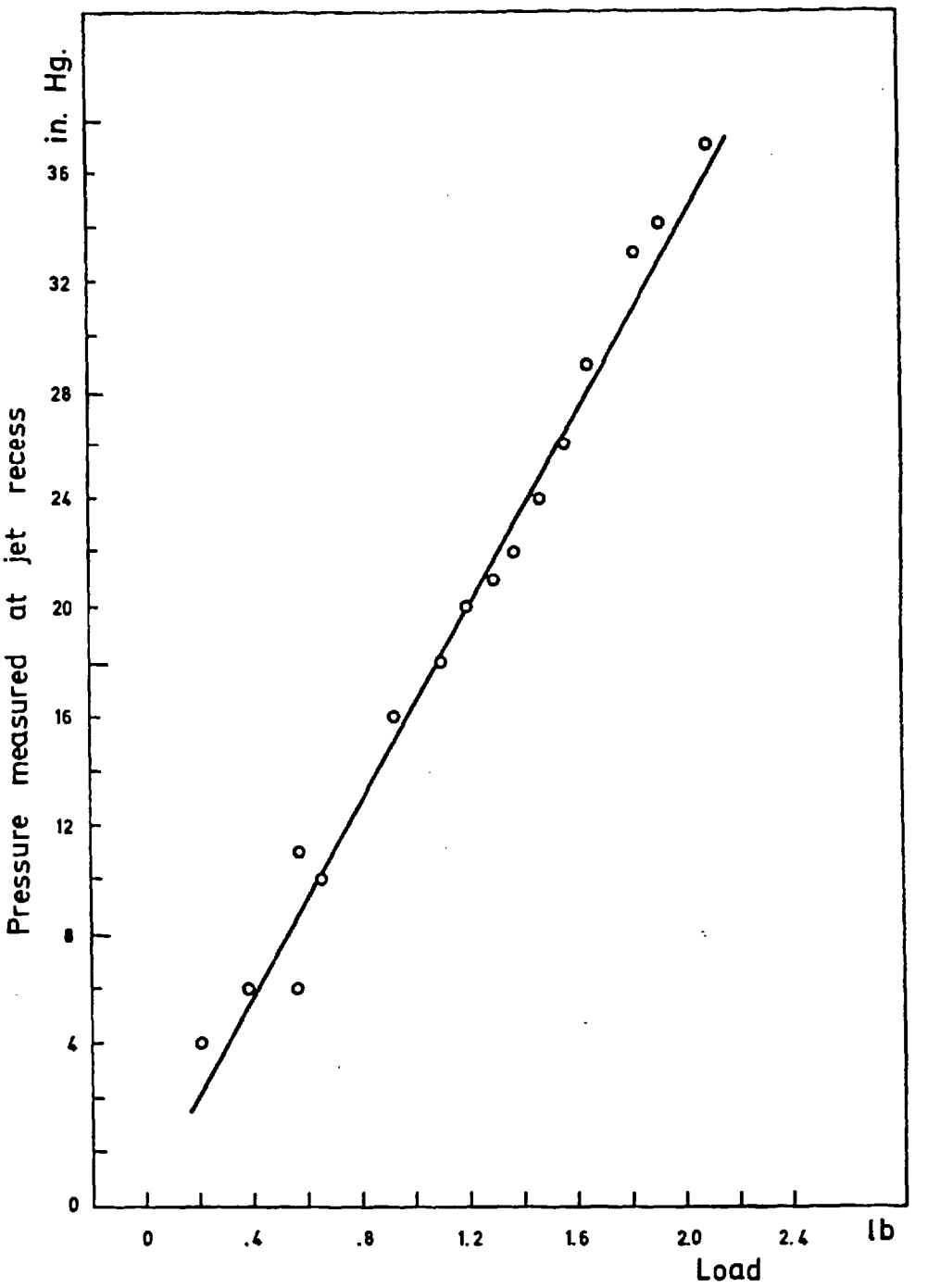

FIG. A.1.9 Measured pressure and corresponding generated force at squeeze film bearing.

APPENDIX 2

DESIGN OF TORQUE SETTING APPARATUS

The experiments referred to in Chapter 5 require the use of a torque wrench set to several torques. This torque was applied to tighten each of the six bolts of the ceramic-metallic base arrangement. For this purpose a wrench torque was available, but it needed an accurate torque calibrating apparatus. This apparatus, represented in Fig. A.2.1, was made at Imperial College. Basically it consists of a beam of rectangular section (H), from which weights can be hung (I). This produces a torque that should rotate the beam around an axis about which the wrench (F) is also applied. The wrench is held stationary, and tends to oppose this rotation.

The useful range of the torque wrench was defined by the manufacturers as being 7 to 140 Kg cm (.68 t0 13.7 Nm) but for our experiment the maximum value used was 3.91 Nm . So as the total length of the beam .05 m was chosen and 1.2×10^{-4} mm^2 as cross-section. To minimise the friction, ball bearings (F) were used to support the beam axle. These bearings were housed in a support (A), which also provided the fixing of the apparatus in a vice by (D). The beam weight itself was used to produce the resistant torque. A

small counterpoise (C) provided the rounding of the value of the fixed torque T_r to 12 Kg cm (1.17 Nm). To immobilise the torque wrench there is a pin (C) adjustable by an eccentric (K). To guarantee that in this position the beam is in a horizontal position, there is a small level (J) bonded to the beam. The material used for the beam was steel and that of the support, wood. The wrench had a torque adjusting screw in the handle. After putting the weight(s) at the convenient distance(s) to produce the desired torque, the wrench torque is reduced using the screw until there is rotation at point 1. The wrench torque is then very slightly increased and this is considered as the required torque setting.

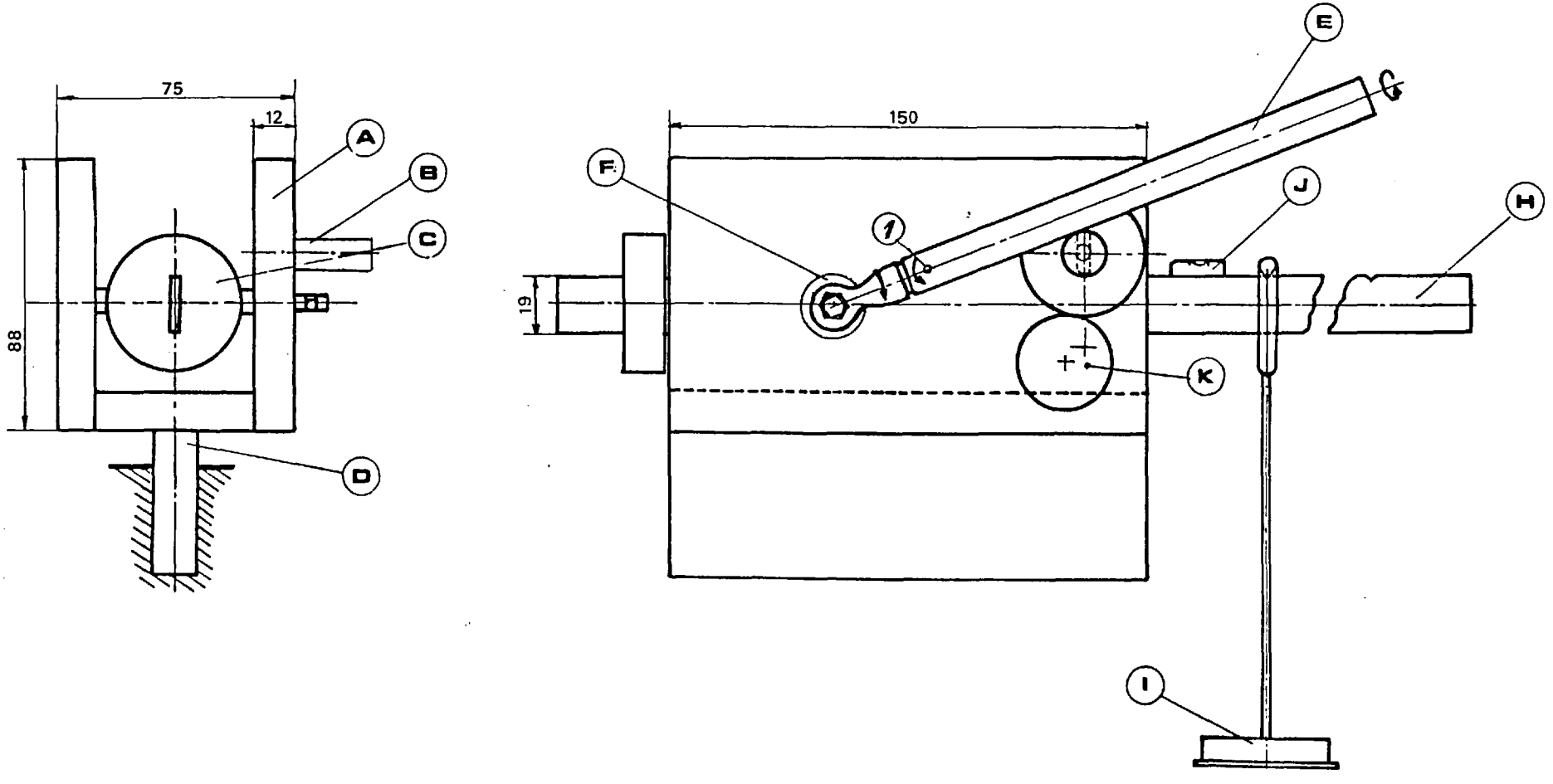

FIG. A.2.1 Torque-setting apparatus.

APPENDIX 3

```
C          PROGRAMME PRESSURE DISTRIBUTION 2
C        THIS PROGRAMME USES THE NEWTON RAPHSON METHOD
      DIMENSION H(36,13),DH(36,13),DDH(36,13),U(36,13),P(36,13)    ,
     1 RLOCEX(36),DISPLM(36),T(13),CN(36),CNW(36),CNE(36),
     2 CNF1(36),CNF2(36),DDEF1(36),DDWF2(36),DGI(36),DGP1(36),DGM1(30
     3 ,SA(36),SB(36),SC(36),SD(36),CORR(36),ERROR(36)
      EXTERNAL    RAPNEW
      READ (5,20)    (DISPLM(I),I=1,36)
   20 FORMAT (F8.5)
      N=35
      IN =N+1
      L=12
      IL =L+1
      DELEX =1./FLOAT(N)
      DELT=3.14159/16.
      RKAPAA =3.72
      RB=17.2
      RA=42.5
      VISCOS =1.32E-11
      YM=207.E3
      PK=RKAPAA/RA
      TH=2.*10.E-1*RA
      PA=1.013E-1
      HO=25.4E-4
      PARAM=VISCOS/(PA*HO**2)
      D=YM*TH**3/(12.*0.91)
      W=SQRT(D*PK**4/(7850.*TH*10E-9))
      SQUENU=12.*W*RA**2*PARAM
      WRITE(6,2002) W,SQUENU
 2002  FORMAT(20X,3H W=,F8.2,20X,8H SQUENU=,F9.3)
      DO   601 I=1,IN
      RLOCEX(I)=DISPLM(I)/2.54
      DO 602  J=2,IL
      T(J)=(FLOAT(J-2)+0.5)* DELT
      H(I,J)= 1.-RLOCEX(I)*SIN(T(J))
  602  CONTINUE
       T(1)=0.
      H(I,1)=1.-RLOCEX(I)*SIN(T(1))
   601   CONTINUE
       DO 621 J=1,IL
      DO 604 I=2,N
      DH(I,J)=(H(I+1,J)-H(I-1,J))/(2.*DELEX)
      DDH(I,J)=(H(I+1,J)-2.*H(I,J)+H(I-1,J))/(DELEX**2)
  604   CONTINUE
      DH(IN,J)=DH(N,J)
      DH(1,J)=0.
      DDH(IN,J)=DDH(N,J)
       DDH(1,J)=2.*(H(2,J)-H(1,J))/DELEX**2
  621    CONTINUE
      DO 631 I=1,IN
      U(I,1)=H(I,1)
      P(I,1)=U(I,1)/H(I,1)
  631  CONTINUE
      J=1
      CALL            RAPNEW (H,DH,DDH,U,J,N,L,SQUENU)
       DO 606 J=2,L
      CALL            RAPNEW (H,DH,DDH,U,J,N,L,SQUENU)
  606      CONTINUE
      DO 654  J=1,IL
      WRITE (6,2005) J
 2005 FORMAT (20X,40H THE NEXT VALUES ARE FOR THE TIME STEP =,I2)
      WRITE (6,2006)
 2006  FORMAT (25X,10H POINT REF,8X,10H LOC EXCUR,15X,8H LOC GAP,18X,
     117H PRESSURE DISTRIB)
      DO 605 I=1,IN
       P(I,J)=U(I,J)/H(I,J)
      WRITE (6,2007)     I,RLOCEX(I),H(I,J), P(I,J)
 2007 FORMAT (23X,I2,13X,F9.6,16X,F10.7,18X,F10.7)
  605  CONTINUE
  654  CONTINUE
       STOP
       END
       SUBROUTINE  RAPNEW (H,DH,DDH,U,J,N,L,SQUENU)
      DIMENSION H(36,13),DH(36,13),DDH(36,13),U(36,13),T(13),CN(36),
     1CNW(36),CNE(36),CNF1(36),CNF2(36),DDEF1(36),DDWF2(36),DGI(36),
     2 DGF1(36),DGM1(36),SA(36),SB(36),SC(36),SD(36),CORR(36),ERROR(36)
     3 ,A(36),B(36),DDWF1(36)
C      CNW IS W
C      CNE IS QUI
C      CNF1 IS F1
C      CNF2 IS F2
C      DDW1 IS DERIVATIVE OF F1 TO W
C      DDW2 IS DERIVATIVE OF F2 TO W
C      DDEF1 IS DERIVATIVE OF F1 TO QUI
C      DGI IS DERIVATIVE OF GI TO PSI IN I POINT
```

```
C      DGM1 IS DERIVATIVE OF GI TO PSI IN I-1 POINT
C      DGP1 IS DERIVATIVE OF GI TO PSI IN I+1 POINT
C      CN IS FI
       IL=L+1
       IN=N+1
       DELT=3.14159/18.
       DELEX =1./FLOAT(N)
       CN(IN)=U(IN,J)
       CN(1)=U(1,J)
       DO 582 I=2,N
       CN(I)=U(I,J)
  582   CONTINUE
C
C      FOR  I=1 IS NECESSARY TO SUBSTITUTE THE VALUE IN POINT I-1 BY THE
C        I+1 VALUE FOR THE VARIABLES U,CN
  250  DO 581 I=1,N
       CNW(I)=(CN(I)+U(I,J))/2.
       IF(I.EQ.1)   CNE(I)=0.
       IF (I.EQ.1)     GO TO 80
       CNE (I)=(CN(I+1)-CN(I-1)+U(I+1,J)-U(I-1,J))/(4.*DELEX)
   80  CNF1(I)=(-CNW(I)**2*DDH(I,J)+H(I,J)*CNE(I)**2-CNW(I)*CNE(I) *
      1DH(I,J))/SQUENU
       CNF2(I)=H(I,J)*CNW(I)/SQUENU
       DDWF1(I)=(2.*CNW(I)*DDH(I,J)+CNE(I)*DH(I,J))/(-SQUENU)
       DDWF2(I)=H(I,J)/SQUENU
       DDEF1(I)=(2.*H(I,J)*CNE(I)-CNW(I)*DH(I,J))/SQUENU
       IF(I.EQ.1)  DGI(I)=1.-DELT*DDWF1(I)/2.-DELT*(-2.*CN(I)+2.*CN(I+1)+
      12.*U(I+1,J)-2.*U(I,J))/(4.*DELEX**2)+DELT*CNF2(I)/DELEX**2
       IF(I.EQ.1)    GO TO 81
       DGI(I)=1.-DELT*DDWF1(I)/2.-DELT*(CN(I+1)-2.*CN(I)+CN(I-1)+
      1 U(I+1,J)-2.*U(I,J)+U(I-1,J))/(4.*DELEX**2)+DELT*CNF2(I)/DELEX
      2**2
         IF (I.EQ.N)     DGP1(I)=0.
         IF (I.EQ.N)   GO TO 89
   81   DGP1(I)=-DELT*DDEF1(I)/(4.*DELEX)-DELT*CNF2(I)/(2.*DELEX**2)
         IF(I.EQ.1)    DGM1(I)=0.
       IF (I.EQ.1)     GO TO 83
   89  DGM1(I)=DELT*DDEF1(I)/(4.*DELEX)-DELT*CNF2(I)/(2.*DELEX**2)
   83    SA(I)=DGP1(I)
         SB(I)=-DGI(I)
         SC(I)=DGM1(I)
       IF (I.EQ.1)  SD(I)=(-CN(I)+U(I,J)+DELT*CNF1(I)+2.*CN(I+1)-2.*
      1CN(I)+2.*U(I+1,J)-2.*U(I,J))*DELT*CNF2(I)/(2.*DELEX**2)
       IF (I.EQ.1)    GO TO 82
         SD(I)=(-CN(I)+U(I,J)+DELT*CNF1(I)+CN(I+1)-2.*CN(I)+CN(I-1)+
      1 U(I+1,J)-2.*U(I,J)+U(I-1,J))*DELT*CNF2(I)/(2.*DELEX**2)
   82    A(1)=0.
         B(1)=0.
         A(I+1)=SA(I)/(SB(I)-SC(I)*A(I))
         B(I+1)=(SC(I)*B(I)-SD(I))/(SB(I)-SC(I)*A(I))
  581   CONTINUE
C
C
       DO 701 K=1,N
         I=N+1-K
       CORR(N+1)=0.
         CORR(I)=CORR(I+1)*A(I+1)+B(I+1)
       CN(I)=CN(I)+CORR(I)
  701  CONTINUE
C
       DO 702 I=1,N
       ERROR (I) =ABS(CORR(I)*CN(I))
       ERRMAX=ERROR(1)
       IF (ERROR(I).GE.ERRMAX)      ERRMAX=ERROR(I)
       U(I,J+1)=CN(I)
  702  CONTINUE
         U(IN,J+1)=H(IN,J+1)
       IF (ERRMAX.GT.10.E-4)    GO TO 250
         RETURN
        END
```

APPENDIX 4

```
C                                  FRECON     2
C     ***********RUNGA-KUTTA METHOD IS USED FOR INTEGRATION*******
C      A1,A2,A3,A4,A5,A6, ARE KNOWN VALUES FOR THE VARIABLES
C
C
C*****UNITS IN MKS SYSTEM
C     DZ IS INCREMENT IN Z COORDINATE
C     L REPRESENTS THE NUMBER OF INTEGRATION INTERVALS
C      ALPHA IS HALF APEX ANGLE
C
C*****CALCULATIONS FOR ALUMINIUM CONE AS USED IN EXPERIMENTS
      DIMENSION  AL(15,6),BE(15,6),GA(15,6)
      DIMENSION     VREP(15),WREP(15)
      DIMENSION     V(15),W(15),S(15),RV(15),RO(15),RN(15)
      DIMENSION     VDIFP(15),VERREP(15),D VREP(15)
       REAL  K1,L1,M1,N1,K2,L2, M2,N2,K3,L3, M3,N3,K4,L4,M4,N4
      ALPHA=3.14159/4.
C     NDET DEFINES THE PROGRAMME REQUIRED OUTPUT
C     IF NDET=1  ONLY FREQUENCIES ARE FOUND
      NDET=1
      FREMUL=1000.
      IM=1
 30   RFREQ=13000.+FLOAT(IM)*FREMUL
C     WF IS FREQUENCY IN RAD PER SECOND
      L=14
       WF=2.*3.14159*RFREQ
      WRITE (6,1500)     WF
 1500  FORMAT (55X,26H NEXT RESULTS REFER TO WF=,F8.1)
      PIN=0.
       MIN.QU=1
      A1=1.
      A2=0.
      A3=0.
       A4=0.
       A5=1.
      A6=COS(ALPHA)/SIN(ALPHA)
      B1=0.
      B2=0.
      B3=1.
      B4=0.
      B5=0.
      B6=COS(ALPHA)/SIN(ALPHA)
      C1=1.
      C2=0.
        C3=0.
         C4=1.
          C5=0.
      C6=COS(ALPHA)/SIN(ALPHA)
       A=10.5E-3
      B=30.E-3
 95   AL(1,1)=A1
      AL(1,2)=A2
      AL(1,3)=A3
      AL(1,4)=A4
      AL(1,5)=A5
      AL(1,6)=A6
      BE(1,1)=B1
      BE(1,2)=B2
      BE(1,3)=B3
      BE(1,4)=B4
      BE(1,5)=B5
      BE(1,6)=B6
      GA(1,1)=C1
      GA(1,2)=C2
      GA(1,3)=C3
      GA(1,4)=C4
      GA(1,5)=C5
      GA(1,6)=C6
 96    AA1=A1
      AA2=A2
      AA3=A3
      AA4=A4
       AA5=A5
       AA6=A6
       DO 100   I=1,L
        DZ=(B-A)/FLOAT(L)
       Z=A
      CALL FUCAL   (Z,A1,A2,A3,A4,A5,A6,F1,F2,F3,F4,F5,F6,WF)
      K1=DZ*F1
       L1=DZ*F2
        M1=DZ*F3
      N1=DZ*F4
      P1=DZ*F5
      Q1=DZ*F6
```

```
      Z=Z+.5*DZ
      A1=A1+.5*K1
      A2=A2+.5*L1
      A3=A3+.5*M1
      A4=A4+.5*N1
      A5=A5+.5*P1
      A6=A6+.5*Q1
      CALL FUCAL  (Z,A1,A2,A3,A4,A5,A6,F1,F2,F3,F4,F5,F6,HF)
      K2=DZ*F1
      L2=DZ*F2
      M2=DZ*F3
      N2=DZ*F4
      P2=DZ*F5
      Q2=DZ*F6
      A1=A1+.5*K2
      A2=A2+.5*L2
      A3=A3+.5*M2
      A4=A4+.5*N2
      A5=A5+.5*P2
      A6=A6+.5*Q2
      CALL FUCAL  (Z,A1,A2,A3,A4,A5,A6,F1,F2,F3,F4,F5,F6,HF)
      K3=DZ*F1
      L3=DZ*F2
      M3=DZ*F3
      N3=DZ*F4
      P3=DZ*F5
      Q3=DZ*F6
      Z=Z+.5*DZ
      A1=A1+K3
      A2=A2+L3
      A3=A3+M3
      A4=A4+N3
      A5=A5+P3
      A6=A6+Q3
      CALL FUCAL  (Z,A1,A2,A3,A4,A5,A6,F1,F2,F3,F4,F5,F6,HF)
      K4=DZ*F1
      L4=DZ*F2
      M4=DZ*F3
      N4=DZ*F4
      P4=DZ*F5
      Q4=DZ*F6
      AA1=AA1+(K1+2.*(K2+K3)+K4)/6.
      AA2=AA2+(L1+2.*(L2+L3)+L4)/6.
      AA3=AA3+(M1+2.*(M2+M3)+M4)/6.
      AA4=AA4+(N1+2.*(N2+N3)+N4)/6.
      AA5=AA5+(P1+2.*(P2+P3)+P4)/6.
      AA6=AA6+(Q1+2.*(Q2+Q3)+Q4)/6.
      A1=AA1
      A2=AA2
      A3=AA3
      A4=AA4
      A5=AA5
      A6=AA6
      M=I+1
      IF (NINEQU.EQ.2)                GO TO 91
      IF (NINEQU.EQ.3)                GO TO 92
      AL(M,1)=AA1
      AL(M,2) =AA2
      AL(M,3) =AA3
      AL(M,4) =AA4
      AL(M,5) =AA5
      AL(M,6) =AA6
      GO TO 100
C     THESE CALCULATIONS RESPECT ONLY ALPHAS.NEXT IS BETAS CALCULATION
   91 BE(M,1) =AA1
      BE(M,2) =AA2
      BE(M,3) =AA3
      BE(M,4) =AA4
      BE(M,5) =AA5
      BE(M,6) =AA6
      GO TO 100
C     NEXT IS GAMA CALCULATION
   92 GA(M,1) =AA1
      GA(M,2) =AA2
      GA(M,3) =AA3
      GA(M,4) =AA4
      GA(M,5) =AA5
      GA(M,6) =AA6
  100 CONTINUE
      NINEQU=NINEQU+1
      IF (NINEQU.EQ.3)        GO TO 24
      IF (NINEQU.EQ.4)           GO TO 25
      A1=B1
      A2=B2
      A3=B3
```

```
      A4=C4
      A5=C5
      A6=C6
        GO TO 96
   24 A1=C1
      A2=C2
      A3=C3
      A4=C4
      A5=C5
      A6=C6
        GO TO 96
   25 TA=AL(15,3)*GA(15,4)*AL(15,5)
      TB=BE(15,3)*GA(15,4)*AL(15,5)
      TC=GA(15,3)*AL(15,4)*BE(15,5)
      TD=AL(15,5)*BE(15,4)*GA(15,3)
      TE=AL(15,3)*BE(15,5)*GA(15,4)
      TF=AL(15,4)*BE(15,3)*GA(15,5)
      DET1=TA+TB+TC
      DET2=TD+TE+TF
      DET=DET1-DET2
      WRITE (6,6700)      DET1,DET2
 6700 FORMAT (40X,F25.5,10X,F25.5)
      RNATR    =NF/(2.*3.14159)
           WRITE      (6,6600)          RNATR   ,DET
 6600        FORMAT   (40X,14H FOR MAT FREQ=,F9.3,5X,5H DET=,F20.5)
      IF    (IM.EQ.1)          PREDET=DET
      IF    (PRED.LT.0..AND.DET.LT.0.)          FREMUL=FREMUL/10.
      IF    (PRED.GT.0..AND.DET.LT.0.)          IM=IM-2
      IF(PREDET.LT.0..AND.DET.GT.0.)            IM=IM-2
      IF(PREDET.LT.0..AND.DET.GT.0.)            FREMUL=FREMUL/10.
      PREDET=DET
      CHEDET=ABS(DET)
      IM=IM+1
      IF(NDET.NE.1)          GO TO 28
      IF(NDET.EQ.1)     GO TO 30
      IF (CHEDET.LE.10.E-3)          STOP
C     *     *     *     *     *     *     *     *     *     *     *     *
CCC   *     *     *     *     *     *     *     *     *     *     *     *
CCCC
C***** NOW CALCULATE FORCES AND MOMENTS AT THE INNER BOUNDARY
   28 RHS=10.E-52
      RNA=0.
      RQA=0.
      RQ2=AL(15,3)*BE(15,5)-BE(15,3)*AL(15,5)
      RQ2P=AL(15,3)*BE(15,5)/AL(15,4)
      RQ3=RQ2P-BE(15,3)*AL(15,4)
      RM3=AL(15,4)*BE(15,5)-AL(15,5)*BE(15,4)
      RQ4P=RQ2P
      RQ4=RQ2P-BE(15,4)*AL(15,3)
      RQ1=AL(15,4)*BE(15,5)*GA(15,3)
      RQ2=AL(15,5)*GA(15,3)*BE(15,4)
      RQ3=GA(15,3)*BE(15,4)*AL(15,5)
      RQ4=AL(15,5)*BE(15,5)*GA(15,4)
      RQ5=AL(15,4)*GA(15,5)*BE(15,3)
      RQ6=GA(15,4)*BE(15,3)*AL(15,5)
      RQCA=-RQ1-RQ2+RQ3+RQ4+RQ5-RQ6
      RQA=(RC1*RQP-RQ2*RNB-RC3*RM3+RC4*RNB)/RQCA
      R11=AL(15,5)/AL(15,5)
      R12=AL(15,5)*GA(15,3)/AL(15,5)-GA(15,3)
      R13=(AL(15,3)*BE(15,5)-BE(15,3)*AL(15,5))/AL(15,5)
      RNA=(R13-R11*RNB+RM2*RQA)/(-R13)
      RMA=(RNB-BE(15,5)*RNA-GA(15,5)*RQA)/AL(15,5)
      H=3.E-3
      EDGAR =2.*3.14159*A*SIN(ALPHA)*H/COS(ALPHA)
      FORCE=(RNA*COS(ALPHA)+RQA*SIN(ALPHA))*EDGAR
      WRITE    (6,2007)
 2007 FORMAT (25X,3HRMA,20X,3HRNA,12X,3HRQA,12X,5HFORCE)
      IF (PIN.EQ.1.)          RSA=RMA
      IF (PIN.EQ.0.)     WRITE(6,2008)       RMA,RNA,RQA,FORCE
      IF (PIN.EQ.1.)     WRITE(6,2008)       RSA,RNA,RQA,FORCE
 2008 FORMAT (20X,E14.7,5X,E14.7,5X,E14.7,5X,E14.7 )
      WRITE(6,2009)
 2009 FORMAT (1HX,4HV(Z),6X,4HW(Z),2X,4HS(Z),10X,5HRN(Z),6X,5HRQ(Z),
     1 8X,5HRN(Z),5X,7HVREP(Z),5X,7HWREP(Z),5X,9HDVREP(Z))
      DO 101 IC=2,15
      V(IC)=AL(IC,6)*RNA+BE(IC,6)*RMA+GA(IC,6)*RQA
      W(IC)=AL(IC,1)*RNA+BE(IC,1)*RMA+GA(IC,1)*RQA
      S(IC)=AL(IC,2)*RNA+BE(IC,2)*RMA+GA(IC,2)*RQA
      RM(IC)=AL(IC,3)*RNA+BE(IC,3)*RMA+GA(IC,3)*RQA
      RQ(IC)=AL(IC,4)*RNA+BE(IC,4)*RNA+GA(IC,4)*RQA
      RN(IC)=AL(IC,5)*RNA+BE(IC,5)*RMA+GA(IC,5)*RQA
      VREP(IC)=V(IC)/FORCE
      WREP(IC)=W(IC)/FORCE
```

```
      VDISP(IC)=V(IC)*COS(ALPHA)+W(IC)*SIN(ALPHA)
      VREP(IC)=VDISP(IC)/FORCE
      DBVREP(IC)=20.*ALOG(ABS(VREP(IC)))/ALOG(10.)
      WRITE (6,2010) V(IC),W(IC),S(IC),RM(IC),RO(IC),RN(IC),VREP(IC),
     1DISP(IC),DBVREP(IC)
2010  FORMAT(2X,9E12.4)
101   CONTINUE
      IF (FREQ.GT.6000.)          GO TO 28
      H=3.E-3
      R1=6.E-3
      R2=25.5E-3
      HCONE =20.E-3
      RMASS=2720.
      CONE=3.14159*HCONE*(R1+R2+H)*H
      COMASS=CONE*RMASS
      CONREP CHECKS  REACTANCES USING APPARENT MASS
      CONREP=-20.*ALOG(WF**2*COMASS)/ALOG(10.)
      WRITE (6,2012)      CONREP
2012  FORMAT (  46X,7HCONREP=,F7.2)
****  NEXT CALCULATIONS ARE FOR PINNED INNER EDGE CONDITION
      PIN=PIN+1.
      WRITE (6,2015)
2015  FORMAT (////,50X,19H****PINNED COND****,//)
      A1=1.
      A2=0.
      A3=0.
      A4=0.
      A5=1.
      A6=COS(ALPHA)/SIN(ALPHA)
      B1=0.
      B2=1.
      B3=0.
      B4=0.
      B5=0.
      B6=0.
      C1=0.
      C2=0.
      C3=0.
      C4=1.
      C5=0.
      C6=0.
        STOP
        END
      SUBROUTINE   FUCAL  (Z,A1,A2,A3,A4,A5,A6,F1,F2,F3,F4,F5,F6,WF)
      THE SUBROUTINE FUCAL CALCULATES THE VALUES OF THE FUNCTIONS
       ALPHA=3.14159/4.
      E=69.9E9
      H=1.5E-3
      R=33.E-3
       H=7.E-3
      RMASS=2720.
      POIS=.3
       RCONST=RMASS*WF**2*H
        D=E*H**3/(12.*(1.-POIS**2))
       CT=COS(ALPHA)/SIN(ALPHA)
      AA=(1.-POIS**2)*D/Z**2
      BB=-(1.-POIS)/Z
      CC=E*H*CT**2/Z-RCONST
      DD=POIS*CT/Z
        EE=E*H*CT/Z
      FF=EE
      GG=(1.-POIS)/Z
       HH=E*H/Z-RCONST
       RM=DD
      RN=(1.-POIS**2)/(E*H)
      F1=A2
       F2=(-POIS/Z)*A2+A3/D
      F3=-AA*A2+BB*A3+A4
      F4=CC*A1-A4/Z-DD*A5-EE*A6
       F5=-FF*A1-GG*A5+HH*A6
      F6=RM*A1+RN*A5+(-POIS/Z)*A6
        RETURN
        END
```

APPENDIX 5

```
C**********PROGRAMME FREQIS 3**********
C
C
C     THIS PROGRAMME EVALUATES NATURAL FREQUENCIES OF ANNULAR DISCS
C     ADDITIONAL FREQUENCY EVALUATION BY MAXIMUM TOTAL RECEPTANCE
C     BASICALLY IS FREQIS WITH ADDITIONAL FEATURES
C     CALCULATION OF DETERMINANT FOR THE NATURAL FREQUENCIES IS MADE BY
C     A LIBRARY SUBROUTINE THAT IS NOT COMPATIBLE WITH -WNF- COMPILER
C
C
C     SLIDING AND CLAMPED INER BOUNDARY CONDITIONS ARE CONSIDERED
C     FREE OUTER BOUNDARY CONDITION
C
C
C
C        *** VARIABLE NAMELIST***
C     H IS PLATE THICKNESS
C     POC IS POISSON COEFFICIENT
C     BRAD IS INNER RADIUS(CM)
C     ARAD IS OUTER RADIUS(CM)
C     RMASS IS SPECIFIC MASS(7.85 G/CM3 FOR STEEL AND 2.72G/CM3 FOR
C     ALUMINIUM
C     W IS FREQUENCY VALUE(RAD/S)
C     COEF IS RATIO INNER/OUTER RADIUS
C     YMOD IS YOUNG MODULUS(207.E10 DYNES/CM2 FOR STEEL AND 68.9E10
C     DYNES/CM)
C     FRE2,FRE4, AND FRE5 ARE RESONANT FREQUENCIES FROM EXPERIMENTS FOR
C     DISCS WITH  2,4 AND .5 NECK COEFFICIENT
C     RK IS FREQUENCY PARAMATER
C     CRYSTI IS CRYSTAL STIFFNESS(DYNES/CM)
C
C     TOMAS IS MASS OF BASE+NECK-INLUDING INSIDE OF ANNULUS-(G)
C       NOTE THAT MATERIAL FOR THE BASE CAN BE STEEL OR ALUMINIUM
C
C     IREP CONTROLS RECEPTANCES OUTPUT
C     IREP=1 SLIDING+CLAMPED CONDITIONS CONSIDERED-OUTPUT BOTH DTERM,
C     IREP=2 SLIDING COND+TOTAL RECEPTANCE-OUTPUT TOTAL RECEPTANCE FOR
C     POINT AT INNER BOUNDARY
C     IREP=3 RECEPTANCE CALCULATION FOR EVERY POINT ALONG THE RADIUS-
C     OUTPUT TOTAL RECEPTANCE AND SIMPLE DISC RECEPTANCE
C     NCON CONTROLS CHECKING BRANCH
C     NCON=1 PRODUCES CHECKING OF B. FUNCTIONS AND DETERMINANT
C     NCON=2  NO CHECK FOR SUBROUTINES
C     IM IS FREQUENCY RANGE COUNTER
C     IFINT IS NUMBER OF FREQUENCY INTERVALS
C     FSTOP IS FINAL VALUE FOR FREQUENCY
      DIMENSION   R(4,4), A(4,4)
      EXTERNAL ID
      EXTERNAL INVE
      INTEGER DIM
C
      COEF=.2
C
C
  555 NCON=2
      IREP=2
      IDIS=0
      IAL=0
C
      FRE2=4002.
      FRE4=6171.
      FRE5=8067.
      CRYSTI=7.23E10
C     IAL IS MATERIAL SELECTOR FOR THE BASE AND NECK-IAL=0 CHOOSES STEEL
      IF(IAL.EQ.1)      GO TO 30
C          'STEEL BASE(AND NECK)*
      TOMAS2=233.8
      TOMAS4=257.7
      TOMAS5=283.7
      IF(IAL.EQ.0)      GO TO 31
C     *ALUMINIUM BASE(AND NECK)*
   30 TOMAS2=79.7
      TOMAS4=89.3
      TOMAS5=98.2
C
```

```
   31  POC=.3
       ARAD=3.
C
C      IDIS  IS MATERIAL SELECTOR FOR THE DISC- IDIS=0 CHOOSES STEEL
       IF(IDIS.EQ.0)      GO TO 51
C        *ALUMINUM DATA*
       RMASS=2.72
       YMOD=68.9E10
       IF(IDIS.EQ.1)     GO TO 51
C          *STEEL DATA*
   50  RMASS=7.85
       YMOD=207.E10
   51  H=.3
       FSTART=3.E3
       FSTOP=5.E3
       IFINT=10
       FSTEP=(FSTOP-FSTART)/IFINT
C
C
C
       IF(IDIS.EQ.0)     WRITE(6,25)
       IF(IDIS.EQ.1)     WRITE(6,26)
       IF(IAL.EQ.0)      WRITE(6,27)
       IF(IAL.EQ.1)      WRITE(6,28)
   25  FORMAT(50X,20H DISC MATERIAL=STEEL)
   26  FORMAT(50X,20H DISC MATERIAL=ALUM.)
   27  FORMAT(50X,20H BASE MATERIAL=STEEL)
   28  FORMAT(50X,20H BASE MATERIAL=ALUM.)
   61  BRAD=ARAD*COEF
       IF(IREP.NE.3)                GO TO 599
       IF(COEF.EQ..2)           FREQ=FRE2
       IF(COEF.EQ..4)           FREQ=FRE4
       IF(COEF.EQ..5)           FREQ=FRE5
       IF(IREP.EQ.3)            GO TO 599
  500  IM=1
       FSTART=FSTART-FSTEP
       FREQ=FSTART
  300  FREQ=FREQ+FSTEP
  599  W=FREQ*2.*3.1416
       IF(COEF.EQ..2)           TOMAS=TOMAS2
       IF(COEF.EQ..4)           TOMAS=TOMAS4
       IF(COEF.EQ..5)           TOMAS=TOMAS5
       AJL=12.*RMASS*(1.-POC**2)*ARAD**2
       ADENC=YMOD*4.**2
       RSQ=SQRT(AJL/ADENC)
       RK=SQRT(RSQ)
       RKAPAA=RK*ARAD
       RKAPAB=RK*BRAD
       WRITE (6,1000)      FREQ,COEF,RKAPAA
 1000  FORMAT(20X,32H THE NEXT VALUES ARE FOR FREQUE=,E12.4,15H  AND FOR
      1COEF=,F4.2,10X,8H RKAPAA=,F12.3)
       RJ=(POC-1.)/RKAPAA
       X=RKAPAA
       N=0
       DI=.001
       CALL BESJ(X,N,BJ,DI,IER)
       CALL BESY(X,N,BY,IER)
       CALL BESK(X,N,BK,IER)
       CALL I0(X,RI0)
       BJOA=BJ
       BYOA=BY
       BKOA=BK
       BIOA=RI0
       X=RKAPAB
       CALL BESJ(X,N,BJ,DI,IER)
       CALL BESY(X,N,BY,IER)
       CALL BESK(X,N,BK,IER)
       CALL I0(X,RI0)
       BJOB=BJ
       BYOB=BY
       BKOB=BK
       BIOB=RI0
       N=1
       RN=1.
       X=RKAPAA
       CALL BESJ(X,N,BJ,DI,IER)
       CALL BESY(X,N,BY,IER)
       CALL BESK(X,N,BK,IER)
       ZI=BIOA
       CALL  INUL       (X,RN,ZI,RI)
       BJ1A=BJ
       BI1A=RI
       BY1A=BY
       BK1A=BK
       X=RKAPAB
```

```
      R(3,2)=BY13
      R(3,3)=-BI13
      R(3,4)=BK13
      R(4,1)=BJ1A
      R(4,2)=BY1A
      R(4,3)=BI1A
      R(4,4)=-BK1A
      Y=DET(R,DIM,ND)
      WRITE(6,2006)          Y
 2006 FORMAT (55X,19H DETERM(S-F) VALUE=,F15.7)
      IF(IREP.EQ.1)          GO TO 809
      DETSF=Y
      IF(ABS(DETSF).LE.1.E-5)        GO TO 809
      IF(ABS(DETSF).LE.1.E-5)      GO TO 808

C     NEXT ARRAYS RESPECT SLIDING-FREE RECEPTANCE CALCULATION
      G4A=.JOA+RO*BJ1A
      G5A=BICA+RO*BI1A
      G12A=BYOA+RO*BY1A
      G13A=BKCA+RC*BK1A
      DIM=3
      ND=3
      R(1,1)=BY13
      R(1,2)=-BI13
      R(1,3)=BK13
      R(2,1)=BY1A
      R(2,2)=BI1A
      R(2,3)=-BK1A
      R(3,1)=G12A
      R(3,2)=-G5A
      R(3,3)=-G13A
      Y=DET(R,DIM,ND)
      DELA=Y
      R(1,1)=BJ13
      R(1,2)=-BI13
      R(1,3)=BK13
      R(2,1)=BJ1A
      R(2,2)=BI1A
      R(2,3)=-BK1A
      R(3,1)=G4A
      R(3,2)=-G5A
      R(3,3)=-G13A
      Y=DET(R,DIM,ND)
      DELB=Y
      R(1,1)=BJ13
      R(1,2)=BY13
      R(1,3)=BK13
      R(2,1)=BJ1A
      R(2,2)=BY1A
      R(2,3)=-BK1A
      R(3,1)=G4A
      R(3,2)=G12A
      R(3,3)=-G13A
      Y=DET(R,DIM,ND)
      DELC=Y
      R(1,1)=BJ13
      R(1,2)=BY13
      R(1,3)=-BI13
      R(2,1)=BJ1A
      R(2,2)=BY1A
      R(2,3)=BI1A
      R(3,1)=G4A
      R(3,2)=G12A
      R(3,3)=-G5A
      Y=DET(R,DIM,ND)
      DELC=Y
      DA=YMCO*H**3
      DB=12.*(1.-ROC**2)
      D=DA/DB
      XDENOM=D*BK**3*2.*3.1416*DETER*BRAD
      IF(ABS(XDENOM).LE.1.E-5)          WRITE(6,2021)
 2021 FORMAT(50X,25H DETERMINANT NEXT TO ZERO)
      IF(IREP.EQ.3)                GO TO 809
      XNUM=-DELA*BJOB+DELB*BYOB-DELC*BIOB+BILD*BKOB
      IF(IREP.EQ.4)                GO TO 808
      ALPHAB=XNUM/XDENOM
      ALPHAE=CRYSTL-W**2*TCMAS+1./ALPHAB
      ALTOTB=1./ALPHAP
      RMOB=ALTOTB*W
      CON/=ALOG(10.)
      RIO=20.*ALOG(ABS(RMOB))/CON/
      WRITE (6,2022)     ALPHAB,ALPHAP,ALTOTB,RMOB
 2022 FORMAT(10X,8H ALPHAB=,E12.4,5X,7H ALPHAP=,E12.4,5X,8H ALTOTB=,E12.4
     1,5H RMOB=,F12.6)
      IF(IREP.EQ.2)          GO TO 809
```

```
C
C       BRANCH FOR DISPLACEMENT CALCULATION
  808   WRITE(6,2025)
 2025 FORMAT(20X,6H POINT,5X,6H COORD,5X,7H RECEPT,5X,9H TORECEPT)
       DI=1.E-3
       X=RKAPAA
       DO 550 I=1,31
       X=X+(RKAPBB-RKAPAA)/31.
       N=0
       CALL BESJ(X,N,BJ,DI,IER)
       CALL BESY(X,N,BY,IER)
       CALL BESK(X,N,BK,IER)
       CALL I0(X,RI0)
       BJC=BJ
       BYC=BY
       BKC=BK
       BI0=RI0
       XNUM=-DELA*BJO+DELB*BYO-DELC*BI0+DELD*BKO
       ALPHAR=XNUM/XDENOM
       ALPHR=CRYSTI-W**2*TCHAS+1./ALPHAR
       ALTOIR=1./ALPHR
       WRITE(6,2028)     I,X,ALPHAR,ALTOIR
 2028 FORMAT(20X,I3,5X,F9.4,3X,E14.5,3X,E14.5)
  550  CONTINUE
       GO TO 810
  809  IM=IM+1
  800  IF(IM.LE.IFINT)              GO TO 300
  810  IF(COEF.EQ..5)          GO TO 444
       IF(COEF.EQ..4)          GO TO 333
       IF(COEF.EQ..2)          COEF=.4
       GO TO 555
  333  COEF=.5
       GO TO 555
  444  STOP
       END
       NOLIST
       SUBROUTINE   I0   (X,RI0)
       RI0 =ABS (X)
       IF (RI0 -3.75)    1,1,2
    1  Z=X*X*7.111111E-2
       RI0 =((((( 4.5813E-3*Z+3.60768E-2)*Z+2.659732E-1)*Z+1.206749E0)
      1*Z+3.0899424E0)*Z+3.5156229E0)*Z+1.
       RETURN
    2  Z=3.75/RI0
       RI0=EXP(RI0)/SQRT (RI0)*((((((((3.92377E-3*Z-1.647633E-2)*Z
      1 +2.635537E-2)*Z-2.057706E-2)*Z+9.16281E-3)*Z-1.57565E-3)*Z
      2+2.25319E-3)*Z+1.328592E-2)*Z+3.989423E-1)
       RETURN
       END
       SUBROUTINE INUE(X,RN,ZI,RI)
       IF(RN)      10,10,1
    1  FN=RN+RN
       QI =X/FN
       IF(ABS(X)-5.E-4)     6,6,2
    2  AJ =1.
       AI =0.
       BJ=0.
       BI=1.
       FI=FN
    3  FI=FI+2.
       AN =FI/ABS(X)
       A=AN*AI+AJ
       B=AN*BI+BJ
       AJ=AI
       BJ=BI
       AI=A
       BI=B
       QJ=QI
       QI=A/B
       IF  (ABS ((QI-QJ)/QI) -1.E-6)    4,4,3
    4  IF (X) 5,6,6
    5  QI=-QI
    6  K=IFIX(FN)
    7  QI=X/(FN+X*QI)
       RI =QI
       FN =FN-2.
       K=K-1
       IF (K)   8,8,7
    8  FI=ZI
       FI =FI*RI
       RI=FI
   10  RETURN
       END
```

APPENDIX 6

APPENDIX 6

DETERMINANT VALUES FOR DISC RECEPTANCE CALCULATION

(a) Force excitation at a free edge:

$$\Delta_A = \begin{vmatrix} G_{12}(kr_b) & -G_5(kr_b) & -G_{13}(kr_b) \\ Y_1(kr_a) & I_1(kr_a) & -K_1(kr_a) \\ G_{12}(kr_a) & -G_5(kr_a) & -G_{13}(kr_a) \end{vmatrix}$$

$$\Delta_B = \begin{vmatrix} G_4(kr_b) & -G_5(kr_b) & -G_{13}(kr_b) \\ J_1(kr_a) & I_1(kr_a) & -K_1(kr_a) \\ G_4(kr_a) & -G_5(kr_a) & -G_{13}(kr_a) \end{vmatrix}$$

$$\Delta_C = \begin{vmatrix} G_4(kr_b) & G_{12}(kr_b) & -G_{13}(kr_b) \\ J_1(kr_a) & Y_1(kr_a) & -K_1(kr_a) \\ G_4(kr_a) & G_{12}(kr_a) & -G_{13}(kr_a) \end{vmatrix}$$

$$\Delta_D = \begin{vmatrix} G_4(kr_b) & G_{12}(kr_b) & -G_5(kr_b) \\ J_1(kr_a) & -I_1(kr_a) & I_1(kr_a) \\ G_4(kr_a) & G_{12}(kr_a) & -G_5(kr_a) \end{vmatrix}$$

(b) Force excitation at a sliding edge:

$$\Delta_A = \begin{vmatrix} Y_1(kr_b) & -I_1(kr_b) & K_1(kr_b) \\ Y_1(kr_a) & I_1(kr_a) & -K_1(kr_a) \\ G_{12}(kr_a) & -G_5(kr_a) & -G_{13}(kr_a) \end{vmatrix}$$

$$\Delta_B = \begin{vmatrix} J_1(kr_b) & -I_1(kr_b) & K_1(kr_b) \\ J_1(kr_a) & I_1(kr_a) & -K_1(kr_b) \\ G_4(kr_a) & -G_5(kr_a) & -G_{13}(kr_a) \end{vmatrix}$$

$$\Delta_C = \begin{vmatrix} J_1(kr_b) & Y_1(kr_b) & K_1(kr_b) \\ J_1(kr_a) & Y_1(kr_a) & -K_1(kr_a) \\ G_4(kr_a) & G_{12}(kr_a) & -G_{13}(kr_a) \end{vmatrix}$$

$$\Delta_D = \begin{vmatrix} J_1(kr_b) & Y_1(kr_b) & -I_1(kr_b) \\ J_1(kr_a) & Y_1(kr_a) & I_1(kr_a) \\ G_4(kr_a) & G_{12}(kr_a) & -G_5(kr_a) \end{vmatrix}$$

where:

$$G_4(kr_i) = J_o(kr_i) + \frac{\nu-1}{kr_i} J_1(kr_i)$$

$$G_5(kr_i) = I_o(kr_i) + \frac{\nu-1}{kr_i} I_1(kr_i)$$

$$G_{12}(kr_i) = Y_o(kr_i) + \frac{\nu-1}{kr_i} Y_1(kr_i)$$

$$G_{13}(kr_i) = K_o(kr_i) - \frac{\nu-1}{kr_i} K_1(kr_i)$$

REFERENCES

REFERENCES

1. TIPEI, N. (1954) Equatile Lubrificatiei cu Gaze. Communicarile, Acad. R.P. Romine, 4, p. 699.

2. REINER, M. (1958) A Centripetal Pump Effect in Air. Proc. 9th Congr. Appl. Mech., Brussels, 1, pp. 424-438.

3. TAYLOR, G.I. and SAFFMAN, P.G. (1957) Effects of Compressibility at Low Reynolds Numbers. J. Aero. Sciences, 24, p. 533.

4. LANGLOIS, W.E. (1962) Isothermal Squeeze Films. Quart. Appl. Math., XX, (2), p. 131.

5. MICHAEL, W.A. (1962) Approximate Methods for Time-Dependent Gas Film Lubrication. I.B.M. Research Report RJ-205. Also, J. Appl. Mech., 30, p. 509 (1963).

6. SALBU, E.O.J. (1964) Compressible Squeeze Films and Squeeze Bearings. Trans. ASME, (D), (J. Basic Eng.), pp. 355-364.

7. PAN, C.H.T. (1964) Analysis, Design and Prototype Development of Squeeze Film Bearings for AB-5 Gyro. MIT, Report 64-TR-66.

8. CHIANG, T. and PAN, C.H.T. (1965) Analysis and Design Data for the Axial Excursion, Transducer of Squeeze Film Bearings. MIT Report 65-TR-25.

9. ORCUTT, F.K., KISSINGER, C. and PAN, C.H.T. (1965) Investigation of an Axial Excursion Transducer for Squeeze Film Bearings. MIT Report 65-TR-63.

10. MALANOSKI, S.B. and PAN, C.H.T. (1964) Discussion of Ref. 6, Trans. ASME, (D), (J. Basic Eng.), pp. 364-366.

11. PAN, C.H.T. (1967) On Asymptotic Analysis of Gaseous Squeeze Film Bearings. Trans. ASME, (F),

(J. Lubric. Tech.), 89, pp. 245-253.

12. PAN, C.H.T. and BROUSSARD, P.H. Jr. (1967) Squeeze Film Lubrication. Gas Bearing Symp., Univ. Southampton, Paper 12.

13. PAN, C.H.T., MALANOSKI, S.B., BROUSSARD, P.H. Jr. and BURCH, J.L. (1966) Theory and Experiments of Squeeze Film Bearings: Part I - Cylindrical Journal Bearing. Trans. ASME, (D), (J. Basic Eng.), 88, p. 191.

14. CHIANG, T., MALANOSKI, S.B., and PAN, C.H.T. (1967) Spherical Squeeze-Film Hybrid Bearing with small Steady State Radial Displacement. Trans. ASME, (F), (J. Lub. Tech.), 89, p. 254.

15. BECK, J.V. and STRODTMAN, C.L. (1967) Stability of a Squeeze-Film Journal Bearing. Trans. ASME, (F), (J. Lub. Tech.), 89, pp. 369-373.

16. ELROD, H.G. (1967) A Differential Equation for Dynamic Operation of Squeeze Film Bearings. Gas Bearing Symp., Univ. of Southampton, Paper 1.

17. DIPRIMA, R.C. (1968) Asymptotic Methods for an infinitely long Slider Squeeze-Film Bearing. Trans. ASME, (F), (J. Lub. Tech.), 90, pp. 173-183.

18. CHIANG, T. (1968) Dynamic Behaviour of the Spherical Hybrid Bearing. ASME Paper 68, LUB S-37.

19. BECK, J.V. and STRODTMAN, C.L. (1968) Load Support of Spherical Squeeze-Film Gas Bearings. ASME Paper 68, LUB S-3.

20. PAN, C.H.T. (1967) Discussion of Ref. 12, Gas Bearing Symp., Univ. of Southampton.

21. PAN, C.H.T. and CHIANG, T. (1968) On Error Torques of Squeeze Film Cylindrical Journal Bearings. Trans. ASME, (F), (J. Lub. Tech.), 90, p. 191.

22. STRODTMAN, C.L. (1968) Discussion of Ref. 21, Trans. ASME, (F), (J. Lub. Tech.), 90, p. 659.

23. BECK, J.V. and STRODTMAN, C.L. (1968) Load Support of the Squeeze Film Journal Bearing of Finite Length. Trans. ASME, (F), (J. Lub. Tech.), 90, pp. 157-161.

24. PAN, C.H.T. (1970) The Gaseous Squeeze Film at Moderately Large Squeeze Numbers. MIT Report 70-TR-26.

25. PAN, C.H.T. and Chiang, T. (1968) Discussion of Ref. 23, Trans. ASME, (F), (J. Lub. Tech.), 90, pp. 655-658.

26. CHIANG, T., PAN, C.H.T. and ELROD, H.G. (1970) Dynamic Response of a Double Squeeze Film Thrust Plate. Trans. ASME, (F), (J. Lub. Tech.), 92, pp. 363,369.

27. STRODTMAN, C.L., BECK, J.V. and HOLLIDAY, W.G. (1968) Experimental Analysis of a Flat Disc Squeeze Film Bearing including Effects of Supported Mass Motions. ASME Paper 68 LUB S-35.

28. CONSTANTINESCU, V.N. (1969) Gas Lubrication. English translation published by ASME

29. STRODTMAN, C.L. (1970) An Augmented, Small Parameter Equation for the Squeeze Film Journal Bearing. Trans. ASME, (F), (J. Lub. Tech.), 92, pp. 442-449.

30. COOKE, D.D. (1974) Performance Comparisons between Grooved and Ungrooved Squeeze Film Bearings. Royal Aircraft Establishment, Technical Report 74115.

31. HUXLEY, A.S. (1972) Progress in Squeeze Film Technology. Paper 16, 5th Joint ONR/UK Gas Bearing Meeting.

32. LIGHT, L. (1962) Relative Humidity and Condensation of Water Vapour in Air-Lubricated Heads. IBM Research Report, NC 121.

33. GRASSAM, N.S. and POWELL, J.W. (Editors)(1964) Gas Lubricated Bearings. Butterworths, London.

34. GROSS, W.A. (1959) Film Lubrication - Part VIII. IBM Research Paper RJ 117-8.

35. LEES, M. (1959) Apprximate Solutions of Parabolic Equations. J. Soc. Ind. App. Match., 7, pp. 167-183.

36. VON NEUMANN, J. and RICHTMEYER, R.V. (1950) A Method for the Calculation of Hydrodynamical Shocks. J. App. Phys. 21, pp. 232-237.

37. CRANK, S. and NICOLSON, P. (1947) A Practical Method for Numerical Evaluation of Solutions of Parcial Differ ential Equations of the Heat Conduction Type.

38. KANTOROVICH, L.V. (1952) Functional Analysis and Applied Mathematics. Translated from the Russian by C.D. Benster, National Bureau of Standars, Report 1509.

39. CONSTANTINESCU, V.N. (1969) On High Frequency Squeeze Films. Paper 26, Southampton Gas Bearing Symposium Southampton University, 22-25 April.

40. FOTONIC SENSOR KD INSTRUCTIONS MANUAL, MTI, Instruments Division.

41. Private Comunication from MTI, Latham, New York.

42. General Information on Piezoelectric Geramics, (1965), Clevite Corporation, Ohio.

43. ONOE, M., TIERSTEN, H. and MAITZLER, H. (1963) Shift in the Location of Resonant Frequencies caused by large Electromechanical Coupling in Thickness-Mode Resonators. J. Acoust. Soc. Am., 35. (1).

44. LAWSON, A.W. (1942) The Vibration of Piezoelectric Plates Proceedings of Cambridge Philosophical Society, Vol. 43, pp 50-67. Phys. Rev., 62, p. 71. July.

45. STEPHENSON, C.V. (1956) Vibrations in long Rods of Barium Titanate with Electric Field Parallel to the length J. Acoust. Soc. Am., 28, p. 1192.

46. TIERSTEN, H.F. (1963) Thickness Vibrations of Piezoelectric Plates. J. Acoust. Soc. Am., 35, p. 53.

47. PAN, C.H.T. and VOHR, J.H. (1966) Gas Lubrication for Non-contact Suspension of Instruments. Gas Bearing Proc., 1, December.

48. MERKULOV, J.G. (1957) Design of Ultrasonic Concentration Soviet Physics-Acoustics, 3, pp. 246-255.

49. MERKULOV, J.G. and KHARITONOV, A.V. (1959) Theory and Analysis of Section Concentrators. Soviet Physics Acoustics, 5, p. 183.

50 SALTER, J.P. (1960) Steady State Vibration. Ed. Kenneth Mason.

51. STRUTT, M.J.O. (1933) Free Vibrations of Conical Shells Ann. Physik, 17, (7), pp. 729-735.

52. VAN URK, A.T. and HUT, G.B. (1933) Radial Vibrations of Aluminium Cones. Ann. Physik, 17, (8), pp. 915.

53. FEDERHOFER, K. (1938) Natural Vibration Frequencies of Conical Shells. Ingr.-Arch., 9, (4), pp. 288-308.

54. LOVE, A.E.H. (1944) A Treatise on the Mathematical Theory of Elasticity. 4th Edition, Dover Publications, New York.

55. SAUNDERS, H. and PASLAY, P.R. (1959) Inextesional Vibrations of a Sphere-Cone Shell. J. Acoust. Soc. Am., 31, (5), pp. 579-583.

56. SAUNDERS, H., WISNIEWSKI, E.J. and PASLAY, P.R. (1960) Vibrations of Conical Shells. J. Acoust. Soc. Am., 32, (6), pp. 765-772.

57. PLATUS, D.H. (1965) Conical Shell Vibrations. NASA Technical Note TN-D-2767.

58. GOLDBERG, J.E., BOGDANOFF, J.L. and MARCUS, L. (1960) On the Calculation of the Axisymmetric Modes and Frequencies of Conical Shell. J. Acoust. Soc. Am., 32, (6), pp. 738-742.

59. WHITLEY, S. (1959) Review of Research on Gas Bearings in the United Kingdom Atomic Energy Authority. 1st Int. Symp. on Gas Lubricated Bearings, Washington, D.C. pp. 30-70.

60. CONTE, S.D. (1965) Elementary Numerical Analysis - An Algorithmic Approach. McGraw-Hill Company.

61. IRE Standards on Piezoelectric Crystals : Measurements of Piezoelectric Ceramics. (1961) Proc. IRE 49, pp. 1161-1169.

62. McLEOD, A.J. and BOSHOP, R.E.D. (1965) The Forced

Vibration of Circular Plates. Mechanical Engineering Monograph, No. 1, March.

63. RANDERADT, J. VAN and SETTENINGTON, R.E. (Editors) (1974) Piezoelectric Ceramics. Mullard Limited, London.

64. DAWE, D.J. (1965) A Finite Element Approach to Plate Vibration Problems. J. Mech. Eng. Sci., 7, (1), pp. 28, 32.